CONTINUOUS PRODUCTION OF CARBON NANOTUBES USING CARBON ARC REACTOR: ANODE SURFACE TEMPERATURE STUDY AND CFD MODELLING

A thesis submitted in partial fulfilment of the requirements for the

Degree of

Doctor of Philosophy in Chemical and Process Engineering

in the

University of Canterbury

by

Hamdan bin Mohamed Yusoff

University of Canterbury

2008

Acknowledgment

Alhamdulillah, All praises be to Allah, the Most Gracious and The Most Merciful for giving me the strength and the good health to complete my tasks.

I wish to express my sincerest appreciation and gratitude to Professor John Abrahamson for his endless guidance, support, and assistance that (my family & I) had settled well in Christchurch for the past four years and now completing the manuscript. Many thanks to Paul Tolson for his technical input in the course of modifying the reactor, to Rahul and Thomas for sharing the passions and the thrills in working with the arc and also to others who had developed the arc reactor over a number of years: Julianna Keen, Andrew Hill, Prithi Mani, Markus Leistner, Can Ulubay and Ray Archer.

The appreciation should also goes to the following parties; Ministry of Science, Technology and Innovation, Malaysia and University of Putra Malaysia for funding the PhD scholarship and University of Canterbury for providing the space and facilities to carry out the work and also Mac Diarmid Foundation for funding the research.

The never ending prayers, supports and assistance from my families (Akak, Kak Ngah, Abang Mie, Andak, Alang, and Anjang) and friends had given me the strength especially during the ups and downs. The laughter, loves and tears that we shared had intensified our friendships: Just to name - Jali & family, Saufi & family, Zahari & family, Azmi & family, Shidee & family, Nik, Amir & friends, Hanafee & friends, Ummu & friends and others.

This thesis is dedicated to my beloved little families: my late parents, my wife, Dayang, and my four active boys: Abdullah, Aiman, Umar and Uqayl. For the loves and the joyous of lives that we have are the best treasures of all.

Abstract

The mass production of carbon nanotubes (CNTs) by a cost effective process is still a challenge for further research and application of CNTs. This research focussed on the deposition of CNTs on a continuously-fed carbon substrate via arc discharge at atmospheric pressure. In this work, modifications, control and optimization of the available arc-discharge reactor were conducted. New reactor support and new tape feeding mechanisms were added to the reactor for better temperature assessment, longer operating period and better control of the speed of the tape.

The influence of inter-electrode gap, substrate velocity and arc current on the surface temperature were investigated. Multiwalled carbon nanotubes (MWNTs) were produced at lower currents (< 20 A) and at larger inter-electrode gaps. Further investigation shows that inter-electrode gap influenced both the arc characteristic and the anode surface temperature (T_s). Here, Ts was measured by an optical pyrometer.

The inter-electrode gap was found to indirectly affect the formation of NTs. Anode surface temperature (T_s) varied with gap, reaching a minimum at an intermediate gap. Higher CNTs yield was found at this lowest T_s. This minimum T_s is consistent with the presence of a cloud of nanoparticles ejected by the heated graphite/carbon surfaces. These graphene fragments are thought to later fold and form nanotube "seeds" and then develop into multiwall nanotubes. This cloud of nanoparticles also may affect the electrical conductivity at the front of the anode. Simulation of the arc behaviour, *i.e.* temperature distributions and flow properties of the plasma, using a computer package Comsol Multiphysics 3.2, was stable only when the electrical conductivity of a dusty plasma near to the electrodes was included.

Our experiments show that carbon nanotubes grew better at a T_s range of ~ 3650 K – 3700 K and at the tape speed of 3 mm/s. The results from our work also strongly suggested that tiny carbon crystallites are the main intermediates for CNT growth in an electric arc. The limiting factor for a solid state growth mechanism, therefore, is high temperature annealing of carbon or graphene fragments. Further work should aim to understand the growth mechanism of CNTs, produce comprehensive analysis on the arc plasma composition and also explore the possibility of producing CNTs at higher rates.

Table of Content

Acknowledgments i
Abstract ii
Nomenclature viii
Abbreviation xii
List of Figures xiv
List of Tables xx

Chapter 1: Introduction 1-1
1.1 A brief history of carbon nanotubes (CNTs) 1-1
1.2 Nanotube structure 1-1
1.2.1 Single walled Nanotubes (SWNTs) 1-2
1.2.2 Multi-walled Nanotubes 1-4
1.3 Nanotube properties and potential application 1-6
1.3.3 Mechanical properties 1-6
1.3.4 Electrical properties 1-7
1.4 Synthesis method 1-7
1.4.5 Arc discharge method 1-7
1.4.6 Chemical Vapour Deposition (CVD) 1-9
1.4.7 Laser ablation 1-10
1.4.8 Other methods 1-12
1.5 Research objectives 1-13
1.6 Outline of this work 1-13
1.7 References 1-15

Chapter 2: CNT Growth in an Electric Arc 2-1
2.1 Introduction 2-1
2.2 Theories of CNT growth 2-1
2.2.1 Vapour phase growth 2-1
2.2.2 Liquid phase growth 2-5
2.2.3 Solid phase growth 2-6
2.2.4 The crystallization model 2-7

2.3 What do CNT growth from?....2-7
2.3.5 Nuclei for the growth of CNT....2-7
2.4 Growth of CNTs....2-10
2.4.1 Carbon cluster nucleation....2-10
2.4.2 Nucleation Temperature....2-10
2.4.3 CNT growth process....2-11
2.4.4 Electric field....2-12
2.4.5 End of growth (Growth termination)....2-13
2.5 Catalytic growth of SWNTs....2-14
2.6 New thought of CNT formation....2-18
2.6.1 Nanoparticles as feed stock for CNT formation....2-19
2.6.2 Anode surface temperature measurement....2-21
2.7 References....2-22

Chapter 3: Experimental design and set-up 3-1
3.1 Introduction....3-1
3.2 History of 2000's batch reactor....3-1
3.2.1 Batch Reactor design....3-4
3.2.2 Comparison with 1978's reactor....3-6
3.3 Continuous arc reactor....3-7
3.3.1 Reactor design....3-7
3.3.2 Querrioux's work....3-11
3.3.3 Constraints in the continuous reactor design....3-13
3.4 Modifications of the apparatus for this work....3-14
3.4.1 Reactor support....3-14
3.4.2 Tape feeding system....3-15
3.4.3 Lens holder....3-16
3.4.4 Safety consideration....3-16
3.5 Anode surface temperature measurement....3-17
3.5.1 Optical pyrometer....3-18
3.5.2 Filters....3-20
3.5.3 Camera selection....3-20
3.5.4 Extrapolation of temperature range....3-22

3.5.5 Standard carbon arc 3-26
3.5.6 Calibration of intensity versus surface temperature 3-27
3.6 Materials 3-28
3.7 Operating procedure 3-30
3.8 Scanning Electron Microscopy (SEM) 3-32
3.9 References 3-33

Chapter 4: Results 4-1
4.1 Introduction 4-1
4.2 Analysis of the substrate surface images 4-1
4.3 Effect of Inter-electrode gap 4-3
4.3.1 Substrate surface temperature 4-3
4.3.2 Effect of inter-electrode gap on CNTs growth 4-7
4.4 Effect of nitrogen flushing through anode support 4-9
4.5 Effect of the speed of carbon tape 4-11
4.6 Effect of the arc current 4-13
4.7 Effect of buffer gases in the reaction chamber 4-15
4.7.1 Argon 4-15
4.7.2 Helium 4-18
4.7.3 Comparison of surface temperatures in 100 % nitrogen, argon and helium environment at 1 atmosphere 4-20
4.8 High speed camera analysis on the arc 4-21
4.9 References 4-27

Chapter 5: Plasma Modelling 5-1
5.1 Conceptual framework for modelling arc discharge 5-1
5.2 Physics of the arc discharge 5-4
5.2.1 Carbon arc 5-5
5.2.2 Physics near the electrode 5-7
5.3 Plasma Properties and transport coefficient 5-11
5.3.1 Plasma composition 5-11
5.3.2 Thermodynamic properties 5-12
5.3.3 Transport properties 5-14

5.4 Computational Fluid Dynamic (CFD) 5-15
5.4.1 Comsol Multiphysic 5-15
5.5 Arc Plasma Modelling 5-18
5.5.1 Modeling task 5-18
5.5.2 Mathematical model 5-19
5.5.3 Model geometry and boundary conditions 5-21
5.5.4 Application Modes 5-24
5.5.5 Modelling strategy 5-26
5.6 Measurement of boundary conditions 5-27
5.6.1 Nitrogen velocity on the anode surface 5-27
5.6.2 Anode surface temperature 5-28
5.6.3 Electrical conductivity of plasma in the anode layer 5-28
5.7 Results 5-38
5.7.1 Surface mesh 5-39
5.7.2 Analysis of the variables 5-39
5.7.3 Effect of nanoparticles on plasma temperature 5-41
5.7.4 Effect of anode surface temperature 5-44
5.7.5 Effect of Nitrogen flushing 5-45
5.7.6 Effect of inter-electrode gap 5-48
5.8 Reliability of the model 5-50
5.9 References 5-51

Chapter 6: Discussion 6-1
6.1 Dusty plasma in carbon arc 6-1
6.2 Overall observation 6-2
6.2.1 Effect of inter-electrode gap 6-3
6.2.2 Effect of arc current 6-6
6.2.3 Effect of nitrogen flushing 6-7
6.2.4 Effect of substrate speed 6-9
6.2.5 Effect of background gases 6-11
6.3 Growth mechanisms of multiwalled NT by arc-evaporation 6-14
6.4 References 6-22

Chapter 7: Conclusion and Future Directions 7-1
7.1 Conclusions 7-1
7.2 Future works 7-2
7.3 References 7-4

List of Publication

Appendices

Nomenclature

$\vec{v}$	Velocity vector
μ	Molecular viscosity
ρ	Plasma density
σ	Plasma electrical conductivity
Φ	Scalar variables
λ_p	thermal conductivity of plasma.
λ	Wavelength
α	Ionization degree of the particle
Γ_Φ	Diffusion coefficient
ρ_e	electric charge density
φ_l	Energy required to remove an electron from solid particle of an element (work function)
A	Ampere
Å	Amstrong
A_{anode}	anode emission area
B	magnetic flux vector
B_θ	Azimuthal component of magnetic flux
C	Speed of light
C_h	Chiral vector
C_p	Specific heat of plasma at constant pressure

D	Electric flux density
E	Electric field
E	Electric field intensity
e	Electronic charge
E_i	Ionization energy
F	Force that exists such as gravity
fps	Frame per second
h	Planck constant
H	Magnetic field density
He	Helium
I	Spectral radiance, energy per unit time per unit surface area per unit solid angle per unit frequency
J	Current density
J_r	Radial component of current density
J_z	axial component of current density
k	Boltzmann Constant
K	Kelvin
K	thermal conductivity tensor
$K_l(T)$	equilibrium constant
LTE	Local thermal equilibrium
m_e	electron mass
N	Neutral number densities

N_0	number density of neutral gas molecule
N_e	Electron density
Ni	Ion number densities
N_l	number density of solid particles that are ionized l times
P	pressure
ppm	part per million
Q	Electron-neutral particle collision cross-section
Q_0	electron collision cross-section of neutral gas molecule
Q_i	Partition functions of ions
S_Φ	Source term
S_R	radiation heat loss per unit volume
T	plasma temperature
$T_{black\ body}$	Temperature of the black body
T_0	ambient temperature
T_1	room temperature
T_2	anode surface temperature
T_s	Surface temperature
T_{vib}	Vibrational Temperature
u	axial component of plasma velocity
u	velocity field
v	radial component of plasma velocity

V	Volt (Electrical Potential)
V_{N2}	nitrogen flow at room temperature
δ_{ts}	time-scaling coefficient
ε_0	permittivity of a vacuum

Abbreviations

AC	Alternating Current
Ar	Argon
CAD	Computer Aided Design
CCD	Charge coupled device
CFD	Computational Fluid Dynamics
CMOS	Complementary metal–oxide–semiconductor
CNT	Carbon nanotube
CO	Carbon monoxide
Co	Cobalt
CVD	Chemical Vapour Deposition
DC	Direct Current
EDS	Energy dispersive x-ray spectroscopy
FDM	Finite Difference Method
Fe	Ferum
FEM	Finite Element Method
FESEM	Field emission scanning electron microscopy
HRTEM	High resolution transmission electron microscopy
MEM	Microelectromechanical System
MWNT	Multiwalled nanotube
N_2	Nitrogen

NH_3	Ammonia
Ni	Nickel
NT	Nanotube
PAH	Polycyclic aromatic hydrocarbons
PDE	Partial Differential Equation
RF	Radio Frequency
SWNT	Single-walled nanotube
SEM	Scanning Electron Microscope
STM	Scanning Tunnelling Microscopy
TGA	Thermogravimetry
XRD	X-ray diffraction

List of Figures

Figures

Page

Figure 1.1 Some SWNTs with different chiralities. The difference in structure is easily shown at the open end of the tubes. a) zigzag structure b) armchair structure c) chiral structure (Saito, Dresselhaus et al. 1999). 1-2

Figure 1.2 A bare section of a single-wall carbon nanotube with adhering fullerenes(Bethune, Kiang et al. 1993) 1-3

Figure 1.3 Chiral vector definition. 1-4

Figure 1.4 A transmission electron micrograph of the finer fibres on an SPK graphite anode (Abrahamson, Wiles et al. 1979) . 1-5

Figure 1.5 High resolution transmission electron microscopy image of a concentric MWNT prepared by electric arc. 1-5

Figure 1.6 Schematics of an arc-discharge apparatus, along with electron microscopy pictures of the products obtained with doped and pure anodes (Harris 1999). 1-8

Figure 1.7 Schematic diagram of thermal CVD apparatus(http://www.iljinnanotech.co.kr/en/home.html). 1-9

Figure 1.8 An example of free-standing MWNT array. Each square-base rod is a bunch of MWNTs aligned perpendicular to the substrate surface (Fan, Chapline et al. 1999). 1-10

Figure 1.9 Schematics of a laser ablation set-up, reproduced from (Yakobson and Smalley 1997). 1-11

Figure 1.10 Low magnification of TEM images of a typical raw SWNTs material obtained from the laser vaporisation method.(Monthioux, Smith et al. 2001). 1-12

Figure 2.1 A model for the open-end growth of the CNT (Iijima 1993). 2-2

Figure 2.2 Typical gated ICCD images of the total visible emission for laser ablation at (a) 1200°C and (b) room temperature. (Kokai, Takahashi et al. 2000). 2-5

Figure 2.3 The capping of the tube with polyhedral where (a) a symmetrical cap with an apex, (b) an asymmetrical cap, and (c) a symmetrical with flat head (Iijima 1993). 2-13

Figure 2.4 Schematic of a capped multiwalled nanotube.(Crespi 1999). 2-14

Figure 2.5 Two general growth modes of nanotube. 2-15

Figure 2.6 Summary of the result from Puretzky et al. Actual images of the laser plume (t<200μs) and Rayleigh-scattering images of the plume (t>200μs) are shown vs. time.(Puretzky, Schittenhelm et al. 2002). 2-16

Figure 2.7 Illustration of the solid-liquid-solid mechanism for growth of SWNTs (Gorbunov, Jost et al. 2002). 2-17

Figure 2.8 Illustration of a model proposed by Kataura and colleagues (Kataura, Kumazawa et al. 2000). 2-17

Figure 2.9 Three snapshots from the molecular dynamic simulation of the free oscillation of a graphitic nanofragment.(Volpe and Cleri 2001). 2-19

Figure 3.1 CNT produced on anode (Abrahamson, Wiles et al. 1999) 3-2

Figure 3.2 SEM micrograph showing details of carbon whisker deposit on graphite cathode crater (37 A , under 1 atm Nitrogen atmosphere). Apparent random broken by arc spot (Wiles 1979). 3-3

Figure 3.3 Flow chart of batch reactor, adapted from (Ulubay 2002) 3-5

Figure 3.4 Photograph showing the continuous reactor with right-angled electrode position and major parts labelled, adapted from (Ulubay 2002). 3-8

Figure 3.5 Photograph of carbon substrate, Carbonic GmbH fabric (on the right is the image of carbon tape). 3-9

Figure 3.6 Flowchart of the first continuous reactor (Ulubay 2002) 3-10

Figure 3.7 Anode cathode configuration in continuous arc reactor 3-12

Figure 3.8 Anode cap (anode support) 3-13

Figure 3.9 A new support for the continuous arc reactor 3-14

Figure 3.10 Details of design of the top spool of the tape feeding system 3-15

Figure 3.11 New design of lens holder 3-16

Figure 3.12 Photograph of the continuous arc reactor after modifications 3-17

Figure 3.13 Schematic diagrams of apparatus for surface temperature measurement 3-19

Figure 3.14 Relationship between pyrometer reading and actual surface temperature. 3-25

Figure 3.15 Anode face images at different arc currents; anode diameter was 8 mm for all runs 3-27

Figure 3.16 Calibration of image intensity versus surface temperature 3-27

Figure 3.17 Photograph of a) Carbonic GmbH carbon tape b) Anode support 3-28

Figure 3.18 Flow chart of the continuous arc discharge after modification 3-31

Figure 4.1 Substrate image viewed through the pyrometer. The carbon tape used was UVIS TR-3/2-22 Carbonics GmbH T with a speed of 3 mm/s. Arc current was 16 A 4-1

Figure 4.2 Surface temperatures across the substrate at 16 A arc current and 5.2 mm inter-electrode gap using UVIS TR-3/2-22 Carbonic tape 4-2

Figure 4.3 Average substrate surface temperatures at different gaps for 16 A arc using UVIS TR-3/2-22 Carbonic tape at a speed of 3 mm / s 4-3

Figure 4.4 Substrate (UVIS TR-3/2-22 Carbonic tape) images at different inter-electrode gap a) 4 mm, b) 5 mm and c) 6 mm at 16 A current and 3 mm / s tape speed. 4-4

Figure 4.5 Temperature changes during the run with the nitrogen as a background gas for 16 A arc current. The tape used was UVIS TR-3/2-22 Carbonic GmbH. 4-6

Figure 4.6 Temperature variations with arc gap, —▲— immediately after changing the gap and —♦— after 30 s. 4-6

Figure 4.7 CNTs growth at no anode flushing condition (0 L/min nitrogen flow) and at (a) 2.7 mm gap (b) 5.2 mm gap and (c) 7.7 mm gap for 16 A arc current. 4-8

Figure 4.8 The surface temperature across the substrate at 5.2 mm gap, —O— no Flow and —▲— 0.6 L/min nitrogen flow. 4-9

Figure 4.9 SEM images of CNTs growth at 5.2 mm gap and different anodic flushing flow rate, (a) 0 L/min (b) 0.6 L/min. 4-10

Figure 4.10 Anode surface temperatures at different tape speed for 5.2 mm gap and 16 A current. 4-11

Figure 4.11 Carbon nanostructures at a different speed of the carbon tape, a) at 0.85 mm/s, b) at 2.56 mm/s, c) at 4.13 mm/s and d) at 5.64 mm/s for 16 A arc current and 5.2 mm inter-electrode gap. 4-12

Figure 4.12 The uniform cauliflowers formed with the high current arc at 20 A current. 4-13

Figure 4.13 Anode surface temperatures at different arc gap with the current of 20 A,  for 3 mm cathode and  for 8 mm cathode using the high current supply. Carbon tape speed was at 4.13 mm/s. 4-14

Figure 4.14 Anode surface temperatures with Argon as inert background gas at 20-22 A arc current and 8 mm cathode diameter. 4-15

Figure 4.15 CNTs formation under an argon environment and 16 A current with a high current power supply, a) 3.3 mm inter-electrode gap b) 5.0 mm inter-electrode gap c) 6.3 mm inter-electrode gap. 4-17

Figure 4.16 Anode surface temperatures at different inter-electrode arc gaps under helium atmosphere and arc current of 16 A (high current power supply). 4-18

Figure 4.17 Images from SEM analysis on substrate surfaces under helium atmosphere environment and 16 A arc current with a high current supply, a) 3.3 mm inter-electrode gap b) 5.0 mm inter-electrode gap c) 6.3 mm inter-electrode gap d) 8 mm inter-electrode gap. 4-19

Figure 4.18 Anode surface temperatures at different inter-electrode arc gaps under nitrogen (low current power supply) atmosphere, helium or argon atmosphere (high current power supply). The arc current used was 16 A for all runs. The anode surface temperatures for argon were higher by >100 K compared to the temperatures in the helium environment. 4-20

Figure 4.19 High speed camera images of a particle from cathode at optimum arc condition i.e. 16 A arc current and 5.2 mm gap. 4-21

Figure 4.20 a) Projection of particle in front of the cathode -for a period of 3 milliseconds and in-front of anode –for a period of 5 milliseconds, b) velocity profile of a particle ejected from cathode surface. 4-22

Figure 4.21 Anode plume development for the 16 A arc current and 5.2 mm inter-electrode gap. On the left images from high speed camera and on the right the true colours images. 4-23

Figure 5.1 Development of arc discharge science and technology (Wendelstorf 2000). 5-1

Figure 5.2 Survey of arc temperatures and electron densities (Boulos, Fauchais et al. 1994) 5-2

Figure 5.3 Typical electric arc discharges consisting of three regions 5-3

Figure 5.4 Definition of arc modelling module 5-4

Figure 5.5 The I-V characteristic of carbon arc in air. Values of L indicate the inter-electrode gap (Raizer 1997) 5-6

Figure 5.6 Carbon arc in air at a current of 200 A (a) a photograph, (b) measured temperature field (Raizer 1997). 5-7

Figure 5.7 Bulk temperature rise at the anode and the cathode with time after arc initiation for different arc currents (Murooka and Hearne 1972) 5-9

Figure 5.8 Composition of nitrogen plasma at 100 kPa (Boulos, Fauchais et al. 1994) 5-12

Figure 5.9 Mass density of a nitrogen plasma at 100 kPa (Boulos, Fauchais et al. 1994) 5-13

Figure 5.10 Heat capacity for various gases at a variation of temperature (Gleizes, Gonzalez et al. 2005) 5-13

Figure 5.11 Thermal conductivity of air, Argon and CO_2 versus temperature (Gleizes, Gonzalez et al. 2005). 5-14

Figure 5.12 Electrical conductivity of air 5-14

Figure 5.13 Comsol Multiphysics modelling steps 5-16

Figure 5.14 Low current arc geometry 5-22

Figure 5.15 Variation of Λ_p with $Z\delta$ (from Newby (1967)) 5-35

Figure 5.16 Surface mesh of carbon arc plasma 5-39

Figure 5.17 Temperature profile for arc plasma at 16 A current. The electrical conductivity of the plasma near to the anode surface is fixed at 100 A/V.m. 5-40

Figure 5.18 Temperature isotherm for 16 A arc at optimum inter-electrode gap 5-42

Figure 5.19 Velocity profile for 16 A at optimum inter-electrode gap (5.2 mm) 5-43

Figure 5.20 Temperature isotherms of the 16 A arc plasma in Case B and Case C 5-44

Figure 5.21 Temperature isotherms of the plasma a) with maximum nitrogen velocity~2.5 m / s, b) without nitrogen flow from the anode 5-46

Figure 5.22 Velocity field in the plasma, a) with maximum nitrogen velocity 5-47

Figure 5.23 Temperature and velocity profile of arc plasma at 16 A and 7.7 mm inter-electrode gap (Case F) 5-49

Figure 5.24 Temperature and velocity profile of arc plasma at 16 A and 2.7 mm inter-electrode gap (Case G). 5-49

Figure 6.1 Arc characteristics and surface deposit type for 16 A arc current s using a 3 mm dia. cathode, for nitrogen. All done with anode flushing 0.6 L/min and tape speed of 3 mm / s. 6-3

Figure 6.2 Arc characteristics and surface deposit type for a 20 A arc using a 8 mm diameter cathode. Tape speed is 4.13 mm/s. 6-7

Figure 6.3 Mapping for CNT formation at various substrate speeds. 6-9

Figure 6.4 Arc characteristics and surface deposition using different atmospheres with 3 mm cathode diameter and arc current of 16 A. 6-13

Figure 6.5 Schematic illustration of the solid phase growth model for multiwalled carbon nanotubes.(Harris, Tsang et al. 1994). 6-18

Figure 6.6 Electric field distribution around MWNTs with various amounts. (MWNT amount, N = 1, 2 and 100, length L = 100 nm, diameter D = 20 nm and inter-tube distance d = 20 nm) (Bao, Zhang et al. 2007) 6-20

Figure 6.7 Acceleration of charged cluster due towards anode surface due to polarization,(adapted from (Shastry 2007)). 6-21

List of Tables

Table 2.1 Parameters to be considered during the formation of carbon nanotubes (Querrioux 2004) 2-9

Table 3.1 Variation in new reactor compared to 1978's reactor. 3-6

Table 3.2 Comparison between Abrahamson's arc-discharge with conventional arc-discharge used for producing carbon nanotubes. 3-7

Table 3.3 Sony Cybershot camera set-up. 3-21

Table 3.4 Properties of Carbonics woven tape. 3-28

Table 3.5 Descriptions of buffer gaseous used in the reactor . 3-29

Table 4-1 Anode current densities at various arc gaps with no gas flushing. 4-5

Table 4-2 Relation of camera image size with number of video frames. 4-21

Table 4-3 Radial expansion velocity of anode plume. 4-25

Table 5.1 The relation between maximum cathode temperature and arc current (Murooka and Hearne 1972). 5-9

Table 5.2 Boundary condition for the low current carbon arc. 5-22

Table 5.3 The trend of anode surface temperature with varying gap. 5-28

Table 5.4 Effect of anode surface temperature on the plasma conductivity at near anode plasma region. 5-37

Table 5.5 Simulation details. 5-38

Chapter 1: Introduction..... 1-1
1.1 A brief history of carbon nanotubes (CNTs)..... 1-1
1.2 Nanotube structure..... 1-1
1.2.1 Single walled Nanotubes (SWNTs)..... 1-2
1.2.2 Multi-walled Nanotubes..... 1-4
1.3 Nanotube properties and potential application..... 1-6
1.3.3 Mechanical properties..... 1-6
1.3.4 Electrical properties..... 1-7
1.4 Synthesis method..... 1-7
1.4.5 Arc discharge method..... 1-7
1.4.6 Chemical Vapour Deposition (CVD)..... 1-9
1.4.7 Laser ablation..... 1-10
1.4.8 Other methods..... 1-12
1.5 Research objectives..... 1-13
1.6 Outline of this work..... 1-13
1.7 References..... 1-15

Chapter 1: Introduction

1.1 A brief history of carbon nanotubes (CNTs)

In 1985, Kroto et al reported the discovery of a new form of carbon, buckminister fullerene (C_{60}) or the "buckyball", which gives a strong impact and marked the beginning of the new era in carbon material science (Kroto, Heath et al. 1985). Few years later, Iijima presented the discovery of CNT with a diameter of 3-10 nm and the length of up to 1 μm(Iijima 1991). This initial work, followed by the large synthesis of CNT, excited scientific communities all over the world. However, it was found later that there was published evidence for the existence of CNT prior to Iijima's discovery. CNT has been seen as early as 1978, by Abrahamson *et al* (Abrahamson, Wiles et al. 1999) while working with standard carbon arc. They published an article describing " a thick mat of fine fibres has been found on the surface of the graphite and carbon anode of the low current arc operated in nitrogen"(Wiles and Abrahamson 1978). Unfortunately, due to research climate at that time, their discovery and the potential of this new material stayed unnoticed until two decades later.

During the last decade, extensive studies have been done all over the world to improve the synthesis method of producing CNTs and to explore the potential applications of it. Abrahamson introduced a modified version of a conventional arc discharge apparatus in 2000 to improve CNTs synthesis process. Details of this invention can be found in Chapter 3. A lot of efforts have also been made to understand the formation mechanism of carbon nanotubes. A brief discussion on CNTs growth mechanisms is presented in the next chapter.

1.2 Nanotube structure

The structure of a nanotube is similar to graphite, with the difference that the sheets are rolled to form a tube and capped at least one ends. The rolling-up of the graphene sheet can be performed in several ways. It can be rolled-up along one of the symmetric axis, producing a zigzag or an armchair tube. It also possible to roll-up the sheet in any direction that differs from a symmetry axis and forms a chiral nanotube. Fig.1.1 shows each of three different structures of carbon nanotubes.

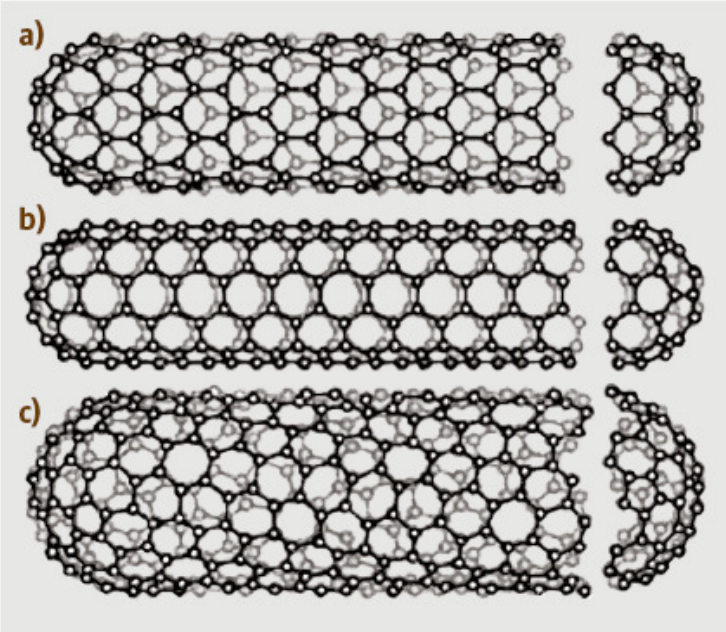

Figure 1.1 Some SWNTs with different chiralities. The difference in structure is easily shown at the open end of the tubes. a) zigzag structure b) armchair structure c) chiral structure (Saito, Dresselhaus et al. 1999).

Carbon nanotubes can be classified as single-walled nanotubes (SWNTs) or multi-walled nanotubes (MWNTs) depending on the tube layers.

1.2.1 Single walled Nanotubes (SWNTs)

Single-walled carbon nanotubes were first prepared by metal catalysed direct current arc using graphite electrodes under a helium atmosphere by Bethune *et* al(1993) at IBM and Iijima(1993) at NEC. Most single-walled nanotubes (SWNT) have a diameter of close to 1nm, with a tube length that can be many hundreds of times as shown in Figure 1.2. The number of aspect ratio of SWNTs varying from 100-10000, but these numbers tend to increase lately.

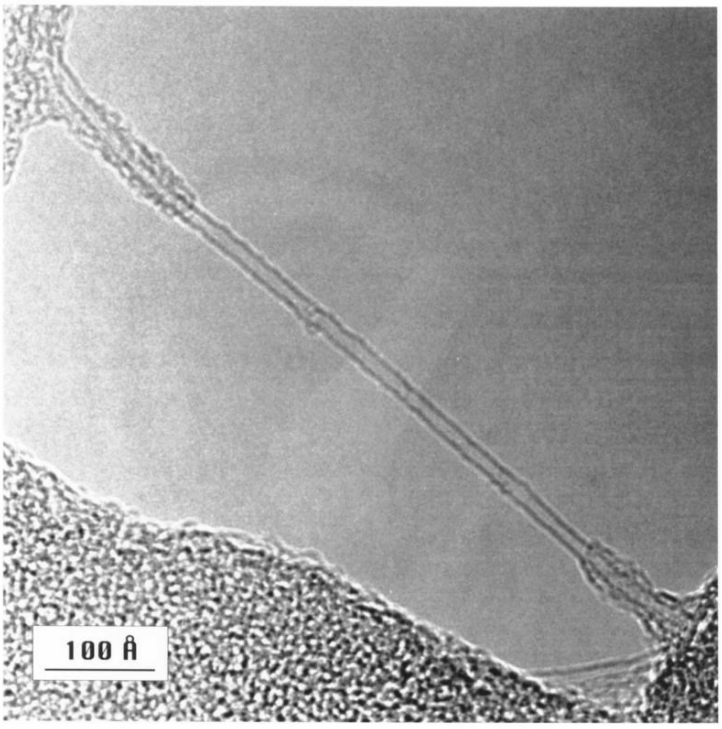

Figure 1.2 A bare section of a single-wall carbon nanotube with adhering fullerenes(Bethune, Kiang et al. 1993)

The structure of a SWNT can be conceptualized by wrapping a layer of graphene sheet into a seamless cylinder as mentioned earlier. The way the graphene sheet is rolled is represented by a pair of indices (*n*,*m*) which known as chiral vector.

The chiral is defined as:

$$C_h = n\mathrm{a}_1 + m\mathrm{a}_2$$

a_1 and a_2 being the unit vector and integers *n* and *m* denote the number of unit vectors along two directions in the hexagonal lattice of graphene. If *m*=0, the nanotubes are called "zigzag". If *n*=*m*, the nanotubes are called "armchair". Otherwise, they are called "chiral" as shown in Figure 1.3.

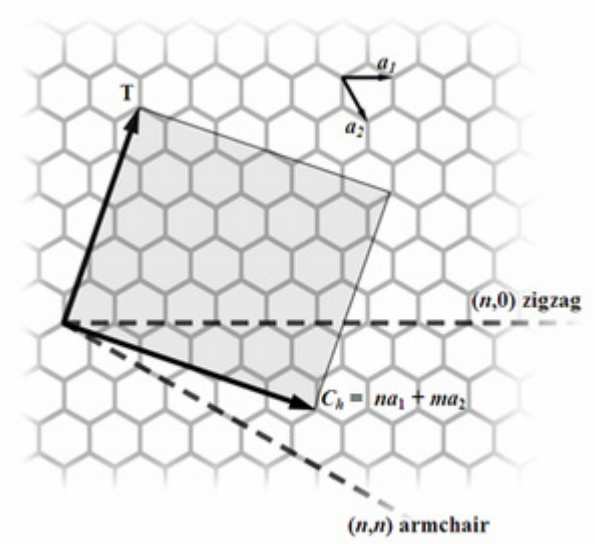

Figure 1.3 Chiral vector definition.

The chiral structure has a direct effect on the electrical properties of carbon nanotube. For a given (n,m) nanotube, if $2n + m=3q$ (where q is an integer), then the nanotube is metallic, otherwise the nanotube is a semiconductor. Thus all armchair ($n=m$) nanotubes are metallic, and nanotubes (6,4), (9,1), etc. are semi conducting. In theory, metallic nanotubes can have an electrical current density more than 1,000 times greater than metals such as silver and copper

1.2.2 Multi-walled Nanotubes

The carbon structures observed by Abrahamson and Wiles (Abrahamson and Wiles 1978) on graphite and carbon anodes, following low current arc operation in nitrogen at atmospheric pressure, have been possibly MWNTs. In their study, they found several carbon fibres with a diameter range from about 4 nm to 100 nm and lengths of up to 15 µm. Many small crystalline particles were attached on these fibres, especially around intersections of touching fibres. A transmission electron micrograph of the fibres showing the attached particles is given in Figure 1.4.

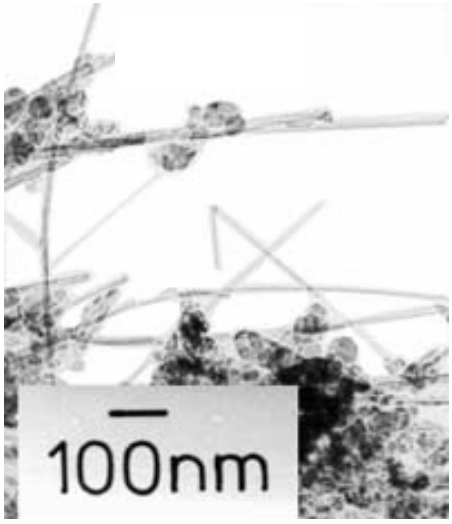

Figure 1.4 A transmission electron micrograph of the finer fibres on an SPK graphite anode (Abrahamson, Wiles et al. 1979) .

From the electron diffraction study they reported that the fibres consisted of wrapped graphitic basal layers with a hollow core. These structures are later known as multi-walled carbon nanotubes. Typical MWNTs contained 2-50 concentric graphite cylinders with a diameter of 3-10 nm with a length up to 1μm (Iijima 1991). A copy of high resolution transmission electron microscopy (HRTEM) normally produced in a catalyst-free electric arc or by catalyst enhance thermal cracking of hydrocarbon gases at high temperature is shown in Figure 1.5.

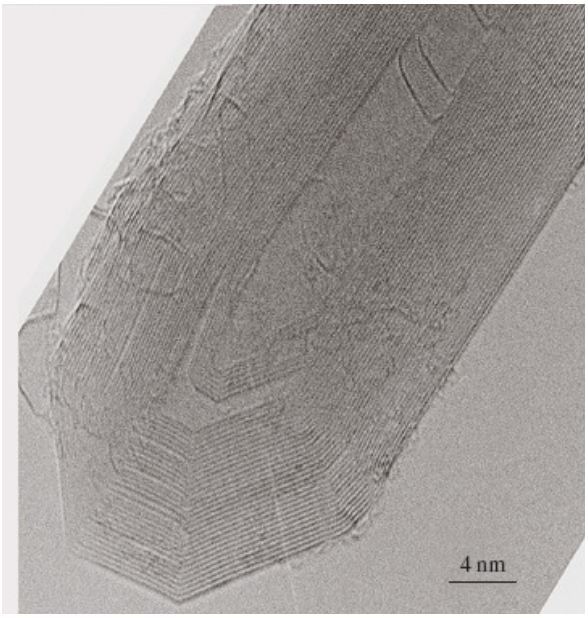

Figure 1.5 High resolution transmission electron microscopy image of a concentric MWNT prepared by electric arc

The layers are separated by 0.345 nm distance, which is slightly higher than inter-layer spacing in graphite (0.335 nm). This is because the number of atoms increases from the inner tube to the outer tube. Therefore, it is unlikely that the perfect ABAB stacking will be maintained as in graphite (Rao, Satishkumar et al. 2001).

1.3 Nanotube properties and potential application

Carbon nanotubes are unique nanostructures which are known to have remarkable mechanical and electronic properties. Extensive studies have been made to study these properties of carbon nanotubes.

1.3.3 Mechanical properties

A nanotube has a very high Young's Modulus value, a tensile strength hundred times stronger than steel and can tolerate a high strain before mechanical failure. The tensile strength of SWNTs can be 20 times higher than steel with a measured value equal to ~ 45 Gpa (Walters, Ericson et al. 1999). MWNTs (without any structural defect and both ends capped) may have a very high tensile strength. Measurement by (Demyczyk, Wang et al. 2002) using MWNTs from electric arc showed a tensile strength value as high as 150 GPa. Experimental results have also shown a very high elastic modulus of carbon nanotubes. For example, Salvatet *et al*. found that multi-walled carbon nanotubes grown by arc discharge method had a modulus of about 1Tpa (Salvatet 1999).

When nanotubes are compressed, they bend over to large angles, before they start to ripple and buckle, and finally, kinks are developed. Since nanotubes are elastic, all these deformations disappear when the load is removed (Yu, Lourie et al. 2000). They also found the value of tensile strength of carbon nanotube, ranging from 11 – 63 GPa, which is few times higher than the steel alloy, which normally breaks at 2 Gpa. The density of bundled nanotubes is 1330 – 1440 kg/m^3. This is very low compared to aluminium, possessing density of 2700 kg/m^3.

The mechanical behaviour of CNTs is exciting since nanotubes are seen as the strongest fibre ever made. Nanotubes are an ideal material for reinforcement of nanostructural composite, polymer and concrete. Because of the low density, these materials are very useful for cars, aeroplanes and space vehicles (Baughman, Zakhido et al. 2002).

1.3.1 Electrical properties

Much theoretical and experimental work has been focused to relate the structure of carbon nanotubes to their electronic properties. A SWNT can be metal or semi-conductor depending on its structure and diameter. The fact that a metallic nanotube is a good conductor is underlined by comparing them with copper. A bundle of nanotubes, could conduct about $1x10^{9}$ A/cm^2, whilst copper wires saturated at about $1x10^{-6}$ A/cm^2 (Collins and Avouris 2000). This fact makes them very useful for making minuscule electronic devices like logic circuits composed of several transistors. The making of tiny circuits might be promising for the semiconductor industry.

The electronic properties of single-walled carbon nanotubes have been shown to be extremely sensitive to the chemical environment (Collins, Bradley et al. 2000). Exposure to air or oxygen dramatically affects the nanotube resistance and other electronic properties.

Another very interesting electronic property of carbon nanotubes is their field emission; they will emit electrons from their tips when placed in the electric field (Rinzler, Hafner et al. 1995). Due to the very sharp tip, the nanotubes emit electrons at lower voltage than electrodes made from most other materials. The strong carbon bond in nanotube allows them to operate for longer periods without damage.

1.4 Synthesis method

Since the discovery of CNT, several ways of preparing them have been developed. In general, three methods are commonly used *i.e.* - arc discharges, chemical vapour deposition and laser ablation.

1.4.1 Arc discharge method

The arc discharge method used initially for producing C_{60} fullerene, is the most common and perhaps the easiest way to produce carbon nanotubes. In the customary arc discharge method, as shown in Figure 1.6, current flows between closely spaced carbon electrodes, typically 1-4 mm, creating an arc between them. The arc temperature is presumably in excess of 6000 K and the electrode surface temperature is about 4000 K.

Carbon of the electrode then vaporizes and form a vapour which then condense as nanoparticles and carbon nanotubes(Gamaly and Ebbesen 1995).

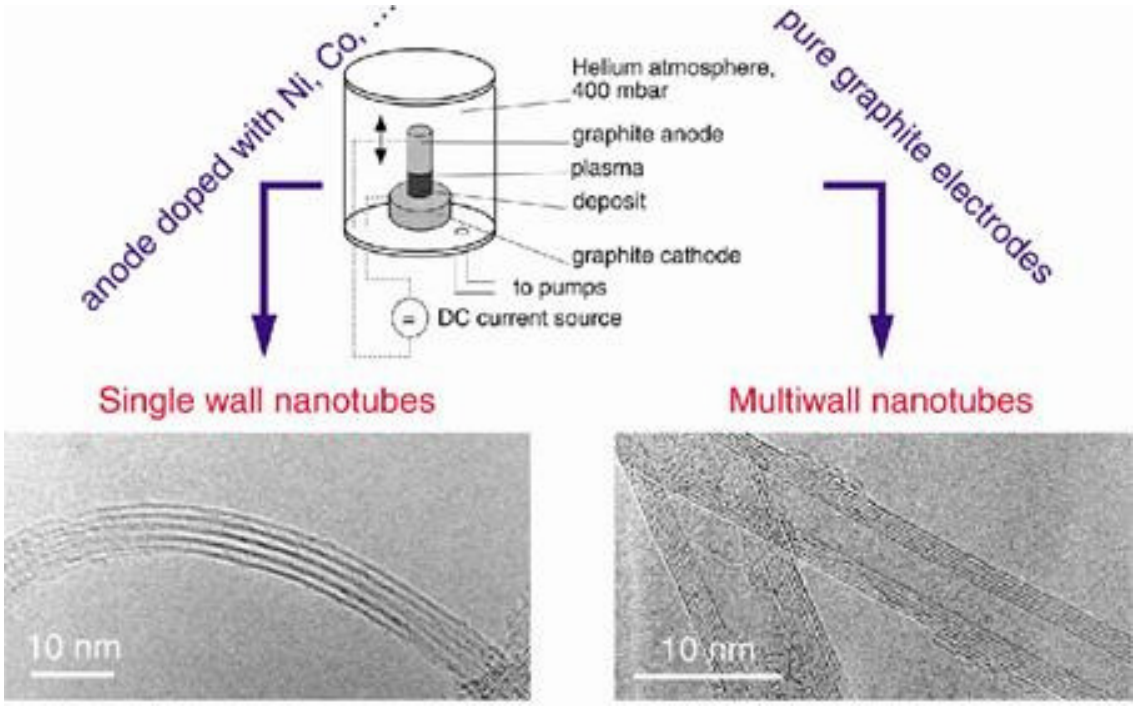

Figure 1.6 Schematics of an arc-discharge apparatus, along with electron microscopy pictures of the products obtained with doped and pure anodes (Harris 1999).

The arc discharge is normally created within the vacuum chamber with connection both to a vacuum line and an inert gas supply (normally Helium and Argon). A continuous flow of gas is preferred over a static atmosphere. The position of the electrodes is adjustable from outside the chamber so that a constant gap can be maintained during the process. The conventional arc discharge for producing CNTs normally operates at a low voltage of ~ 20V and a current of 50-100 A, depending on the size of the electrodes.

Single-walled nanotubes can be generated in a form of soot if the graphite rod used as an anode is doped with a metal catalyst such as Fe or Co (Bethune, Kiang et al. 1993). The crystallinity and perfection of carbon nanotubes produces by this method are generally high and the yield per unit time is also higher compared to other methods.

1.4.2 Chemical Vapour Deposition (CVD)

In 1993, Endo et al reported the synthesis of carbon nanotubes by pyrolizing benzene at 1100 °C. Their experiment was carried out in the apparatus which had previously been used for production of vapour grown carbon fibre (Endo, Takeuchi et al. 1993). Generally, the growth process involves heating of catalyst material to high temperatures (600-1100 °C) in the furnace under the flowing hydrocarbon gaseous over a period of time. The catalysts used are normally transition metal such as Fe, Co and Ni. This process is considered as a 'low temperature' process compared to arc discharge and laser ablation methods (Dai 2002).

Nowadays, various CVD methods have been developed to produce CNTs. A schematic diagram of thermal CVD is shown in Figure 1.7.

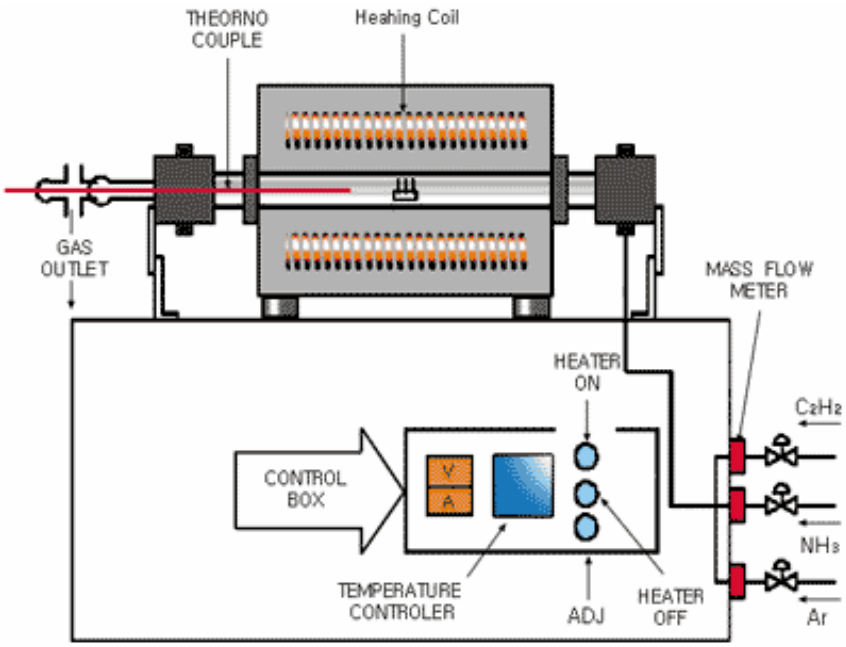

Figure 1.7 Schematic diagram of thermal CVD apparatus (http://www.iljinnanotech.co.kr/en/home.html).

This method is capable of controlling the growth direction of CNTs on the substrate and synthesizing large quantities of carbon nanotubes. In this process, Fe, Ni or Co, is initially deposited on a substrate. The substrate is then etched and put in a quartz boat. The boat is placed in a CVD reaction furnace. An additional etching of the catalytic metal film, using NH_3 gas produced nano-size metal particles (http://www.iljinnanotech.co.kr/en/home.html 2006). Carbon nanotubes are grown on

these fine catalytic metal particles when hydrocarbon gaseous such as acetylene, ethylene or methane is introduced into the reaction chamber. Nanotubes are formed on the substrate by decomposition of the hydrocarbon at temperatures between 600-1100 C and at atmospheric pressure (Ando, Zhao et al. 2004).

By patterned the catalyst deposited on the substrate surface, this process allows the formation of CNTs in the design arrays. Figure 1.8 shows the image of tree standing MWNTs array obtained from the pyrolisis of gaseous carbon sources over catalyst nanoparticles previously deposited onto a patterned substrate.

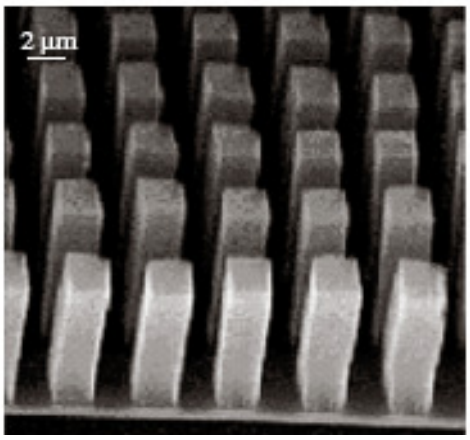

Figure 1.8 An example of free-standing MWNT array. Each square-base rod is a bunch of MWNTs aligned perpendicular to the substrate surface (Fan, Chapline et al. 1999).

1.4.3 Laser ablation

The laser furnace method had been originally used as a source of clusters and ultra fine particles was developed for fullerene and CNT production. The laser vaporization method is widely used for the production of SWNTs. The laser is suitable for materials with a high boiling temperature such as carbon as the energy density of lasers is much higher than that of other vaporization devices.

The method of producing CNTs using laser ablation was introduced by the Smalley group in 1995 (Guo, Nikolaev et al. 1995). In this technique a laser is used to vaporise a graphite target held in a controlled environment oven as shown in Figure 1.9. The carrier gas used was helium or argon, and the oven temperature was approximately 1200 °C. The nanotubes and nanoparticles were found in the condensed material collected at the cooled target. The group later produced high quality carbon nanotubes bundled together into

crystalline ropes of metallic character (Thess, Lee et al. 1996). A disadvantage of this method is that it requires an expensive laser.

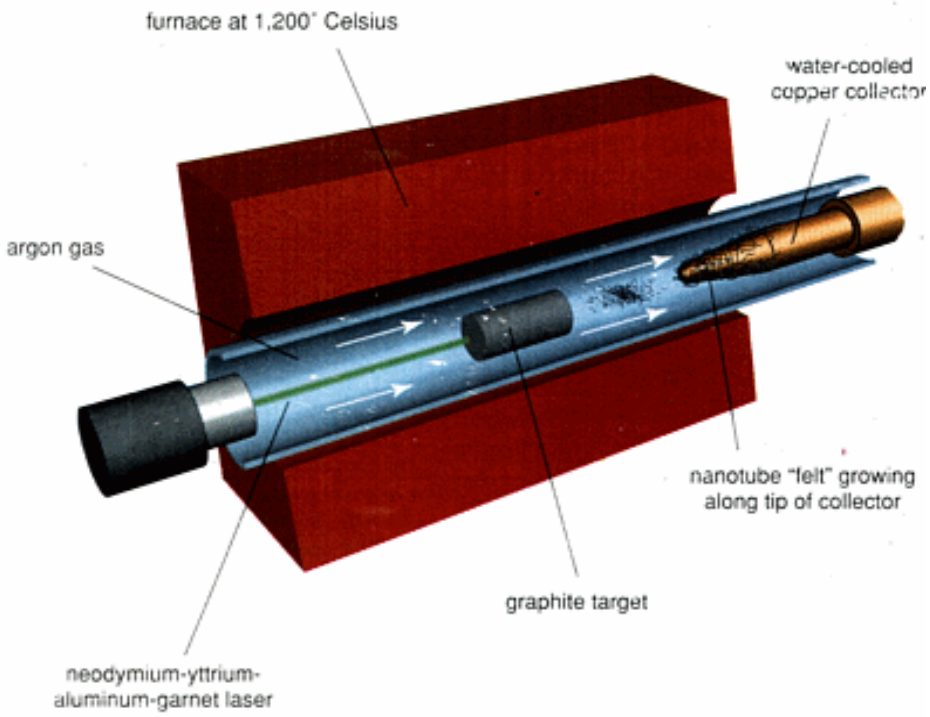

Figure 1.9 Schematics of a laser ablation set-up, reproduced from (Yakobson and Smalley 1997)

In this process, the energy of the laser beam focussed on the graphite target allows it to vaporize and sublime the graphite. These were done through the continuous bombardment on the graphite surface. The carbon species swept away by the flow of the carrier gas are then deposited in the different regions; on the conical water-cooled copper collector, on the quartz tube wall and on the backside of the graphite target.

In the absence of metal catalyst in the graphite target, the soot collected mainly consists of MWNTs. Their length can reach 300 nm. Their quality and quantity are dependent on the oven temperature. The best quality is obtained for an oven temperature of 1200 °C. At lower oven temperatures, the nanotube quality deteriorates and many defects were observed (Guo, Nikolaev et al. 1995). SWNTs were formed when small quantities of catalyst are incorporated in the graphite target. The yield of SWNTs strongly depends on the type of transition metal used and it seems to increase with the oven temperature. The SWNTs produced have a uniform diameter and they self-organized into rope-like crystallite 5-20 nm in diameter and up to few hundreds of micrometer in length as shown in Figure 1.10.

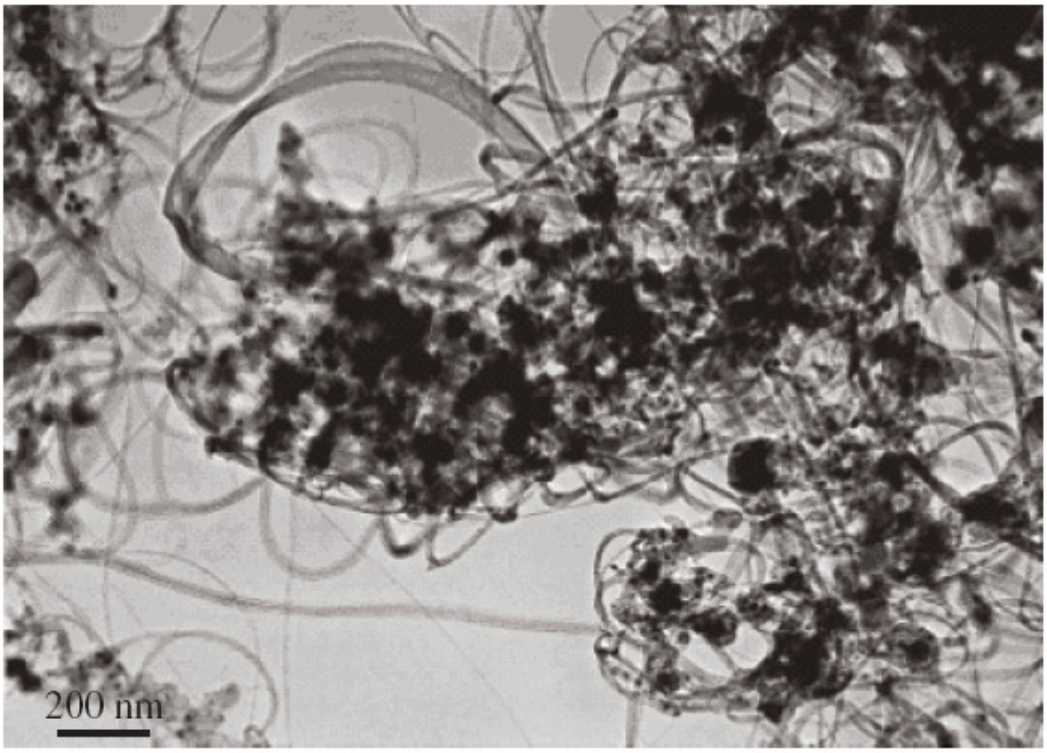

Figure 1.10 Low magnification of TEM images of a typical raw SWNTs material obtained from the laser vaporisation method. Dark materials are catalyst remnant. Raw SWNTs from electric arc also exhibit the similar aspect (Monthioux, Smith et al. 2001).

1.4.4 Other methods

In addition to the major techniques described in Section 1.4.1-1.4.3, many attempts can be found in the literature to synthesis nanotubes. These includes ball milling method (Pierard, Fonseca et al. 2001; Chen, Conway et al. 2004), high pressure CO disproportionation process (HiPco),(a technique for catalytic production of SWNTs in a continuous-flow gas phase using CO as the carbon feedstock and $Fe(CO)_5$ as the iron-containing catalyst precursor (Nikolaev, Bronikowski et al. 1999)) and flame synthesis (Wal, L et al. 2001).

1.5 Research objectives

The aim of this work is to optimize the operating conditions of the developed continuous arc reactor producing CNTs. In this work, modifications, control and optimization of the arc discharge reactor will be conducted. The effect of arc running parameters such as inter-electrode gap, substrate velocity, tape speed and arc current on the growth of CNTs will be studied. The idea of the presence of nanoparticles (graphene fragments) in front of the anode surface will be tested. These clouds of nanoparticles may affect the observed anode surface temperature. A method to study this temperature will be developed and its relationship with CNTs growth will be studied. The arc plasma model will also be developed using computer package Comsol Multiphysics 3.2 in order to understand the arc behaviour.

1.6 Outline of this work

A new method for depositing carbon nanotubes in a continuous manner, used in this study, was developed in the University of Canterbury. This method was invented by Abrahamson soon after 2000 (Abrahamson 2002). Since that, a lot of efforts have been made to improve the operating condition of this continuous arc discharge process. To further improve the operation of the process, it is necessary to identify the important optimum conditions for the arc discharge. A new method of measuring anode surface temperature was developed to support our hypothesis on the formation of CNTs as described later in this thesis. Growth mechanisms of CNTs in arc discharge, previously proposed by other researchers, have also been discussed in Chapter 2.

A brief history of the 1970's batch reactor and comparison with the continuous reactor is discussed in Chapter 3. Modifications of the reactor configurations were made to enable the measurement of the anode surface temperature and the emission spectrum next to the anode. Details of these modifications and method used in experimental works are described in Chapter 3.

In Chapter 4, the effect of various arc parameters, such as inter-electrode gap, concentration of argon in nitrogen, substrate speed and arc current on the anode surface temperature, are presented. Later, a relationship between anode surface temperature and CNTs' growth is discussed. This is followed by the high speed video analysis on the trajectories of the particles emitted from the electrodes surfaces.

The modelling approach to understand the arc properties is discussed in Chapter 5. Here, the first section of Chapter 5 described the physic of the electric arc followed by the plasma properties and transport coefficients. The computational fluid dynamic packages used, *i.e*. COMSOL Multiphysics version 3.2 is also described in this chapter. Initially a simple arc configuration is selected to model the plasma in the arc. The impact of suspended particles on the electrical properties of the plasma region close to the anode surface is then added in to the model in order to get a better solution. The rest of the chapter is dedicated to the validation of the model by comparison with available experimental data.

A proposed mechanism of CNTs formation is discussed in Chapter 6. Chapter 7 summarises the achievements, further investigation needed to improve the proposed formation mechanism and possible future enhancements of the arc model.

1.7 References

Abrahamson, J. (2002). Continuous Method for Producing Inorganic Nanotubes. W. I. P. Organization. **WO 03/082733 A2**.

Abrahamson, J. and P. G. Wiles (1978). "Carbon fibre layers on Arc Electrodes I: their properties." Carbon **16**: 341-349.

Abrahamson, J., P. G. Wiles, et al. (1979). Structure of carbon fibres found on carbon arc anodes. 14th Biennial Conference on Carbon, Penn. State Univ., University Park, Penn., USA.

Abrahamson, J., P. G. Wiles, et al. (1999). "Structure of carbon fibres found on carbon arc anodes." Carbon **37**: 1873-1874.

Ando, Y., X. Zhao, et al. (2004). Growing carbon nanotubes. Materials Today. **October 2004:** 22-29.

Baughman, R. H., A. A. Zakhido, et al. (2002). "Carbon Nanotubes--the Route Toward Applications." Science **297**: 787-792.

Bethune, D. S., C. H. Kiang, et al. (1993). "Cobalt-catalysed growth of carbon nanotubes with single-atomic-layer walls." Nature(363): 605-607.

Chen, Y., M. J. Conway, et al. (2004). "The nucleation and growth of carbon nanotubes in a mechano-thermal process " Carbon **42**: 1543-1548.

Collins, P. G. and P. Avouris (2000). Nanotubes for electronics. Scientific Americans**:** 38-45.

Collins, P. G., K. Bradley, et al. (2000). "Extreme oxygen sensitivity of electronic properties of carbon nanotubes." Science **287**: 1801-1804.

Dai, H. (2002). "Carbon nanotubes: Opportunities and challenges." Surface Science **500**(1-3): 218-241.

Demyczyk, B. G., Y. M. Wang, et al. (2002). "Direct mechanical measurement of the tensile strength and elastic modulus of multiwalled carbon nanotubes." Mater. Sci. Eng. A **334**: 173-178.

Endo, M. Takeuchi, et al. (1993). "Production and structure of pyrolytic carbon nanotubes (PCNTs)." Journal of Physics and Chemistry of Solids **54**(12): 1841.

Fan, S., M. Chapline, et al. (1999). "Self-oriented regular arrays of carbon nanotubes and their field emission properties." Science **283**: 512-514.

Gamaly, E. G. and T. W. Ebbesen (1995). "Mechanism of carbon nanotube formation in the arc discharge." Physic review B **52**(3): 2083-2089.

Guo, T., P. Nikolaev, et al. (1995). "Catalytic growth of single-walled nanotubes by laser vaporization." Chemical Physics Letters **243**(1-2): 49.

Harris, P. J. F. (1999). Carbon Nanotube and related structures, Cambridge University Press.

http://www.iljinnanotech.co.kr/en/home.html. (2006). Retrieved 23 March, 2006.

Iijama, S. (1993). "Single-shell carbon nanotubes of 1-nm diameter." Nature(363): 603 - 605.

Iijima, S. (1991). "Helical microtubules of graphitic carbon." Nature **354**: 56-58

Kroto, H. W., J. R. Heath, et al. (1985). "C(60): Buckminsterfullerene." Nature **318**: 162-163.

Monthioux, M., B. W. Smith, et al. (2001). "Sensitivity of nanotubes to chemical processing: An electron microscopy investigation." Carbon **39**: 1261-1272.

Nikolaev, P., M. J. Bronikowski, et al. (1999). "Gas-phase catalytic growth of single-walled carbon nanotubes from carbon monoxide." Chemical Physics Letters **313**(1-2): 91-97.

Pierard, N., A. Fonseca, et al. (2001). "Production of short carbon nanotubes with open tips by ball milling " Chemical Physics Letters **335**(1-2): 1-8.

Rao, C. N. R., B. C. Satishkumar, et al. (2001). "Nanotubes." ChemPhysChem **2**: 78-105.

Rinzler, A. G., J. H. Hafner, et al. (1995). "Unraveling Nanotubes - Field-Emission from an Atomic Wire." Science **269**(5230): 1550-1553.

Saito, R., G. Dresselhaus, et al. (1999). Physical properties of carbon nanotubes, Imperial Collage Press, London.

Salvatet (1999). "Elastic and shear moduli of single-walled carbon nanotube ropes." Phys. Rev. Lett. **82**: 944.

Thess, A., R. Lee, et al. (1996). "Crystalline ropes of metallic carbon nanotubes." Science **273**(5274): 483.

Wal, V., R. L, et al. (2001). "Flame and Furnace Synthesis of Single-Walled and Multi-Walled Carbon Nanotubes and Nanofibers." J. Phys. Chem. B **105**(42): 10249-10256.

Walters, D. A., L. M. Ericson, et al. (1999). "Elastic strain of freely suspended single-wall carbon nanotube ropes." Appl. Phys. Letter **74**: 3803-3805.

Wiles, P. G. and J. Abrahamson (1978). "Carbon fibre layers on arc electrodes I - their properties and cooldown behaviour." Carbon **16**: 341-349.

Yakobson, B. I. and R. E. Smalley (1997). American Scientist **85**: 324.

Yu, M. F., O. Lourie, et al. (2000). "Strength and breaking mechanism of multiwalled carbon nanotubes under tensile load " Science **287**: 637-640.

Chapter 2: CNT Growth in an Electric Arc 2-1
2.1 Introduction 2-1
2.2 Theories of CNT growth 2-1
2.2.1 Vapour phase growth 2-1
2.2.2 Liquid phase growth 2-5
2.2.3 Solid phase growth 2-6
2.2.4 The crystallization model 2-7
2.3 What do CNT growth from? 2-7
2.3.5 Nuclei for the growth of CNT 2-7
2.4 Growth of CNTs 2-10
2.4.1 Carbon cluster nucleation 2-10
2.4.2 Nucleation Temperature 2-10
2.4.3 CNT growth process 2-11
2.4.4 Electric field 2-12
2.4.5 End of growth (Growth termination) 2-13
2.5 Catalytic growth of SWNTs 2-14
2.6 New thought of CNT formation 2-18
2.6.1 Nanoparticles as feed stock for CNT formation 2-19
2.6.2 Anode surface temperature measurement 2-21
2.7 References 2-22

Chapter 2: CNT Growth in an Electric Arc

2.1 Introduction

The formation of CNTs in an electric arc is a very complex phenomenon and only partially understood. This is due to the extreme conditions *e.g.* high temperature and low pressure in the synthesis process, which involves a kinetic controlled mechanism. These rough conditions also make it difficult to validate the theories via experimental work (Marcos, Lopez et al. 1997). This chapter is devoted to the formation and growth of CNTs. The main attention is given to a new continuous method of CNTs production in arc discharge and measurements made of nanotubes deposition on a carbon substrate.

The growth mechanism of CNTs in a carbon arc and in the laser ablation method will also be discussed. The mechanism for these two methods is probably different but closely related due to the similarity in the extreme condition that exists, *i.e.* high temperatures involved in the process. The main questions needed to be answered are 'What do the CNTs grow from?', 'What is the region of the CNTs formation?' and 'How do they grow?'

2.2 Theories of CNT growth

Harris (Harris 2007) in his review described the possible theories for MWNTs growth, which are:

a) Vapour phase growth
b) Liquid phase growth
c) Solid phase growth
d) The crystallization model

2.2.1 Vapour phase growth

Several possible mechanisms have been proposed for the growth of MWNTs such as shell by shell growth (Endo and Kroto 1992) and simultaneous growth of all shells (Iijima 1993). They assumed that the nucleation and growth of CNTs are due to the carbon vapour condensation from the vapour or plasma phase. According to the shell by shell growth model, each next shell results from carbon adsorption onto the surface of the preceding inner shell. The open-end growth model by Iijima (1993) states that the end of

the tube is kept open when the tube is growing in the carbon arc plasma. The tube end then quickly closes when the growth condition becomes inappropriate. The temperature, pressure, carbon flux and current density may be fluctuating and disturbing the CNTs growth. Figure 2.1 illustrates Iijima's open-end growth model.

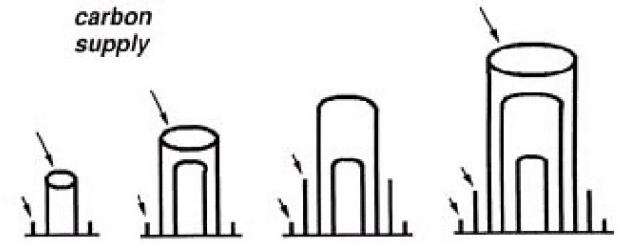

(a)

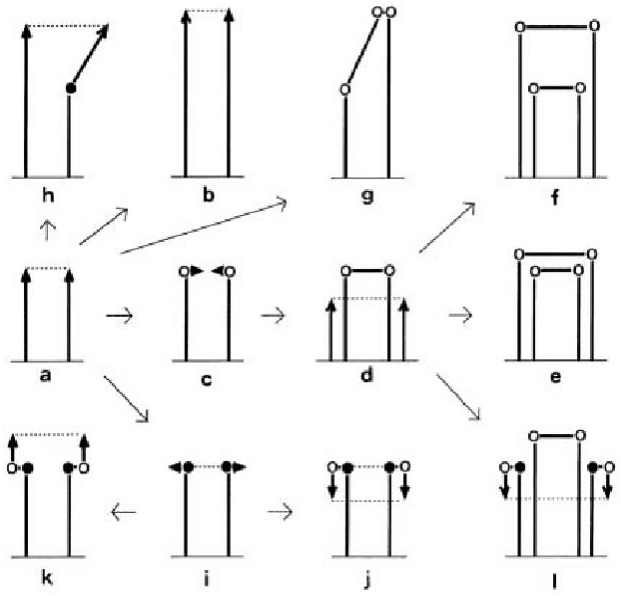

(b)

Figure 2.1 A model for the open-end growth of the CNT (a) The tubule end is open while growing by accumulating carbon atoms at tube peripheries in the carbon arc. Once the tube is closed, there will be no more growth on that tube but a new tube may start on the side wall. (b) Evolution of CNT terminations based on the open-end tube growth. Arrows represent passes for the evolution. Arrow heads represent termination of the tubes and also growth direction. Open and solid circle represent locations of pentagons and heptagons respectively (Iijima 1993).

Iijima argues that carbon atoms can be deposited on the tube peripheries as long as the tube end is opened as shown in Figure 2.1 (a). Introducing six pentagons will then enclose the tube end, and the tube caps become inactive and stop the growth on that particular tube shell. Another shell may start to grow on the outer side wall (See Figure 2.1 (b)-e). These tubes may eventually be enclosed due to some reasons mentioned earlier. By repeating the process, Iijima explains why CNTs produced are usually long and have several layers (Iijima 1993).

Another detailed analysis of arc discharge producing CNT was presented by Gamaly and Ebbesen (1995). They proposed that the bimodal carbon velocity distribution (ions with drift velocity and isotropic neutral) determines the NT creation near the cathode surface. According to them, the CNT deposition may consist of many cycles and each of these cycles consists of four steps which include:

(i) seed structure formation

(ii) growth process

(iii) termination of growth

(iv) tube end capping

Little (2003) presented 12 stages of growth mechanism for CNTs that ranged from carbon atomization to the termination of CNT growth. These stages were described in chronological orders. The chronological order, however, was found not to be realistic since the intermediate species may exist from the beginning. Also some of the steps are likely to occur simultaneously (Little 2003) and only the first six stages will be discussed here.

The first stage involves energy transformation, transition and transport. In the electric arc, electron and photon bombardment rapidly transfers high energy fluxes from the cathode to the anode (carbon substrate), breaks the carbon bond and thus releases all the carbon species. Similarly, in laser ablation unit, the heat vaporises the electrode (anode) surface forming a plasma plume which explodes off the surface in $\Delta t \sim 1$ μs (Kokai, Takahashi et al. 2000; Puretzky, Geohegan et al. 2000).

The second step is the expansion of carbon vapour from the atomisation site onto the reactive solution. This step is very important to isolate carbon species before they can chemically recombine. Here, the carbon intermediates move outward from their atomisation point to the reactive solution area. The expansion is thermally driven in the carbon plasma plume with the expansion energy supplied by the arc or laser source.

The third stage is the "carbon fixation and rehybridization" period. It concerns with the formation of sp-hybridized state of carbon atoms from their electronic or chemical states. The conservation of energy and momentum during electronic rearrangement determines whether the fixation of carbon and metal atom will occur. The intensity and frequency of the collision of carbon atoms, ions and metal atoms increase with temperature of carbon plume. This explains the ability of the arc method to produce high CNTs yield (Koshio, Yudasaka et al. 2002), to produce CNT without the needs for background heating (Takizawa, Bandow et al. 1999) and to form MWNT without the presence of metal catalysts (Koshio, Yudasaka et al. 2002).

The fourth stage is also known as the carbon confinement stage. Here, the uncondensed carbon plasma-plume, the background gas pressure and inter-atomic potential affect the carbon confinement process. The background pressure should be high enough to confine the plume and allow sufficient carbon fixation to occur which leads to formation of C_2 and also the nucleation and growth of CNTs. If the background pressure is too high, the plume will be small and thus deter the carbon isolation process.

The fifth stage is the cooling of the system which may precede step 2 and 3 or may occur co-current with these steps. CNTs formation may be quenched if the cooling is too fast (Bandow and Asaka 1998); MWNT, on the other hand, will be formed if cooling is done too slow (Koshio, Yudasaka et al. 2002).

The sixth stage is the "distortion of reactive media" stage. During this period, the system loses its kinetic energy as a result of complex interaction and dynamics between the carbon solution and the background gases. A strong background gas can distort the weaken plasma plume. Using a pulsed laser method, Kokai et al.(2000) managed to visualise the above-mentioned stages. Their illustrations are as shown in Figure 2.2.

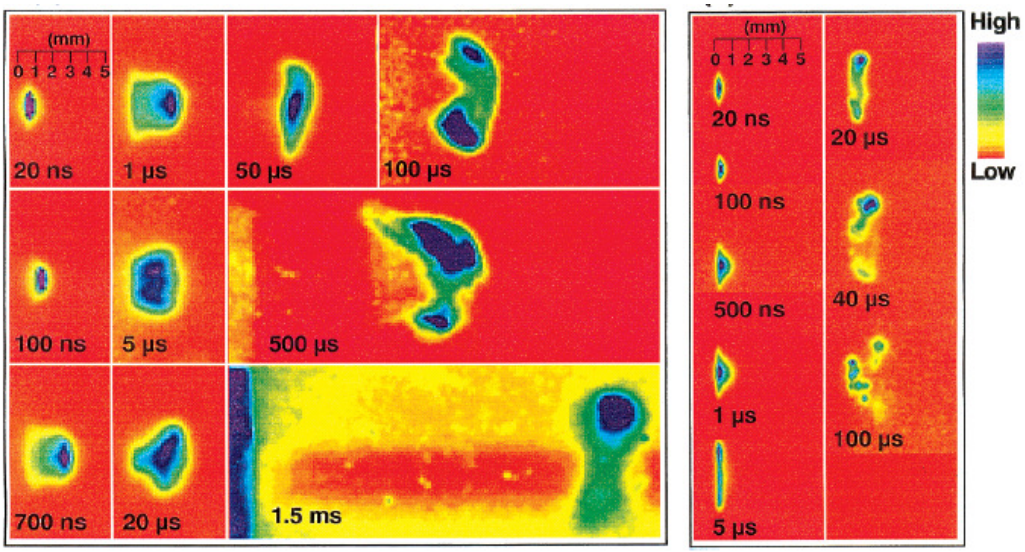

(a) (b)

Figure 2.2 Typical gated ICCD images of the total visible emission for laser ablation at (a) 1200°C and (b) room temperature. These images are two sets of those taken for different laser shots at various delay times. The images at 0.02-2 µs were taken with a gate width of 0.003 µs, those at 5-50 µs with gate widths of 0.01-0.1 µs, and those at 100, 500, and 15 000 µs with gate widths of 0.15, 0.3, and 5 µs, respectively. All the images are normalized relative to each maximum signal level. Also shown are the scale for the length from the target and the colour look-up table for emission intensity, where the red background colour is zero counts and the maximum signal is purple (Kokai, Takahashi et al. 2000).

2.2.2 Liquid phase growth

In 2005, De Heer and colleagues proposed the liquid phase model of MWNT growth (De Heer, Poncharal et al. 2005). In their work, they found their tubes always decorated with beads of amorphous carbon, which was suggested to be solidified liquid carbon. They argued that anode is locally heated by electron bombardment from the cathode causing the surface to liquefy. The liquid carbon globules are then ejected from the anode. Due to the different cooling rate between the surface of the globules and the interior, the liquid carbon becomes supercooled. Carbon nanotubes and nanoparticles are then nucleated and grow within this supercooled liquid carbon (De Heer, Poncharal et al. 2005).

2.2.3 Solid phase growth

Harris *et al* (Harris, Tsang et al. 1994) introduced the idea of solid phase CNT growth. In their work, fullerene soot was heated to 3000 °C in a positive -hearth electron gun. From their observation, nanotube-like structures such as SWNT and cones can be produced by high temperature heat-treatment of fullerene soot. From this finding they suggested that a solid state model of nanotube growth, in which fullerene soot is an intermediate product. In their model, they proposed that carbon vapour condenses onto the cathode during the initial stage of arc-evaporation and formed fullerene soot-like material. Due to the high temperature in the arc process, this material transformed into a CNT seed and then formed MWNTs. A work by Chang and colleagues in 2000 (Setlur, Doherty et al. 2000) also shows that heating of a non-graphitizing microporous carbon (doped with boron) to 2200-2400 °C can produced MWNTs which have a similar structure to those formed by arc discharge. The group later reported the MWNTs can also be produced from carbon black (Buchholz, Doherty et al. 2003).

In 2004, Chen *et al.*(2004) reported that NT can be formed without a vapour phase from a mechano-thermal process. In this method, the graphite powder was mechanically ground at room temperature for 150 hours and then annealed at 1400^{o}C for 3 hours (Chen, Conway et al. 2004). The results showed that clusters containing CNT and nanoparticles were found in the sample after the annealing process. The high resolution TEM micrograph clearly showed the presence of MWNT structure with hemispherical cap (Chen, Conway et al. 2004). No nanotubes were formed during the ball milling process.

The ball milling process may create precursor containing nucleation seed. A large number of a metastable curved graphene layers might be produced during this process. These layers transform to a more stable shape and geometry, such as nanotubes on annealing. Chen *et al*. (Chen, Conway et al. 2004) also found that MWNT are normally formed at the temperature range of 1000 – 1500^{o}C. However, if the heating is increased to 1800^{o}C, a thick NT bamboo (> 20nm diameter) were observed. From the study, they concluded that the source of carbon atoms for CNTs formation must be disordered carbon since no vapour phase exists at low annealing temperature, T ~ 1400K (Chen and Yu 2005).

2.2.4 The crystallization model

This model was proposed by Zhou and Chow (Zhou and Chow 2003) when describing HRTEM observation of defective nanotube-like structure produced by arc-evaporation. They suggest that the tubes were formed through two stages crystallization model. In the first stage, amorphous carbon "assemblies' with variety of shapes are formed on the surface of the cathode. The graphitization of these "assemblies' was then occurred during the cooling process in the second stage. This process began from the surface and progressed towards the centre. The model was supported by the work of Huang and colleagues (Huang, Chen et al. 2006). In their work, they grew amorphous carbon nanowires *in-situ* by electron-beam deposition inside a HRTEM. They observed that the wire evolved into graphitized structures when resistively heated to temperatures higher than 2000 °C.

2.3 What do CNT growth from?

In order to understand the nature of the NT precursors, we must define the arc discharge environment. Plasma in any arc is characterised by its ability to carry an electric current and sustain external stresses. This can be achieved by having ionized substances in the plasma. All substances become ionized if they are heated to sufficiently high temperature. In an arc discharge, ionization depends on the production of an electric avalanche (Frank-Kamanetskii 1972). As the arc strikes, the electrons accelerate between anode and cathode and collide with the atoms and other particles as they cross their paths. A collision can either increase the kinetic energy of the atom or ionize it. Charged solid particles are also generated via collision with an electron (Beynon 1972). Details of these mechanisms are also described in Chapter 5.

2.3.1 Nuclei for the growth of CNT

The general value for stable carbon arc plasma is around 4000 K. At this temperature, the plasma is not fully ionized. This type of plasma may consist of a mixture of carbon nanoparticles in various forms and sizes. These carbon nanoparticles can

originate from both fully ionized carbon atoms and bigger molecules such as amorphous carbon and graphene fragments.

This hypothesis is also supported by Abrahamson's (Abrahamson, Davies et al. 1980) conclusion that the amorphous phase of the electrode material is the first to be vaporised. Other researchers have also proposed that carbon nanoparticles are the nuclei for the growth of MWNTs in an arc discharge unit (Saito, Fujita et al. 1993). According to the model for CNT growth with an open tip, the nucleus to the NT growth is a cup-like cluster which makes up half of the fullerene formed (Guo, Nikolaev et al. 1995). MWNTs are formed not only in an arc discharge but also in a carbon vapour deposition units that apply a graphite ablation technique (Chernozatonskii, Kosakovskajab et al. 1995). The possibility of graphite ablation in the nanocrystal formation was experimentally examined by Rohlfing (1988). While working with laser vaporization of graphite into a pulsed helium flow, he observed the presence a blackbody emission spectrum. This continua spectrum can be interpreted to be due to the incandescence of hot carbon particles, T ~ 2500-4000 K

The formation mechanisms of MWNTs in a laser ablation unit were found to be similar to those of the arc discharge. Carbon nanoparticles formed from graphite nanocrystals adsorb onto a substrate and thus become the nuclei for the growing nanotubes.

From the review done by Little (2003), it is clear that there are few factors that affect the formation of CNTs in the arc discharge. The main parameters include the plasma temperature and the background gas pressure and temperature. However, the background pressure also has a strong influence as it controls the density and conductivity of the plasma. Querrioux (2004) summarized the role of these parameters on the production of CNTs and based his discussion on the review done by Little (2003). These parameters are shown in Table 2-1 and become the base of this study.

Table 2-1 Parameters to be considered during the formation of carbon nanotubes (Querrioux 2004)

Carbon atomization t = 0 to 1 s	Plasma temperature	The energy delivered is necessary to break the links between the carbons on the tape and reach chemically and electronically excited states(Takizawa, Bandow et al. 1999)	Far from equilibrium, irreversible, non cyclic dynamics	
Carbon expansion t = 1 to 100 s	Plasma temperature	Thermally driven in the plasma – it's relaxation step directly link to the 1st excitation one, and thus the temperature involved	Irreversible, non equilibrium, non cyclic expansion	Paramagnetism, electronic & interatomic interactions(Little 2003)
Carbon fixation t = 1 to 100 s	Plasma temperature	Involves particles collision. The frequency and intensity of collision increases with the temperature of the plasma(Bandow and Asaka 1998)	The huge temperature delivered by the carbon arc explain why it doesn't required any background heating to produce nanotube or metal to MWNT(Koshio, Yudasaka et al. 2002)	Metal catalyst
Carbon confinement t = 1 to 100 s	Background pressure	Prevents dispersion of the energy and mass of the system (excessive cooling and dissipation of carbon precursor)	If pressure too low, the dispersion will occur. If it's too high, it will block the expansion step	
Carbon cooling t = 50 to 100 s	Background temperature	The cooling of the system allowed its relaxation from its discrete states(Little 2003)	The cooling rate determines the production rate, yield and selectivity. Too rapid cooling may quench the CNT formation (Bandow and Asaka 1998), too low cooling rate results in MWNT (Koshio, Yudasaka et al. 2002) or nanorods (B=baker 1989) formation.	
Distortion t = 100 s	Background temperature/pressure	The system slows down. When the influence of interatomic potential takes over the kinetic energy, the shape of the system modified: it's "distortion"(Little 2003)	The absence of distortion may cause surface diffusion and confinement, and the SWNTs mechanics relative to MWNTs and filament growth dynamics.	Static magnetic field(>1 tesla) cause an evolution from CNTs to filaments

2.4 Growth of CNTs

2.4.2 Carbon cluster nucleation

There are several theories presented regarding the growth of CNT. Most of them have a common basis that the carbon cluster nucleation is due to the interaction of small carbon clusters (Endo and Kroto 1992; Takizawa, Bandow et al. 1999; Miyamoto, Berber et al. 2002). In the uncondensed plasma such as arc plasma and laser vaporisation, nucleation occurs due to the high carbon concentration, high temperature, density and pressure and also rapid cooling. In a laser vaporization method, the cluster nucleation occurs when the temperature drops below 2000°C due to loss of kinetic energy by cooling and expansion. This loss induces metal and carbon atoms interaction and start the nucleation (Kanzow and Ding 1999; Takizawa, Bandow et al. 1999; Puretzky, Geohegan et al. 2000). In contrast, Saito *et al*.(1993) proposed that carbon nanoparticles are nucleated through the growth of MWNT in an arc discharge unit (Saito, Fujita et al. 1993).

Another theory suggests that at high temperature and lower carbon concentration, carbon chains, rings and hoops are nucleated by the ring stacking mechanism. On the other hand, at lower temperature and high carbon concentration, the cluster nucleation may also occur through the pentagon road mechanism (Little 2003). The ring stacking mechanism occurs in homogenous and heterogeneous systems. Basically the ring stacking pathway starts with carbon polymerization which involves formation of small carbon cluster such as C_2 and C_3. This is then followed by a combination of C_2 with C_3. Endo and Kroto (1992) have demonstrated the CNT formation by carbon polymerization in their study (Endo and Kroto 1992). Their findings showed that C_4, C_6, polyynes and PAHs form the basic building block for CNT nucleation and growth in the plume.

2.4.3 Nucleation Temperature

Watanabe *et al.* (2006) measured the nucleation temperature of different metal in radio frequency (RF) thermal plasma synthesizing CNTs. In their experiment, the initial stage of CNT growth is considered as the carbon and/or metal nucleation stage The particle formation was observed when the nucleation rate was under 1.0 $cm^{-3}s^{-1}$. They calculated

the nucleation temperature of different metal powders for CNT preparation in RF plasma. Nucleation temperature for carbon was found to be approximately at 3100 K.

2.4.4 CNT growth process

The CNT growth theories share the same idea that after the nucleation, NTs keep growing by addition and insertion of carbon atoms or micro structures. CNT growth may concur with CNT nucleation leading to MWNT formation. The elongation of CNT by C_n insertion may occur at side wall for closed growth. An open growth may occur on the NT tip. According to Bandow *et al.* (1998), the side wall insertion and cap formation are more difficult and can occur only at high temperature. Tip insertion is easier and may involve only simple bonding of C_n to reactive C dangling bond (Endo and Kroto 1992).

The importance of particle collision for CNT growth was argued by Gamaly and Ebbesen (1995). This collision is favoured in high temperature and pressure conditions. Little (2003) suggested that the energetic collisions create defects on the tube and thus increases the tubular vibrational temperature (T_{vib}). This effect increases the diffusion of the carbon atoms along the tube and cause defect into and to the tube tip (Little 2003). The electron bombardment can also create defect on the tube and thus facilitate the fusion of two CNTs to form junction (Banhart 2004). The side wall insertion also requires more energy (Bandow and Asaka 1998).

Since arc discharge usually operates at high temperature, most of the time MWNT will be produced unless catalyst is supplied. In the presence of metal catalyst, the metal is assumed to be located at the NT tip cluster. This prevents its closure during growth (Guo, Nikolaev et al. 1995).

It was also suggested that the open ended growth could be explained by a lip-lip interaction mechanism. The molecular dynamic simulation on MWNT showed that the growing edge is stabilised by the bridging carbon atoms and thus kept the structure open. The lip-lip interaction inhibited dome closure. The bridging bonds were found to continually break and re-form which facilitated the absorption of carbon atoms by the NT edges (Charlier, De Vita et al. 1997).

2.4.5 Electric field

With regards to the electric field, it is suggested that the electric fields align the tube bundle (Colbert and Smalley 1995). In the plasma, the electric field might cause the attraction of particles towards each other. As commonly accepted, the space distribution of potential drop is especially steep near the electrodes. This can occur in a region of positive or negative charge space.

Leistner (2002) suggested that due to the potential drop in the arc, any elevation from the anode surface will disturb the neighbouring gradient of the electric field. Under the influence of this field, the particles tend to follow the gradient which will attach them to the surface of the nanotubes. This is how the addition process is localised (Leistner 2002).

Another important question is how the CNT growth occurs at open tips? This phenomenon is still not understood. At T ~ 3000 ^{o}C, the temperature is higher than the required value to anneal carbon vapour to form spheroidal closed shell (fullerene or onion) with high efficiency. Therefore the issue of how CNT that grows in the arc remains open is not yet clarified.

Colbert and Smalley (1995) suggested that the electric field in the plasma plays an important role for CNT to grow in the arc. Based on the ab-initio structure calculation, they suggest that the high electric field that concentrates at the growing NT tips provide the necessary stabilisation to keep the tip open. They also irradiate the dome-closed NT for 30 s, at 3000 ^{o}C at -75 V bias, to sublime some carbon from the tip to produce open tip CNT. However when the tube was reheated at 0 V bias, the tip was re-closed.

Even with all these discoveries, the role of electric field in affecting the production of aligned CNT is still questionable. In the absence of electric field for example in the CVD unit, aligned CNT can still be produced.

2.4.6 End of growth (Growth termination)

Theoretically a certain amount of pentagonal defect is needed to close a nanotube. Based on Euler's law for the closing of a hemisphere with polygons, Iijima (1993) stated that six pentagons are required to form a nanotube tip. The shape of the cap is determined by the distribution style of these six pentagons as shown in Figure 2.3.

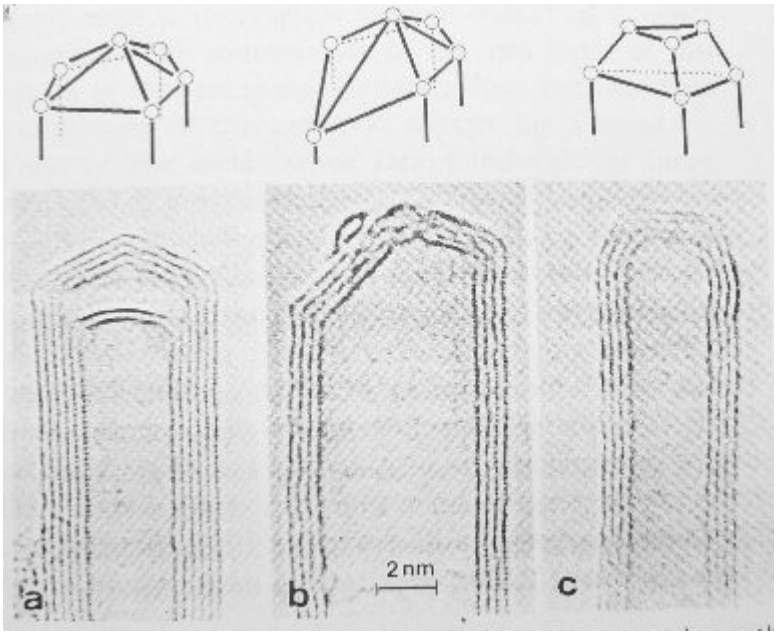

Figure 2.3 The capping of the tube with polyhedral where (a) a symmetrical cap with an apex, (b) an asymmetrical cap, and (c) a symmetrical with flat head (Iijima 1993)

Another type of capping is called a conical capping (Crespi 1999). This type of capping is shown in Figure 2.4. In this case, the first pentagonal defect will initiate a curvature; the tube wall begins to taper inward followed by the NT enclosure by the other five pentagons defects.

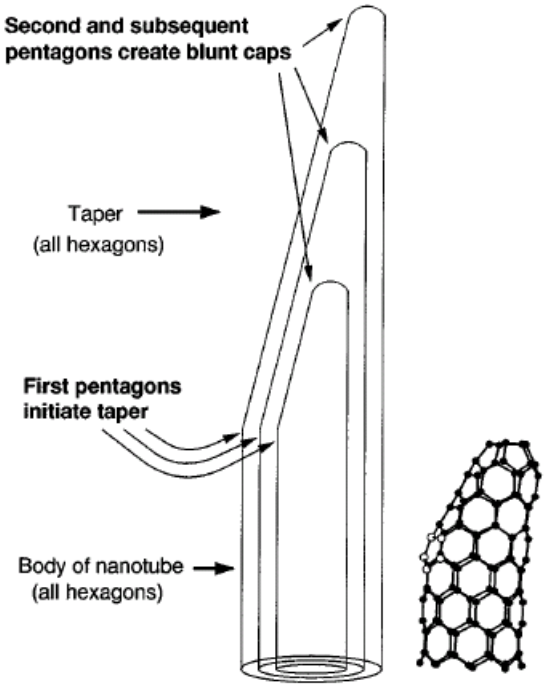

Figure 2.4 Schematic of a capped multiwalled nanotube. The body of the tube is straight and contains a hexagonal ring network of sp^2 bonded carbon. The first pentagonal defect initiates a taper. The second and subsequent pentagons form an abrupt cap. Six pentagon defects are necessary to form a complete closure on the end of the tube. The right-hand figure provides a much smaller-scale atomic model of a taper with the initial pentagon in white (Crespi 1999).

These defects will only exist if there is a temperature annealing. Therefore, it is possible to suggest that the closing of NT occurs due to the fluctuation of temperature. For the arc process, this temperature fluctuation may result from the arc fluctuation at the top of the anode (Gamaly and Ebbesen 1995).

2.5 Catalytic growth of SWNTs

Arc discharge has been developed into an excellent method for both producing high quality MWNTs and SWNTs. For the growth of SWNTs, a metal catalyst is needed in the arc discharge system. The first success of producing SWNTs by arc-discharge was achieved by Bethune and co-workers in 1993 (Bethune, Kiang et al. 1993). In their work, they used anode doped with cobalt catalyst and found that abundant SWNTs formed in the soot materials. On the other hand, Smalley and colleagues (Guo, Nikolaev et al. 1995) reported the growth of high quality SWNTs at the 1 – 10 g scale, using a laser ablation method as described earlier in Chapter 1.

It is believed that the growth mechanisms of SWNTs formation in arc-discharge and laser ablation are very similar. Both processes use a similar starting material, namely a graphite-metal mixture, and both processes involve condensation of carbon atoms generated from evaporation of solid carbon sources.

Many models have been proposed for the growth of SWNTs by these methods. Two growth modes of CNTs are shown in Figure 2.5. In the 'root growth' mechanism, the tubes grow away from the metal particles, with carbon continuously supplied to the base. Once the surface is saturated with carbon, it starts to form a graphite sheet with fullerene cap. More atoms can be inserted into the metal-C sheet so the tubes get growing longer. Most of the metal particles observed in SWNTs have diameters much larger than individual tubes that grow on them and stay at the bottom of the tube (Saito et al, 1994).

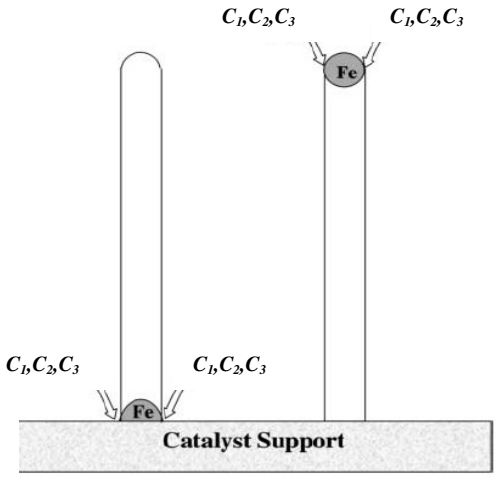

Figure 2.5 Two general growth modes of nanotube

The vapour-liquid-solid (VLS) model was then put forward by Saito when explaining SWNTs growth mechanism in arc-discharge (Saito 1995). The first step is the formation of a liquid nanoparticle of metal supersaturated with carbon. These nanoparticles originate from plasma/vapour condensation in a moderate temperature zone of the arc discharge or laser ablation chamber. During the synthesis, supersaturation is generated by decomposition and absorption of carbonaceous structure on the surface of nanoparticles. A solid phase nanotube begins to grow when the particle is supersaturated (Gavillet, Loiseau et al. 2001).

However, a number of experimental studies have suggested that SWNTs growth may involve a solid state transformation as reported by Geohegan and colleagues (Puretzky, Geohegan et al. 2000; Puretzky, Schittenhelm et al. 2002). They used optical spectroscopy to probe the species, temperature, and size of particles in this plume at the different times as shown in Figure 2.6. They studied these processes under the exact conditions for nanotube growth inside the hot oven to understand how carbon nanotubes grow.

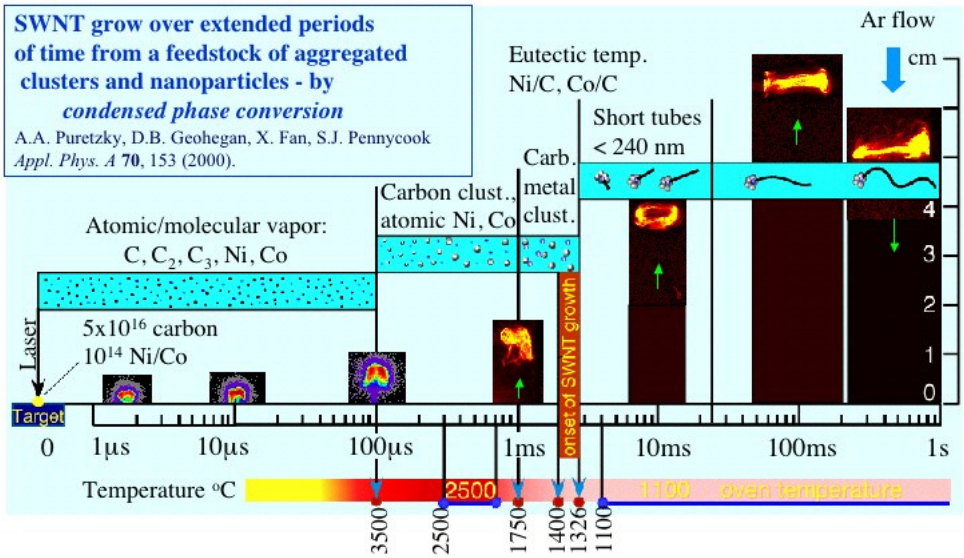

Figure 2.6 Actual images of the laser plume (t<200µs) and Rayleigh-scattering images of the plume (t>200µs) vs. time. (Puretzky, Schittenhelm et al. 2002).

Their data shows that carbon in the plume condenses within the first 0.2 ms after laser vaporization. At this point, the plume changes its appearance as the clusters begin to aggregate and become trapped in a swirling vortex ring. However, the atomic Co and Ni in the plume condense at lower temperatures, and wait for the plume temperature to cool. The ground-state Co population, for example, peaks at 1 ms as excited atoms relax into their ground states. Over the next millisecond, the ground state metal atoms condense, such that by t = 2 ms, the plume is virtually entirely composed of clusters, trapped within the swirling smoke ring. By this time, both carbon and metal atoms are in condensed form, so nanotube growth is largely a solid state process. This "microreactor" is where the single-walled carbon nanotubes grow. If growth is stopped after 20 ms, only short SWNT which are approximately 200 nm long, are found. This indicates that the majority of their growth (up to 10 micron lengths) occurs over a longer period ~ 100 ms to seconds of time – at rates of 0.5–5 µm/s.

Similar studies were carried out by Gorbunov and co-workers (Gorbunov, Jost et al. 2002). They prepared soot using laser-vaporisation at low temperature (800 °C) but no nanotubes were formed. This soot was then annealed at 1200 °C and resulting in the formation of an abundance of SWNTs. Based on their observation, they put forward a solid-liquid-solid (SLS) growth model as illustrated in Figure 2.7. A molten catalyst nanoparticle penetrates an amorphous carbon aggregate dissolving it and precipitating carbon atoms. These atoms then arrange to form a graphene sheet, whose orientation parallel to the supersaturated metal-carbon melt is not energetically favourable. Any local defect of this graphene sheet will therefore result in its buckling and formation of SWNT nucleus.

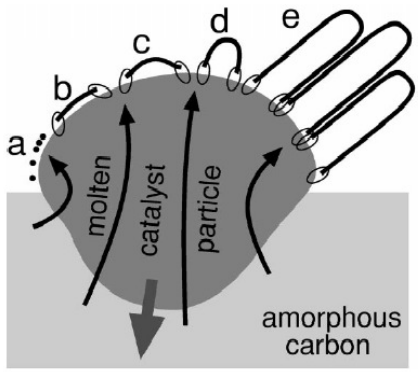

Figure 2.7 Illustration of the solid-liquid-solid mechanism for growth of SWNTs (Gorbunov, Jost et al. 2002).

Kataura and co-workers (Kataura, Kumazawa et al. 2000) proposed a model of SWNTs growth similar to Geohegan's but with emphasis on the key role played by the fullerene-like carbon fragment in nucleating growth. The model is illustrated in Figure 2.8.

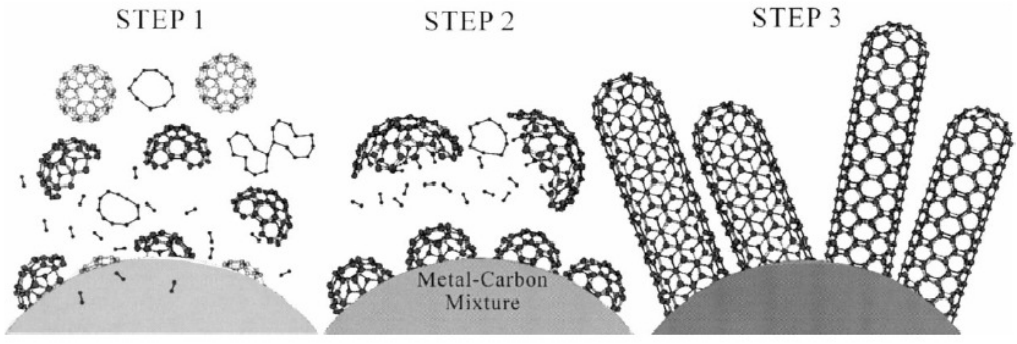

Figure 2.8 Illustration of a model proposed by Kataura and colleagues (Kataura, Kumazawa et al. 2000). Step 1 Carbon clusters and fullerenes are produced and dissolved in metal particles. Step 2 Metal particles saturated with carbon clusters Step 3 SWNTs grow out from the metal particle.

This model consists of three steps. The first step occurs at a very early stage (μs) and very high temperature (2000 – 3000 C) where the nucleation of carbon cluster starts. Some of the clusters are then melted into the metal particle. As the system cools, metal particles become saturated with carbon at around the eutectic temperature and covered with fullerene-like carbon fragment. The fragments then act as a precursor for SWNTs growth. This model would seem to offer the best currently available explanation for SWNTs production by the arc and laser methods (Harris 2007).

2.6 New thought of CNT formation

As discussed before, most of the growth models (Gamaly and Ebbesen (1995), Iijima (1993), Endo and Kroto (1992)) suggest that the primary source of CNT growth comes from carbon vapour. However Chen *et al.*(2004) reported that NT can be formed without a vapour phase from a mechano-thermal process. In this method, the graphite powder was mechanically ground at room temperature for 150 hours and then annealed at 1400^{o}C for 3 hours (Chen, Conway et al. 2004). The results showed that clusters containing CNT and nanoparticles were found in the sample after the annealing process. The high resolution TEM micrograph clearly showed the presence of MWNT structure with hemispherical cap (Chen, Conway et al. 2004). No nanotubes were formed during the ball milling process.

The ball milling process may create precursor containing nucleation seed. A large number of a metastable curved graphene layers might be produced during this process. These layers transform to a more stable shape and geometry, such as nanotubes on annealing. Chen *et al*. (Chen, Conway et al. 2004) also found that MWNT are normally formed at the temperature range of 1000 – 1500^{o}C. However, if the heating is increased to 1800^{o}C, a thick NT bamboo (> 20nm diameter) were observed. From the study, they concluded that the source of carbon atoms for CNTs formation must be disordered carbon since no vapour phase exists at low annealing temperature, T ~ 1400K (Chen and Yu 2005).

2.6.1 Nanoparticles as feed stock for CNT formation

The possibility that nanotube or cylindrical seed can be nucleated by spontaneous rolling of small fragment of graphite sheet or graphene due to high temperature thermal fluctuation has also been studied. Volpe and Cleri (2001) performed a molecular dynamic simulation of the free fluctuation of a small graphite nanofragment at T = 4000K. This temperature represents the arc discharge and laser ablation environment. Their simulation result showed that in the vibrational spectra of finite size nanofragment (*e.g.* N = 160), the density of low-frequency modes increases with temperature. This condition tends to fold over the flat fragment into a cylindrical shape (Volpe and Cleri 2001). The example of their simulation results is shown in Figure 2.9. Two parallel graphenes detach and fluctuate freely at T = 4000K and form a cylindrical structure within about 2 ps from the ablation.

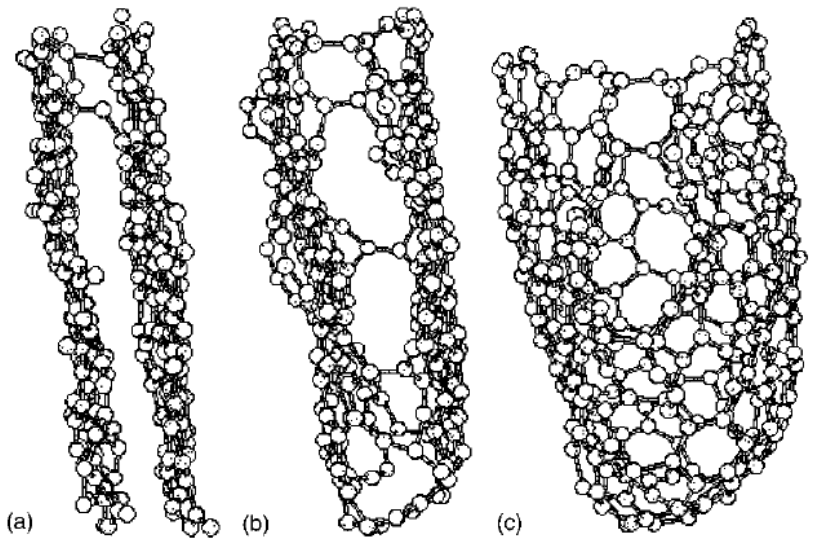

Figure 2.9 Three snapshots from the molecular dynamic simulation of the free oscillation of a graphitic nanofragment made by two parallel N=160 graphenes at T = 4000 K. The two graphenes begin forming bonds starting from the free perimeter (a), then get curved under the effect of constrained thermal fluctuation (b) and, finally, close to form the tip of nanotube(Volpe and Cleri 2001).

Volpe and Cleri (2001) also simulated this process at 1500K, which is closed to the temperature at which carbon nano particle nucleation occurs. At this temperature, the energetic barrier for closing tubes with a diameter of ~ 10 Å can be overcome. At this moment, plane folding become possible on a few ms time scale, which is typical for nanoparticle growth.

Louchev et al (2003) described a detail analysis of nanotube nucleation from a graphitic nanofragment by thermal vibration. Using a molecular dynamic study, they suggest a kinetic pathway in which an initially flat graphite nanosheet formed in a vapour and collided with nanoparticles. The sheet tended to fold into a nanoring segment (Louchev and Hester 2003). They also proposed a model that suggests during the cluster assembly, (Kokai, Takahashi et al. 2000; Puretzky, Geohegan et al. 2000) carbon nanostructure should disintegrate back into a smaller fragments. The existence of cluster assembly was also observed by Kokai *et al* (2000) and Puretzky *et al* (2000), however their descriptions differed from that of Louchev and co-workers *(*Louchev*,* Kanda *et al.* 2004*)*.

These fragments can assemble into a larger structure when they reach a solid substrate where the condensation heat may be easily dissipated by heat conduction into the solid (Louchev, Kanda et al. 2004). Harris *et al* (1994) reported that carbon onion and MWNT were formed when the carbon soot from the arc-evaporation process was heated up at the temperatures between 2500 K to 3500 K.

The presences of small particles ejected from the heated graphite/carbon surfaces at temperature above 3000K have been observed by many researchers (Finkelnburg 1946; Whittaker and Kintner 1969; Abrahamson 1971). A large number of small particles (d ~ 5 – 50 nm) were observed by Whittaker and Kintner (1969) while studying a heated graphite held in a carrier gas (Ar or He) with a velocity about 5 – 10 ms^{-1}. They claimed that these particles could not be formed from carbon vapour condensation because of the presence of a small gap (short time) between the graphite surface and the collection point (Whittaker and Kintner 1969). Most of the particles are cleavage fragment and electron diffraction studies indicated that they were crystalline.

A continuum emission spectrum was observed by Finkelnberg (1946) from an arc discharge with a graphite electrode operated in the air. He also observed a deposition of carbon on the cathode when the high current arc was operated at very narrow gap, less than several centimetres, and the cathode tip was placed in the luminous plume. He also found that about 40% of the carbon ejected from anode was deposited on the cathode.

In some experimental works done by Abrahamson (1971) using a DC electric arc with graphite anode, a milky haze was observed in front of the anode. The arc radiation showed a continuum spectrum which was interpreted as the radiation from many hot graphite particles similar to that observed by Finkelnberg (Abrahamson 1971).

Abrahamson (1974) in his review, recognized that the presence of these small particles will cause an error on the surface temperature measurement using an optical pyrometer. These particles could scatter some of the radiation from the graphite surface or absorb some of the radiation. Therefore as the cloud of these particles build up in the front of the graphite surface, less radiation or lower black body temperature would be observed (Treekrem 1968; Abrahamson 1974). He also suggests that the major fraction of the crystallites ejected from the graphite surface is less than 5 nm in size.

2.6.2 Anode surface temperature measurement

In Section 2.4.1 the possibility of small nanocrystallite or nanofragment as a feed stock for CNTs formation had been discussed. The presence of these nanofragments was also influenced the observed radiation from the anode or heated graphite surface. Therefore, it is proposed that the relationship between the CNT formation and yield and the presence of these nanoparticles in front of the anode surface can be studied indirectly through the measurement of anode surface temperature. This idea will be discussed further in this study to check the idea that the small nanocrystallites are the major source for CNTs formation in a carbon arc.

2.7 References

Abrahamson, J. (1971). Reaction of Coal in a High Intensity Electric Arc. Chemical and Process Engineering, University of Canterbury. **PhD**

Abrahamson, J. (1974). "Graphite Sublimation Temperatures, Carbon Arcs and Crystallite Erosion." Carbon **12**(2): 111.

Abrahamson, J., C. Davies, et al. (1980). "Erosion Rates of Graphite Anodes in High Current Arcs." Industrial & Engineering Chemistry, Fundamentals **19**(3): 233.

Bandow, S. and S. Asaka (1998). "Effect of the Growth Temperature on the Diameter Distribution and Chirality of Single-Walled Carbon Nanotubes." Phys Rev Lett **80**(17): 3779-3982.

Banhart, F. (2004). "Formation and transformation of carbon nanoparticles under electron irradiation " Phil. Trans. R. Soc. London A **362**: 2205-2222.

Bethune, D. S., C. H. Kiang, et al. (1993). "Cobalt-catalysed growth of carbon nanotubes with single-atomic-layer walls." Nature **363**(6430): 605-607.

Beynon, J. (1972). The conduction of electricity through gases. London, Harrap.

Buchholz, D. B., S. P. Doherty, et al. (2003). "Mechanism for the growth of multiwalled carbon-nanotubes from carbon black." Carbon **41**(8): 1625-1634.

Charlier, J.-C., A. De Vita, et al. (1997). "Microscopic growth mechanisms for carbon nanotubes." Science **275**(5300): 646.

Chen, Y., M. J. Conway, et al. (2004). "The nucleation and growth of carbon nanotubes in a mechano-thermal process " Carbon **42**: 1543-1548.

Chen, Y. and J. Yu (2005). "Growth direction control of aligned carbon nanotubes " Carbon **43**(Letters to Editors): 3181-3194.

Chernozatonskii, L. A., Z. J. Kosakovskajab, et al. (1995). "New carbon tubelite-ordered film structure of multilayer nanotubes " Physic Letter A.

Colbert, D. T. and R. E. Smalley (1995). "Electric effects in nanotube growth " Carbon **33**(7): 921-924.

Crespi, V. H. (1999). "Local temperature during the growth of multiwalled carbon nanotubes." Physical Review Letters **82**(14): 2908-2910.

De Heer, W. A., P. Poncharal, et al. (2005). "Liquid carbon, carbon-glass beads, and the crystallization of carbon nanotubes." Science **307**(5711): 907-910.

Endo, M. and H. W. Kroto (1992). "Formation of Carbon Nanofibers." J. Phys. Chem **96**: 6941-6944.

Finkelnburg, W. (1946). The high current carbon arc. FIAT Final Report No.1052. Washington, D.C., Department of Commerce.

Frank-Kamanetskii, D. A. (1972). Plasma-The fourth states of matter. London, MacMillan.

Gamaly, E. G. and T. W. Ebbesen (1995). "Mechanism of carbon nanotube formation in the arc discharge." Physic review B **52**(3): 2083-2089.

Gavillet, J., A. Loiseau, et al. (2001). "Root-growth mechanism for single-wall carbon nanotubes." Physical Review Letters **87**(27 I): 2755041-2755044.

Gorbunov, A., O. Jost, et al. (2002). "Solid-liquid-solid growth mechanism of single-wall carbon nanotubes." Carbon **40**(1): 113-118.

Guo, T., P. Nikolaev, et al. (1995). "Catalytic growth of single-walled nanotubes by laser vaporization." Chemical Physics Letters **243**(1-2): 49.

Harris, P. J. F. (2007). "Solid state growth mechanisms for carbon nanotubes." Carbon **45**(2): 229-239.

Harris, P. J. F., S. C. Tsang, et al. (1994). "High resolution electron microscopy studies of a microporous carbon produced by arc-evaporation." J Chem Soc - Faraday Trans **90**(18): 2799-2802.

Huang, J. Y., S. Chen, et al. (2006). "Real-time observation of tubule formation from amorphous carbon nanowires under high-bias Joule heating." Nano Letters **6**(8): 1699-1705.

Iijima, S. (1993). "Growth of carbon nanotubes." Materials Science and Engineering B **19**(1-2): 172-180.

Kanzow, H. and A. Ding (1999). Phys Rev B **60**: 11180-11186.

Kataura, H., Y. Kumazawa, et al. (2000). "Diameter control of single-walled carbon nanotubes." Carbon **38**(11): 1691-1697.

Kokai, F., K. Takahashi, et al. (2000). "Laser Ablation of Graphite-Co/Ni and Growth of Single-Wall Carbon Nanotubes in Vortexes Formed in an Ar Atmosphere." J. Phys. Chem. B **104**(29): 6777-6784.

Kokai, F., K. Takahashi, et al. (2000). "Laser Ablation of Graphite-Co/Ni and Growth of Single-Wall Carbon Nanotubes in

Vortexes Formed in an Ar Atmosphere." J. Phys. Chem. B **104**: 6777-6784.

Koshio, A., M. Yudasaka, et al. (2002). "Metal-free production of high-quality multi-wall carbon nanotubes, in which the innermost nanotubes have a diameter of 0.4 nm." Chemical Physics Letters **356**: 595-600.

Leistner, M. (2002). Lehrstuhl fur Mechanische, Universitat Kaiserslautern.

Little, R. B. (2003). "Mechanistic Aspects of Carbon Nanotube Nucleation and Growth." Journal of Cluster Science **14**(2): 135-185.

Louchev, O. A. and J. R. Hester (2003). "Kinetic pathways of carbon nanotube nucleation from graphitic nanofragments." Journal of Applied Physics **94**(3): 2002-2010.

Louchev, O. A., H. Kanda, et al. (2004). "Thermal physics in carbon nanotube growth kinetics." Journal of Chemical Physics **121**(1): 446-456.

Marcos, P. A., M. J. Lopez, et al. (1997). "Thermal road for fullerene annealing." Chemical Physics Letters **273**: 367-370.

Miyamoto, Y., S. Berber, et al. (2002). Phys B-Condensed Matter **323**: 78-85.

Puretzky, A. A., D. B. Geohegan, et al. (2000). "In situ imaging and spectroscopy of single-wall carbon nanotube synthesis by laser vaporization." Applied Physics Letters **76**(2): 182-184.

Puretzky, A. A., D. B. Geohegan, et al. (2000). "*In situ* imaging and spectroscopy of single-wall carbon nanotube synthesis by laser vaporization." Applied Physics Letter **76**(2): 182-184.

Puretzky, A. A., H. Schittenhelm, et al. (2002). "Investigations of single-wall carbon nanotube growth by time-restricted laser vaporization." Physical Review B **65**(24): 245425.

Querrioux, T. (2004). Carbon Nanotube Continuous Production. Chemical and Process Engineering, University of Canterbury. **Master of Chemical and Process Engineering**.

Rohlfing, E. A. (1988). "Optical emission studies of atomic, molecular, and particulate carbon produced from a laser vaporization cluster source." J. Chem. Phys. **89**(10): 6103-6111.

Saito, R., M. Fujita, et al. (1993). "Electronic structure and growth mechanism of carbon tubules." Materials science & engineering. B **19**: 185-191.

Saito, Y. (1995). "Nanoparticles and filled nanocapsules." Carbon **33**(7): 979-988.

Setlur, A. A., S. P. Doherty, et al. (2000). "A promising pathway to make multiwalled carbon nanotubes." Applied Physics Letters **76**(21): 3008-3010.

Takizawa, M., S. Bandow, et al. (1999). "Effect of environment temperature for synthesizing single-wall carbon nanotubes by arc vaporization method " Chemical Physics Letters **302**: 146-150.

Treekrem, J. O. (1968). J. Chem. Phys. **49**: 2878.

Chapter 3: Experimental design and set-up 3-1
3.1 Introduction 3-1
3.2 History of 2000's batch reactor 3-1
3.2.1 Batch Reactor design 3-4
3.2.2 Comparison with 1978's reactor 3-6
3.3 Continuous arc reactor 3-7
3.3.1 Reactor design 3-7
3.3.2 Querrioux's work 3-11
3.3.3 Constraints in the continuous reactor design 3-13
3.4 Modifications of the apparatus for this work 3-14
3.4.1 Reactor support 3-14
3.4.2 Tape feeding system 3-15
3.4.3 Lens holder 3-16
3.4.4 Safety consideration 3-16
3.5 Anode surface temperature measurement 3-17
3.5.1 Optical pyrometer 3-18
3.5.2 Filters 3-20
3.5.3 Camera selection 3-20
3.5.4 Extrapolation of temperature range 3-22
3.5.5 Standard carbon arc 3-26
3.5.6 Calibration of intensity versus surface temperature 3-27
3.6 Materials 3-28
3.7 Operating procedure 3-30
3.8 Scanning Electron Microscopy (SEM) 3-32
3.9 References 3-33

Chapter 3: Experimental design and set-up

3.1 Introduction

This section will describe all the electric arc work done at Canterbury since 2000 aimed at finding and optimising the deposition of carbon nanotubes on the carbon electrodes. It includes a brief history of the 2000's batch reactor and the following continuously fed arc reactor. This is followed by description of the modifications to this continuous reactor during the experimental work done in this project. The experimental work can be divided into two major parts:

1. Modification and optimization of the continuous arc reactor,
2. Anode surface temperature measurements

3.2 History of 2000's batch reactor

A project to reproduce the result found by Wiles and Abrahamson in 1978 (Wiles and Abrahamson 1978) was started by Hill and Mani (Hill and Mani 2001) in the early 2000's. Details of the batch reactor are presented in the next section. The original 1970's batch reactor body was mostly used in the attempt to reproduce 1978's work. The 1978's image of fine fibres and crystallites which was found on graphite and carbon anode is shown in Figure 3.1. A similar fine fibre was also found in the cathode but was not published (Wiles 1979). The SEM images of the fine fibre found on the cathode are also shown in Figure 3.2.

The 2000 and 2001 series of experiments were useful for gaining a better understanding of the formation of CNTs and discovering the optimum arc conditions for CNTs growth. A subsequent modification had also been done later by Ulubay (Ulubay 2002) to improve the batch reactor. However, due to some setting variations in the apparatus used, the 2000 batch arc discharges rarely produced nanotubes on the electrode faces.

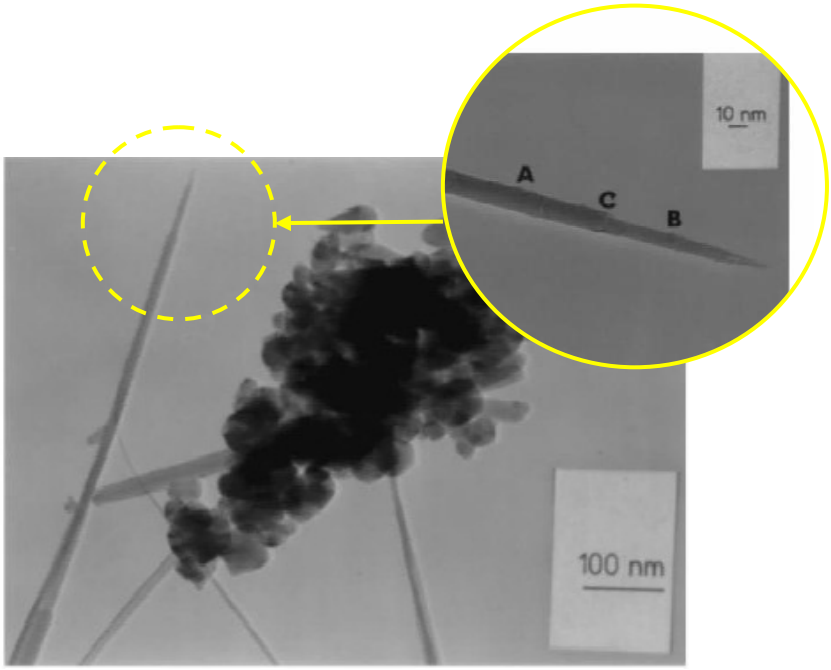

Figure 3.1 TEM micrograph of CNT produced on anode (Abrahamson, Wiles et al. 1999)

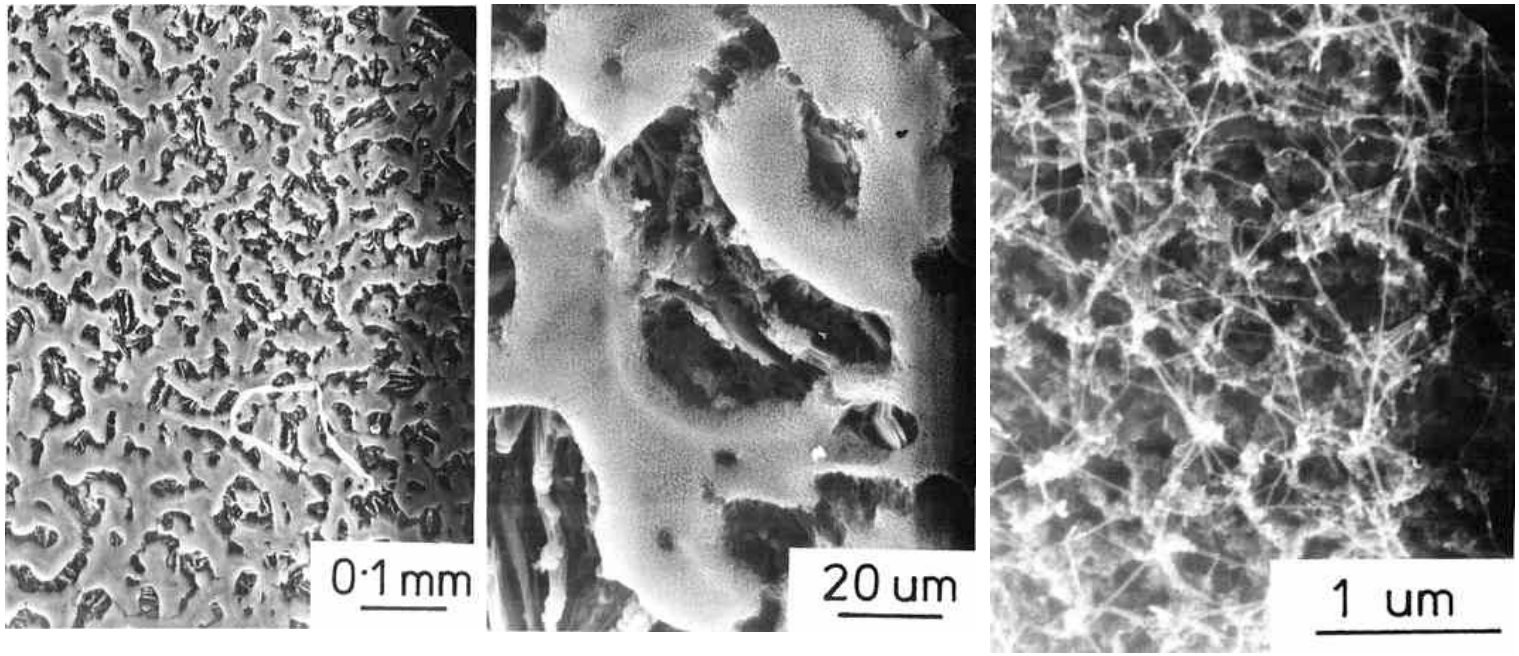

Figure 3.2 SEM micrograph showing details of carbon whisker deposit on graphite cathode crater (37 A , under 1 atm Nitrogen atmosphere). Apparent random broken by arc spot (Wiles 1979).

3.2.1 Batch Reactor design

A brass cylinder capped at both ends with a vertical central axis was used as a reaction chamber. The chamber volume was 0.001 m^3. Both anode and cathode were solid carbon graphite rods for this reactor. The anode feeder was mounted on the front side of the chamber whilst the cathode was fed at the side of the chamber, perpendicular to the anode. A viewing port was placed opposite to the anode face in order to directly view the arc and the anode surface during the operation. Another viewing port was placed at the side of the chamber to allow projection of arc images and measurement of inter electrode distance. The images were projected through lenses onto a paper screen. Both electrodes could be controlled manually by steering wheels to order to keep a constant inter-electrode gap. The anode feeder and the reaction chamber were cooled by water through the copper coils soldered onto the chamber wall. Spectroscopic grade carbon rods, Carbon L 113 SP with a diameter of 6.05 mm and 3 mm were used as anode and cathode respectively. The background gas was introduced to the arc parallel to the anode but at a reasonable distance from anode and cathode junction to avoid disturbance to the arc. The arc reactor was performed in a nitrogen or nitrogen-air atmosphere. The reactor was operated at just above atmospheric pressure. The flow chart of the apparatus used is shown in Figure 3.3.

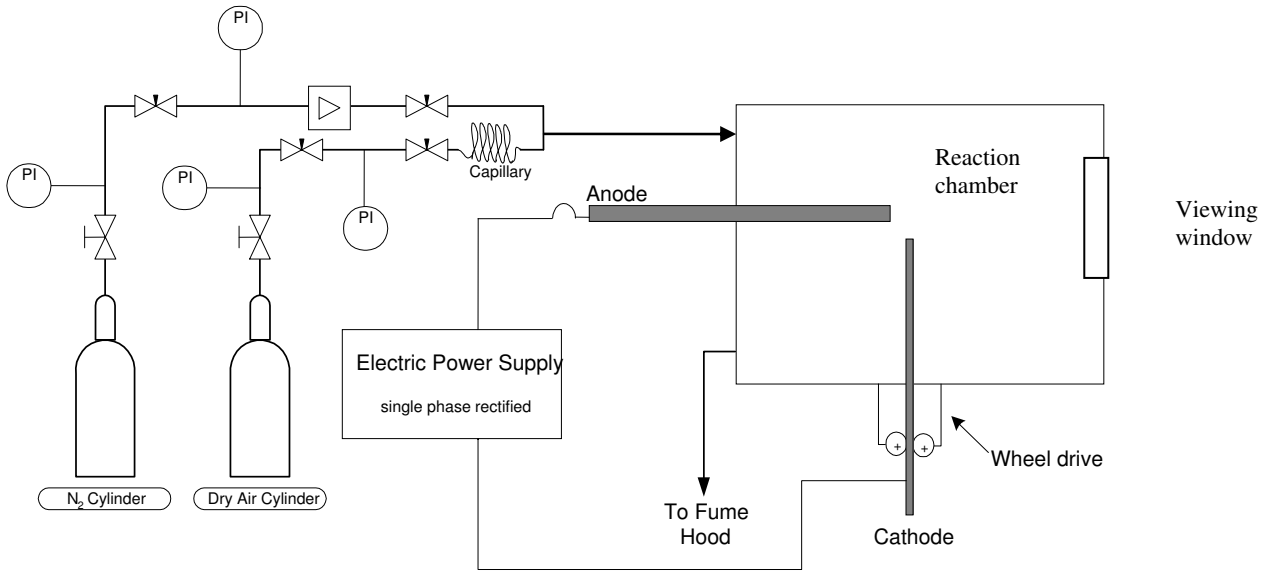

Figure 3.3 Flow chart of batch reactor, adapted from (Ulubay 2002)

3.2.2 Comparison with 1978's reactor

As mentioned earlier, the 2000's batch reactor was not very successful in reproducing the1978's results. This is probably due to the variations in the new reactor as described by Can Ulubay (Ulubay 2002). The differences between the two reactors are as summarised below;

Table 3.1 Variation in new reactor compared to 1978's reactor

	2000's reactor (Ulubay 2002)	1978's reactor
Cathode holder	Copper	Carbon
Gas supply - Nitrogen	Purity 99.998 %	Purity 99.900 %
Power supply	Single-phase DC	Three-phase DC

Further modifications on the new reactor were later done by Ulubay. He replaced the electrode holder from copper to carbon. Dry air was also introduced in the gas supply with a concentration of oxygen in nitrogen ranging from 0 to 8800 ppm to get a nitrogen purity similar to that of Wiles' and Abrahamson's. The major modification probably was the power supply for the reactor. Ulubay found a current ripple of about 10 A with the power supply used by Hill and Mani (Hill and Mani 2001), and for a D.C current in a range of 8-11 A and potential around 60 V , that mean a deviation up to $\pm$ 62.5% for the current and $\pm$ 50 % for the voltage.

Ulubay then was able to reduce the current ripple to 0.3 A and the voltage ripple to 0.4 V by connecting two large capacitor banks, with a total capacity of 35 mF, to the power supply. The resulting plasma was found to be more stable although the attachment zone was still moving around. Unfortunately, Ulubay's attempt to reproduce the 1978's result was also not very successful. One possible reason indicated by Ulubay was probably the use of boron nitride as the electrode insulator. He suggested, at high temperature this material probably evaporated and then acted as catalyst and influenced the formation of carbon nanotubes.

3.3 Continuous arc reactor

Abrahamson started the development with Chan in 2000 (Chan 2000). The reactor was then tested by Markus Leistner (Leistner 2002) and Can Ulubay (Ulubay 2002) with the aim to produce carbon nanotubes directly on the carbon substrate in a single step process without the need of pre- or after treatment. The product of this process (carbon substrate with CNT growth on its surface) has advantages for many practical applications such as field emission lamps and sensors. This method also enables the continuous or at least semi-continuous production of carbon nanotubes. In general the differences between this method and the conventional arc method are summarized in the table below.

Table 3.2 Comparison between Abrahamson's arc-discharge with conventional arc-discharge used for producing carbon nanotubes.

Parameters	Abrahamson's arc	Others
Process type	Continuous	Batch
Inter-electrode gap	2 – 8 mm	< 4 mm
Current	Low current, < 20 A	High current, >50 A
Chamber Pressure	~ 1 atm	< 0.5 atm / vacuum
CNT growth location	Substrate surface (Anode)	Cathode tip

3.3.1 Reactor design

Figure 3.4 shows the photograph of the first continuous reactor used. Here, the cylindrical reaction chamber was made from brass with an internal diameter of 100 mm and wall thickness of 21 mm. This body had a vertical axis of symmetry. The anode had a fixed horizontal position and the cathode could be attached horizontally or vertically.

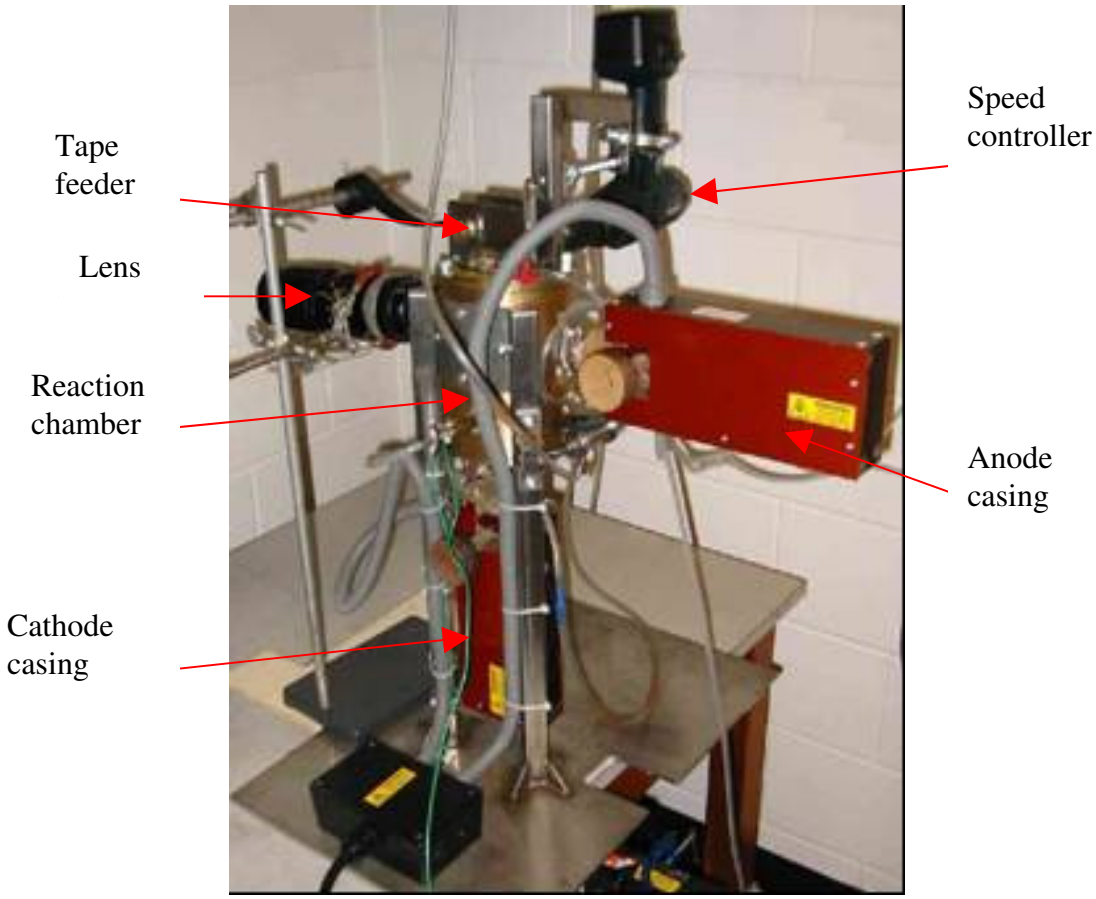

Figure 3.4 Photograph showing the continuous reactor with right-angled electrode position and major parts labelled, adapted from (Ulubay 2002).

The electrodes were fed by grooved wheels on a brass axle and these wheels were kept in contact by the tension provided by four O-rings. The electrode feeders were encased in an insulating housing made of Tufnol® (fibre-reinforced resin board). Two ports were made for the introduction of the cathode - one in the base and one in the cylindrical wall of the arc chamber. The port, which was not being used, was sealed with a small brass plate. A woven carbon fabric was used as the substrate to grow the CNT. The fabric was cut into a small size (defined as carbon tape in this study), approximately 25 mm width x 500 mm long. The carbon tape was fed through a port in the lid by two knurled reels and a motor with controlled speed was attached to one of the reels to drive the tape. An example of the Carbonics tape used is shown in Figure 3.5.

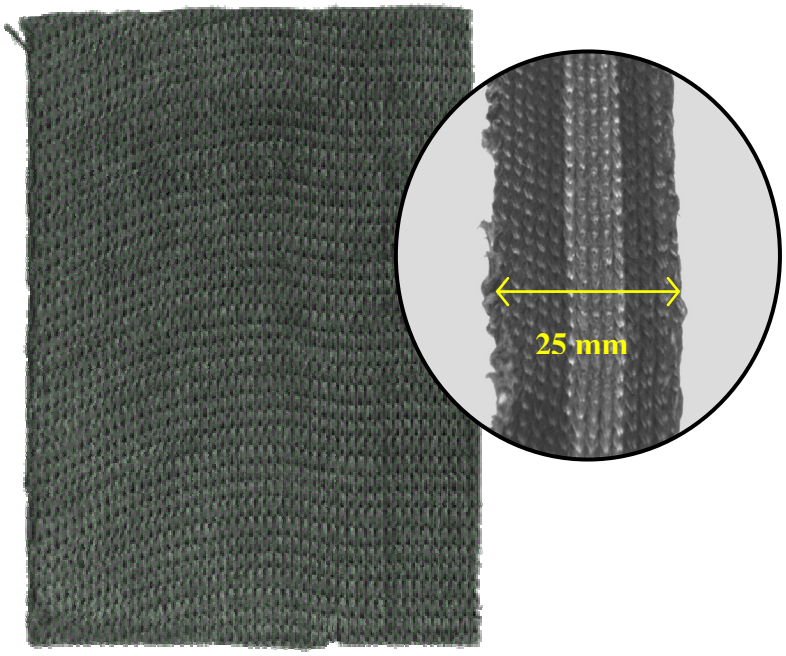

Figure 3.5 Photograph of carbon substrate, Carbonic GmbH fabric (on the right is the image of carbon tape).

Cathodes with a diameter of 3.00 mm, 6.05 mm and 7.66 mm were used by Ulubay in his preliminary experiments. Two electrode holders were built to connect smaller electrodes to the original 7.66 mm rod. Several parameters, including type of carbon tapes, tape speed, oxygen concentration, cooling of anode and tape, cathode position and cathode diameters, were investigated by him. Details of this experimental work can be found in Ulubay (Ulubay 2002)

The tape was passed through between the two electrodes and touching the anode. The tape was then turned 90 ° around a water cooled roller, which led the tape towards the outlet. A weight of approximately 200 g was attached to the end of the tape to provide enough tension and a uniform speed. The tape was cooled down by introducing a nitrogen gas flow through the nozzles both above and below after the treatment. This is shown in Figure 3.6. The carbon tape must be in contact with one of the electrode (in our case, anode) to ensure the substrate becomes part of the anode. Later we found that if the tape is not touching the anode properly, no nanotube will grow on the substrate surface.

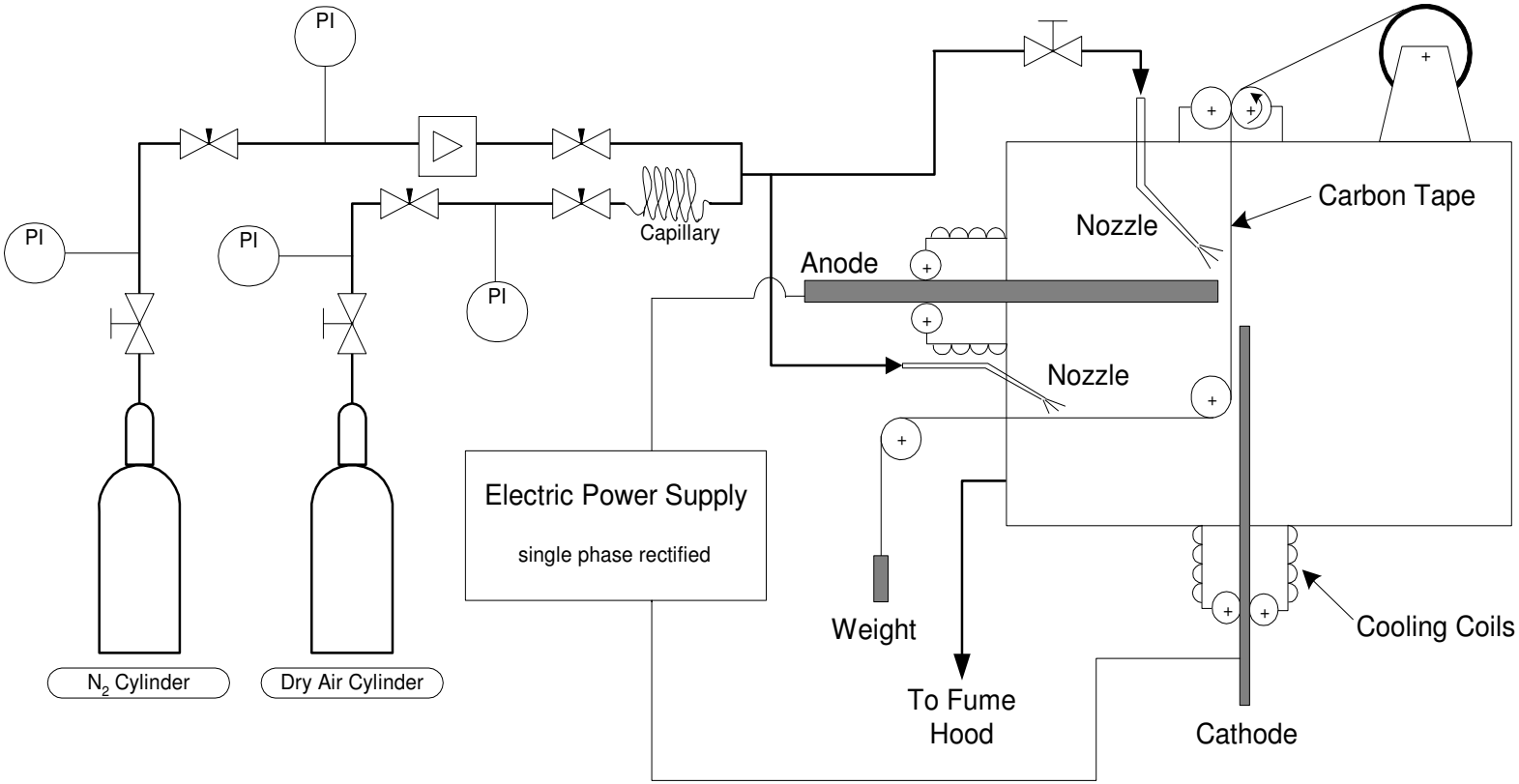

Figure 3.6 Flowchart of the first continuous reactor (Ulubay 2002).

The power supply used was identical with the modified power supply for the batch reactor, 8-20 A. The whole unit was placed under a fume hood with an additional cover to improve the air flow. An additional gas inlet, to cool the anode tip, was added to the reactor by Ulubay as shown in Figure 3.6. He wanted to have rough control of the tape temperature as he expected that the temperature might have major influence in the formation of CNTs.

From his preliminary experiments, he found that carbon nanotubes were not grown in any of the runs using Sigmatex® tape. However, he could not conclude the most possible reasons as a lot of parameters were changed after that experiment, *i.e*. with Carbonics® tape. CNTs were found on the surface of Carbonics® tape when the speed of the tape was below 2.1 mm/s. The nanotubes produced were about 50 nm in diameter and 5 to 10 μm long, which are similar values to those of nanotubes grown on the anode surface of the batch reactor.

3.3.2 Querrioux's work

Querrioux (Querrioux 2004) in his work modified the arc reactor by enlarging the viewing port and designing a movable lens support. Following these modifications, it was then possible to view a clear arc image on the wall and measure the anode inter-electrode gap while the arc was running. At the beginning of his work, he observed that the arc was wandering around the cathode face and caused instability to the arc. The instability of the arc may hinder the formation of CNT in the arc- discharge process. He then changed the cathode diameter to 3 mm and designed an anode support in order to increase the treatment area on the tape, as shown in Figure 3.8. The anode later was enlarged by introducing a graphite cap similar to the one in Figure 3.17(b), but with a flat front face. The cathode was placed horizontally opposite to the anode in order to have a better arc.

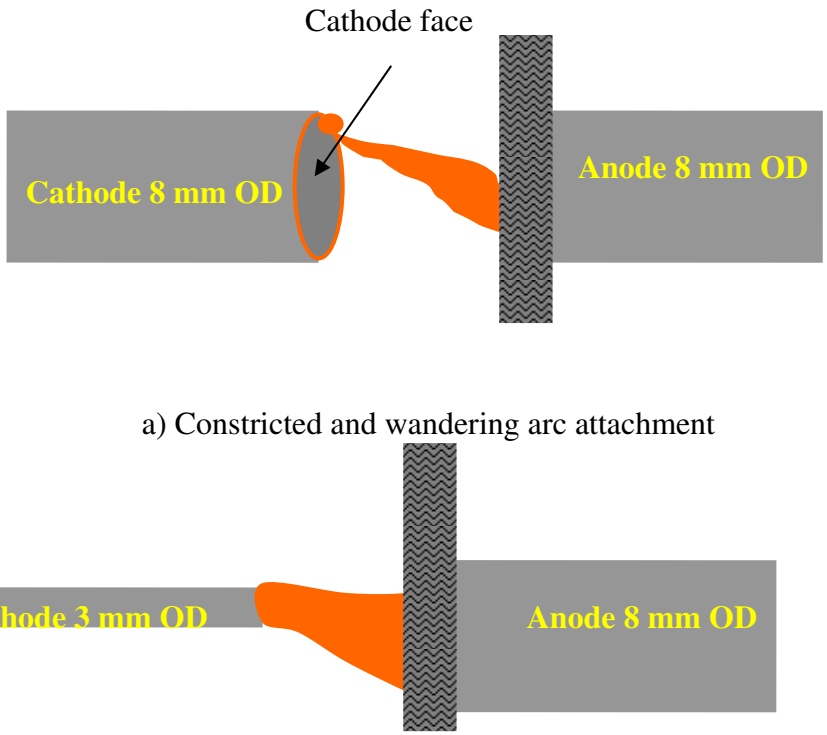

Figure 3.7 Anode cathode configuration in continuous arc reactor.

By changing the cathode size and arrangement, he managed to get a more stable arc and improved quality and density of nanotubes produced. In order to have better cooling and removal of carbon particles from the product, anode flushing from the back was introduced. The anode cap was modified by introducing a tungsten tube attached to the graphite anode support as shown in Figure 3.8.

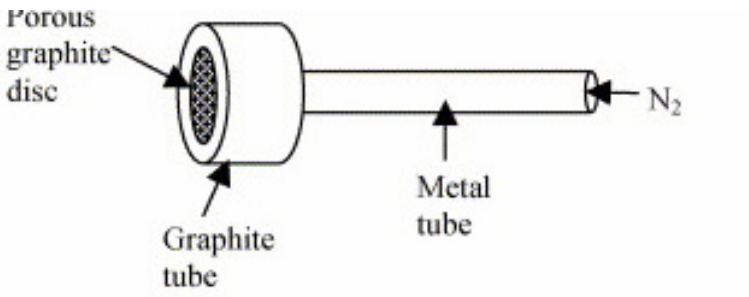

Figure 3.8 Anode cap (anode support)

The gas velocity profile in front of the anode was studied by Querrioux (2004) and he indicated that the nitrogen flushing through the anode improved the quality of nanotubes produced. At the highest point of velocity, i.e. – at the centre of the treated area, the finest nanotube structure was found. It was suggested by Lange et al (Lange, Baranowski et al. 1997) that the inter–electrode gap is also one of the main parameters in the arc discharge producing carbon nanotubes. Unfortunately in Querrioux's works, he did not have a consistent inter-electrode gap for all his runs.

3.3.3 Constraints in the continuous reactor design

One of the main problems with the arc reactor used by previous Canterbury researchers was no proper control over the tape speed. The tape driving mechanism was based on the friction between the tape and the two small rollers. It was difficult to have a constant speed as the tape sometimes slipped when passing through the rollers. Another constraint was a short operating time due to the small size of the wheel used to store the tape. The effective length of the tape for every run was about 40-50 cm. This is equivalent to an about 130 - 170 s run for a 3 mm/s tape speed. In order to perform anode surface temperature and spectroscopic measurement, the existing reactor support needed to be modified. As we can see in Figure 3.4 the reaction chamber was attached to a metal plate and bars which acted as a support for the reactor body. This configuration restricted the access to the reaction chamber.

3.4 Modifications of the apparatus for this work

The main objectives of the reactor modifications were;

1. To have a better support of the reaction chamber and at the same time provide more access for temperature measurement study.

2. To improve the carbon tape feeding mechanism and increase the operation time.

3.4.1 Reactor support

A new reactor support was designed as shown in Figure 3.9. The reaction chamber sat on the round plate and was fixed to it. This round plate was supported by three metal bars which acted as legs. The height of the reaction chamber was increased by positioning the plate higher (~20 – 30 mm above the base plate which sat on the table). This provided more room for alignment of the light path for temperature study. Another viewing port was added on the reactor body which allowed direct viewing onto the anode face. A new carbon tape feeder and lens holder were incorporated in this design. Details of these designs are described in the next sections.

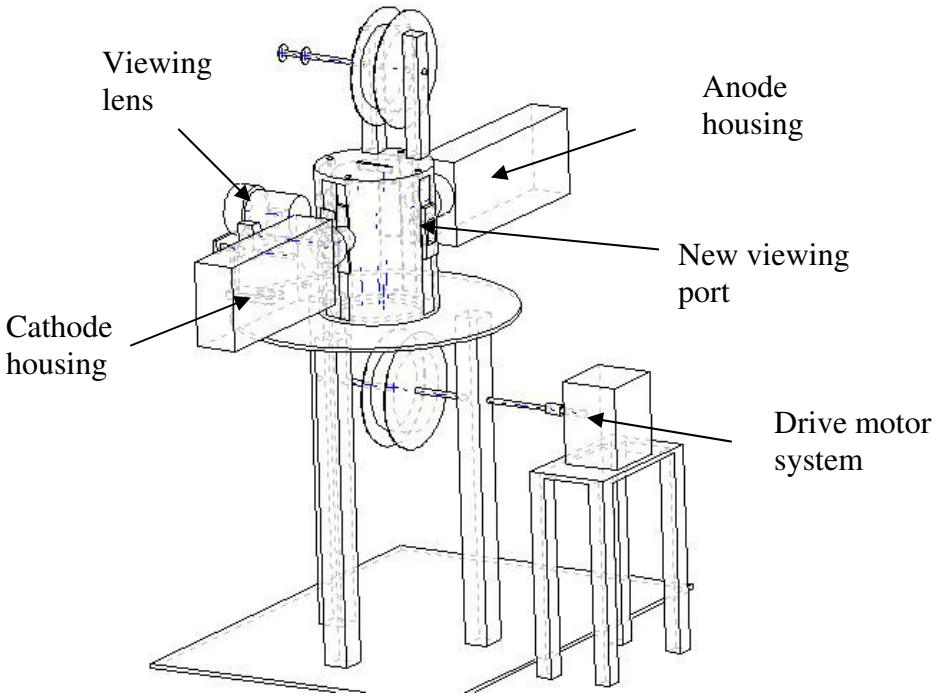

Figure 3.9 A new support for the continuous arc reactor

3.4.2 Tape feeding system

The new system consisted of two spools (with a diameter of 100 mm) and a motor which drove the bottom spool. A reduction gear was attached to the spool and the shaft of the motor in order to reduce the speed. The motor was also connected to a variable speed controller, which allowed changes of the carbon tape speed within a speed range of 1 – 10 mm/s. A reversible switch was also installed to allow tape movement both up and down. Figure 3.10 shows details of design of the top spool. The bottom spool size is similar to the top spool and connected to the drive motor by a 5 mm rod acting as a shaft.

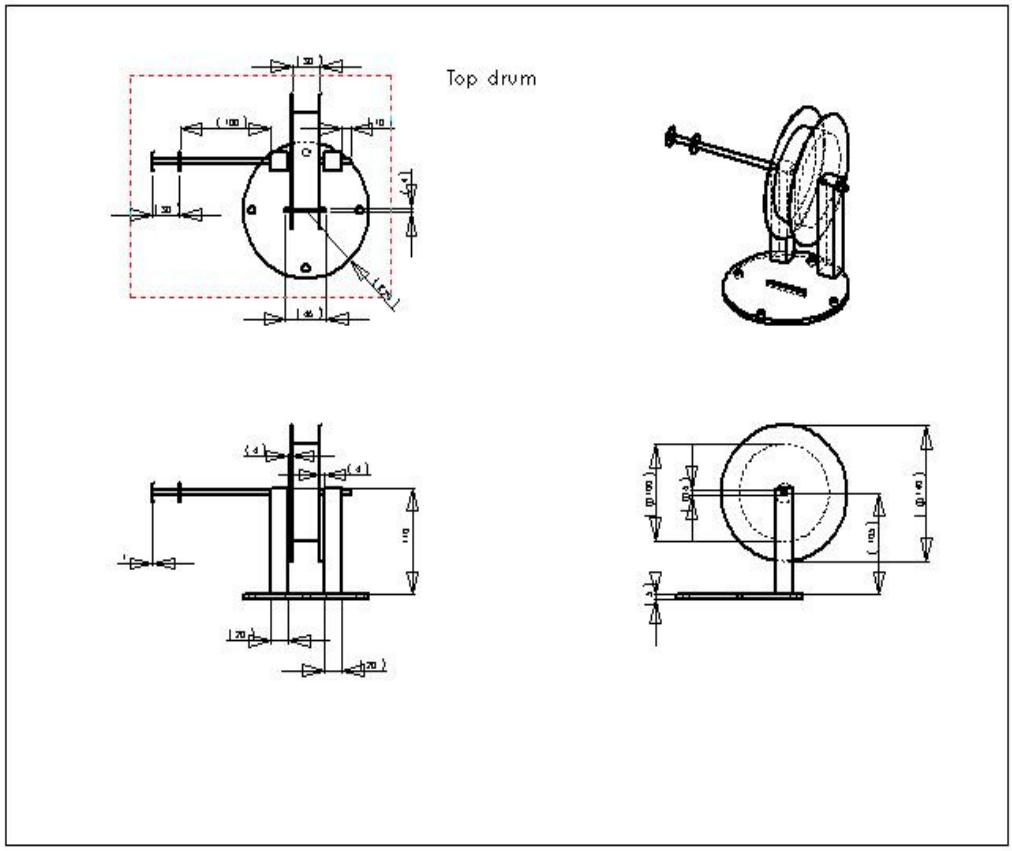

Figure 3.10 Details of design of the top spool of the tape feeding system.

The advantage of this system was that the carbon tape could be wound onto either spool depending on which direction the tape is to move, upward or downward. However, in this study, we chose the upward tape movement as suggested by Querrioux (Querrioux 2004) in his study. A metal block of weight 1 kg was connected to a cord unwinding from a pulley of 20 mm diameter. One of these cord/weigh system was placed on each side of the top spool to provide enough tension in the carbon tape, as shown in Figure 3.12.

3.4.3 Lens holder

Figure 3.11 shows the new lens holder for the modified apparatus. The holder was fixed to the round base support plate of the reactor so that any changes in the reactor position would not affect the image projection on the screen (which was located on the wall). The sliding mechanism allowed repositioning of the lens at the right focal length for the best arc image quality.

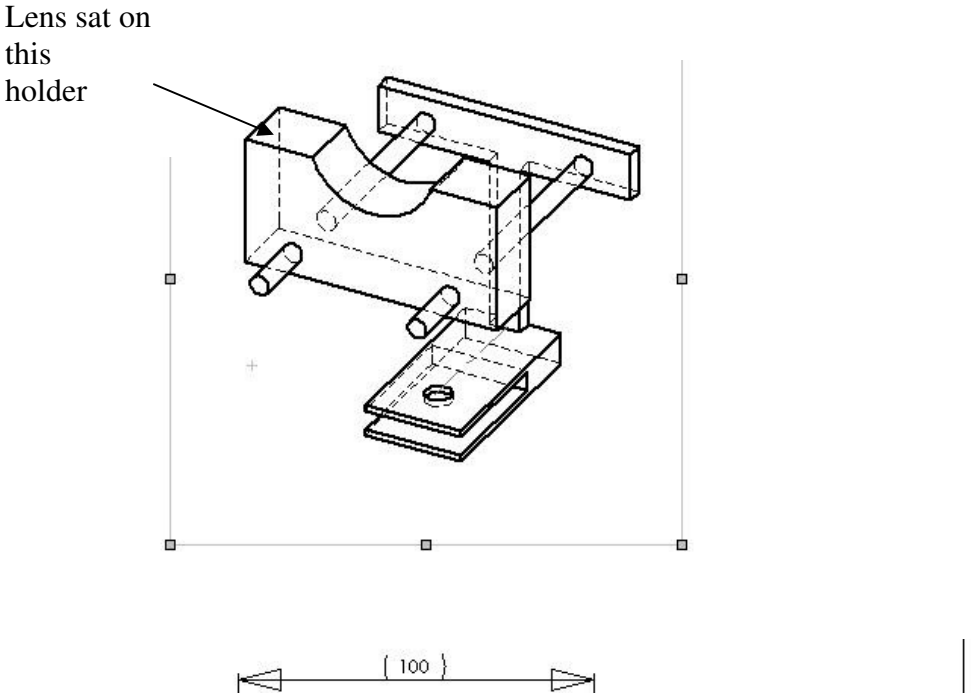

Figure 3.11 New design of lens holder.

3.4.4 Safety consideration

The whole apparatus of the continuous arc reactor including the power supply was placed under a fume hood to remove any possible toxic vapour. Although the arc normally ran in a pure nitrogen atmosphere, there is a possibility of a formation of cyanide compound under the high temperature of the electric arc with traces of hydrogen supplied by hydrocarbon coating on the substrate. Plastic strips were installed around the apparatus to isolate the air flow from that of the operators as shown in Figure 3.12.

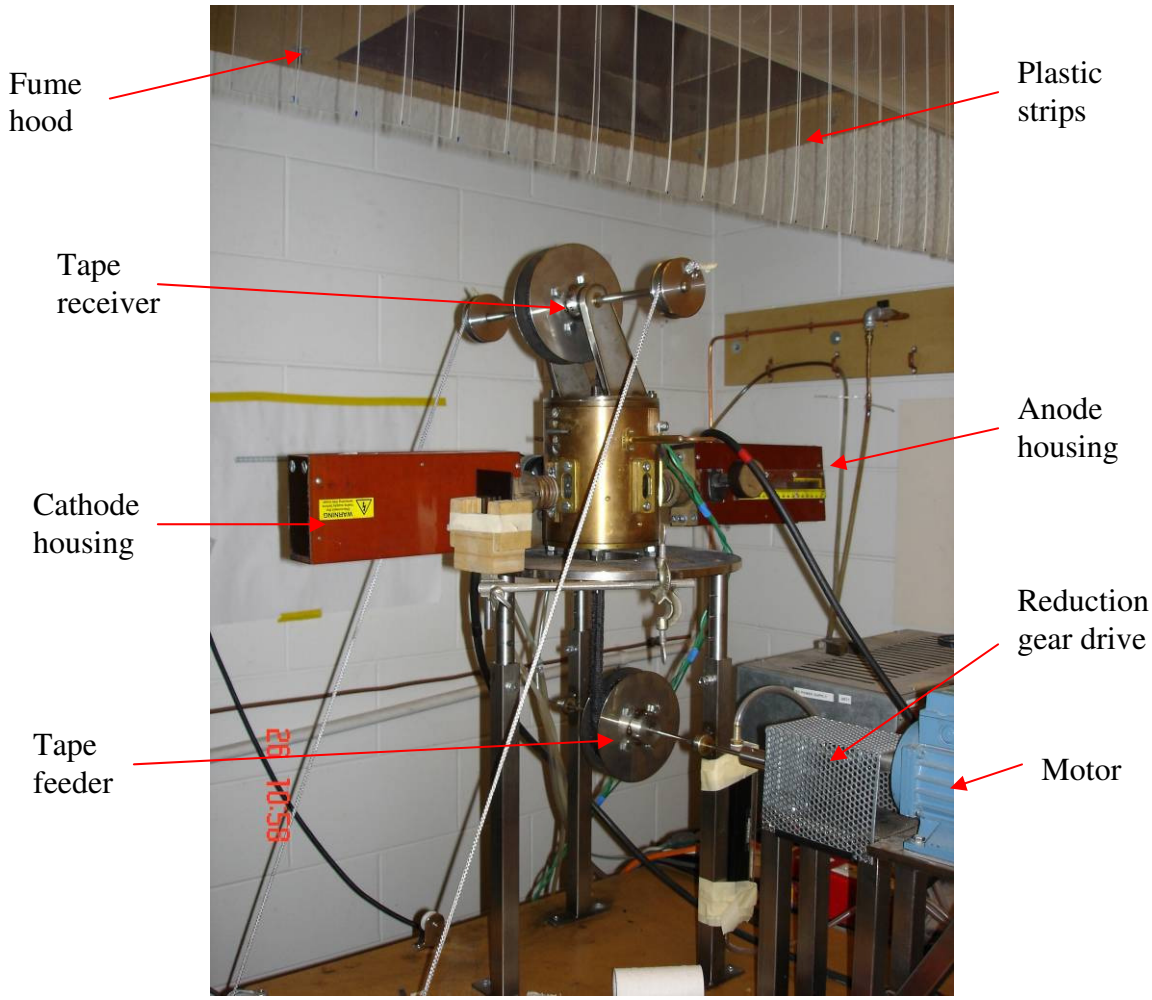

Figure 3.12 Photograph of the continuous arc reactor after modifications

3.5 Anode surface temperature measurement

In order to understand the growth mechanism of CNTs in an arc discharge, it was crucial to study the anode surface temperature, where the CNT grow. Furthermore, the effect of arc parameters, such as the inter-electrode gap, the substrate speed and the background gas used, on the anode surface temperature was important. Most of the recent studies reported only the measurement of temperature between the two electrodes (Lange 1997), (Lange, Huczko et al. 2003), (Zhao, Okazaki et al. 1999) but none ever reported anode or cathode surface temperature. This may have been caused by the difficulty of seeing the electrode surfaces due to the narrow inter-electrode gap in the conventional arc discharge. This work, however, introduced a novel approach of studying the apparent surface temperature of the anode, which was the substrate to be treated. A frontal view of the anode was able to be viewed and studied due to a larger gap between the electrodes. The principle of measuring the anode surface temperature is shown in Figure 3.13.

In this study the true anode surface temperature was not investigated due to some difficulties. The true surface temperature is normally measured using a monochromator with photomultiplier for fast acquisition and the measurement made at arc shutdown. The recorded signal from the square area of anode (40 μm x 40 μm) is then extrapolated to a time zero in order to subtract the plasma component (Wiles and Abrahamson 1978). The uneven surface of the woven substrate (carbon fabric) which has holes and valleys, may contribute to the difficulties in measuring the signal from the square anode area.

3.5.1 Optical pyrometer

The pyrometer used (Optical Pyrometer, OPTIX Ox 4001/e) operates with light filtered by its own filter to let only the red light passes through at an average wavelength of 660 nm. As normally used, it detects a surface temperature by viewing the measured surface through an adjustable filter. The user can then compare the surface image with a dot of calibrated intensity (the dot intensity remaining constant for all observations). Rotation of the graduated filter until the dot and background intensities are equal gives a temperature reading on a scale attached to the rotary filter.

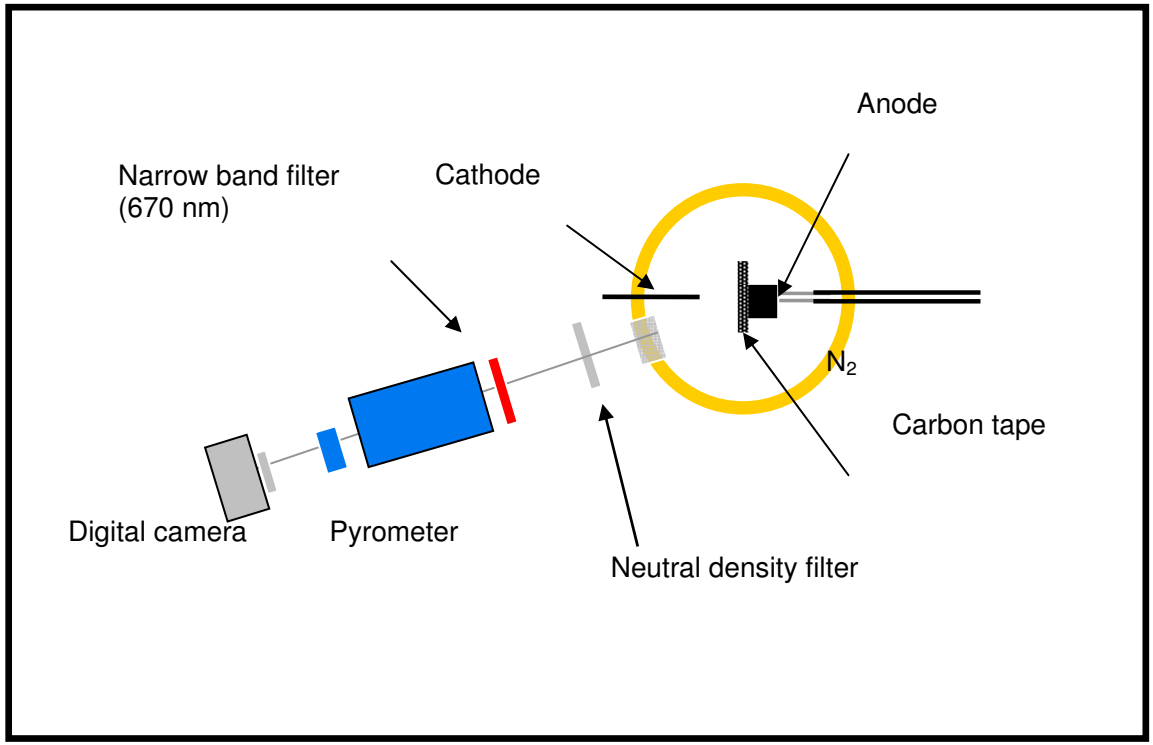

Figure 3.13 Schematic diagrams of apparatus for surface temperature measurement

The optical pyrometer that can cover all visible radiation above 750 °C was used to measure the actual anode's surface temperature in this study. This pyrometer has a small dot in the field of vision (a small elliptical floating luminous index mark for luminosity comparison). To measure the surface temperature, the luminous mark was compared to the body (surface) to be measured. At distance of 1 m from the hot surface being studied, the luminous index mark covers an area of about 4 mm across. The range of measurement of this pyrometer is 1000 -1800 °C and with a clip-on filter (supplied by the manufacturer) new measurement range can be achieved, *i.e.* ~ 1800-3000 °C. In order to extend the temperature range, special filters needed to be placed in front of the pyrometer as discussed in section 3.5.2.

3.5.2 Filters

As mentioned in Section 3.5.1, to measure the temperature of a surface, the pyrometer maintains a luminous mark at a constant intensity; the intensity of the image of the studied surface is varied to match the standard source. By adding another neutral density filter, a new temperature range could be achieved. Roland neutral density filters with a transmission of 1%, 10 %, 33 % and 50 % were considered to be used for this project. In addition, a narrow-band filter (Ealing electro-optics wavelength 670 nm, band width 665–675 nm) was also added in-line with those filters. At this narrow wavelength emission spectra from atomic species such as N, N_2 and C_2 are not found (Johnson 1956; Hattenburg 1967). A standard arc of 3800 K was used for calibration. Knowing the temperature of the surface by reading it off the scale and using Planck's law to calculate the intensity of the red light, the second filter can be calibrated. By using both filters together, a new temperature range (~ 2460–4371 K) was achieved. Methods of extrapolating the temperature data are further discussed in Section 3.5.4

3.5.3 Camera selection

Initially, a DSE digital camera with a 3.14 Megapixel CMOS detector was used to capture the images for temperature measurement. The CMOS technology was chosen because it could prevent "overflow of light intensity" to the neighbouring pixels when capturing the arc images. The standard carbon arc (cathode and anode diameter ~ 3 and 6.05 mm, respectively with the current flow of ~ 8-16 A) was used to assess the digital

camera. However, after few tests, it was found that the images captured were not good enough for the measurement of surface temperature as the images were not sharp.

A Sony Cybershot DSC-W1 digital camera with a 5.0 Megapixel CCD detector was then selected for capturing the images. Table 3.3 shows the set-up of the camera used in this project. The blooming effect on the image captured by CCD detector was eliminated by properly choosing the shutter speed of the camera.

Table 3.3 Sony Cybershot camera set-up.

Features	Sony DSC-W1
Detector	CCD 5.0 Mega pixel
Optical zoom	6 X
Focus range	1 m
EV (Exposure values)	-2.0
Mode	Manual
White balance	Auto
ISO	400
Shutter speed	1/100 s
Picture quality	Fine
Picture mode	Normal
Picture effect	Off
Saturation	Normal
Contrast	Normal
Aperture	F2.8
Sharpness	Normal

3.5.4 Extrapolation of temperature range

In physics, the spectral intensity of electromagnetic radiation from a surface at temperature *T* is given by Planck's law of black body radiation. In this study, Planck's radiation law was used to calculate the new temperature range.

Planck's law is described as:

$$I(\lambda,T) = \frac{2hc^2}{\lambda^5}\frac{1}{e^{\frac{hc}{\lambda kT}} - 1} \qquad \text{(Eqn 3.1)}$$

where ;

I - spectral radiance, energy per unit time per unit surface area per unit solid angle per unit frequency

h - Planck constant

k_B Boltzmann Constant

T temperature of the black body

c Speed of light

λ Wavelength

Knowing the wavelength and the temperature, the intensity at that temperature can be calculated. When one of the neutral density filters was placed in front of the pyrometer, the actual intensity was cut down by the filter. For example, if the ND 0.1 neutral density filter was used, the actual intensity was reduced to only 10 % from the real value. The experiment gives T_{sub} with pyrometer, and this T was used to calculate intensity. The temperatures recorded for various filters combination are shown below:

a. Wide filter + Narrow band filter + 33 % transmission ND filter ---→ 2680°C
b. Wide filter + 10 % transmission ND filter---→ 2440 °C
c. Wide filter + 33% transmission ND filter --→ > 3000 °C
d. Narrow band filter + 33 % transmission---→ < 1800°C

For case (a)

$$I_{sub}\delta\lambda_{wf}(0.1) = I_{b_{2440°C}}\delta\lambda_{wf} \qquad \text{(Eqn 3.2)}$$

Where,

I_{sub} is a radiance intensity of subject (anode surface)

$I_{b_{2440°C}}$ is a radiance intensity of blackbody at pyrometer

scale 2440 °C

$\delta\lambda_{wf}$ is the wide filter wavelength

Equation (3.2) is simplified to form the following;

$$I_{sub} = 10 I_{b_{2440°C}} \qquad \text{(Eqn 3.3)}$$

For case (b)

$$I_{sub}\delta\lambda_{nf}(0.33) = I_{b_{2680°C}}\delta\lambda_{wf} \qquad \text{(Eqn 3.4)}$$

Here,

I_{sub} = radiance intensity of subject (anode surface)

$I_{b_{2440°C}}$ = radiance intensity of blackbody at pyrometer

scale 2680 °C

$\delta\lambda_{nf}$ = narrow band filter wavelength

By manipulating equation (3.4), the radiance intensity of the subject can be calculated using the following equation,

$$I_{sub} = I_{b_{2680°C}} \frac{\delta\lambda_{wf}}{\delta\lambda_{nf}} \left(\frac{1}{0.33} \right) \qquad \text{(Eqn 3.5)}$$

Therefore, for any pyrometer reading, T, it can be deduced that,

$$I_{sub}\delta\lambda_{nf}(0.33) = I_{b_{scaleT}}\delta\lambda_{wf} \qquad \text{(Eqn 3.6)}$$

From equation (3.3) and (3.5)

$$\frac{\delta\lambda_{wf}}{\delta\lambda_{nf}} \left(\frac{1}{0.33} \right) = \frac{10\, I_{b_{2440°C}}}{I_{b_{2680°C}}} \qquad \text{(Eqn 3.7)}$$

Inserting equation (3.7) into (3.6), the ratio is found to be;

$$\frac{I_{sub}}{I_{b_{scaleT}}} = \frac{I_{b_{2440°C}}}{I_{b_{2680°C}}}(10) \qquad \text{(Eqn 3.8)}$$

Using the Planck's law and equation (3.1)) and knowing the wide filter wavelength as 650 nm the intensity at 2480°C and 2680°C were calculated.

Therefore,

$$I_{sub} = 5.25 I_{b_{scaleT}} \qquad \text{(Eqn 3.9)}$$

The transmission of combination (b) is $\frac{1}{5.25} \times 100\% = 19\%$.

By rearranging equation (3.1) and substitute the new value of intensity, I_{sub}, the actual temperature can be estimated.

$$T = \frac{hc}{\lambda k_B} \frac{1}{\ln\left(\frac{2hc^2}{\lambda^5 I_{sub}} + 1\right)} \qquad \text{(Eqn 3.10)}$$

Using this value, a new temperature range was calculated for combination (b) *i.e.* ~ when using the narrow band filter and 33 % ND filter. The graph is shown in Figure 3.14.

Original pyrometer scale	1800 °C – 3000 °C
New range	2453 K – 4329 K

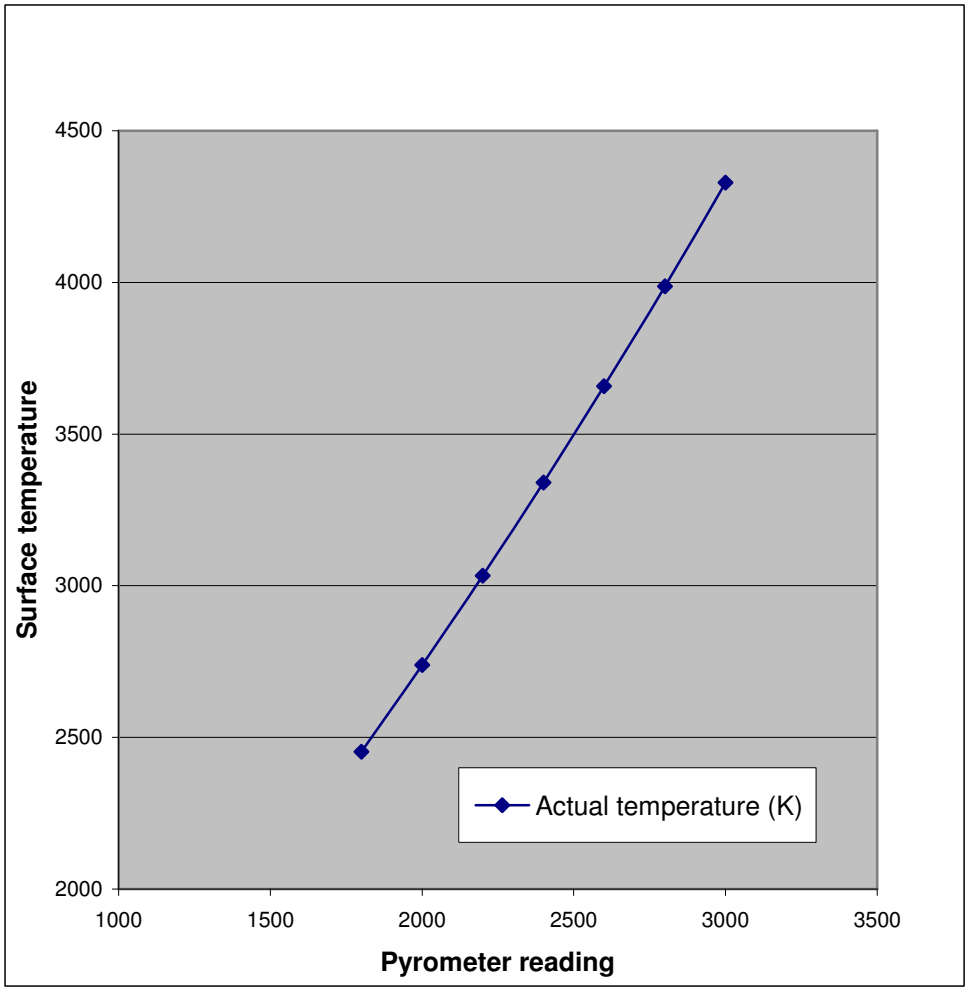

Figure 3.14 Relationship between pyrometer reading and actual surface temperature.

3.5.5 Standard carbon arc

A standard carbon arc was used for calibrating the images intensity relation with surface temperature. The brightness temperature of the standard carbon arc has been well accepted as 3810 K (Chaney, Hamister et al. 1936; MacPhearson 1940) and has been widely used as high temperature reference point. Under specific conditions it will give a reproducible maximum brightness temperature of the positive crater (anode). The arc must be operated slightly below the overloading current in order to get maximum brightness temperature. This is from 10-12.5 A, for 6.35 mm diameter anode. The arc voltage will be between 60-70 V from the 110 V DC power supply (MacPhearson 1940). Just after the arc is started it will hiss and after few minutes the arc will burn quietly. As the current increases, the bright incandescent area expands until it covers the end of the electrode.

Through the red glass (0.65 nm wavelength) in the optical pyrometer, the maximum brightness of the positive crater (anode) viewed normally 3810 K with uncertainty of 7°. This is an average value taken from three laboratories observation, namely National Bureau of Standard, General Electric Company and National Carbon Company. The arc will give a same brightness temperature whether operated in air, nitrogen or argon.

In our work, spectroscopic grade electrodes with diameter of 3.00 mm and 6.05 mm were used as a cathode and anode, respectively. The arc current was varied from 16 to 8 A, and the surface temperature was recorded using the pyrometer described in section 3.5.1. At 16 A, this carbon arc will produce a temperature of 3800 K. However, as the current decreases the surface temperature drops as reported by Nottingham in his probe measurements study (Nottingham 1928).

3.5.6 Calibration of intensity versus surface temperature

As described earlier in Section 3.4.3, a Sony Cyber shot digital camera was used to capture the images of the anode surface for the standard carbon arc at different arc current as shown in Figure 3.15.

(a) 8 A b) 11 A c) 16 A

Figure 3.15 Anode face images at different arc currents; anode diameter was 8 mm for all runs.

The camera images of the anode face (seen through the pyrometer, including the reference dot) were then analyzed for intensity using the image analysis software Sigma Scan Pro 5.5. The relationship between images intensity with surface temperature (pyrometer reading) is then developed as shown in Figure 3.16.

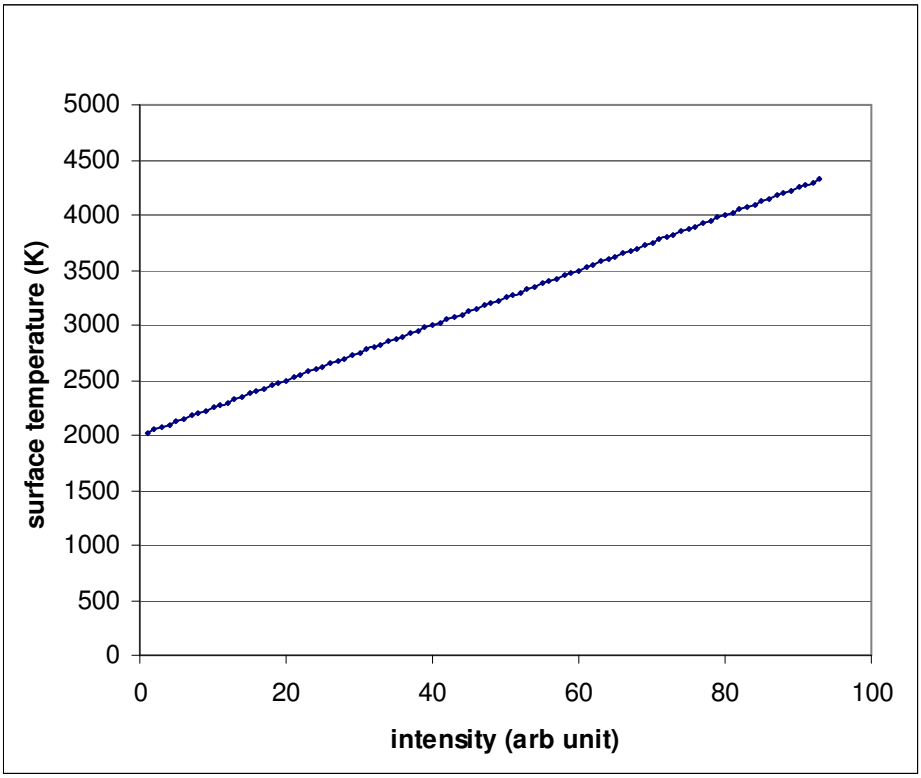

Figure 3.16 Calibration of image intensity versus surface temperature.

3.6 Materials

Woven carbon substrates, UVIS TR-3/2-22 Carbonics GmbH T, were used most often as the anode substrate on which to grow the CNTs in this study. The 2 mm thick substrate was cut into a size approximately 25 mm wide and 2 m long. The main properties of this fabric were listed in the table below.

Table 3.4 Properties of Carbonics woven tape.

Specific weight	**700 g/m^3**
Thickness	2 mm
Width	200 mm
Carbon content	99.9 %

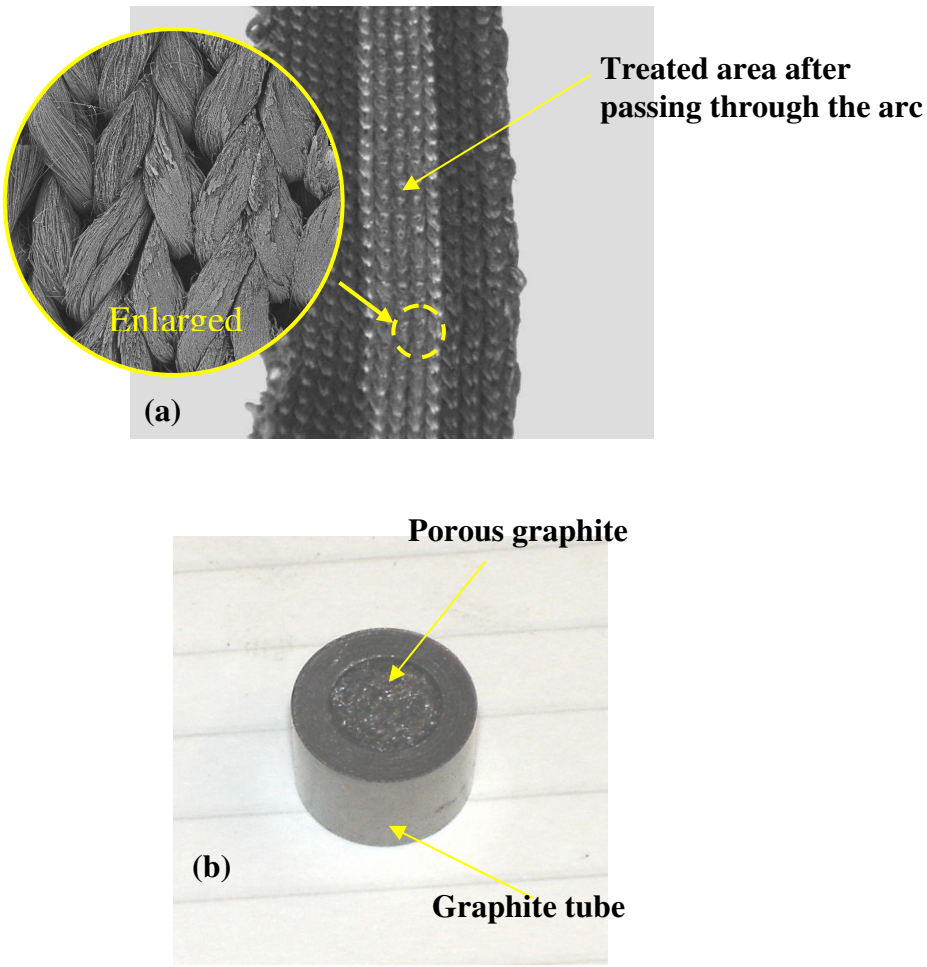

Figure 3.17 Photograph of a) Carbonic GmbH carbon tape b) Anode support.

Figure 3.17 (a) shows the images of woven carbon tape (with treated central path) and the anode support used in the arc discharge. Two graphite rods (99 % pure) with diameters of 12 and 3 mm were used as anode support and cathode, respectively. The anode support was built using a graphite tube and a 6 mm diameter carbon porous rod was inserted at the end of the tube which rubbed against the moving substrate. The anode cap was mounted on a tungsten tube which was welded onto a stainless steel tube and connected to a buffer gas supply.

Nitrogen was used as a buffer gas with a flow rate ranging from 0 to 0.6 L/min except in Series 5 (see below). Details of the buffer gaseous used are shown in Table 3.5.

Table 3.5 Descriptions of buffer gaseous used in the reactor.

Type of gaseous	Purity (%)	Grade	Supplier
Nitrogen	99.998	Zero grade	BOC
Argon	99.998	Zero grade	BOC
Helium	99.998	Zero grade	BOC
Oxygen	99.998	Food grade Code 101	BOC

3.7 Operating procedure

The carbon tape substrate was passed between the two electrodes, touching the positive contact so that the substrate functioned as the anode surface and thus, the positive contact is called the “anode support”. CNTs were then grown on the surface of the carbon substrate where the arc discharge contacted the tape. During the process, the cathode slowly sublimed. Its position was manually adjusted from outside the chamber to maintain a constant arc gap. The plasma was observed via a window of the chamber. A magnified image of the plasma and the electrodes was projected onto a screen using a lens; a grid on the screen was used as a scale. This projected image allowed easy manual adjustment of the distance between the cathode and the substrate.

The reactor was operated at atmospheric pressure using the DC power supply fed with a single phase 230 V AC (with a current of 16 A and 70 V voltage). The inter-electrode gap was varied over the range of 2.0–8.0 mm but no larger because at higher inter-electrode gaps the arc became unstable. As noted above, the flow of the anode buffer gas was set in the range of 0.0–0.6 L/min. A larger flow ($\geq$ 10.0 L/min) of the same gas was introduced into the arc reactor away from the arc, to flush the arc environment. The speed of the tape could be varied between 1-10 mm/s for any runs. Each series of run was done in duplicate to study the repeatability of the process.

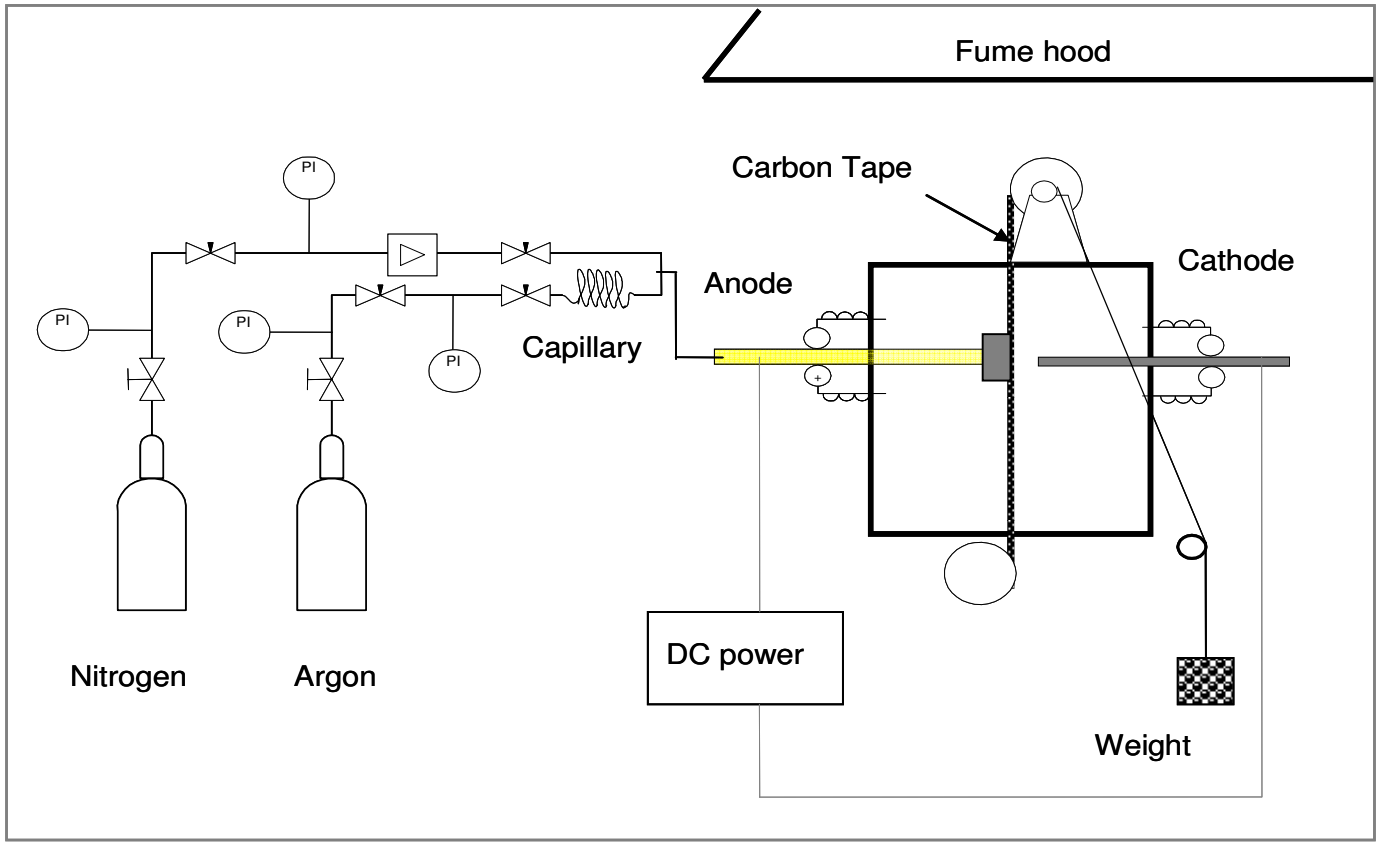

Figure 3.18 Flow chart of the continuous arc discharge after modification.

Effect of the arc parameters on substrate surface temperature and CNTs growth was studied as listed below:

Series 1 Effect of Inter electrode gap

Series 2 Effect of Nitrogen flushing through anode

Series 3 Effect of Substrate speed

Series 4 Effect of Arc current

Series 5 Effect of buffer gas – Argon, Nitrogen and Helium

Series 6 High speed camera analysis

3.8 Scanning Electron Microscopy (SEM)

In order to conduct microscopic analysis, it is necessary to use the scanning electron microscope (SEM). SEM uses the scattering of electron from the surface of the sample to reveal the topography of the material. This technique was used extensively in this research project. The treated carbon tape was analysed using a LEICA 440 SEM. One of the advantages is that the sample/specimens can be analyzed directly without pre-treatment (gold pre-coat) and can be simply attached to the sample slide.

Although the SEM can be useful in imaging the tubular one-dimensional (1-D) structures of MWNTs, there is another method of electron microscopy that can be much more helpful in the structure studies of carbon nanotubes. This method is transmission electron microscopy (TEM), and it is a powerful technique that allows one to determine the number of walls in the MWNT (Andrews, Jacques et al. 1999) or give an image of an isolated SWNT. Another benefit of TEM is that the possible use of electron diffraction. Electron diffraction has been used in 1979 by Abrahamson (Abrahamson, Wiles et al. 1979) to determine structures of tube they found in their arc discharge . It can also be used to determine average helicity and the local variation of helicity of the individual SWNT within the ropes of SWNTs (Cowley, Nikolaev et al. 1997). In conjunction with x-ray energy dispersive spectroscopy (EDS), TEM has also enabled the identification of the catalyst composition responsible for nanotube nucleation (Liao, Serquis et al. 2003).

3.9 References

Abrahamson, J., P. G. Wiles, et al. (1979). Structure of carbon fibres found on carbon arc anodes. 14th Biennial Conference on Carbon, Penn. State Univ., University Park, Penn., USA.

Abrahamson, J., P. G. Wiles, et al. (1999). "Structure of carbon fibres found on carbon arc anodes." Carbon **37**: 1873-1874.

Andrews, R., D. Jacques, et al. (1999). "Continuous production of aligned carbon nanotubes: A step closer to commercial realization." Chemical Physics Letters **303**(5-6): 467-474.

Chan, S. K. (2000). Production of carbon nanotubes by electric arc method. Final Year Project Report, Department of Chemical and Process Engineering, University of Canterbury, Christchurch, New Zealand.

Chaney, N. K., V. C. Hamister, et al. (1936). "The properties of Carbon at the Arc Temperature." Transaction of the Electrochemical Society: 107-150.

Cowley, J. M., P. Nikolaev, et al. (1997). "Electron nano-diffraction study of carbon single-walled nanotube ropes." Chemical Physics Letters **265**(3-5): 379-384.

Hattenburg, A. T. (1967). "Spectral Radiance of Low Current Graphite Arc." APPLIED OPTICS **6**(1): 95-99.

Hill, A. M. and P. Mani (2001). Carbon nanotube production by the electric arc method. Final Year Project Report, Department of Chemical and Process Engineering, University of Canterbury, Christchurch, New Zealand.

Johnson, F. S. (1956). "Spectral Radiance of the Carbon Arc from 1900 to 2500 Angstroms." Journal of the Optical Society of America **46**(2): 101-105.

Lange, H. (1997). "Spectral diagnostics of helium-carbon arc plasma during carbon nanostructure formation." Fullerene Science and Technology **5**(6): 1177-1201.

Lange, H., P. Baranowski, et al. (1997). "An optoelectronic control of arc gap during formation of fullerenes and carbon nanotubes." Review of Scientific Instruments [H.W. Wilson - AST] **68**: 3723.

Lange, H., A. Huczko, et al. (2003). "Carbon arc plasma as a source of nanotubes: Emission spectroscopy and formation mechanism." Journal of Nanoscience and Nanotechnology **3**(1-2): 51-62.

Leistner, M. (2002). The formation of carbon nanotubes on carbon substrates using batch or continuous arc reactors. Lehrstuhl fur Mechanische, Universitat Kaiserslautern.

Liao, X. Z., A. Serquis, et al. (2003). "Effect of catalyst composition on carbon nanotube growth." Applied Physics Letters **82**(16): 2694-2696.

MacPhearson, H. G. (1940). "The Carbon Arc as a Radiation Standard." Journal of Optical Society of America **30**(189): 1141-1149.

Nottingham, W. B. (1928). "Probe measurement in the normal electric arc." 43-55.

Querrioux, T. (2004). Carbon Nanotube Continuous Production. Chemical and Process Engineering, University of Canterbury. **Master of Chemical and Process Engineering**.

Ulubay, C. (2002). Development and testing of a continuous reactor for deposition of carbon nanotube on the substrate. Lehrstuhl fur Mechanische Verfahrenstechnik Universitat Kaiserslautern, Germany. **Diplom-Ingenieur**.

Wiles, P. G. (1979). Production of Acetylene by a Carbon Arc. (Phd thesis ; Chemical & Process Engineering). Christchurch, University of Canterbury.

Wiles, P. G. and J. Abrahamson (1978). "Carbon Fibre Layers on Arc Electrodes-I : Their Properties and Cool-down Behaviour." Carbon **16**: 341 - 349.

Zhao, X., T. Okazaki, et al. (1999). "Optical Emission Spectra during Carbon Nanotube Production by Arc Discharge in H_2, CH_4 or He Gas." Jpn. J. Appl. Phys. **38**(Part 1, No. 10): 6014-6016.

Chapter 4: Results..... 4-1
4.1 Introduction 4-1
4.2 Analysis of the substrate surface images.....4-1
4.3 Effect of Inter-electrode gap.....4-3
4.3.1 Substrate surface temperature.....4-3
4.3.2 Effect of inter-electrode gap on CNTs growth 4-7
4.4 Effect of nitrogen flushing through anode support.....4-9
4.5 Effect of the speed of carbon tape 4-11
4.6 Effect of the arc current 4-13
4.7 Effect of buffer gases in the reaction chamber 4-15
4.7.1 Argon 4-15
4.7.2 Helium 4-18
4.7.3 Comparison of surface temperatures in 100 % nitrogen, argon and helium environment at 1 atmosphere.....4-20
4.8 High speed camera analysis on the arc 4-21
4.9 References 4-27

Chapter 4: Results

4.1 Introduction

This chapter will describe the measurement made in the study. Section 4.2 describes methods used in the study to analyse the images found. Next, Sections 4.3 – 4.7 present the study on effects of different operating conditions used in the process, i.e. the surface temperature and the microscopic study of the treated carbon tape. Particle movements in the arc are discussed in Section 4.8.

4.2 Analysis of the substrate surface images

As described in Section 3.4, the substrate surface (anode surface) images were analysed using Sigma Scan Pro 5.5. Figure 4.1 shows a sample of a substrate surface image captured by a Sony Cybershot digital camera. In the experiment, about 30 seconds of waiting period was allowed for the arc to stabilise before capturing the image. The image was then used to estimate the substrate's surface temperature. The red colour on the surface is the woven carbon fibre whilst the black holes represent the valleys in the weave.

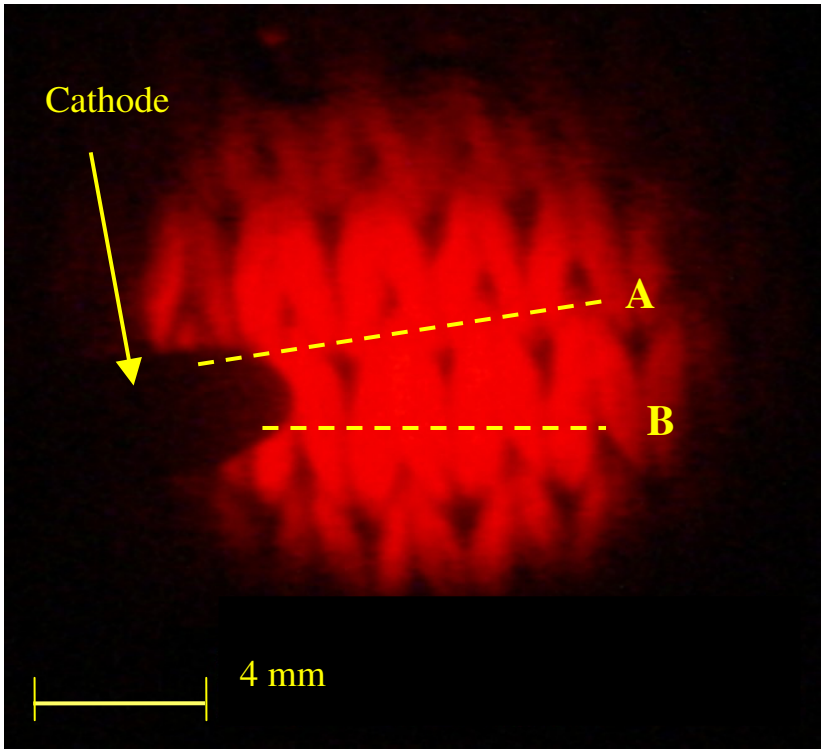

Figure 4.1 Substrate image viewed through the pyrometer. The carbon tape used was UVIS TR-3/2-22 Carbonics GmbH T with a speed of 3 mm/s. Arc current was 16 A.

Then, a line-scan (along the dotted line as shown in Figure 4.1) was performed on each image captured. The intensity along that line was then translated into a surface temperature using a method described in Section 3.4 (with a sensitivity of 25 K for each intensity value) and resulted in an estimated temperature profile across the arc attachment on the substrate as shown in Figure 4.2. These temperature profiles have been taken in such a way that the valleys in the weave, where local dips in temperatures occurred, were avoided (seen as black patches in Figure 4.1). An average temperature was then calculated for the region where the temperatures were approximately constant.

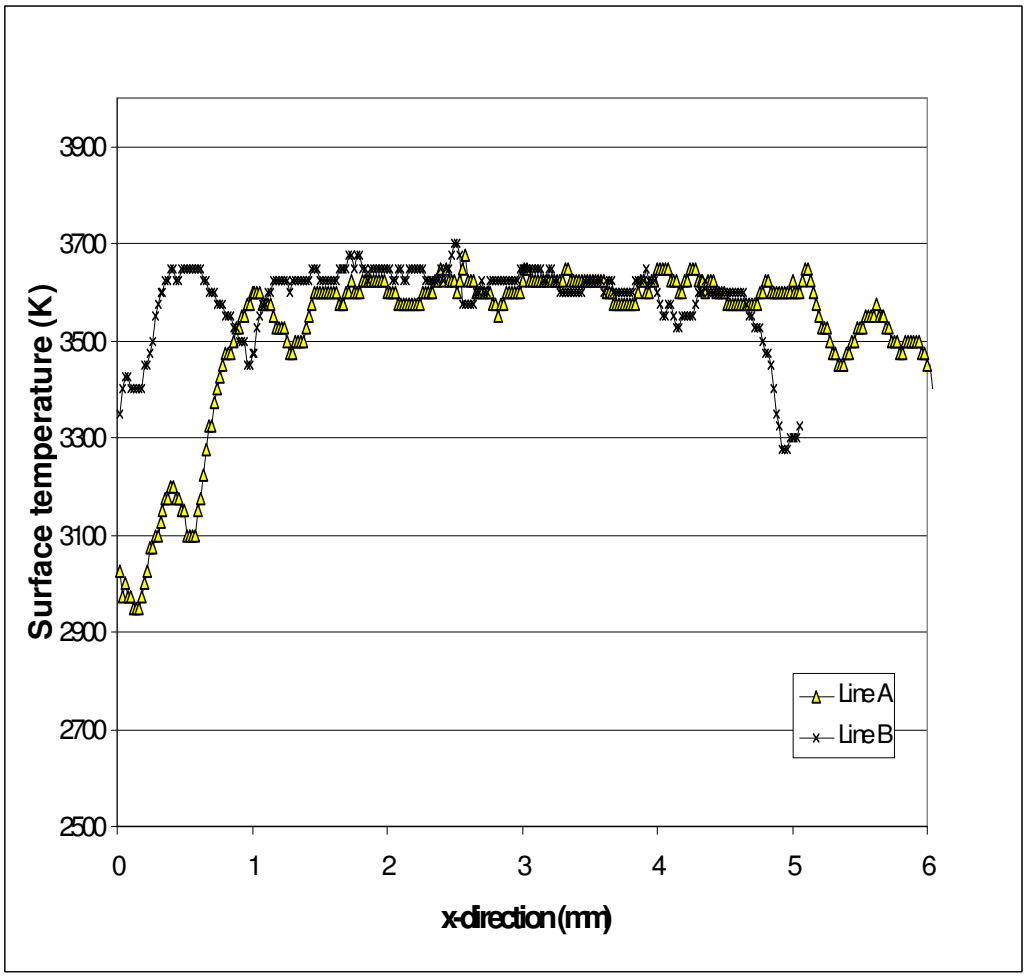

Figure 4.2 Surface temperatures across the substrate at 16 A arc current and 5.2 mm inter-electrode gap using UVIS TR-3/2-22 Carbonic tape.

4.3 Effect of Inter-electrode gap

The aim of this series of runs was to identify the inter-electrode gap for optimum growth of the CNTs in the continuous arc reactor. The inter-electrode gap is one of the main arc parameters in the conventional arc and has been studied by several groups (Lange, Baranowski et al. 1997; Meunier 1999; Farhat, Hinkov et al. 2004; Shashurin and Keidar 2008). In this work, the experimental procedures described in Section 3.4 were used to study the effect of the arc parameters on substrate surface temperature and CNTs growth.

4.3.1 Substrate surface temperature

The temperature profile across the substrate for different inter-electrode gaps is plotted in Figure 4.3. At a very narrow gap *i.e.* 2.7 $\pm$ 0.2 mm, the substrate's surface temperature was found to be significantly higher ~ 3855.0 $\pm$ 50 K. The surface temperature, then, decreased to 3747.0 $\pm$ 44 K as the gap was increased by one millimetre. At 5.2 $\pm$ 0.2 mm gap, the temperature recorded was much lower with the average value of 3644.5 $\pm$ 50 K. As the gap was further increased to 7.7 + 0.2 mm, the substrate surface temperature rose until it finally reached 3815.5 $\pm$ 74 K. Thus, the temperature difference between the highest and the lowest surface temperature was approximately 200 K.

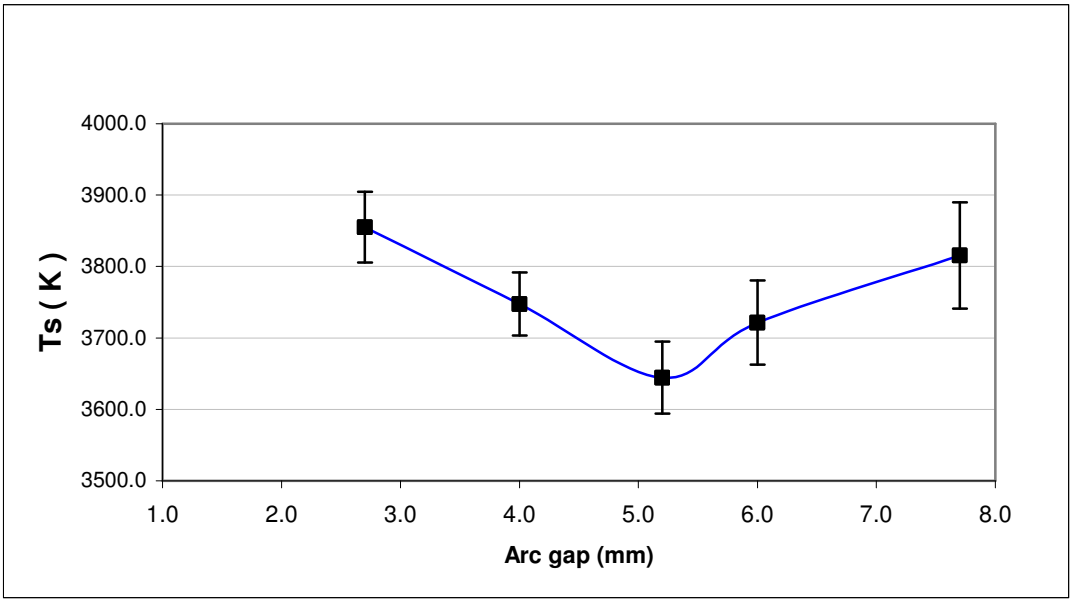

Figure 4.3 Average substrate surface temperatures at different gaps for 16 A arc using UVIS TR-3/2-22 Carbonic tape at a speed of 3 mm / s.

The substrate images produced at different inter-electrode gaps, namely at 4mm, 5 mm and 6 mm, are shown in Figure 4.4 (all at the same magnification). From this figure, it can be observed that the anode attachment size varies with the change of the inter-electrode gap. The circles represent the anode attachment area. These circles were drawn based on the region where the temperatures were approximately constant (see Section 4.1, Figure 4.2). It is also observed that the intensity of the image dropped as the gap was increased from 4 mm to 5mm. However, when the gap was increased to 6 mm, the intensity became higher. The drop and increase in the intensity reflects the temperature changes that occurred on the surface of the substrate as illustrated by Figure 4.3.

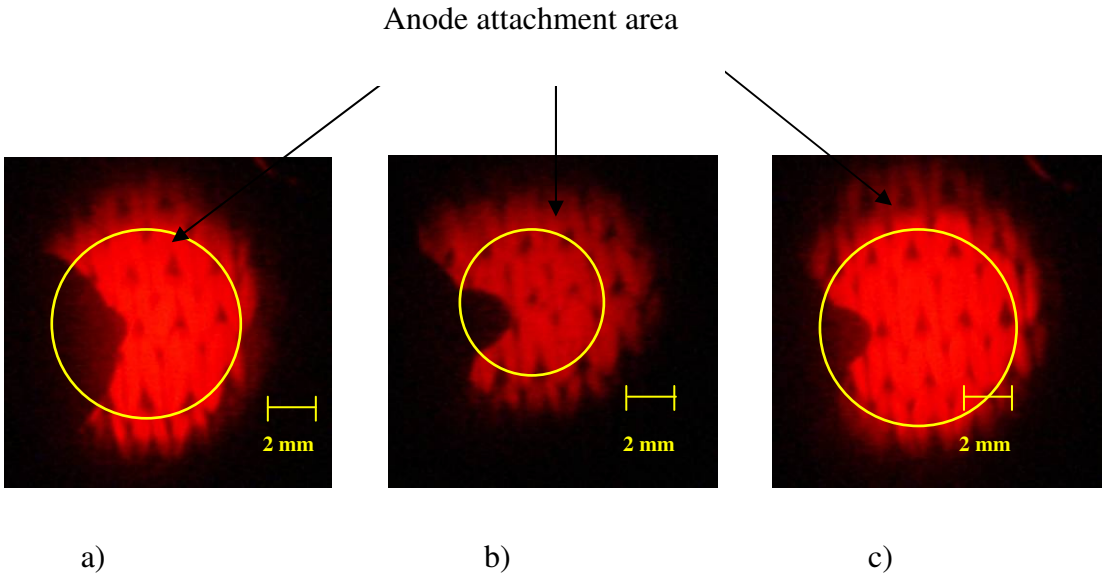

Figure 4.4 Substrate (UVIS TR-3/2-22 Carbonic tape) images at different inter-electrode gap a) 4 mm, b) 5 mm and c) 6 mm at 16 A current and 3 mm / s tape speed.

The anode current densities at different arc gap were estimated based on the area of the anode attachment. The values of these current densities are tabulated as follows:

Table 4-1 Anode current densities at various arc gaps without flushing gas. Arc current was 16 A.

Arc gap (mm)	Current density (A/mm^2)
2.7	0.57
4.0	0.61
5.2	1.26
6.0	0.50
7.7	0.77

To study the necessity of having a waiting period (~ 30 seconds), *i.e*. to allow the arc to stabilise, another experiment was conducted. Here, the gap was reduced gradually by 1 mm, *i.e*. from 7 mm to 3 mm, while the arc was running. The substrate's images were photographed both immediately (1 – 2 s) after changing the inter-electrode gap and after the 30 s waiting period. The total time taken for this run was 220 sec. The temperature profiles produced are as shown in Figure 4.5; here, it is noted that generally the surface temperatures of the stable arc were slightly lower than that taken immediately after changing the gap. This trend was observed for all gaps except for 7 mm. However, the temperature profile for both immediately changed condition and after 30 s waiting period is similar, as shown in Figure 4.6. The major decrease over 30 s was for the 5 mm gap.

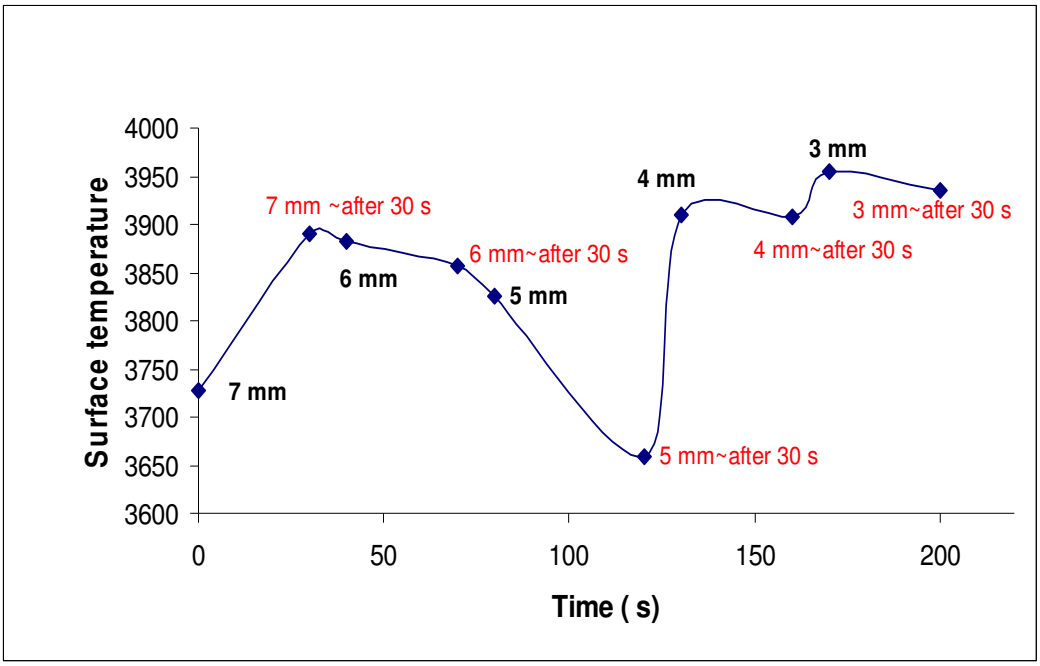

Figure 4.5 Temperature changes during the run with the nitrogen as a background gas for 16 A arc current. The tape used was UVIS TR-3/2-22 Carbonic GmbH.

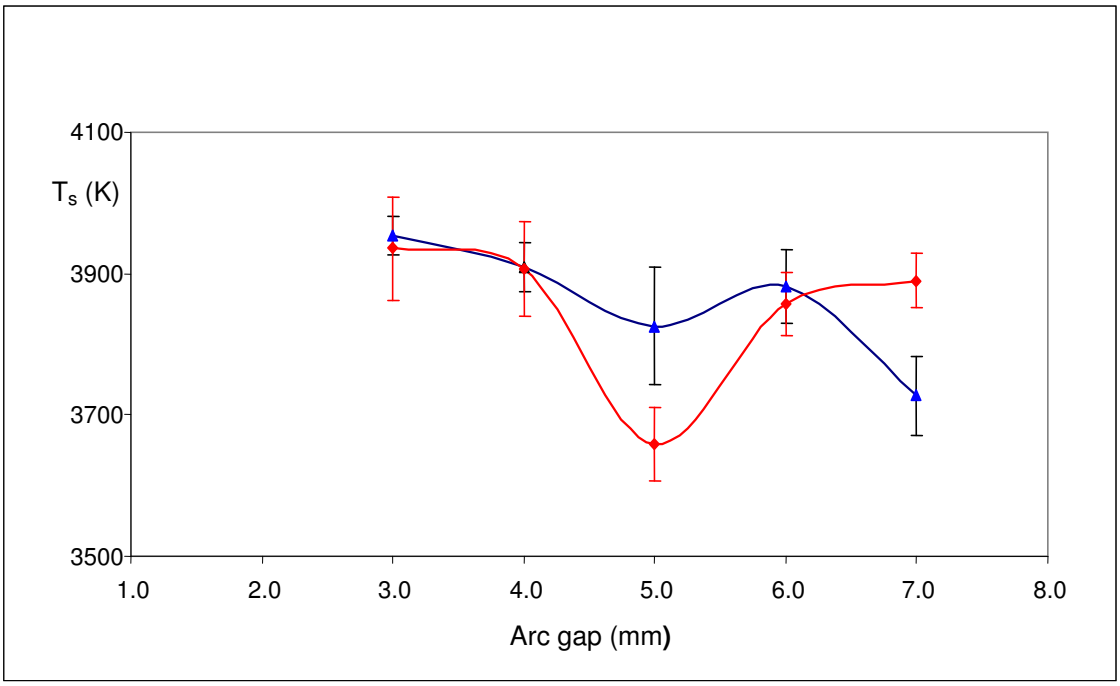

Figure 4.6 Temperature variations with arc gap, ▲ immediately after changing the gap and ◆ after 30 s.

4.3.2 Effect of inter-electrode gap on CNTs growth

The growth of CNTs on the substrate was analysed using the SEM technique. The treated carbon tape (substrate) was analysed using a LEICA 440 SEM. The structures of the fine fibres in these SEM images show similar characteristics to the CNTs normally produced by arc-discharge method.

From the SEM analysis, it was found that varying the inter-electrode gap also changed the nanotube yield as shown in Figure 4.7(a)-(c). At the shortest gap, i.e. 2.7 $\pm$ 0.2 mm only a few nanotubes were observed whereas at 5.2 $\pm$ 0.2 mm gap, the CNTs produced were plentiful and at the arc gap of 7.7 $\pm$ 0.2 mm no nanotubes were formed. The nanotubes formed at 5.2 $\pm$ 0.2 mm gap were longer (>8 μm) than those were formed at 2.7 $\pm$ 0.2 mm gap (<5 μm).

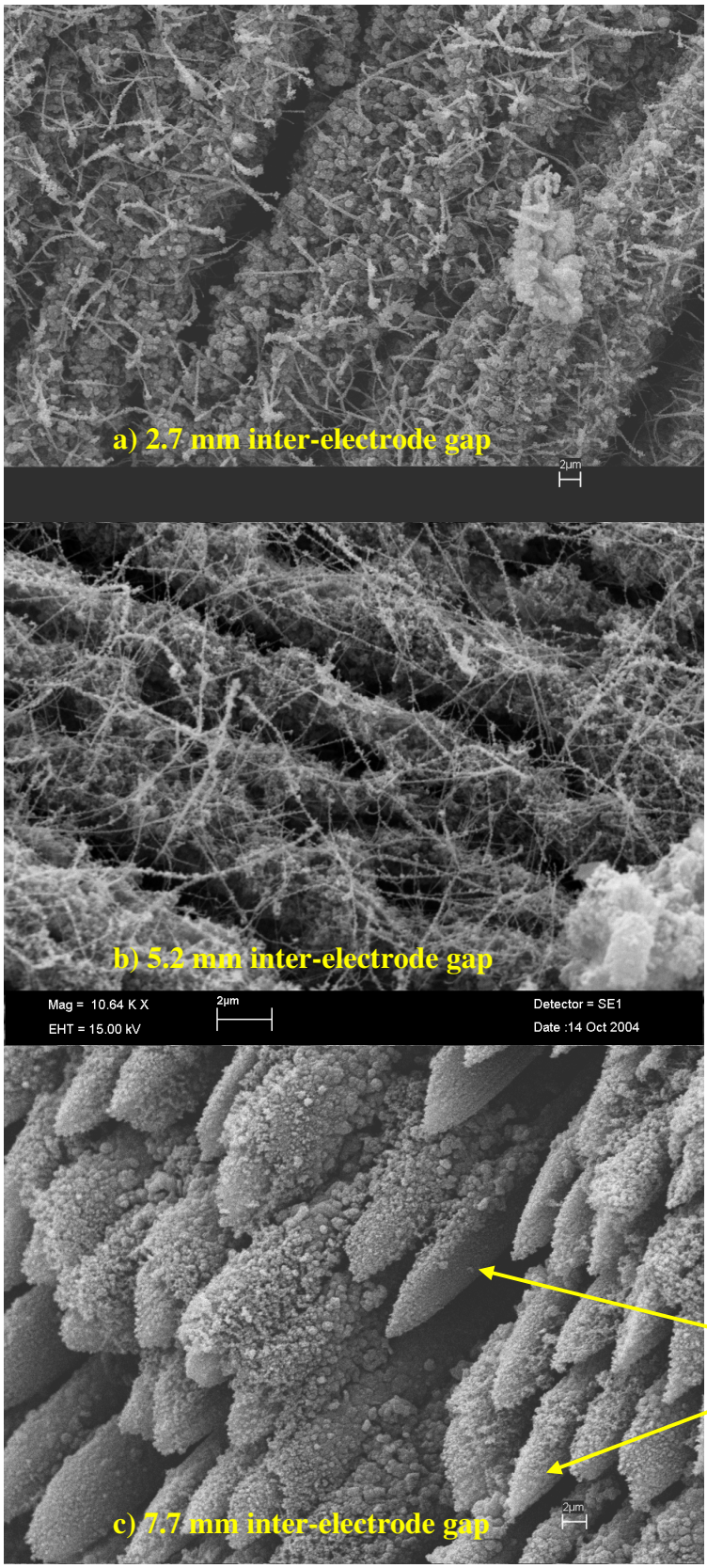

Figure 4.7 CNTs growth at no anode flushing condition (0 L/min nitrogen flow) and at (a) 2.7 mm gap (b) 5.2 mm gap and (c) 7.7 mm gap for 16 A arc current.

4.4 Effect of nitrogen flushing through anode support

A previous study by Querrioux (2004) investigated the effect of anode flushing on CNTs growth in this continuous reactor. However, in his study, the arc gap was not maintained at a controlled value. Therefore, it is essential to re-examine the contribution of anodic flushing on the CNTs growth, at a constant arc gap. From this run, it was found that varying the nitrogen flow rate in the range of 0 - 0.6 L/min, at 5.2 $\pm$ 0.2 mm gap, had no significant effect on the substrate's surface temperature. The average temperature remained essentially constant at 3700 $\pm$ 50 K as shown in Figure 4.8.

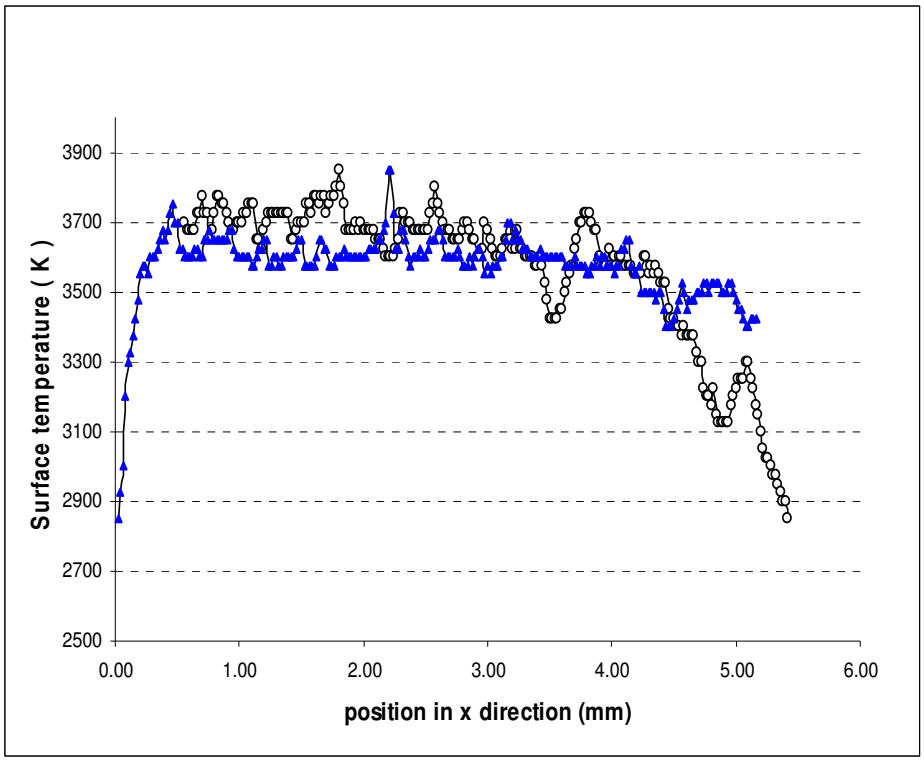

Figure 4.8 The surface temperature across the substrate at 5.2 mm gap, —O— no Flow and —▲— 0.6 L/min nitrogen flow.

Significantly, it was found that CNTs produced with anodic flushing have higher purity (less attached carbon particles) compared to those produced at 0 L/min. Figure 4.9 illustrates the SEM images for both conditions (an image (b) was at higher magnification). From Figure 4.9(b) it was noted that fewer crystallite attached along the length of the nanotubes. The diameter of the CNTs produced also become smaller (from 50-60 nm to 30-40 nm) when the nitrogen flow into the system is increased. However, there was no appreciable change observed in the number of nanotubes produced.

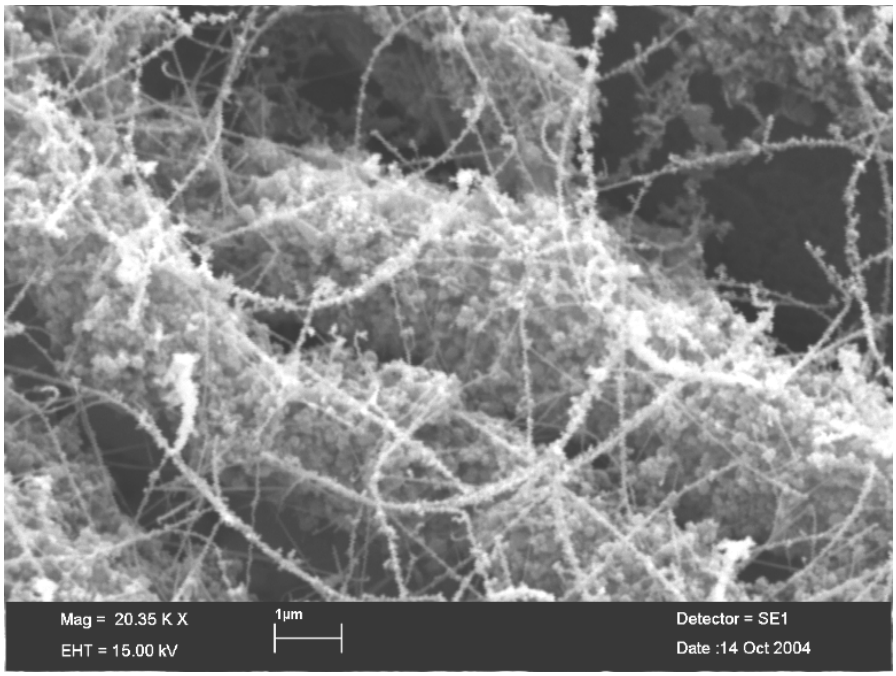

(a) Anodic flushing 0 L/min

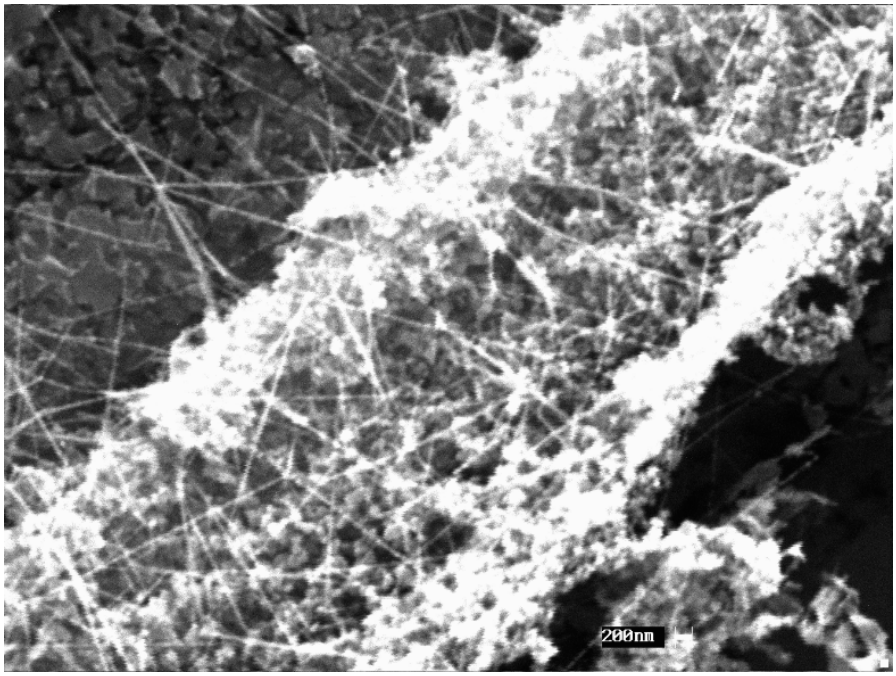

(b) Anodic flushing 0.6 L/min

Figure 4.9 SEM images of CNTs growth at 5.2 mm gap and different anodic flushing flow rate, (a) 0 L/min (b) 0.6 L/min.

4.5 Effect of the speed of carbon tape

The purpose of this series of experiments was to identify the optimum speed of the carbon tape and to see the influence of this speed on the substrate's surface temperature and also on the yield of nanotubes grown on the substrate.

Figure 4.10 illustrates the surface temperature of the anode as the speed increases. From the figure, it was found that when the tape moved at 5mm/s or below, the anode surface temperatures seem to be independent of the speed of the carbon substrate, in which it's fluctuating around 3700 $\pm$ 60 K. However, at a speed closed to 6 mm/s, the surface temperature dropped to about 3600 $\pm$ 30 K.

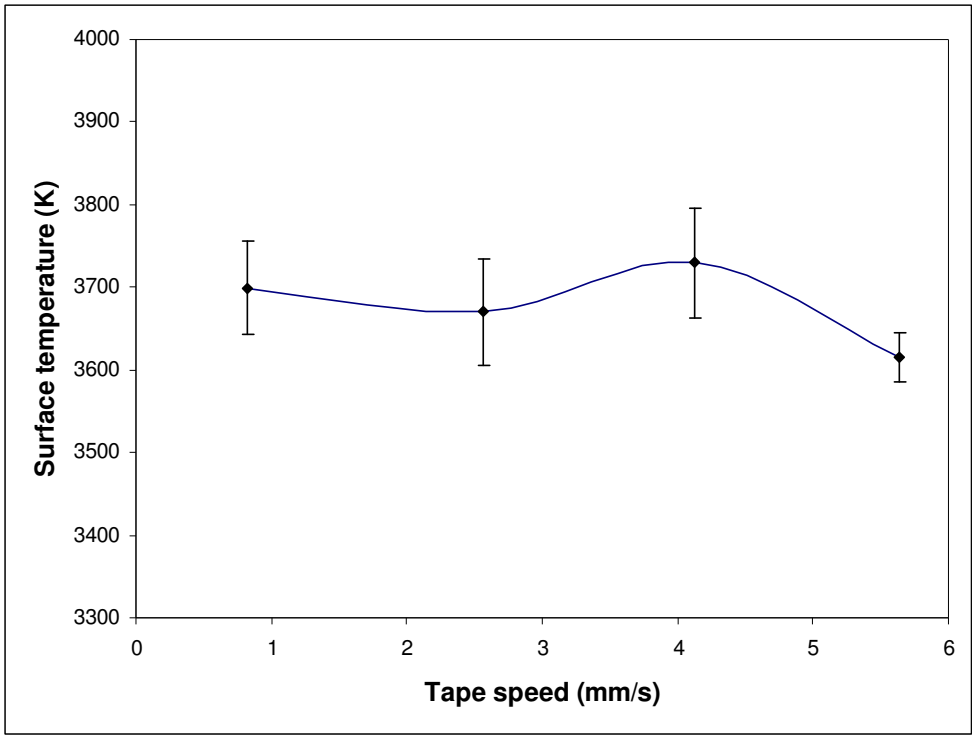

Figure 4.10 Anode surface temperatures at different tape speed for 5.2 mm gap and 16 A current.

The SEM images of the treated carbon tapes at various tape speed are shown in Figure 4.11. In contrast to the anode surface temperature, the growth of CNTs seems to be strongly dependent on the speed of the carbon tape. At a very low speed, 0.85 mm/s nanorods and cauliflowers were formed while at 2.56 mm/s plentiful nanotubes were found on the substrate surface. Another type of nanostructures, *i.e.* "honeycomb" like structures, was produced when the tape's speed was set at 4.2 mm/s. Finally, at a speed of 5.64 mm/s, the carbon cauliflowers structures were observed.

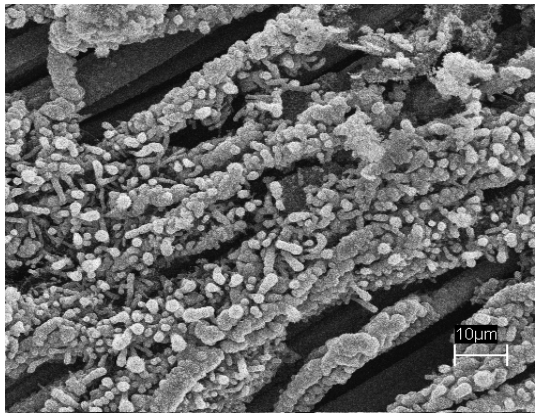

a) 0.85 mm/s

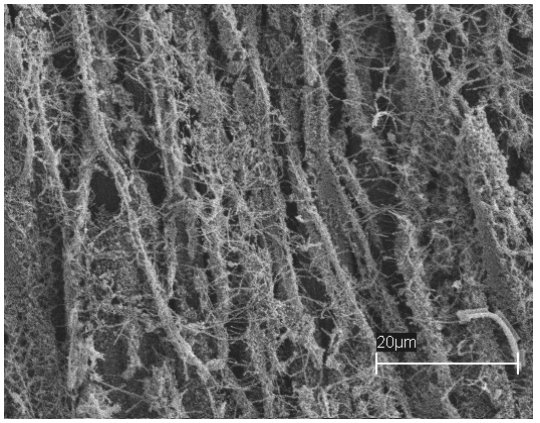

b) 2.56 mm/s

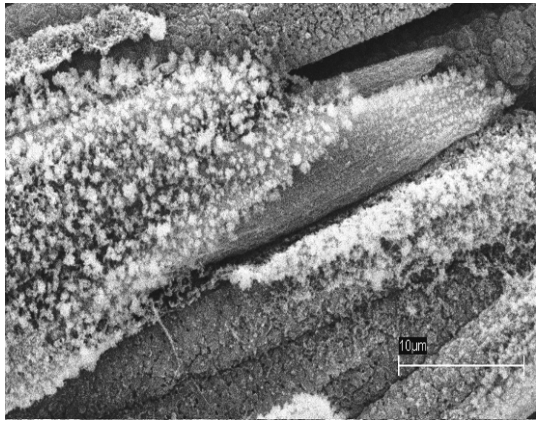

c) 4.13 mm/s

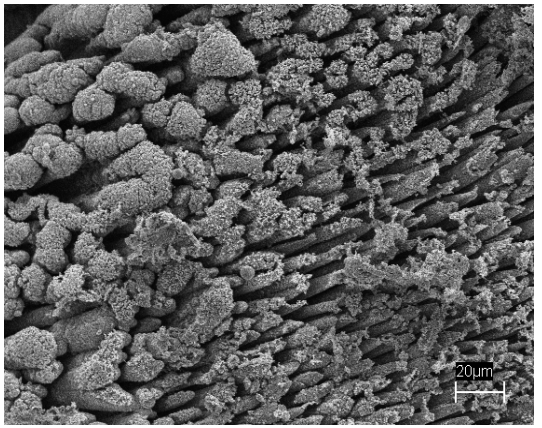

d) 5.64 mm/s

Figure 4.11 Carbon nanostructures at a different speed of the carbon tape, a) at 0.85 mm/s, b) at 2.56 mm/s, c) at 4.13 mm/s and d) at 5.64 mm/s for 16 A arc current and 5.2 mm inter-electrode gap.

4.6 Effect of the arc current

The objective of the following experimental work describe below was to explore the possibilities of producing CNTs at higher volume per unit time by introducing a higher current power supply. It was expected that at a higher current, more substrate will be evaporated which will then condense as carbon nanotubes.

To investigate this effect, the continuous arc reactor was connected to a higher current supply. A DC power supply with a capacity of at least up to 50 A with a voltage of 200 V was used; for experimental purposes, the current supply was set at 20 A. At this current value, the minimum inter-electrode gap was found to be 5 mm. The tape was excessively damaged when the inter-electrode gap was set at lower than 5 mm. Initially, the speed of the carbon tape was increased from 3 mm/s to about 5 mm/s to reduce the damaged on the carbon tape and to get a stable arc while searching for a suitable inter-electrode gap. After several attempts, it was observed that stable arc was formed when the tape speed was set at 4.13 mm/s with 20-22 A current and 40-60 V arc voltage. The width of the treated area on the substrate surface was also found to increase from 6-10 mm for a 16 A arc current to a range of 16-20 mm width for the 20 A current.

The treated tapes were then analysed using SEM. Only carbon with cauliflower shapes were observed when the arc was run at the lowest gap, i.e. at 6.5 mm. No nanotubes were found at other inter-electrode gaps. The carbon cauliflowers formed have a uniform size and distribution throughout the treated area as shown in Figure 4.12.

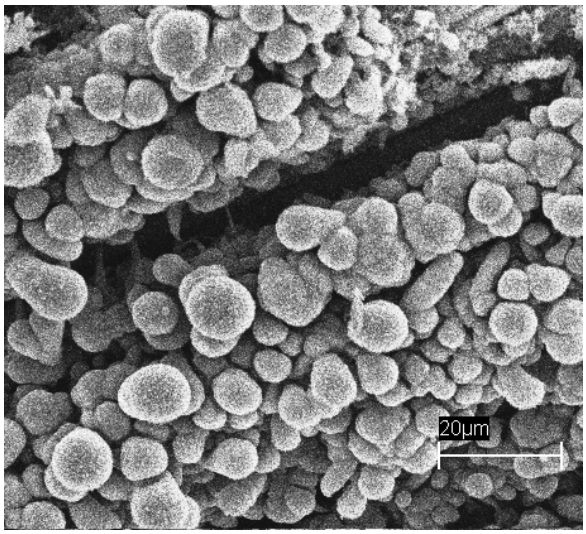

Figure 4.12 The uniform cauliflowers formed with the high current arc at 20 A current.

The anode effect of arc current on surface temperature at various arc gaps is shown in Figure 4.13. It was found that for these conditions and using a 3 mm diameter cathode, the average anode surface temperatures were very high, i.e. > 4100 ± 100 K. The cathode was then changed from a 3 mm to an 8 mm graphite rod in order to reduce the cathode jet (by reducing cathode current density), and perhaps the anode surface temperature. The anode surface temperatures with the 8 mm cathode were generally lower than the temperatures when running with a 3 mm cathode.

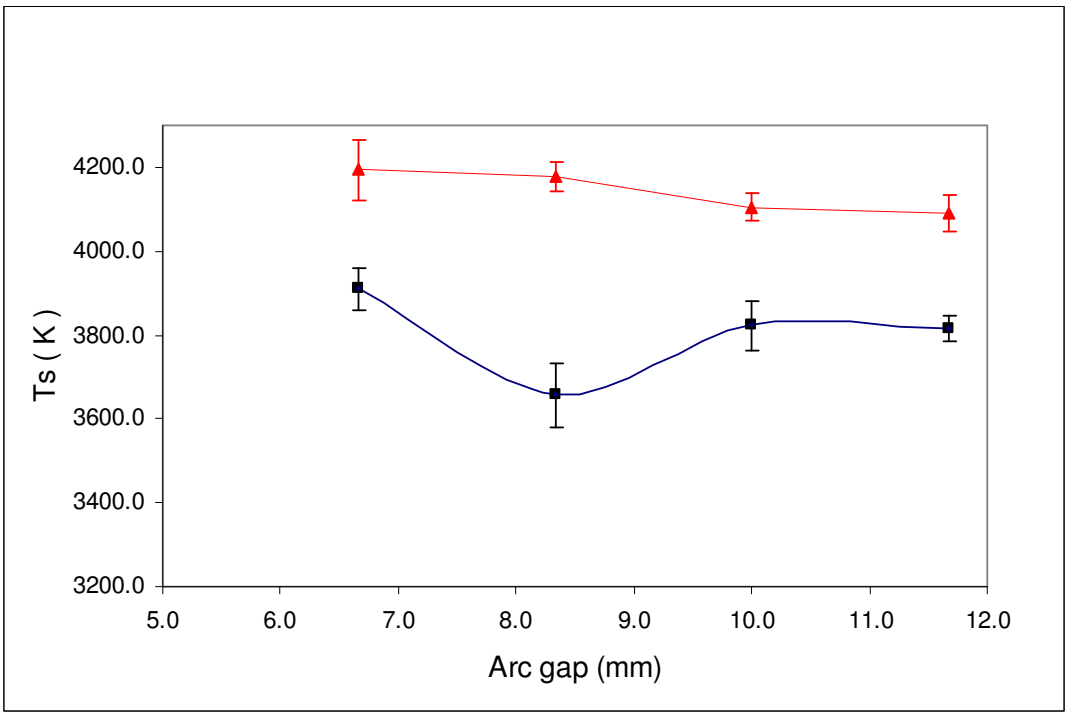

Figure 4.13 Anode surface temperatures at different arc gap with the current of 20 A, ---▲--- for 3 mm cathode and ---■--- for 8 mm cathode using the high current supply. Carbon tape speed was at 4.13 mm/s.

For the 8 mm cathode, the anode surface temperature was found to be lower by about 300-400 K. At 6.5 $\pm$ 0.2 mm gap the surface temperature was 3910 $\pm$ 49 K compared to 4194 $\pm$ 72 K with a 3.0 mm cathode and no nanotubes were formed. When the gap was increased to 8.5 mm, the anode surface temperature dropped to 3657 $\pm$ 77 K. From the SEM analysis, it was found that nanotubes were formed when the arc operated at this gap. The anode surface temperature then became higher again, close to 3822 $\pm$ 58 K when the inter-electrode gap was set at a longer distance as shown in Figure 4.13, and again no nanotubes were formed at these higher temperatures.

4.7 Effect of buffer gases in the reaction chamber

Nitrogen, helium or argon atmosphere has been used for preparation of nanotubes in a conventional arc discharge (Zhang, Xue et al. 1999; Zhao, Okazaki et al. 1999; Lange and Huczko 2001). However, in their work, the arc was operated at low pressure and they found different optimal pressure for different kind of atmosphere. The objective of this experimental works was to study the effect of different background gaseous on the substrate surface temperature and growth of CNTs in the continuous arc reactor.

4.7.1 Argon

Three sets of trials were carried out to investigate the effect of argon in producing CNTs for the continuous arc reactor. The inter-electrode gap was initially set at 8 mm and adjusted down, ending with 3 mm gap. All images were taken after about 30 sec. The average surface temperatures for the argon run are shown in Figure 4.14.

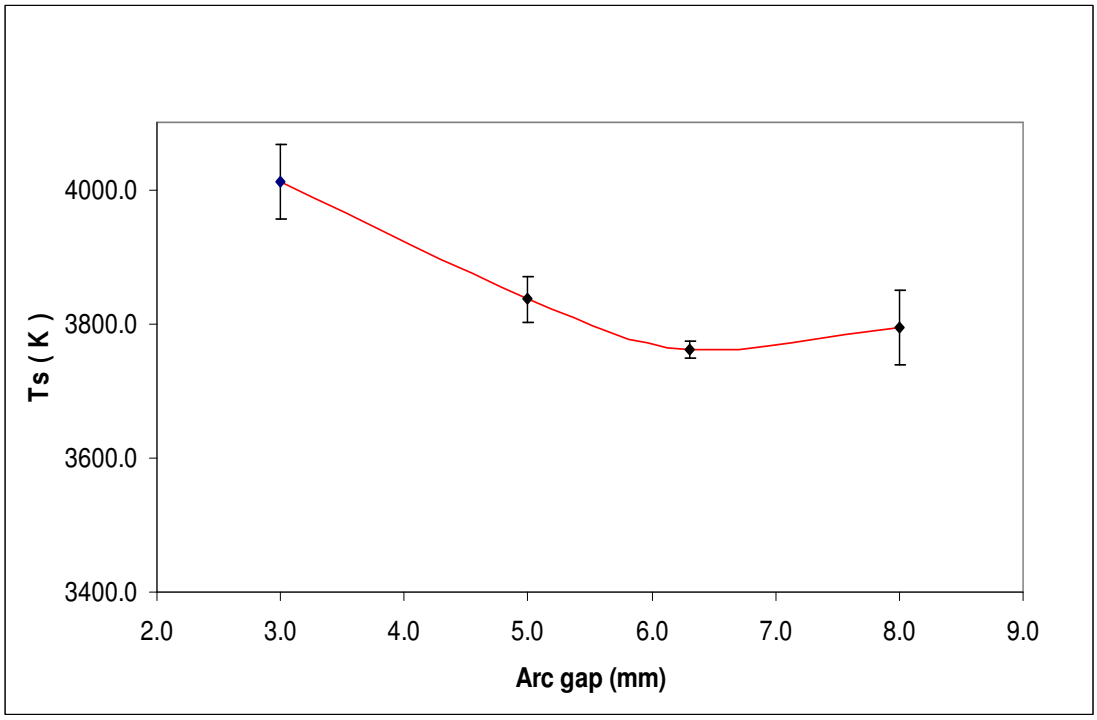

Figure 4.14 Anode surface temperatures with Argon as inert background gas at 20-22 A arc current and 8 mm cathode diameter.

Figure 4.14 shows that the anode surface temperatures were high at lower gaps, i.e. 4043 $\pm$ 56 K at a 3.0 mm gap and 3839 $\pm$ 35 K at a 5.0 mm gap. However at 6.3 mm gap the anode surface temperature dropped to 3748 $\pm$ 12 K and the temperatures stayed below 3800 K even at the highest gaps. At 8.0 mm inter-electrode gap the anode surface temperature was 3745 $\pm$ 56 K.

From the micrograph analyses it was found that carbon nanotubes were also formed when the continuous arc was operated under the argon environment. However the CNTs produced were far fewer compared to the run with nitrogen used as a buffer gas. This is shown in Figure 4.15 (a-c). These nanotubes were formed when the arc was operated with the inter-electrode gap in a range of 6.3 to 8 mm. A large amount of CNTs was produce when the reactor operated at the lowest gap *i.e.* 3.0 mm. Here, the nanotubes produced were short and have a big diameter. However, when the gap was increased to 5.0 mm, cauliflowers with a size varied from 1-5 micrometers covered the carbon tape surface. Ironically, at higher inter-electrode gap of 6.3 mm, the cauliflowers disappeared and a small amount of CNTs was formed. The nanotubes produced were long and very small in diameter compared to the tubes produced at the lowest gap.

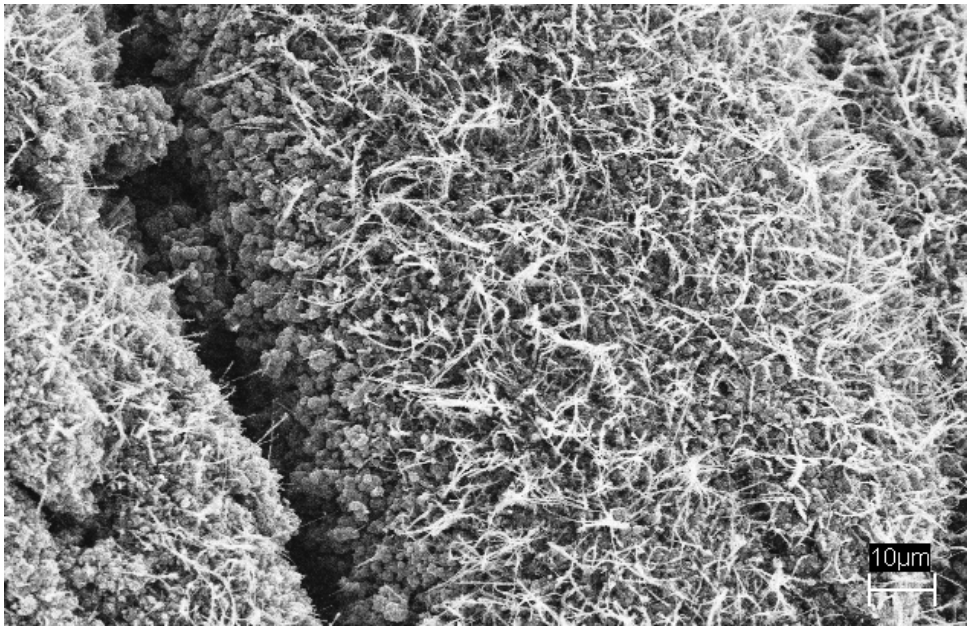

a) 3.3 mm gap

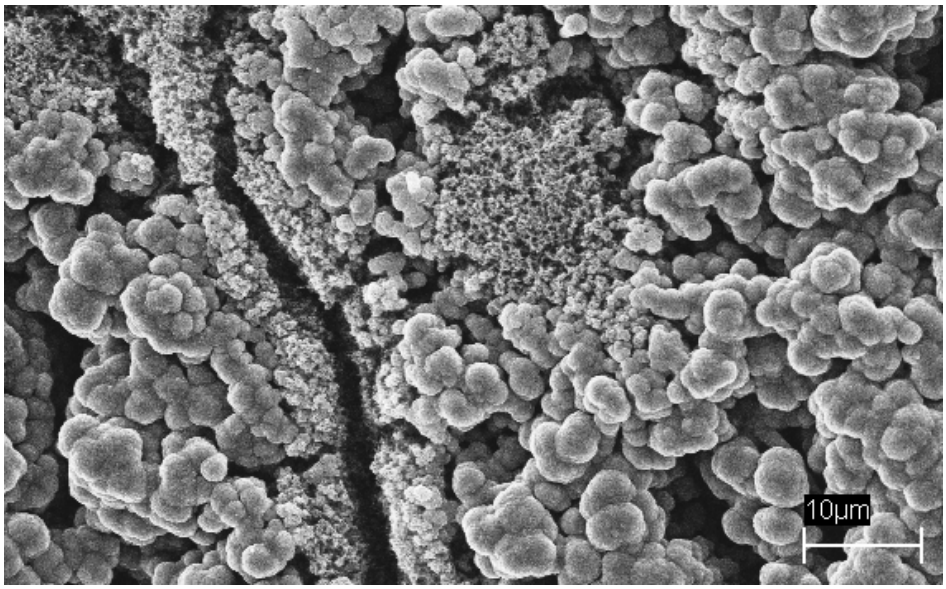

b) 5.0 mm gap

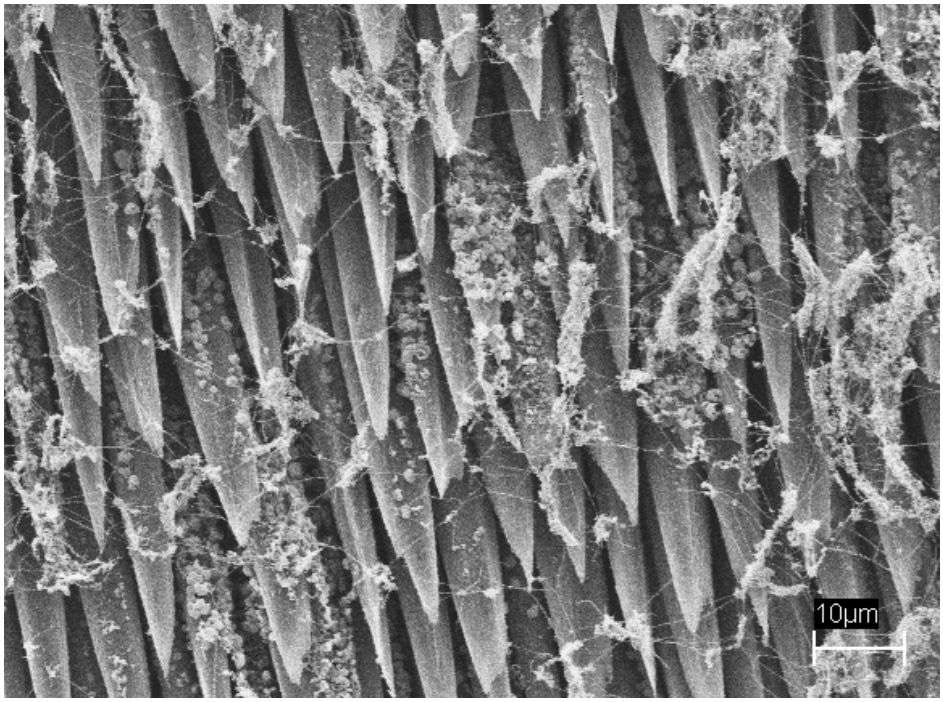

c) 6.3 mm gap

Figure 4.15 CNTs formation under an argon environment and 16 A current with a high current power supply, a) 3.3 mm inter-electrode gap b) 5.0 mm inter-electrode gap c) 6.3 mm inter-electrode gap

4.7.2 Helium

Another set of trials was carried out to investigate the effect of helium in producing CNTs in this continuous arc reactor. A similar procedure to that for the argon experiment was used for these runs. The average surface temperatures for the helium run are shown in Figure 4.16.

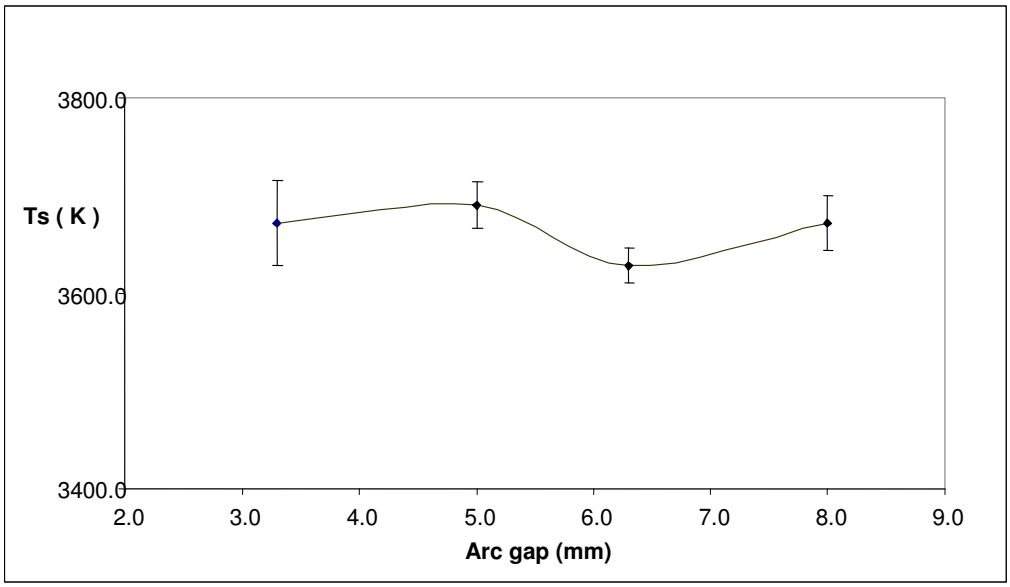

Figure 4.16 Anode surface temperatures at different inter-electrode arc gaps under helium atmosphere and arc current of 16 A (high current power supply).

The anode surface temperatures under helium atmosphere were found to be less than 3800 K for all inter-electrode gaps. At the lowest gap the anode surface temperature 3672 $\pm$ 44 K. The lowest anode surface temperature was 3628 $\pm$ 17 K, at 6.3 mm inter-electrode gap. Unfortunately, from the SEM analysis, it was found that CNTs were not produced in any of these runs as shown in Figure 4.17. This is very strange as several groups have reported formation of CNTs under helium atmospheres. At the lowest inter-electrode gap, cauliflowers were formed with a few nanorods protruding from the cauliflower bunch.

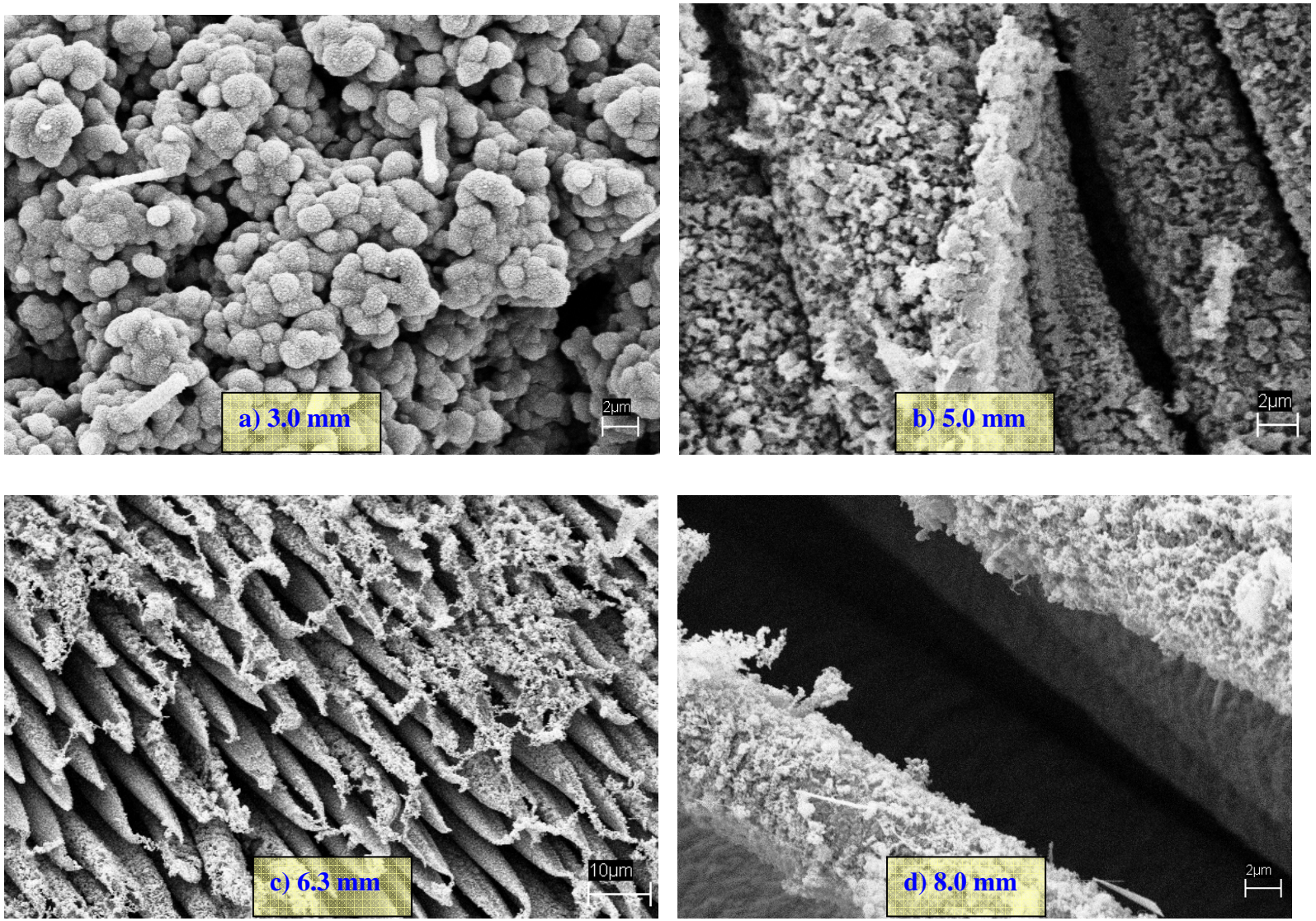

Figure 4.17 Images from SEM analysis on substrate surfaces under helium atmosphere environment and 16 A arc current with a high current supply, a) 3.3 mm inter-electrode gap b) 5.0 mm inter-electrode gap c) 6.3 mm inter-electrode gap d) 8 mm inter-electrode gap

4.7.3 Comparison of surface temperatures in 100 % nitrogen, argon and helium environment at 1 atmosphere.

By comparing the results from previous sections (shown in Figure 4.18), it was found that the anode surface temperature profile for argon and are very similar without any dropped in surface temperature at any inter-electrode gap. However, for all runs, anode surface temperatures in an argon atmosphere were higher than the helium atmosphere.

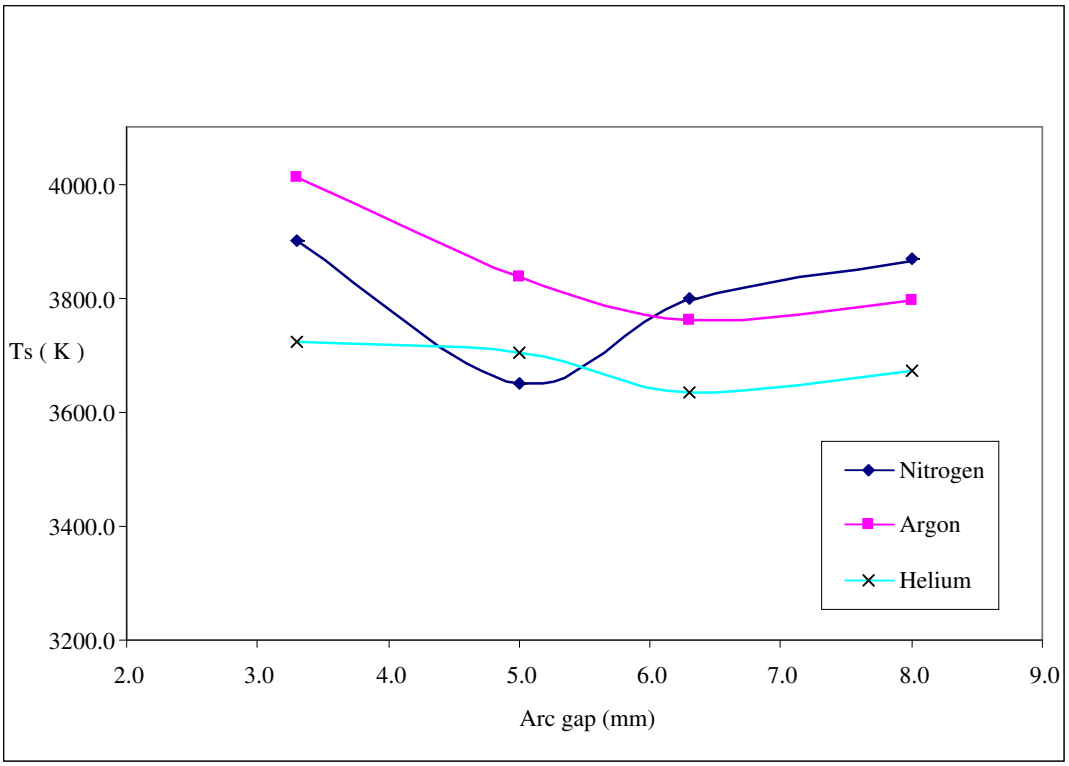

Figure 4.18 Anode surface temperatures at different inter-electrode arc gaps under nitrogen (low current power supply) atmosphere, helium or argon atmosphere (high current power supply). The arc current used was 16 A for all runs. The anode surface temperatures for argon were higher by >100 K compared to the temperatures in the helium environment.

4.8 High speed camera analysis on the arc

The purpose of this experimental work is to investigate the movement of particles ejected from the electrode surfaces. The images were photographed using a high speed B/W CMOS camera (Model # CPL MS50 K) with a rate of 1080 frame per second (fpr). The number of frames per second can be varied by changing the image size as shown in the following table.

Table 4-2 Relation of camera image size with number of video frames

Image size	Number of frame per second
1280 x 1020	500 fps
1289 x 512	1000 fps
1280 x 256	2000 fps
1280 x 100	5000 fps
1280 x 50	10000 fps

Three movies at different image sizes were taken using the high speed camera at 500 fps, 1080 fps and 3200 fps. Details of the still images from the movies are shown in Appendix A.

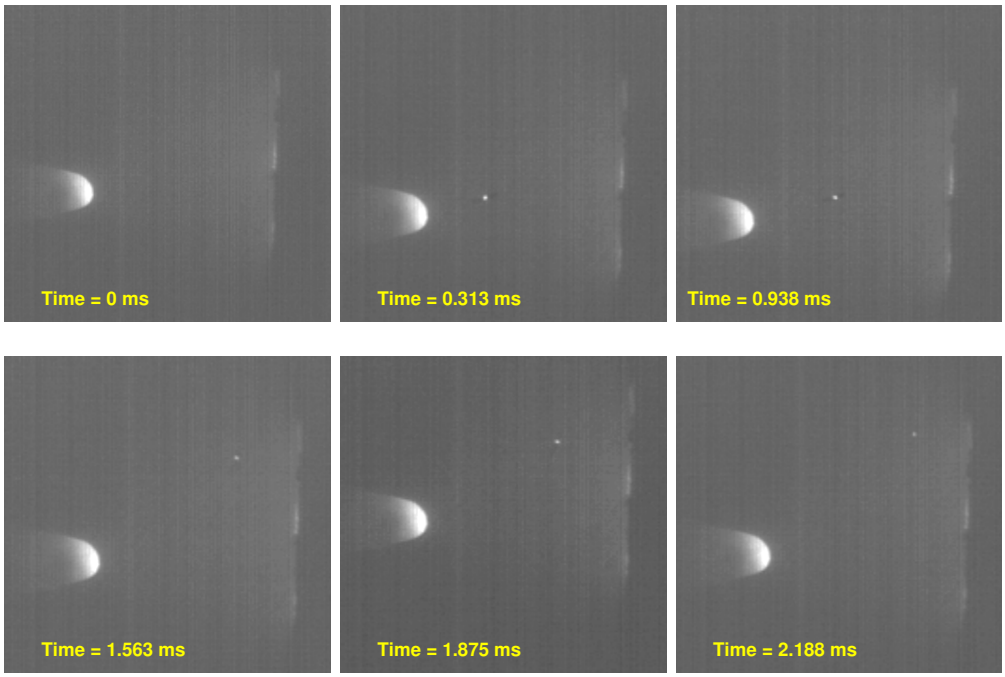

Figure 4.19 High speed camera images of a particle from cathode at optimum arc condition i.e. 16 A arc current and 5.2 mm gap.

Figure 4.19 shows the some of the images extracted from the high speed camera movie taken at 3200 fps. The size of the particle ejected from the cathode tip was approximately 100 µm. This particle was ejected towards the outer side of the arc plasma and within 5 ms the particle had reached the anode region. From the analysis, it was found that the particle was ejected from the cathode tip at a speed of 0.7 m/s and then reached a maximum velocity of 5.0 m/s within 1 ms. The particle was pushed to the side by the expansion from the anode surface and loss its momentum. The particle was then re-circulating in-front of the anode surface. The path of the particle movement and the velocity profile is shown in Figure 4.20(a). Another interesting observation was that the particle ejected from the anode surface (details are not shown here) seems to be re-circulating with-in about 1 mm from the anode surface with a similar frequency to cathode particle.

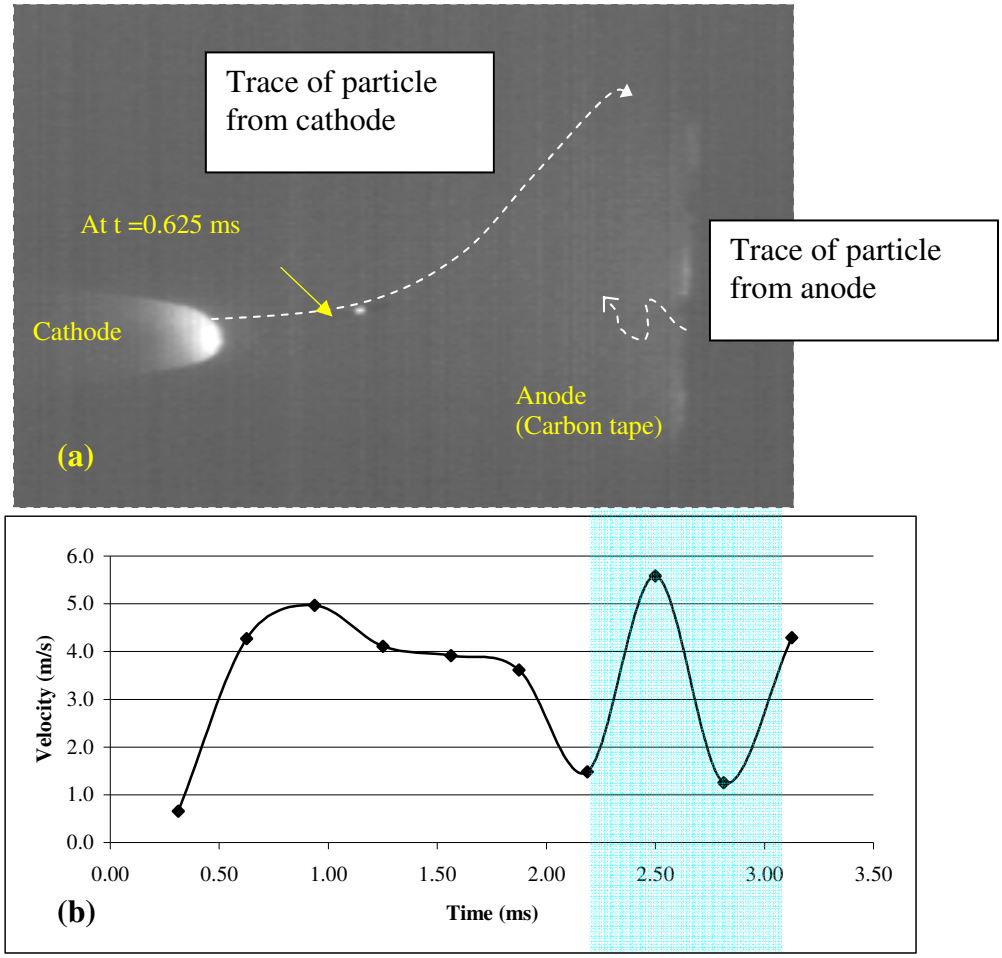

Figure 4.20 a) Projection of particle in front of the cathode -for a period of 3 milliseconds and in-front of anode –for a period of 5 milliseconds, b) velocity profile of a particle ejected from cathode surface

The development of the anode plume was also recorded using the high speed camera. Images of arc showing radiation from electrodes and the plasma plume evolution is presented in Figure 4.21.

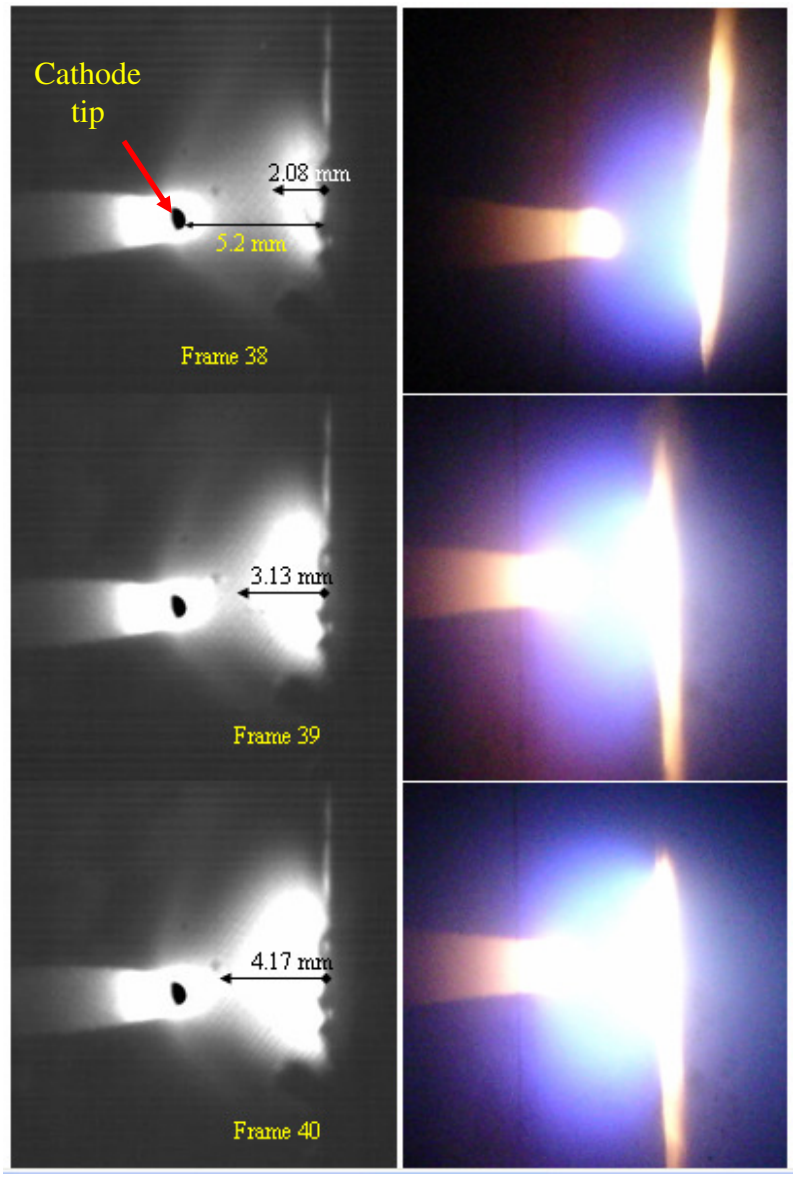

Figure 4.21 Anode plume development for the 16 A arc current and 5.2 mm inter-electrode gap. On the left images from high speed camera and on the right the true colours images.

Immediately after the arc ignition, when the anode was cold, the arc operated as conventional cathodic arc. At this stage, ~ 1-8 ms after arc ignition, the plasma jet produced by the cathode spot, expand into the inter-electrode gap. Part of the cathode material was deposited on the anode surface. The anode was heated by cathode plasma jets. It reached a temperature at which the anode (carbon substrate) starts to evaporate/sublime from the anode surface and form a plasma plume. The area enlarges with time, with a radial expansion velocity of about 1.12 m/s.

The appearance of the anode plasma plume is clearly seen in Figure A.3 (see Appendix A). Both radial and axial extent of the anode plasma plume, increase with time and filled much of the inter-electrode gap. In the final stage, the dense plasma of anode plume completely covered the anode surface and fill the gap at a characteristic time of $t=t_{fill}$ ~ 3-10 m s. For $t >> t_{fill}$ the cathode plasma jet are completely dissipated into the anode plume and heat flux to the anode is from this plasma plume, in contrast with the beginning stage when cathode spot plasma jets determine the anode heating. As the substrate moving (with speed of 3 mm/s) along the process, the arc plasma then extinguished and the process are repeated. However, at certain cycle the anode plasma plume stays for a very long time before extinguish.

Another interesting observation is that the cathode tip appears to be black in the high speed camera images but glowing in the true colours images. The black colour in those images represents the lower temperature region. However, in the true colour images the tip looks glowing and the sharp tip did not appear. Since a narrow band filter was used when we photographed the arc using the high speed camera, the UV radiation may be block and only certain amount of light captured by the camera.

As described earlier, images in Figure 4.21 were captured by the high-speed camera with the number of frames per second at 1080 fps, therefore

$$t = \frac{1000}{1080} = 0.926 \text{ ms}$$

The anode plume expansion velocity, $v_{anode\ plume}$ was calculated by analysing Frame 38 and Frame 39

$$v_{anode\ plume1} = \frac{(3.13 - 2.08)\text{ mm}}{0.926\text{ ms}}$$
$$= 1.13 \text{ m/s}$$

And for the Frame 39 and Frame 40

$$v_{anode\ plume2} = \frac{(4.17 - 3.13)\text{ mm}}{0.926\text{ ms}}$$
$$= 1.12 \text{ m/s}$$

Therefore the average anode plume expansion velocity is

$$v_{plume\ (ave)} = \frac{1.13 + 1.12}{2} \text{ m/s}$$

$$= 1.125 \text{ m/s}$$

The radial expansion velocity was calculated using the same method. The results are shown in the table below.

Table 4-3 Radial expansion velocity of anode plume.

Frame No	Plume diameter (mm)	Radial expansion Velocity (m/s)
38	3.33	
39	5.42	1.13
40	6.25	0.45

The development of cathode and anode plumes may be related to the presence of graphite crystallites in the plasma. The presence of graphite crystallites with low ionization potential in the space close to the anode surface suggests that the positive current may be carried in this region by crystallites rather than molecules. The crystallites are often much more easily charged than gaseous species under the same conditions (Abrahamson 1974).

Finkelnberg (Finkelnburg 1946) observed at the noisy state, the anode attachment wandering around the surface and it relate to the rapid fluctuation in voltage and current. In the quiet state, the anode attachment evenly covers the anode surface and contracts to a small foot in the noisy state. In term of particulate theory, it is expected the quiet state operates with crystallites as positive charge carrier. The crystallites, coming from the anode surface, tend to spread the arc attachment over that surface (diffuse attachment). The transition between quiet and noisy state is then brought about by more rapid removal of crystallites by irradiation. Once all the crystallites vaporises as carbon vapour, the arc

attachment is extinguished and localized heating is started. Gaseous ions are then generated by localized heating of the anode surface with constricted arc attachment. At this state this mechanism (crystallite as charge carrier) is no longer valid and gaseous ion becomes a positive carrier. From the high speed image analysis (at 16 A current and 5.2 mm inter-electrode gap), this constricted state periodically occurred between periods of diffuse attachment. (~ 1-4 ms of noisy constricted attachment whereas the quiet state normally stays for a longer time ~ up to 35 ms).

The observations of carbon anode arc behaviour appear to be consistent with the idea proposed above. Our observation is that when the arc is first struck, it is noisy and becomes quiet only as normal electrode temperatures are approached. The area at the centre of arc attachment will be heated most intensively by electron condensation, which results in more rapid vaporisation of the crystallites as they pass out through the porous surface layer. A stage will be reached where the current carrying ability of the crystallite electron plasma just above the area is markedly reduced. While there is easy access to further anode surface, the anode attachment will expand. When further expansion becomes difficult (down the side of the anode) a transition to a small gas-ionised attachment will occur. Thus strict control of the current density over the quiet attachment appears to be achieved by means of sublimation of crystallites from electrode and possible deposition from that carbon loss.

4.9 References

Abrahamson, J. (1974). "Graphite Sublimation Temperatures, Carbon Arcs and Crystallite Erosion." Carbon **12**(2): 111.

Farhat, S., I. Hinkov, et al. (2004). " Arc Process Parameters for Single-Walled Carbon Nanotube Growth and Production: Experiments and Modeling." Journal of Nanoscience and Nanotechnology **4**(4): 377-389.

Finkelnburg, W. (1946). The high current carbon arc. FIAT Final Report No.1052. Washington, D.C., Department of Commerce.

Lange, H., P. Baranowski, et al. (1997). "An optoelectronic control of arc gap during formation of fullerenes and carbon nanotubes." Review of Scientific Instruments [H.W. Wilson - AST] **68**: 3723.

Lange, H. and A. Huczko (2001). "Influence of nitrogen on carbon arc plasma and formation of fullerenes." Chemical Physics Letters **340**(1-2): 1-6.

Meunier, J.-L. (1999). "Cathodic arc carbon plasma/gas interaction in fullerene synthesis study." J. Appl. Phys. **85**(3): 1992-1994.

Shashurin, A. and M. Keidar (2008). "Factors affecting the size and deposition rate of the cathode deposit in an anodic arc used to produce carbon nanotubes." Carbon **46**(13): 1826-1828.

Zhang, H., X. Xue, et al. (1999). "The effect of different kinds of inert gases and their pressures on the preparation of carbon nanotubes by carbon arc method." Materials Chemistry and Physics **58**(1): 1-5.

Zhao, X., T. Okazaki, et al. (1999). "Optical Emission Spectra during Carbon Nanotube Production by Arc Discharge in H_2, CH_4 or He Gas." Jpn. J. Appl. Phys. **38**(Part 1, No. 10): 6014-6016.

Chapter 5: Plasma Modelling 5-1
5.1 Conceptual framework for modelling arc discharge 5-1
5.2 Physics of the arc discharge.....5-4
5.2.1 Carbon arc 5-5
5.2.2 Physics near the electrode.....5-7
5.3 Plasma Properties and transport coefficient 5-11
5.3.1 Plasma composition.....5-11
5.3.2 Thermodynamic properties.....5-12
5.3.3 Transport properties.....5-14
5.4 Computational Fluid Dynamic (CFD).....5-15
5.4.1 Comsol Multiphysic 5-15
5.5 Arc Plasma Modelling.....5-18
5.5.1 Modelling task 5-18
5.5.2 Mathematical model 5-19
5.5.3 Model geometry and boundary conditions 5-21
5.5.4 Application Modes 5-24
5.5.5 Modelling strategy.....5-26
5.6 Measurement of boundary conditions 5-27
5.6.1 Nitrogen velocity on the anode surface 5-27
5.6.2 Anode surface temperature.....5-28
5.6.3 Electrical conductivity of plasma in the anode layer.....5-28
5.7 Results 5-38
5.7.1 Surface mesh 5-39
5.7.2 Analysis of the variables 5-39
5.7.3 Effect of nanoparticles on plasma temperature 5-41
5.7.4 Effect of anode surface temperature.....5-44
5.7.5 Effect of Nitrogen flushing.....5-45
5.7.6 Effect of inter-electrode gap.....5-48
5.8 Reliability of the model.....5-50
5.9 References 5-51

Chapter 5: Plasma Modelling

5.1 Conceptual framework for modelling arc discharge

Understanding and modelling the arc discharge or electric arc has been a matter of scientific interest since the first discovery of arcing phenomena by Sir Humphrey Davy about 200 years ago (Chaney, Hamister et al. 1936). The arc discharge not only forms a basis for efficient discharge lamps but also was an initiator for the development of plasma physics in the 1920's. From the history of the arc, for every 50 years there is advancement in the development paradigm as that shown in Figure 5.1 (Wendelstorf 2000).

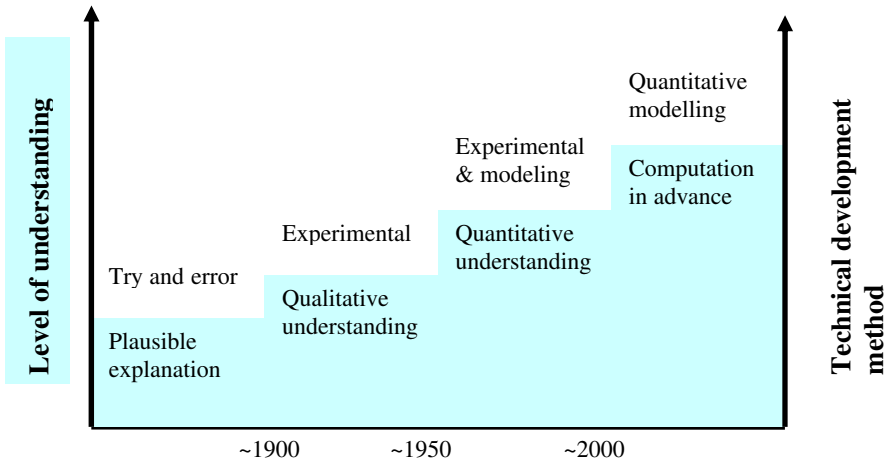

Figure 5.1 Development of arc discharge science and technology (Wendelstorf 2000).

Most of the processes that occur in the arc discharge technique cannot be computed in advanced and thus can be regarded as not fully understood. The arc discharge can be classified into several types based on the arc temperatures and electron densities. These two parameters can vary over a very wide range as shown in Figure 5.2. These properties are determined by the arc parameters such as the plasma compositions, plasma properties and the geometry of the arc itself. With the availability of the high-speed computer, the modelling of the arc plasma is much easier and becomes an important research tool.

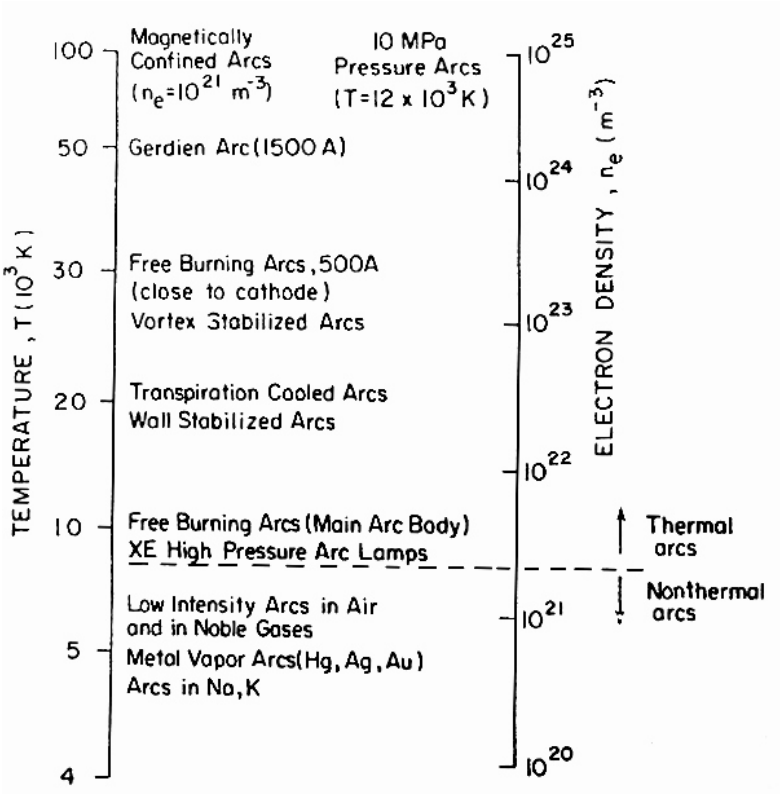

Figure 5.2 Survey of arc temperatures and electron densities (Boulos, Fauchais et al. 1994).

To ease and simplify the analysis, the physical regions in the arc can be divided into at least three regions as that shown in Figure 5.3:

1. The electrodes and their surfaces
2. The arc column in local thermal equilibrium (Walters, Ericson et al.) condition
3. The electrodes' boundary layers (anode & cathode drops) which consist of sheath and pre-sheath

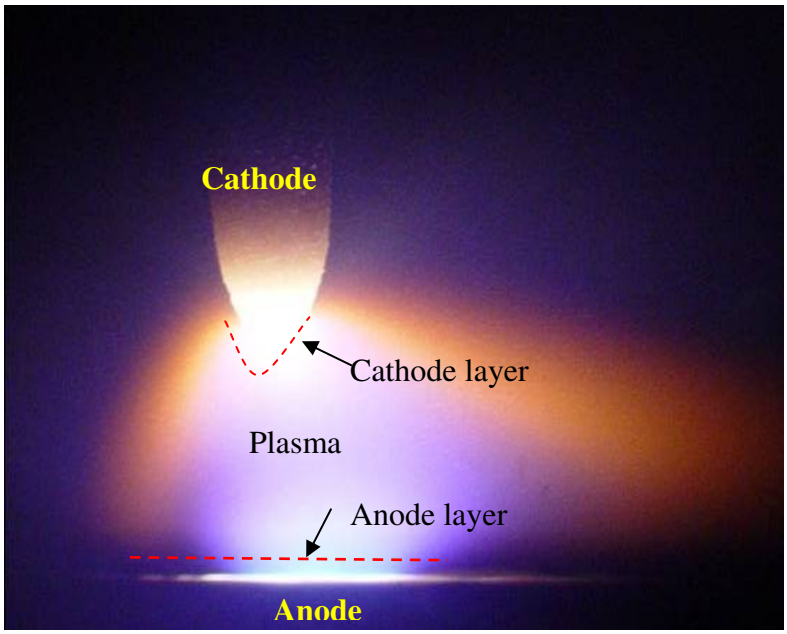

Figure 5.3 Typical electric arc discharges consisting of three regions.

The electrode with a higher or the positive potential is known as an anode while that with the lower or the negative potential is called a cathode. The plasma column is terminated by the electrode layers, where a major part of the voltage drop is located and the condition of local thermal equilibrium (Walters, Ericson et al.) is not applicable. In most cases, a one-dimensional treatment of these layers is justified while the arc column has to be treated at least as a two dimensional system by assuming it is cylindrically symmetrical.

Modelling of an arc discharge includes a wide range of physical phenomena with high degree of complexity. To make it simpler, one can define the arc model as a black box as presented in Figure 5.4.

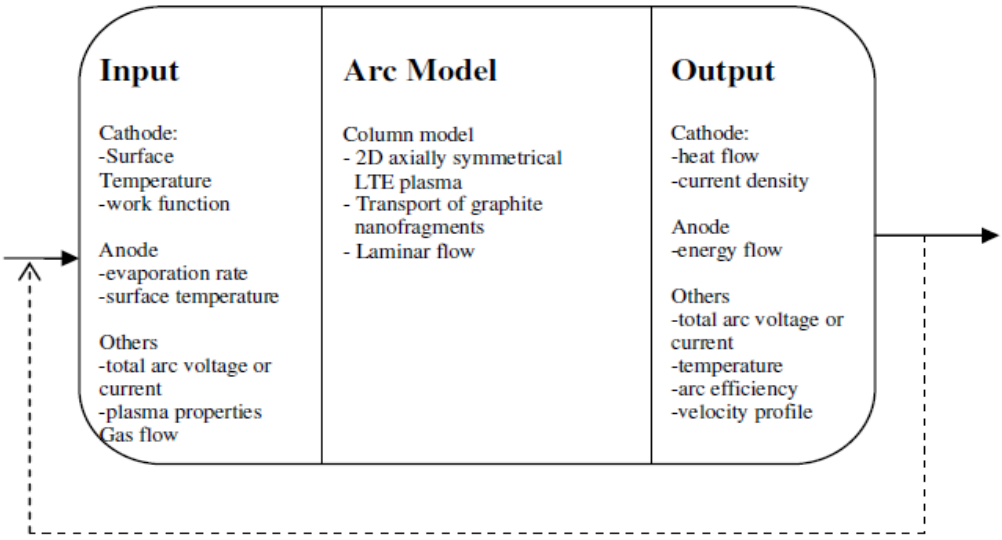

Figure 5.4 Definition of arc modelling module.

A simple mathematical model cannot describe the electric arc. The steps of the physical process happening in the different regions arc must be understood to model the arc. The process may change when it is operated at different scales and with different specific features. For this reason, we will focus only on the modelling of the low current carbon arc with graphite electrodes. This unit may physically differ from a normal arc welding which has been extensively modelled by various group (Lowke 1979; Hsu and Pfender 1983; Lago, Gonzalez et al. 2004).

5.2 Physics of the arc discharge

The properties of the arc discharge, in particular one at low current and with graphite or carbon rods as electrodes, will be discussed next. Much excellent literature is available that discusses arc discharges in general. Boulos *et al*. (1994), for example, describes excellently the fundamentals of arc discharge in their text. Similarly, Raizer's (1997) is also a good source of understanding the physics of arc discharge.

It is common knowledge that the easiest way to initiate an arc is by connecting the electrodes to a suitable power supply, which must be capable of providing sufficient current. To strike the arc, the electrodes are first brought into contact and then slowly separated into a certain gap. The electrodes may turn white-hot at the contact point and may partly vaporize and produce emission. When the cloud of ionized vapour reaches the anode, the arc starts burning.

In general, the arc discharge is characterized by large current, *i.e.* ~ 1-10^5 A. The cathode current density is also always large. It ranges from 1 A/mm^2 to 10^5 A/mm^2 depending on the modes of operations. The arc cathode receives a large amount of energy from the current and reaches high temperature. This high temperature is either experienced by the entire cathode face or localised on one or more small spots. This phenomenon usually happens for a very short time interval. The cathode will then be eroded and vaporized (Boulos, Fauchais et al. 1994).

5.2.1 Carbon arc

The carbon arc is a classic example of an electric arc. It is essentially an electric discharge (usually in air) between two carbon electrodes. Some carbon particles vaporise from both electrodes and form atomic molecules and ions. Raizer (1997) grouped the carbon arc into several different categories depending on the operating gas pressure. He classified the carbon arc operated at atmospheric pressure into the high-pressure hot-cathode arcs group. Then he further divided this group into high current and low current sub-categories. The arc that runs with current less than 50 A is classified as a low current arc and those that run with up to 1kA current are named as high current arcs (Raizer 1997).

A typical low current carbon arc operates at atmospheric pressure between two cylindrical carbon electrodes that are separated by a few millimetres. The operating voltage and current are usually between 50-80 V and 10-30 A, respectively. The carbons are continuously consumed in the arc. The vapour eruption from the cathode influences the arc mechanism. The anodic current density for a low current arc is about 0.4 A/mm^2 compared to high current arc, which is normally 3-10 times higher.

The current–voltage (I-V) characteristic of a carbon arc is illustrated in Figure 5.5. This diagram shows the arc voltage as a function of current and electrode gap. At a certain current value, the I-V curve becomes almost horizontal; at this point, the arc starts to hiss. Raizer (1997) deduced that the hissing sound at high current was due to the strong vaporization of the anode in a fast moving anode spot.

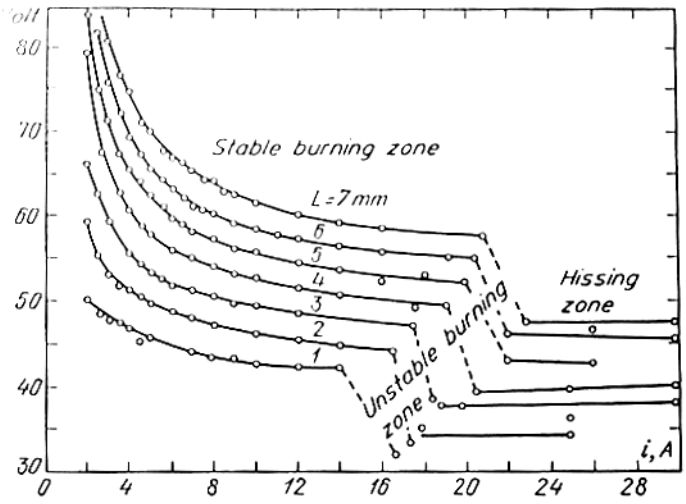

Figure 5.5 The I-V characteristic of carbon arc in air. Values of L indicate the inter-electrode gap (Raizer 1997).

The kinetics mechanism of the arc is always an interesting and important discussion. Theoretically, in the arc plasma, the positive ions are travelling towards the cathode. They are accelerated near the cathode with a voltage drop of approximately 10 V where they strike the negative basis of the arc and heat it up to a temperature of 3200 to 3600 K. At this temperature, carbon thermionically emits a number of electrons. These electrons then travel towards the anode and accelerate in the anode drop. By transferring energy to anode crater, they heat it up to a temperature of 3600 K to 4200 K. Here, the anode temperature is observed to be higher than that of the cathode because the anode was cooled only by radiation and conduction, whereas, the cathode loses some more energy by electron emission.

At the same time in the plasma column, the conduction of current occurs. Here, the number of electrons and ions produced are just enough to compensate for the loss of electrons and ions by radial diffusion and recombination. Therefore, in the plasma column, the potential gradient is nearly constant along its length.

The electrons, ions and neutral molecules in the arc are always in continual thermal motions because most collisions are perfectly elastic. In the equilibrium state, the velocities are distributed according to the Maxwell distribution. The much greater mass of ions and neutrals also means that they move at much lower velocities than the electrons. This leads to an inefficient energy transfer from the high speed electrons and therefore requires more collisions to occur before all species have similar kinetic energies. Higher electric field especially near the cathode will be needed.

The number of collisions occurred in a low-pressure arc (P < 10-2 bar) is usually low. Therefore the electron temperatures (T_e), are of order of a thousand Kelvin, are estimated from the kinetic energy distribution. The gas temperature does not escalate much above room temperature. Electron temperature is usually very different from those of ions and neutral species for low-pressure system. With a high-pressure arc (P > 10^{-1} bar), collisions are more frequent and generally the electron temperature does not rise above the 'gas temperature' by more than few percent. Temperatures from 5000 K to 20000 K are commonly measured by spectroscopic means as shown in Figure 5.6.

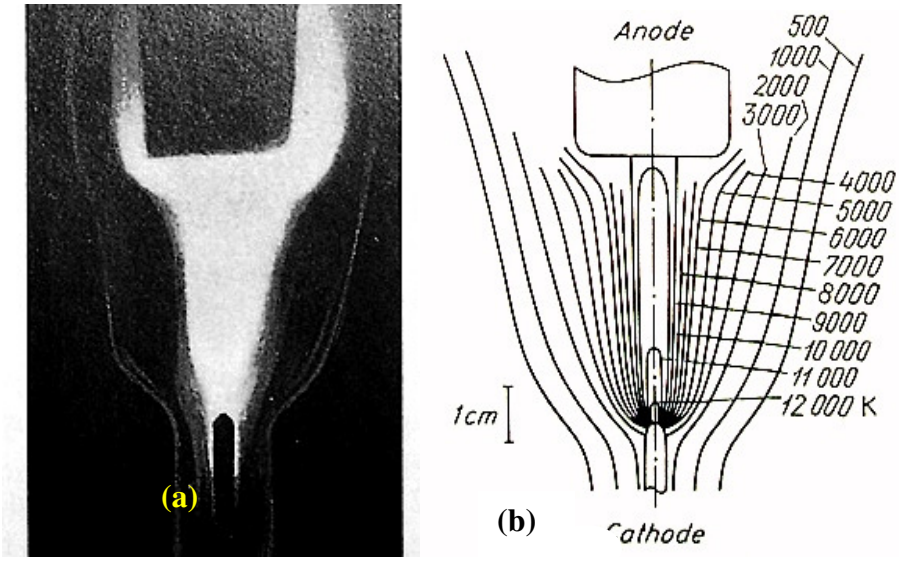

Figure 5.6 Carbon arc in air at a current of 200 A (a) a photograph, (b) measured temperature field (Raizer 1997).

5.2.2 Physics near the electrode

If one looks in more detail at the near-electrode region, the following question will be asked: "How is the current continuity maintained from the highly conductive electrode to the less conductive plasma near the electrode?" In the electrodes and in the plasma, the current is supported by the electron flow. However, the electron density in these media is different and this means different mechanisms of current continuity at the plasma/anode and plasma/cathode interfaces.

At the cathode, only a small area of the surface contacts the plasma regions, which later moves onto the cathode surface. This bright spot, that can disappear and re-appear within a very short time (Beilis 2001), is known as the cathode spot. During the start-up, the arc is expected to operate in the 'Thermo-Field' or cold-cathode electron emission

mode. During this, only tiny spots with a size of normally, r ~ 10^{-6}-10^{-4} m exist. They move randomly on the cathode surface at velocities between 10-100 m/s. These small cathode spots later merge to form a larger spot within few seconds. The arc-discharge then operates in a thermal arc regime with dominantly thermionic electron emission or hot cathode mode. When thermionic emission dominates, the cathode spot occupies a fixed position and operates very stably. The larger spot moves at a lower speed of about 0.1-1 m/s. It also has a higher evaporation rate than the small cathode spot (Raizer 1997). Current continuity in the cathode region depends on several factors such as atomic evaporation, cathode electron emission and the electric field at the cathode surface (Beilis 2006). The value of cathode fall for the carbon arc is normally between 11-14 V as measured by several researchers (Davis and Miller 1969; Zhu and Engel 1982).

Murooka and Hearne (1972) produced extensive data on arc electrode temperature for graphite electrodes in an argon and air environment over a current range of 5 – 50 A. Their finding shows that the anode surface temperature increases more rapidly with time for larger arc currents as shown in Figure 5.7

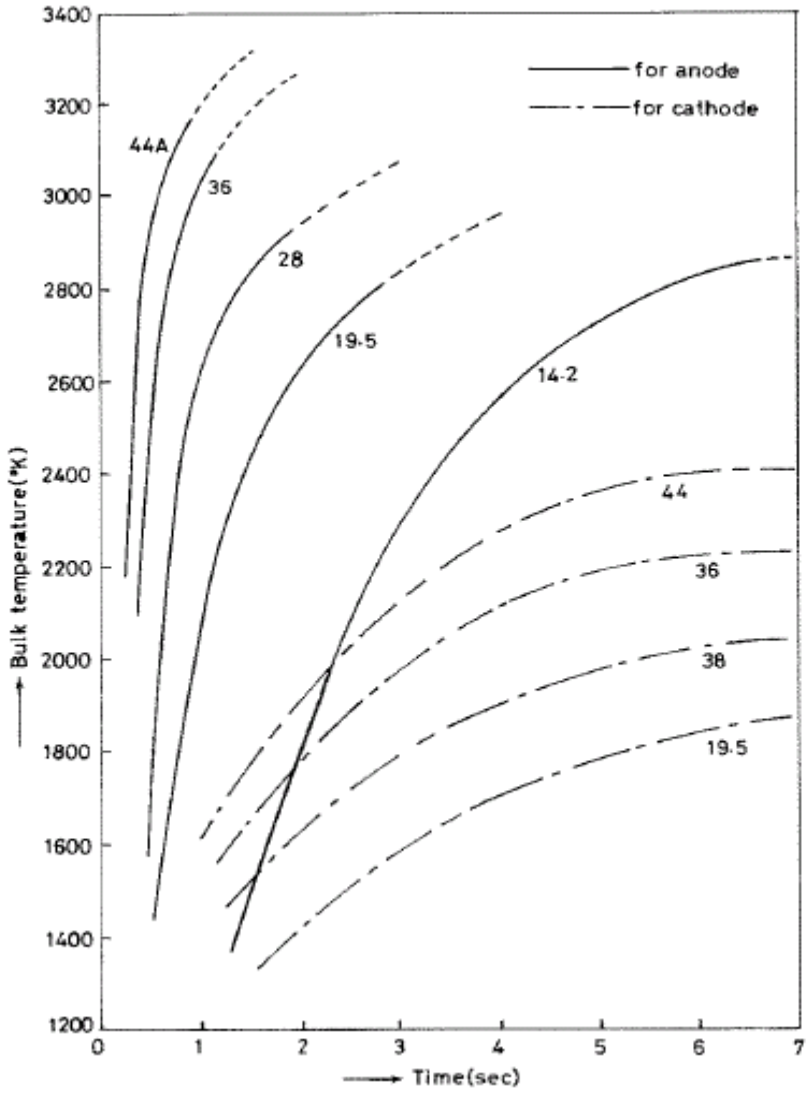

Figure 5.7 Bulk temperature rise at the anode and the cathode with time after arc initiation for different arc currents The electrodes used were 3.2 mm diameter spectrographically pure graphite(Murooka and Hearne 1972).

The cathode spot is probably established soon after arc ignition and moves quicker than the anode spot. The maximum temperatures reached as a function of arc current are shown in Table 5.1

Table 5.1 The relation between maximum cathode temperature and arc current for the carbon arc (Murooka and Hearne 1972)

I (A)		4.5	9.8	19.5	28	36
T_s (K)	Anode	……	…….	3250	3450	3550
	Cathode	3280	3400	3700	3724	3750

Like the cathode, the anode processes in the anode layer are also complex. The anode operates as the electron collector either in evaporating or cold mode depending on the discharge and electrode condition (Ushio 1988). The arc may be attached to the anode surface in two different ways (Raizer 1997).

- Diffuse anchoring is a phenomenon where the current is spread over the large area of anode.
- Anode spot happens when the size of diffuse attachment grows with current until it is destabilized and contracted at the anode surface. The current density in the spot normally reaches 10 - 1000 A/mm^2 (Beilis 2000).

The anode region has a steep temperature gradient and in which the thermodynamical state is far from equilibrium. Ionization, recombination, decomposition and other chemical reaction may occur in the thin boundary layer and its vicinity. It is normally accepted that there is a strong electric field in this boundary layer creating beams of charged particles (electrons, ions etc) delivering or removing energy to and from the surface and providing electrical conduction (Lago, Gonzalez et al. 2004). The physics in this collisionless and strong electric field zone simply cannot be treated using an equilibrium thermodynamic approach.

However, in the model being applied in this thesis a different approach has been introduced. The presence of graphite crystallites with low ionization potential in the space close to the anode surface suggests that the current may be carried in this region by crystallites rather than molecules. The crystallites are often much more easily charged than gaseous species under the same conditions. Approximating the crystallites to spherical particles with Φ=4.6 eV, Abrahamson (Abrahamson 1974) estimates that a crystallite of 50 nm dia could carry more than 100 electronic charges before the ionization potential rose to 11 eV, to be in competition with the most easily ionized molecules. Similarly, a 10 nm crystallite could carry 20 charges and 1 nm crystallite only 3 charges. Therefore, the electrical properties of the arc will be altered by the presence of the cloud of nanoparticles. The increases of electrical conductivity in this boundary layer are expected to reduce the deviation from local thermodynamic equilibrium (LTE) (Bilodeau, Pousse et al. 1998).

5.3 Plasma Properties and transport coefficient

In this section, a brief overview of plasma properties will be discussed. This includes plasma composition, thermodynamic properties and transport properties. The plasma composition and properties strongly vary with temperature. For the purpose of the modelling, all of these properties were taken from Boulos *et al* works (Boulos, Fauchais et al. 1994).

5.3.1 Plasma composition

The basic plasma composition can be described by a set of equations consisting of the Eggert-Saha equation, Dalton's law and the condition for quasi-neutrality of the plasma.

$$\frac{N_e N_i}{N} = \frac{2Q_i}{Q}\left(\frac{2\pi m_e kT}{h^2}\right)^{3/2} exp\left(-\frac{E_i}{kT}\right) \qquad \text{(Eqn 5.1)}$$

$$p = (n_e + n_i + n)kT \qquad \text{(Eqn 5.2)}$$

$$n_e = n_i \qquad \text{(Eqn 5.3)}$$

In the Eggert-Saha equation, N_e is the electron density, while N_i and N represent ion and neutral number densities, respectively. The partition functions of the ions and neutrals are denoted by Q_i and Q respectively. The symbol h is the Plank's constant, k_B is the Boltzmann's constant, m_e is the electron mass and E_i represents the ionization energy (Boulos, Fauchais et al. 1994).

For nitrogen plasma, the number of possible species in the plasma is high due to the presence of molecular species. Chemical processes such as dissociation of molecules to atoms and ionization of atoms may occur. The formation of molecular ions will be neglected. The dissociation process in nitrogen plasma can then be presented as:

$$N_2 \rightleftharpoons N + N \qquad \text{(Eqn 5.4)}$$

The plasma composition can then be calculated by considering the dissociation, ionization processes that took place and the presence of the additional species. Figure 5.8 shows the calculated result of the nitrogen plasma composition at pressure of 100 kPa (Boulos, Fauchais et al. 1994).

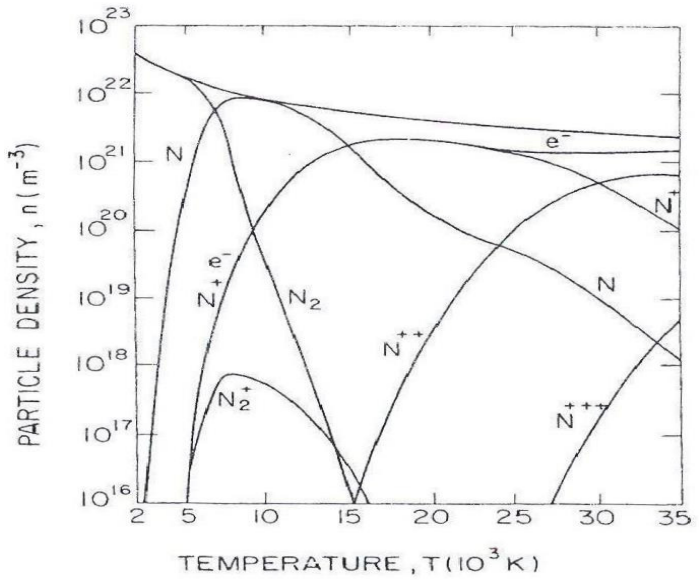

Figure 5.8 Composition of nitrogen plasma at 100 kPa (Boulos, Fauchais et al. 1994).

5.3.2 Thermodynamic properties

The thermodynamic properties of the plasma such as density, enthalpy, specific heat and entropy of plasma are estimated using both Hemholtz and Gibbs functions. The plasma density is calculated directly from the plasma composition as shown in Equation 5.5

$$\rho = \sum_i n_i m_i \quad \text{(Eqn 5.5)}$$

Figure 5.9 shows the nitrogen plasma density at 100 kPa.

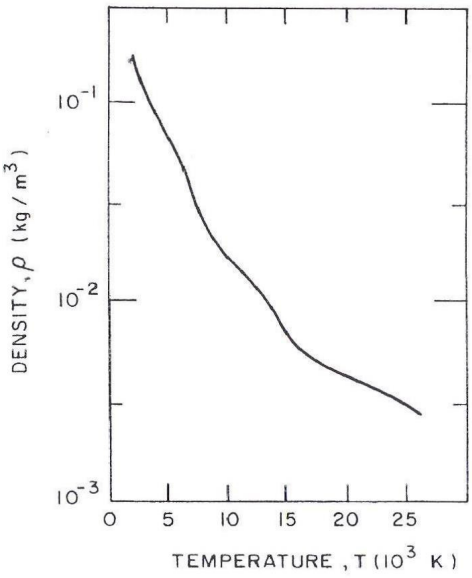

Figure 5.9 Mass density of a nitrogen plasma at 100 kPa (Boulos, Fauchais et al. 1994).

The specific heat, enthalpy and entropy of plasma were calculated using the partition function of each species. Figure 5.10 shows the specific heat of various gases at atmospheric pressure and for this modelling; the value of specific heat at a temperature range of 500-10000 K was taken from the data.

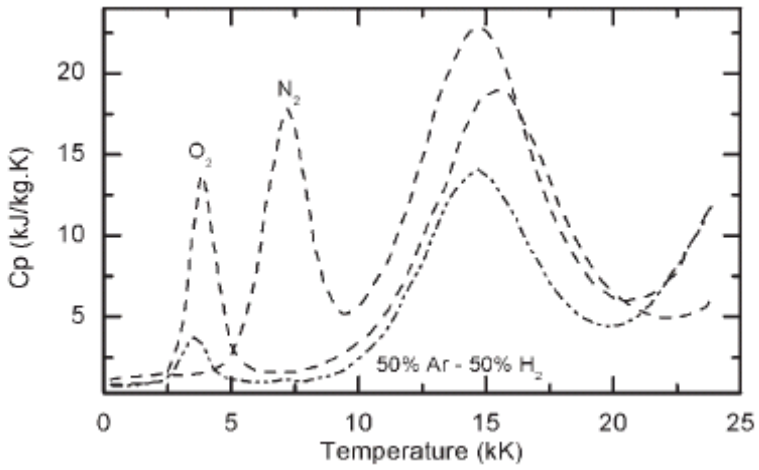

Figure 5.10 Heat capacity for various gases at a variation of temperature (Gleizes, Gonzalez et al. 2005).

5.3.3 Transport properties

The detailed discussion of measurement and computation of the transport properties of the plasma was given by Boulos *et al.* (1994) which include thermal conductivity, viscosity and electrical conductivity. These properties are dependent on the collision cross-section area between particles. For a pure and simple gas mixture, their transport coefficients are available as those listed by Boulos *et al.* (1994). However, for a more complex plasma system, these properties still have a high degree of uncertainty since the experimental data on the cross-section collision is very limited.

The typical example of the thermal conductivity and electrical conductivity of common plasmas are given in Figure 5.11 and Figure 5.12, respectively.

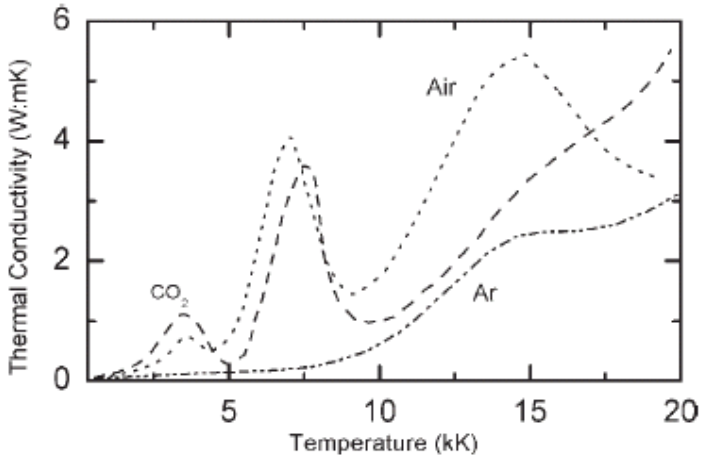

Figure 5.11 Thermal conductivity of air, Argon and CO_2 versus temperature (Gleizes, Gonzalez et al. 2005).

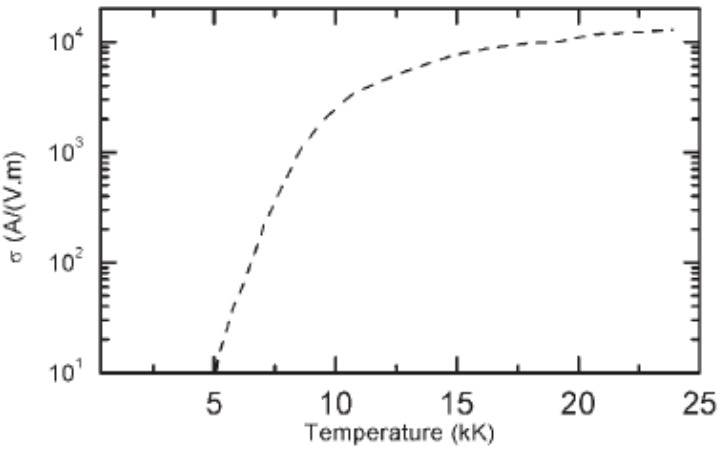

Figure 5.12 Electrical conductivity of air.

In this work, the electrical conductivity was estimated based on the motion of charge carrier and the charge mobility, μ_e. This property is defined by the following expression assuming that electrons dominate the conduction

$$\sigma = \frac{N_e e^2}{\sqrt{2\pi m_e T}\, NQ} \qquad \text{(Eqn 5.6)}$$

In the expression, N is the number density of the neutral particle and Q is the electron-neutral particle collision cross-section. The number density of electron and ions are assumed to be lower than that of the neutral particles. The mean free path of electron is then due to the collision with the neutral species. This oversimplified expression shows that electrical conductivity mainly depends on the electron density. Therefore, the electrical conductivity is almost negligible at temperature below 6000 K for most common plasma gases such as nitrogen, argon and helium (Boulos, Fauchais et al. 1994).

5.4 Computational Fluid Dynamic (CFD)

The CFD software used here results from combination of both theoretical and experimental study of fluid dynamic. In CFD, finite difference method (FDM) and finite element method (FEM) were used to solve the partial differential equations (PDEs). Since these work came into picture, both methods have been developed extensively in the fluid dynamic, heat transfer and other related areas. Historically, FDM has dominated the CFD community because of it simplicity in formulation and computations. However, in recent times, superior performances have also been displayed with the use of FEM.

5.4.1 Comsol Multiphysic

COMSOL Multiphysics is a modelling package for the simulation of any physical process that can be described with partial differential equations (PDEs). It was designed to provide ease of use and flexibility by having a solver that addresses complex problems quickly and accurately. One can easily model most phenomena through predefined modelling templates. Modifying these to specific applications is possible through equation-based modelling capabilities. This simulation software works based on the finite element method (FEM).

COMSOL Multiphysics covers all facets of modelling process as shown in Figure 5.13. It contains CAD tools for geometry drawing, interfaces for physics and equation specifications, mesh generation, a variety of optimized solvers and finally visualization and post processing tools.

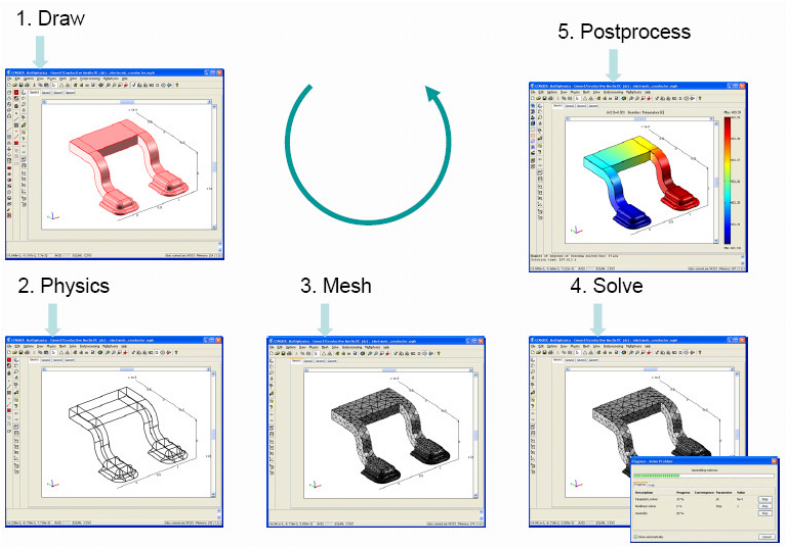

Figure 5.13 Comsol Multiphysics modelling steps

One of the advantages of this simulation package is that a large number of ready to use application modules have been incorporated. They are specific to a physical process such as heat transfer or are related to a set of equations such as the Navier-Stokes equations. These add-ons use standardize terminologies, material libraries, solvers and elements, as well as visualization tools. In addition to custom solutions, each of the add-on modules comes with a large number of ready-to-run and well documented example modules. These modules are

Heat transfer Module

Electromagnetics Module

Chemical Engineering Module

Earth Science Module

Microelectromechanical Systems (MEMS) Module

Structural Mechanics Module

However, only the first two modules, which were used in this study, will be discussed in the next sections.

5.4.1.1 Heat transfer module

Problems involving any combination of conduction, convection and radiation are solved easily with the Heat Transfer Module. This module is supplied with modelling interfaces for general heat transfer (General Heat Transfer Mode), heat transfer in a Thin layer (Thin Conductive Shell Mode), non-isothermal flow (Non-Isothermal Flow Mode) and heat transfer in live tissue (Bioheat Equation Mode).

The General Heat Transfer application mode is a backbone of this module. The definitions of heat transfer through conduction, convection and radiation were included in this mode. The radiation transport can be defined as surface-to-ambient or surface-to-surface radiation. The Thin Conductive Shell application mode handles three-dimensional thin structure using shell elements where temperature distribution across the thickness of the shell is assumed uniform. The Non-Isothermal Flow application mode models fluid flow where changes of density have to be described in the model. Here, an arbitrary equation can be inserted to describe the dependence of density on pressure and temperature. The boundary condition for the fluid flow can be defined as analytical expressions that are typed in. The last application mode, the Bioheat Equation, gives a possibility to enter empirical effective properties into a standardized formulation of heat transfer in live tissue.

The Heat Transfer Module was used extensively in systems that involve the generation and flow of heat in any form. A variety of specialized modelling interfaces are available for different formulations and applications such as surface-to-surface radiation, non-isothermal flow, heat transfer in structures made of thin layers and shells, and heat transfer in biological tissue. The Heat Transfer Module allows for arbitrary couplings to other application module in COMSOL Multiphysics and its modules for multiphysics modelling. This is particularly relevant to applications such as thermal management in the electronics industry, thermal processing and manufacturing, and medical technology and bioengineering.

5.4.1.2 Electromagnetics Module

The Electromagnetics Module gives users a comprehensive design and modelling tool for simulating systems and devices in the areas of electromagnetic fields and waves. It allows anyone to quickly and easily define and solve models in radio-frequency (RF) and microwave engineering, alternating current (AC) and direct current (DC) electromagnetics, and even optics and photonics. Examples of the applications include magnet, capacitors, electric motors, antenna and photonic devices.

This module is based on Maxwell's equation and specializes in component design in areas of electromagnetic field simulations—from static and quasistatics to microwaves and photonics. The static, transient, and frequency domain analyses allow for material properties that are complex-valued, anisotropic, and frequency- or time-dependent.

The Electromagnetic module has application for electrostatics, magnetostatics, low-frequency electromagnetics and wave propagation. The multiphysics capability of COMSOL allows the coupling of this electromagnetic simulation with the heat transfer, structural mechanics and fluid flow modules.

5.5 Arc Plasma Modelling

5.5.1 Modeling task

When this project was first started, no simulation on the carbon arc reactor producing CNTs had been published. However, a mathematical model of carbon arc reactor for fullerene synthesis had been developed by Bilodeau et al (1998). Using an 80 A current, they simulated the arc behaviour only at 1 mm and 4 mm inter-electrode gaps in Argon and Helium environment. Since, the reactor used in this study differs from that commonly used for producing CNTs as discussed in Chapter 3; a new plasma simulation is needed.

In general, the aim of this study is to model the interaction between the physical properties of the arc with the CNT formation in the continuous carbon arc reactor. The effect of the presence of small nanoparticles in front of the anode will also be considered in this model. Temperature profiles at different arc parameters such as inter –electrode gap will be simulated. The electromagnetic force and the fluid flow field will also be studied.

5.5.2 Mathematical model

When a standard carbon arc is not under the influence of external forces such as magnetic or convective force, it has a natural axis of symmetry. A two-dimensional model is adequate to describe the plasma system. This configuration is often used in the literature to study arc phenomena or to validate models (Lowke 1979; Hsu, Etemadi et al. 1983; Chabrerie, Devautour et al. 1992). In order to simplify the model, the following assumptions were made:

a) The plasma can be considered as fluid and the Navier-Stokes equations will be used to describe the plasma column. The electromagnetic equations will be added to estimate the electromagnetic properties of the arc.

b) The plasma is a Newtonian fluid and he flow is assumed to be laminar and stationary.

c) The arc is radially symmetric and the resulting equations are two-dimensional. The effects of gravity are neglected in this study. This assumption is commonly used in this type of configuration.

d) The arc is in a steady-state condition. This is achieved by continuously adjusted the cathode position throughout the operating period to maintain a constant inter-electrode gap.

e) The plasma is in local thermodynamic equilibrium (LTE) condition. This assumption enables one to assign unique temperature to any region of the plasma. This LTE may not be valid in regions where there are very steep temperature gradients; however, in most cases this approximation is acceptable.

f) The anode erosion rate is assumed to be uniform over the electrode surface. The value was found from the experiments described in Section 5.6.

g) Energy input in the arc comes from the ohmic heating and also from the enthalpy flux of the electrons

h) Carbon nanoparticles dominate the near electrode regions. Their presence causes a huge increase in the electrical conductivity of the system compared to that of a pure nitrogen gas-plasma system.

i) The electromagnetic force or Lorentz force is assumed to be generated by the interaction of induced magnetic field and current density.

General conservation equations can be written in general form as suggested by Patankar:

$$\vec{\nabla}.(\rho\vec{v}\ \Phi) = \vec{\nabla}.(\Gamma_{\Phi}\vec{\nabla}\Phi) + S_{\Phi} \qquad \text{(Eqn 5.7)}$$

where ρ is the fluid mass density, $\vec{v}$ the velocity vector, Γ_{Φ} the diffusion coefficient, S_{Φ} is the source term and Φ represents the scalar variables Φ that can be in the form of T, the temperature; u or v which are the components of velocity; or V which is the electric potential.

The governing equations are derived from both the Maxwell and Navier-Stokes equations. They can be divided into four sub-groups which are:

1) The equation used for conservation of mass:

$$\frac{1}{r}\frac{\partial}{\partial r}(\rho ru) + \frac{\partial}{\partial z}(\rho v) = 0 \qquad \text{(Eqn 5.8)}$$

2) The equation 5.9 defining the radial and axial momentum conservation:

$$\rho\left(u\frac{\partial v}{\partial z} + v\frac{\partial v}{\partial r}\right) = -\frac{\partial P}{\partial r} + \frac{2}{r}\frac{\partial}{\partial r}\left(\mu r\frac{\partial u}{\partial z}\right) + \frac{\partial}{\partial z}\left[\mu\left\{\frac{\partial u}{\partial r} + \frac{\partial v}{\partial z}\right\}\right] - \frac{2\mu v}{r^2} - j_z B_\theta \qquad \text{(Eqn 5.9)}$$

3) The energy conservation equation:

$$\rho C_p\left(u\frac{\partial T}{\partial r} + v\frac{\partial T}{\partial z}\right) = \frac{1}{r}\frac{\partial}{\partial r}\left(\lambda r\frac{\partial T}{\partial r}\right) + \frac{\partial}{\partial z}\left(\lambda\frac{\partial T}{\partial z}\right) - \frac{J_z^2 + J_r^2}{\sigma} - S_R + \frac{5}{2}\frac{k}{e}\left(J_z\frac{\partial T}{\partial z} + J_r\frac{\partial T}{\partial r}\right) \qquad \text{(Eqn 5.10)}$$

4) The electrical charge conservation equation:

$$\frac{1}{r}\frac{\partial}{\partial r}\left(r\sigma\frac{\partial V}{\partial r}\right)+\frac{\partial}{\partial z}\left(\sigma\frac{\partial V}{\partial z}\right)=0 \qquad \text{(Eqn 5.11)}$$

where B, B_θ, C_p, e and E denote magnetic flux vector, Azimuthal component of magnetic flux, specific heat of plasma at constant pressure, electronic charge and electric field, respectively.

Other notations such as J, J_r, J_z, k, P, S_R, T and T_0 dictate the current density, radial component of current density, axial component of current density, Boltzmann's constant, pressure, radiation heat loss per unit volume, plasma temperature and ambient temperature, respectively..

The symbols $u, \upsilon, r, z, \mu, \sigma, \lambda$ represent axial component of plasma velocity, radial component of plasma velocity, radial coordinate, axial coordinate, molecular viscosity, electrical conductivity of plasma and thermal conductivity of plasma.

5.5.3 Model geometry and boundary conditions

The model geometry and the boundary conditions of the system are schematically shown in Figure 5.14. The plasma was analyzed using a 2D axis-symmetrical model. The plasma is considered as nitrogen plasma since nitrogen was used as the buffer gas in the reactor. The cathode current density was determined based on the applied current in the arc and was one of the most important boundary conditions for the model.

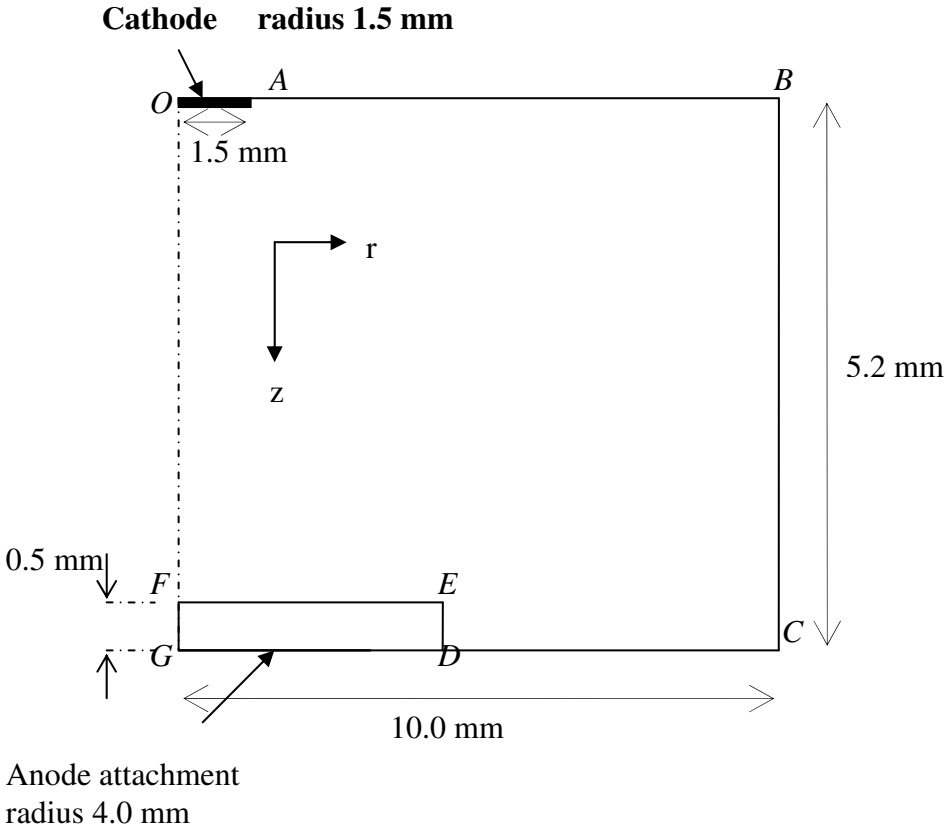

Figure 5.14 Low current arc geometry.

The boundary conditions at the edge of the numerical integration region are tabulated in Table 5.2.

Table 5.2 Boundary condition for the low current carbon arc.

Boundary	OA	AB	BC	CD	DE	EF	FG	GD	FO
u	$u = 0$	$\frac{\partial u}{\partial r} = 0$	$u = 0$	$u = 0$	Internal boundary		$\frac{\partial u}{\partial r} = 0$	$u = 1.11\ \mathrm{ms}^{-1}$	$\frac{\partial u}{\partial r} = 0$
ν	$\nu = 0$	$\nu = 0$	$\frac{\partial \nu}{\partial r} = 0$	$\nu = 0$			$\nu = 0$	$\nu = 0$	$\nu = 0$
T	3800 K	300 K	300 K	T			$\frac{\partial T}{\partial r} = 0$	3700 K	$\frac{\partial T}{\partial r} = 0$
P		$\frac{\partial P}{\partial r} = 0$	101.3 kPa	101.3 kPa			$\frac{\partial P}{\partial r} = 0$		$\frac{\partial P}{\partial r} = 0$

5.5.4 Application Modes

5.5.4.1 The Meridional induction current, vector potential application mode

The Meridional induction current, vector potential application mode for axially symmetry structure, with only currents present in the angular direction was chosen for modelling the electromagnetic properties of the plasma. A PDE for the angular component of the magnetic field can be derived. Taking into account the effects of using cylindrical coordinates for the rotational field, a formulation that differs slightly from the corresponding in-plane case is obtained.

The problem of electromagnetic analysis requires the solving of Maxwell's equations which are subjected to certain boundary conditions. The equations can be written in differential or integral form. For this simulation, the equations are presented in the differential form because Comsol Multiphysics software can handle only that form of equation.

For general time varying fields, the expressions involved are:

$$\nabla \times \mathbf{H} = \mathbf{J} + \frac{\partial \mathbf{D}}{\partial t} \qquad \text{(Eqn 5.12)}$$

$$\nabla \times \mathbf{E} = \frac{\partial \mathbf{B}}{\partial t} \qquad \text{(Eqn 5.13)}$$

$$\nabla . \mathbf{D} = \rho_e \qquad \text{(Eqn 5.14)}$$

$$\nabla . \mathbf{B} = 0 \qquad \text{(Eqn 5.15)}$$

where

E is the electric field intensity

D is the electric flux density

H is the magnetic field density

B is the magnetic flux density

J is the current density

ρ_e is the electric charge density

In the expressions, equations (5.12) and (5.13) are the Maxwell-Ampere's law and Faraday's law, respectively. The last two equations are in the forms of Gauss law in the electric and magnetic forms, respectively.

5.5.4.2 General Heat transfer module

The mathematical model for heat transfer by conduction is in the following version of the heat equation:

$$\delta_{ts}\rho\, C_p \frac{\partial T}{\partial t} + \nabla.(k\nabla T) = Q \qquad \text{(Eqn 5.16)}$$

in which the following material properties were used: δ_{ts} is a time-scaling coefficient, ρ is the density, C_p is the heat capacity, k is the thermal conductivity tensor and Q is the heat source.

5.5.4.3 Incompressible Navier-Stokes application mode

The Incompressible Navier-Stokes application mode was used to model the incompressible flow in fluids. The Navier-Stokes equations for fluid flow are described as follows:

$$\rho\frac{\partial \mathbf{u}}{\partial t} - \eta\nabla^2\mathbf{u} + \rho(\mathbf{u}.\nabla)\mathbf{u} + \nabla P = \mathbf{F}$$

$$\nabla.\mathbf{u} = 0 \qquad \text{(Eqn 5.17)}$$

where **u** is velocity field and **F** is any force that exists such as gravity**.**

These application modes are general enough to account for all types of incompressible flow. In practice, successful analysis of turbulent flows requires simplifications of the description of transport of momentum. However, in this study, the gravity effect is negligible and the plasma has a laminar flow.

5.5.5 Modelling strategy

The Lorentz force was calculated from the Meridional Induction current application mode. This Lorentz force was then used as a source term to solve for the momentum balance equation in the 2-D Navier-Stokes application mode. The calculated plasma velocity from this mode then coupled to the General Heat application mode, and used as a flow speed in the heat transfer field.

The heat generated by electrical resistance (ohmic heating) from the Meridional Induction current mode, will be used for solving energy balance in the General Heat Transfer application mode. This application mode was used to calculate the plasma temperature which individual temperature of the boundary conditions was set. Material properties such as density, viscosity, thermal and electrical conductivities must be treated as functions of temperature as discussed in Section 5.3. In this study, the anode is assumed to be a simple surface at the domain boundary where a temperature profile is imposed as a boundary condition as commonly used (Lowke 1979; Hsu, Etemadi et al. 1983).

As previously mentioned, the equilibrium electrical conductivity at plasma-electrode interfaces is very low *i.e*. at $T < 6000$ K. In real situations, the connection of the arc using either electrode is localised, so that the mechanism of electron generation can be more intense. Cathode surface emit electrons either thermionically or by secondary process so that the electrical conductivity at the electrode surface must be higher than the equilibrium value. Therefore, to ensure the continuity of current intensity between the two media, plasma and anode, we introduced a new approach. We will estimate the actual electrical conductivity in front of the anode surface by taking into account the presence of a cloud of nanoparticles in front of the anode as described earlier.

5.6 Measurement of boundary conditions

The boundary conditions that were measured include the flow of nitrogen that was flushed into the system and the anode surface temperature. The following sections detail the techniques used to measure these parameters which will be later used in the modelling simulations.

5.6.1 Nitrogen velocity on the anode surface

As mentioned in Section 4.3, the nitrogen gas is introduced through the anode cap. The diameter of the porous graphite is approximated to be 4 mm. The volumetric flow rate of the flushing gas (at room temperature) ranged from 0 to 0.6 L/min. Most of the time when the experiment was done, the nitrogen flow was kept between 0.2 to 0.3 L/min. The average value of 0.25 L/min will be used for the calculation. Using the ideal gas law, the nitrogen velocity at anode surface was calculated.

$$v_{N_2} = \frac{V_{N_2}\left(\frac{T_2}{T_1}\right)}{A_{anode}} \qquad \text{(Eqn 5.18)}$$

where V_{N_2} is the nitrogen flow at room temperature, T_1 In equation 5.18, T_2 is the anode surface temperature which is approximated at 3700 K from measurement and A_{anode} is the anode emission area. Detailed calculations on to determine A_{anode} is shown in Appendix B. Substituting the values found into equation 5.18 gives the nitrogen gas velocity

$$= \frac{2.5\times10^{-1}\,\frac{\text{L}}{\text{min}}\left(\frac{1.00\times10^{-3}\text{m}^3}{\text{L}}\right)\left(\frac{\text{min}}{60\text{s}}\right)\left(\frac{3700\text{K}}{300\text{K}}\right)}{4.61\times10^{-5}\text{m}^2}$$

$$= 1.11 \text{ m/s}$$

5.6.2 Anode surface temperature

From Section 4.2.1 it was found that the observed anode surface temperature changed as the gap was varied. The trend recorded is simplified in the following table.

Table 5.3 The trend of anode surface temperature with varying gap

Gap size (mm)	Average Temperature (K)
2.7 ± 0.2	3855.0 ± 50
3.7 ± 0.2	3747.0 ± 44
5.2 ± 0.2	3644.5 ± 50
7.7 + 0.2	3815.5 ± 74

5.6.3 Electrical conductivity of plasma in the anode layer

The plasma in this work was considered as a dusty plasma. The presence of nanoparticles in front of the anode surface is believed to have a huge effect on the electrical conductivity of the plasma. Hence the following section inculcates this assumption to determine the electrical conductivity of the plasma in this study.

5.6.3.1 Solid particle ionization

The thermal ionization of solid nanoparticles is of interest in connection with the study of formation of various nanoparticles such as carbon nanotubes, fullerenes and carbon onions. The electron microscopes indicate these particles are composed of various form of nanoparticles as discussed in Chapter 2. The general formula for the ionization of solid particles in a gas plasma was derived by Einbinder (1957), allowing also for multiple ionization.

When a solid particle in the plasma is ionized, the reaction that takes placed can be represented as

$$[N_{l-1}] \underset{\longleftarrow}{\overset{K_l(T)}{\longrightarrow}} [N_l] + [e] \qquad \text{(Eqn 5.19)}$$

If N_e is the number density of free electrons and N_l is the number density of solid particles that are ionized *l* times, then according to the principle of mass action, the ratio of the more-ionized particle to that of the less-ionized one can be calculated as follows:

$$\frac{N_l N_e}{N_{l-1}} = K_l(T) \qquad \text{(Eqn 5.20)}$$

in which $K_l(T)$ is the equilibrium constant for the above reaction. The equilibrium constant is also expresses as

$$K_l(T) = \frac{2(2\pi m_e k_B T)^{\frac{3}{2}}}{h^3} \exp(-\frac{\varphi_l}{k_B T}) \qquad \text{(Eqn 5.21)}$$

where

m_e is the electron mass [kg]

k_B is Boltzmann's constant $\left[1.380658\times10^{-23}\ \text{JK}^{-1}\right]$

h is Planck's constant $\left[6.626 \text{ x } 10^{-34}\ \text{m}^2\text{kg/s}\right]$

T is the absolute temperature [K]

φ_l is the energy required to completely remove an electron from a solid surface of an element (work function)

Based on Einbender's (1957) work, when the average ionization per particle is not too high $(\frac{N_e}{N} \le 4)$, the following equation can be used to express the ionization of these solid particles.

$$\frac{N_e}{N} = \frac{K}{N_e}\left\{\frac{1+2\frac{K}{N_e}e^{-\delta}+3\left(\frac{K}{N_e}\right)^2 e^{-3\delta}+4\left(\frac{K}{N_e}\right)^3 e^{-6\delta}+5\left(\frac{K}{N_e}\right)^4 e^{-10\delta}+....}{1+\frac{K}{N_e}+\left(\frac{K}{N_e}\right)^2 e^{-\delta}+\left(\frac{K}{N_e}\right)^3 e^{-3\delta}+\left(\frac{K}{N_e}\right)^4 e^{-6\delta}+\left(\frac{K}{N_e}\right)^5 e^{-10\delta}...}\right\}, \left(\frac{N_e}{N} \le 4\right)$$

(Eqn 5.22)

where

$$\delta = \frac{e^2}{4\pi\varepsilon_0 r k_B T} \qquad \text{(Eqn 5.23)}$$

The parameters used are chosen as follows and the pressure is assumed to be at atmospheric pressure (1 atm).

T	temperature	3800	K
e	electron	1.60×10^{-19}	C
r	sphere radius	1.50×10^{-9}	m
φ	graphite work function	4.6	eV
N	total number density of particle	7.43×10^{20}	m^{-3}
ε_0	permittivity of a vacuum	8.85×10^{-12}	$kg^{-1}m^{-3}s^4A^2$

The number density of particles was calculated based on the experimental results by estimating the anode erosion rate. The erosion rate was estimated using the image analysis software, Sigma scan Pro 5.0 as described in Appendix B.

For a 16 A arc current, using the woven carbon fibre, the erosion rate is found to be 180 μg/C. Therefore, the mass flux can be calculated.

$$\text{The mass flux} = I \times \text{erosion rate}$$

Taking a figure by assuming 80 % was ejected as particulate, the vapour mass flux can be determined.

$$\text{Vapour mass flux} = (0.8)\ (\text{mass flux})$$

Therefore,

$$\text{Volumetric flow rate} = \frac{\text{mass flux}}{\rho}$$

From the experimental image analysis in Appendix B, the emission area is 4.164×10^{-5} m^2.

$$\text{Velocity} = \frac{\text{volumetric rate}}{\text{emission area}}$$

Therefore, the mass flow of crystallite can be calculated;

$$\text{Mass flux} = \frac{\text{erosion rate}}{\text{emission area}}$$

By having the velocity and the mass flux of crystallite of 10 mm diameter of treated area, one can estimate the concentration of the crystallites close to the anode surface.

$$\text{Concentration} = \frac{\text{mass flux}}{\text{velocity}}$$

Assuming nanoparticles are 3 nm graphite spheres, the mass of a single particle is about 6×10^{-20} g. Therefore, the number density of the particle can be estimated.

Number of density is = concentration/particle mass

Detailed of this estimation can be found in Appendix C.

If the particle is assumed to be a sphere with a radius of 1.5×10^{-9} m and a temperature of 3800 K, the value δ can be found by plugging in the known parameters in equation 5.23. From this example, it is found that $\delta = 2.932$.

By substituting equation 5.20 into equation 5.21, the Saha equation 5.24 is formed and the value of *K* can be determined.

$$\frac{N_e^2}{N - N_e} = K = \frac{2(2\pi m_e k_B T)^{\frac{3}{2}}}{h^3} \exp(-\frac{\varphi_l}{k_B T}) \qquad \text{(Eqn 5.24)}$$

For the conditions outlined previously, the value of $\exp\left(-\frac{\varphi}{k_B T}\right) = 7.938\times10^{-7}$. Therefore, the value of *K* can be calculated,

$$K = \frac{2\left[2\pi(9.109\times10^{-31}\text{kg})(1.3806\times10^{-23}\ \text{J}/\text{K})(3800\text{K})\right]^{3/2}}{(6.6207\times10^{-34}\text{J.s})^3} \exp\left(-\frac{\varphi}{k_B T}\right)$$

and found to be equal to $8.973\times10^{20}\ \text{m}^{-3}$.

According to Einbinder (1957), if the temperature is sufficiently low that $N_e/N \le \frac{3}{2}$, a useful first approximation to calculate N_e is

$$N_{e1} = (KN)^{\frac{1}{2}} \qquad \text{(Eqn 5.25)}$$

$$= \left[(8.739\times10^{20})(1.502\times10^{21})\right]^{\frac{1}{2}}$$

$$= 1.161\times10^{21}\ \text{m}^{-3}$$

Substituting this N_e on the right-hand side of equation 5.22 gives a second approximation, N_{e2} as in equation 5.26.

$$N_{e2} = (KN)^{\frac{1}{2}} \left\{ \frac{1 + 2\frac{K}{N_{e1}} e^{-\delta} + 3\left(\frac{K}{N_{e1}}\right)^2 e^{-3\delta} + 4\left(\frac{K}{N_{e1}}\right)^3 e^{-6\delta} + 5\left(\frac{K}{N_{e1}}\right)^4 e^{-10\delta} + \ldots.}{1 + \frac{K}{N_{e1}} + \left(\frac{K}{N_{e1}}\right)^2 e^{-\delta} + \left(\frac{K}{N_{e1}}\right)^3 e^{-3\delta} + \left(\frac{K}{N_{e1}}\right)^4 e^{-6\delta} + \left(\frac{K}{N_{e1}}\right)^5 e^{-10\delta} \ldots} \right\}, \left(\frac{N_e}{N} \le \frac{3}{2}\right)$$

(Eqn 5.26)

$$= 8.992 \times 10^{20}\ \mathrm{m}^{-3}$$

Equation (5.22) is then solved iteratively and the final value of the number of electron density for the given conditions is $N_e = 8.398 \times 10^{20}\ \mathrm{m}^{-3}$.

Therefore the average ionization per particle, *Z*, for this case is found to be

$$Z = \frac{N_e}{N} = \frac{8.398 \times 10^{20}\ \mathrm{m}^{-3}}{1.502 \times 10^{21}\ \mathrm{m}^{-3}}$$

$$= 0.560$$

All of the calculated values obtained in this section will be used to calculate the electrical conductivity of the plasma closed to the anode surface. The detail description of this calculation is presented in the next section.

5.6.3.2 Electrical conductivity in a dusty plasma containing nanoparticles

In this calculation the method developed by Sodha (Sodha, Kaw et al. 1965) for determining the electrical conductivity of gases containing thermionically emitting dust suspension was used. In his paper, two graphs were presented in which the electron density and electron frequency due to the solid particle can be directly read for a range of relevant parameters. A straightforward expression for calculating electrical conductivity σ of a gas containing solid particles was given.

$$\sigma = \frac{e^2 N_e}{m_e(v_p + v_0)} \qquad \text{(Eqn 5.27)}$$

and

e is electronic charge

N_e is electron density

m_e is electronic mass

v_p is electron collision frequency due to solid particles and

Or

$$\frac{\sigma}{\sigma_0} = \frac{N_e N_s}{\Lambda_p + (N_0 / N)(r_0^2 / r^2)} \qquad \text{(Eqn 5.28)}$$

where

$$v_0 = \langle \upsilon Q_0 \rangle N_0 = N_0 (3k_B T / m_e)^{\frac{1}{2}} \pi r_0^2 \qquad \text{(Eqn 5.29)}$$

N_0 and Q_0 represent number density of neutral gas molecule and electron collision cross-section of electron with neutral gas molecules, respectively.

$$\sigma_0 = \frac{e^2}{\pi r^2 (N / N_s)(3 m_e k_B T)^{1/2}} \qquad \text{(Eqn 5.30)}$$

A corrected version of Sodha's work was given by Newby(1967) in which the above equations were reduced to

$$\sigma = \frac{e^2 N_e}{(3 m_e k_B T)^{1/2} \left(\frac{N \Lambda_p \pi r^2}{N_0 Q_0}\right)} \qquad \text{(Eqn 5.31)}$$

A revised version of Sodha's figure showing variation of Λ_p with $Z\delta$ at various F value is shown in Figure 5.15

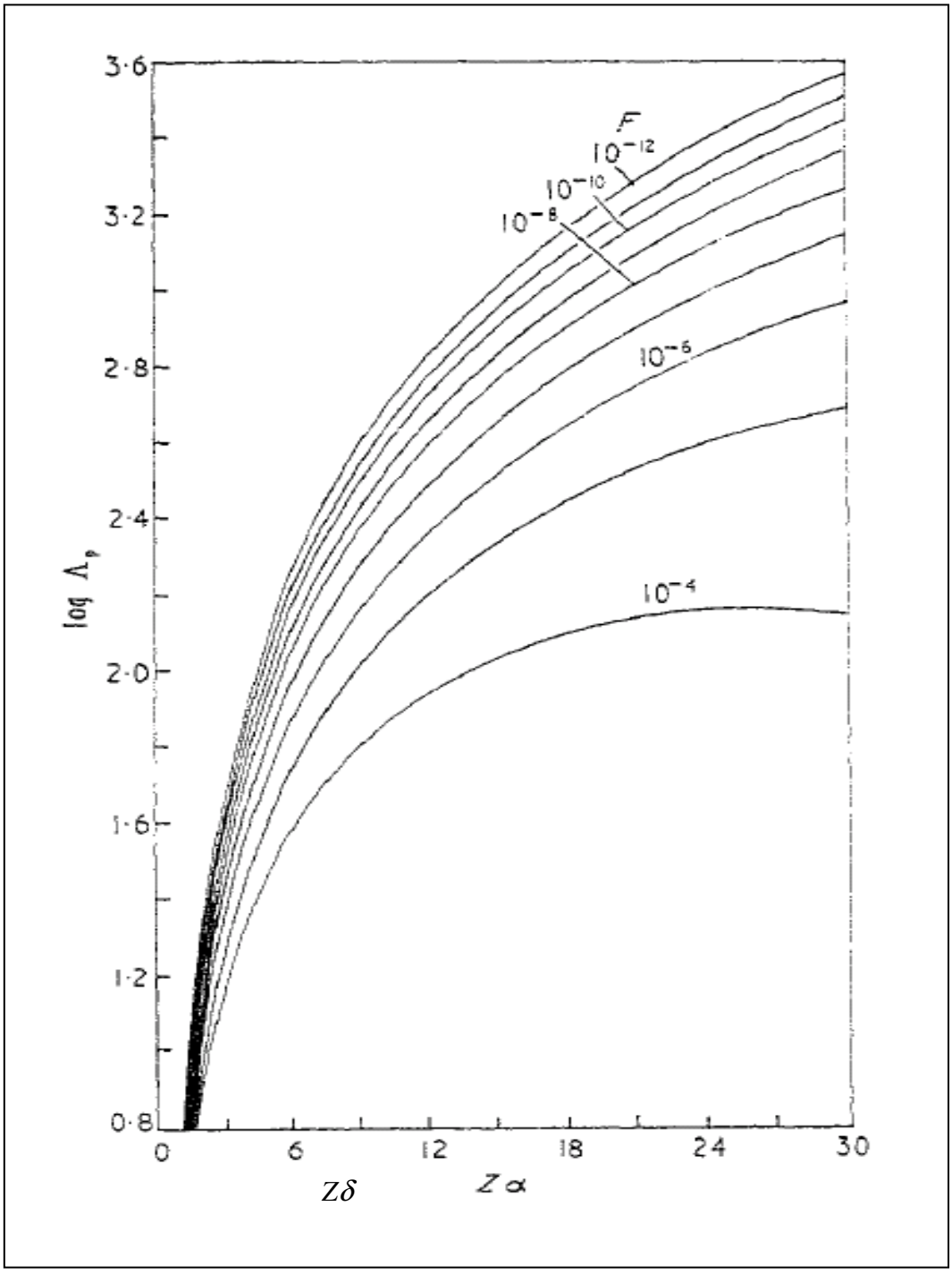

Figure 5.15 Variation of Λ_p with $Z\delta$ (from Newby (1967))

The electron collision frequency v_p due to solid particles (each carrying a charge $+Z_e$) is given by (Sodha, Kaw et al. 1965),

$$\Lambda = \left(\frac{8}{3\pi}\right)^{\frac{1}{2}} (1 + Z\delta) + \frac{4Z^2\delta^2}{9} \ln\left(\frac{\sin\frac{1}{2}x_1}{\sin\frac{1}{2}x_2}\right) \qquad \text{(Eqn 5.32)}$$

where

$$Z = \frac{N_e}{N} = 0.560$$

Therefore,

$$Z\delta = 0.560(2.932)$$

$$= 1.642$$

From Figure 5.15 for $Z\delta = 1.642$ and $F = \frac{4}{3}\pi r^3 N$ is the fraction of total volume occupied by the solid particles, which is $1.05 \times 10^{-5.}$

$$\log_{10} \Lambda_p = 0.8$$

and therefore $\Lambda_p = 6.310$

Using the ideal gas law, N_0 can be calculated,

$$N_0 = \frac{P}{k_B T} \qquad \text{(Eqn 5.33)}$$

$$= \frac{10132 \ \frac{\text{kg}}{\text{m.s}^2}}{(1.3806\times10^{-23} \frac{\text{kg.m}^2\text{s}^{-2}}{\text{K}})(3800 \text{ K})}$$

$$= 1.835 \times 10^{23} \text{ m}^{-3}$$

The electron collision cross-section of electron with neutral gas molecules Q_0 is taken from Michelina *et al* (Michelina, Oliveiraa et al. 2005), which is a cross section for electron-C_2 collision. The value of Q_0 is 4×10^{-20} m^{-3}.

Therefore, the lower bracket of equation (5.32)

$$\frac{N\Lambda_p \pi r^2}{N_0 Q_0} = \frac{(7.43\times10^{20})(6.31)(\pi)(1.5\times10^{-9})^2}{(1.835\times10^{23})(4.0\times10^{-20})}$$

$$= 8.672$$

and the electrical conductivity is,

$$\sigma = \frac{(1.60\times10^{-19}\ \text{A.s})^2(8.398\times10^{20}\ \text{m}^{-3})}{\left[3(9.11\times10^{-31}\ \text{kg})(1.38\times10^{-23}\ \frac{\text{kg.m}^2}{\text{s}^2\text{K}})(3800\ \text{K})\right]^{1/2}(8.672)}$$

$$= 6.565 \times 10^6\ \text{A/V.m}$$

The electrical conductivities at different anode surface temperatures are then calculated and shown in Table 5.4.

Table 5.4 Effect of anode surface temperature on the plasma conductivity at near anode plasma region.

Anode surface temperature, T_s (K)	Electrical conductivity, σ (A/V.m)
3000	2.833×10^6
3400	3.386×10^6
3800	5.760×10^6
4000	1.209×10^7

5.7 Results

The arc plasma producing CNT was successfully simulated using Comsol Multiphysics 3.2. The results of this simulation were analysed and all data were extracted using post processing mode of Comsol Multiphysics. This mode was used to create post processing images and plots for obtaining visual and quantitative information.

Table 5.5 gives the list of simulation conditions used, with different boundary conditions.

Table 5.5 Simulation details

Case No.	Anode surface Temperature, T_s (K)	Anode flushing/N_2 velocity (m/s)	Cathode surface temperature (K)	I/E gap (mm)
Case A	3700	1.0	3800	5.2
Case B	3000	1.0	3800	5.2
Case C	Ts=f(r)	1.0	3800	5.2
Case D	3700	2.5	3800	5.2
Case E	3700	0	3800	5.2
Case F	3900	1.0	3800	2.7
Case G	3800	1.0	3800	7.7

In most cases, the anode surface temperature was considered as a constant temperature. This data were taken from the experimental results. For Case C the anode surface temperature was taken based on the temperature profile obtained from the image analysis. For Case A to E, the inter electrodes gap was taken as 5.2 mm, which is the gap where CNTs were abundantly produced. To find whether the nitrogen flushing from the anode has a significant effect, this effect was simulated in case D and E, for highest and lowest flow, respectively. Lastly, the effect of inter-electrode gap on the arc characteristic was studied by simulating Case F and Case G.

5.7.1 Surface mesh

Meshing of the CFD model chooses those volumes where spatial discretisation takes place. In Comsol Multiphysics it is possible to optimize the mesh locally for each part or model subdomain, through the interactive meshing environment. This makes it possible to build a mesh in an incremental fashion where each meshing operation acts on a set of subdomains. For example, users can start by creating a boundary mesh and then mesh each subdomain sequentially. Furthermore, using interactive meshing they can apply different meshing techniques to different domains of a geometry object. The interactive meshing feature does not require a nodal match on the boundaries between the different subdomains; instead connection occurs through the mathematics of the numerical scheme.

Figure 5.16 gives the mesh of the CAD model. A total of 4783 elements were created. The finer mesh can be seen closed to the surface of the electrodes. Similar dense mesh is observed in the centre of the plasma.

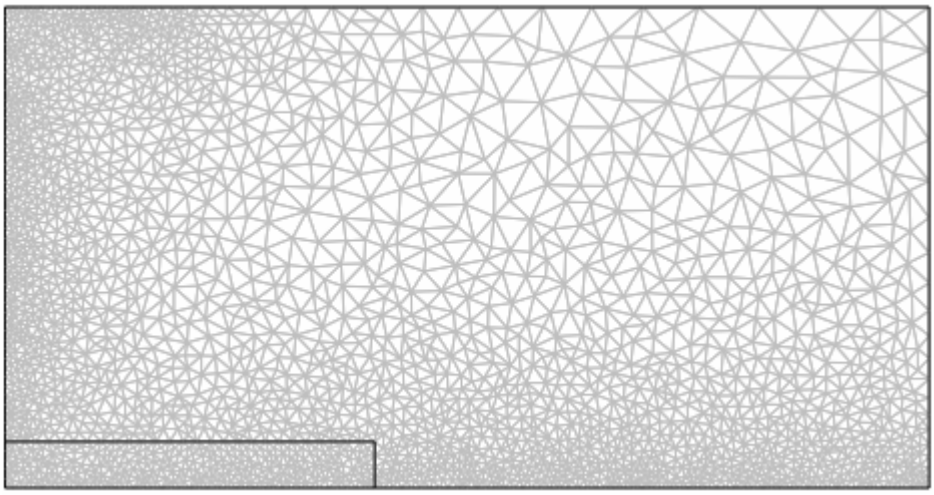

Figure 5.16 Surface mesh of carbon arc plasma

5.7.2 Analysis of the variables

The CFD simulation was plotted against the variables that directly involved. These variables were projected on two-dimensional planes, with different colours indicating the change of the variables involved. Surface plot and arrow plot were merged on to a single plane to get the clear indication of the flow patterns. Parameters plot is a collection of parameters that are plotted to show the magnitude of a variable over a collection of defined points.

In the present work, emphasis is given to the study of plasma temperature and the velocity profile in the arc model. The main region of interest is the subdomain area closed to the anode, which is the area where CNTs are observed to grow.

During the initial stage the model was solved without considering the presence of nanoparticles in front of the anode layer. However, the model was not stable and a solution could not be reached. In order to reach a solution, a fixed value of electrical conductivity, 100 A/V.m2 was used in the near anode region. This value is very much higher compared to the electrical conductivity in pure nitrogen plasma at the same temperature. (For example at 3800 K, the electrical conductivity of pure nitrogen plasma is 5.5961 x 10-4 A/V.m). Figure 5.17 shows the temperature profile of the arc.

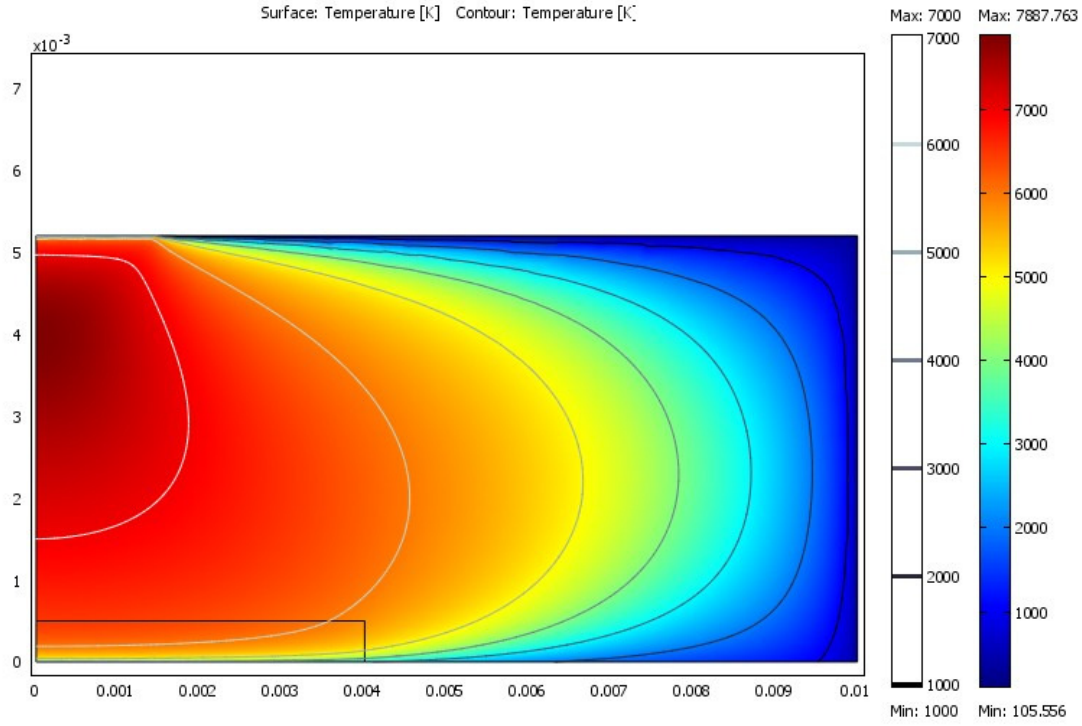

Figure 5.17 Temperature profile for arc plasma at 16 A current. The electrical conductivity of the plasma near to the anode surface is fixed at 100 A/V.m.

5.7.3 Effect of nanoparticles on plasma temperature

As discussed earlier in section 5.6.3, the calculated values for electrical conductivities with carbon nanoparticles included near the anode were then used in order to get a stable solution for the model. These values were taken from Table 5.4. For Case A, the anode surface temperature is taken as 3700 K and the plasma electrical conductivity of 1.567×10^6 A/V.m, as estimated for dusty plasma was used as an input (see section 5.6.3.2). The results of the temperature and the velocity profile in the arc region are illustrated in Figure 5.18 and Figure 5.19, respectively.

The plasma spread out in the radial direction near to the anode surface. The predicted temperature reached the maximum value of 8503 K in the centre of the plasma. Close to the anode surface, we can observe flattened temperature isotherms due to the value of the temperature imposed as a boundary condition at the anode surface. The shape of the plasma from the simulation is also similar to the experimental plasma picture observed through a filter for example in Figure 4.21.

Figure 5.19 shows the predicted flow field in the plasma for 16 A arc current. The high velocity region is shown in the middle of the plasma and shows the pumping action from the cathode like a normal arc welding plasma even though there is no gas flow through the cathode. Plasma flows from the cathode tip to the anode surface along the plasma centre line. The maximum velocity is 4.4 m/s. The simulation also shows that the cathode jet formed is spread outwards after collision with the anode surface and part of it re-circulates back to the centre of the plasma. In this model, the effect of the turbulence can be neglected since the Reynolds number is lower than 200.

We also found that there is no significant contrast between the "gas-only" model (Figure 5.17) and the dusty plasma model (Figure 5.18). The reason is in the "gas-only" model, a fixed value of electrical conductivity was used i.e. ~ 100 A/V.m. This value is very much higher than the electrical conductivity in pure nitrogen plasma at the same temperature. (For example at 3800 K, the electrical conductivity of pure nitrogen plasma is 5.5961×10^{-4} A/V.m). Therefore, Figure 5.17 cannot represent the "gas-only" model. In order to achieve the true gas-only model a very fine mesh must be generated in the near-cathodes region and that is the limiting factor for our simulation software. Attempts to find a solution using the existing mesh and the gas conductivity failed i.e. no stable solution was found.

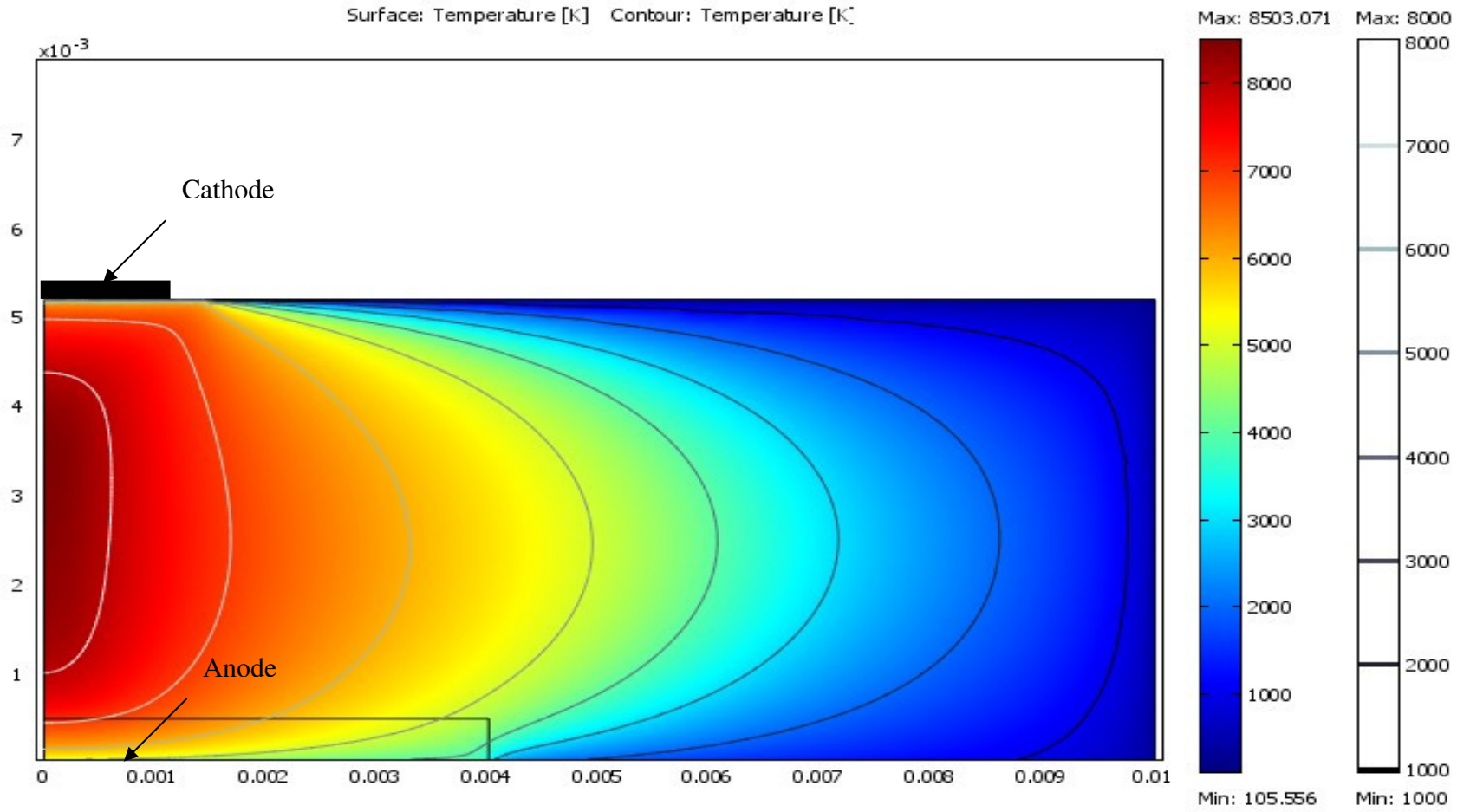

Figure 5.18 Temperature isotherm for 16 A arc at optimum inter-electrode gap

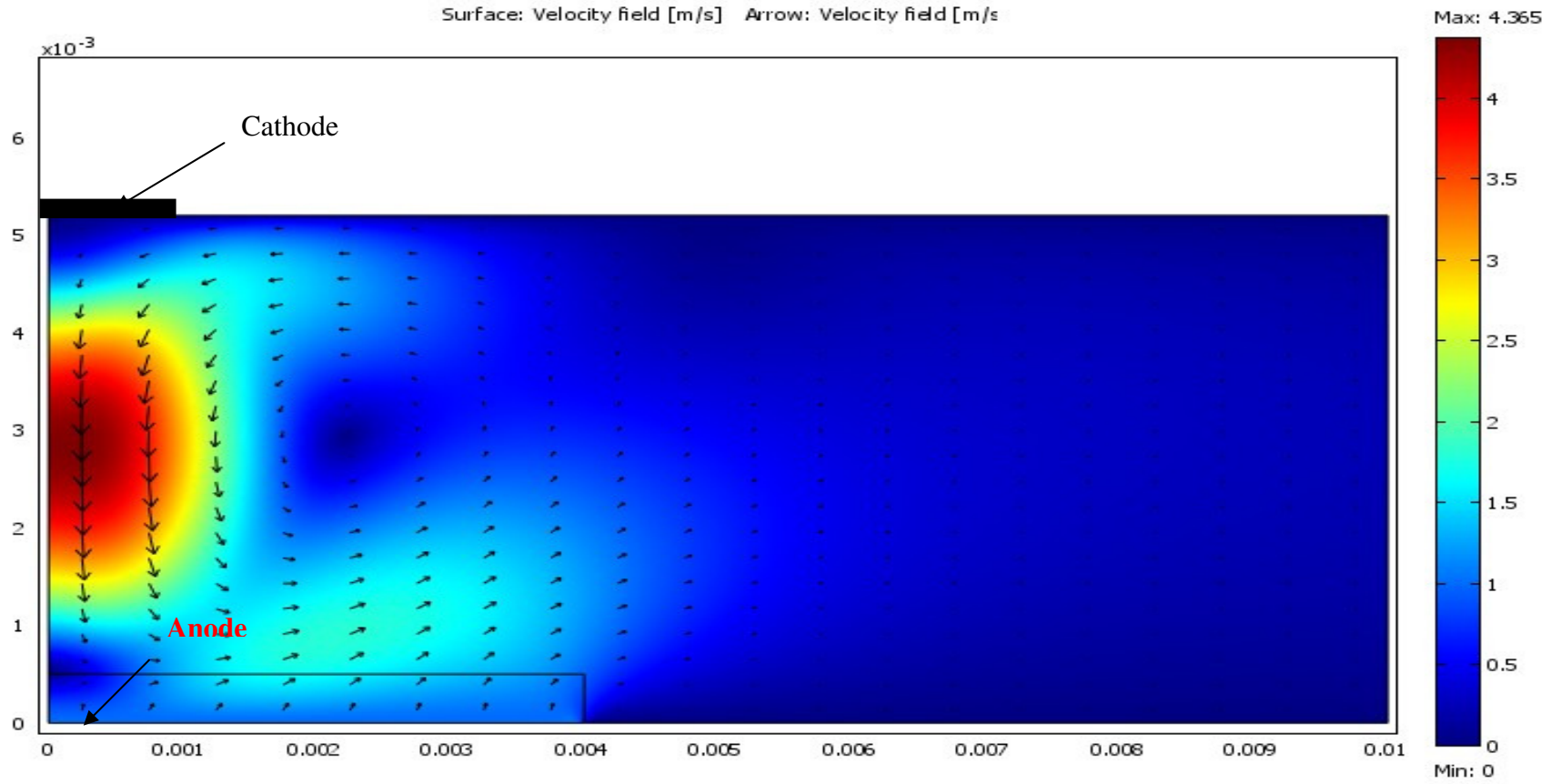

Figure 5.19 Velocity profile for 16 A at optimum inter-electrode gap (5.2 mm)

5.7.4 Effect of anode surface temperature

The effect of anode surface temperature on the plasma temperature was also studied by simulating Case B and Case C. Anode surface temperature was fixed at 3000 K for Case B whereas in Case C, anode surface temperature was based on the temperature profile taken from the experimental work (see Chapter 3). The temperature isotherms for Case B and Case C are shown in Figure 5.20.

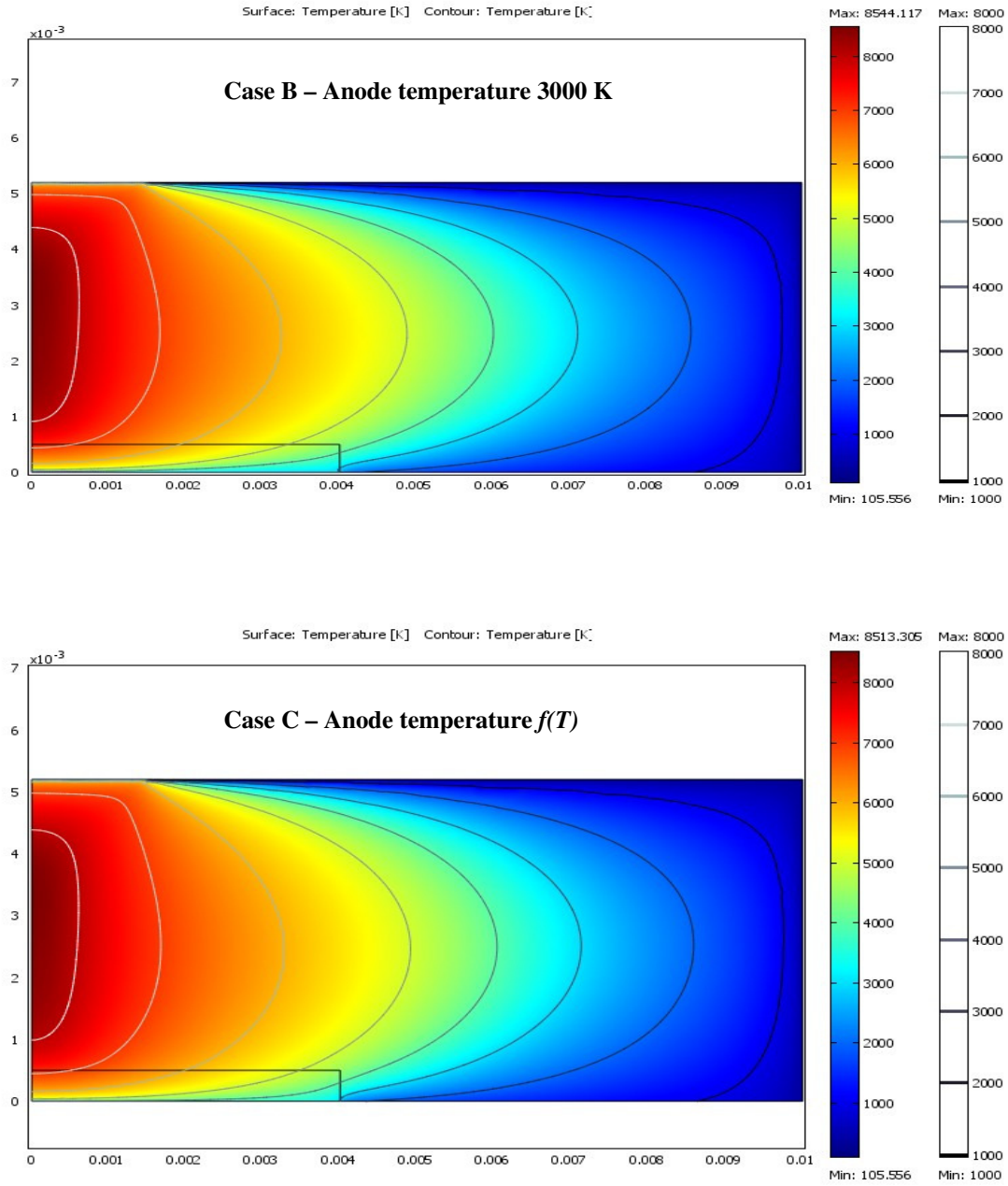

Figure 5.20 Temperature isotherms of the 16 A arc plasma in Case B and Case C

5.7.5 Effect of Nitrogen flushing

The effect of nitrogen flow or anode flushing velocities was also studied in this simulation and was presented in Case D (maximum flow) and Case E (no flow). From the experimental observation, if the nitrogen flow is higher than 0.6 L/min, which is equivalent to 2.5 m / s, the plasma become unstable. Similarly, in this simulation, for a flush velocity higher than 2.5 m / s, the model cannot be solved. The results of plasma temperature at two the different anode flushing rates are shown in

Figure 5.21. From this simulation, it was found that the plasma expansion was influence by anode flushing rate. At the maximum nitrogen flow, the arc plasma expands up to 6.5 mm in the radial direction compared to the plasma with zero nitrogen flow, *i.e*. 5.5 mm from the centre of the arc.

The velocity profiles for both cases are shown in Figure 5.22. At the maximum anode flow, the plasma flows from the cathode are pushed away by the nitrogen gas flowing from the anode surface and part of it moves out of the plasma. Only small part of the plasma then is re-circulated back into the centre of the arc. At low nitrogen flow, the plasma tends to re-circulate strongly as shown in Figure 5.22(b).

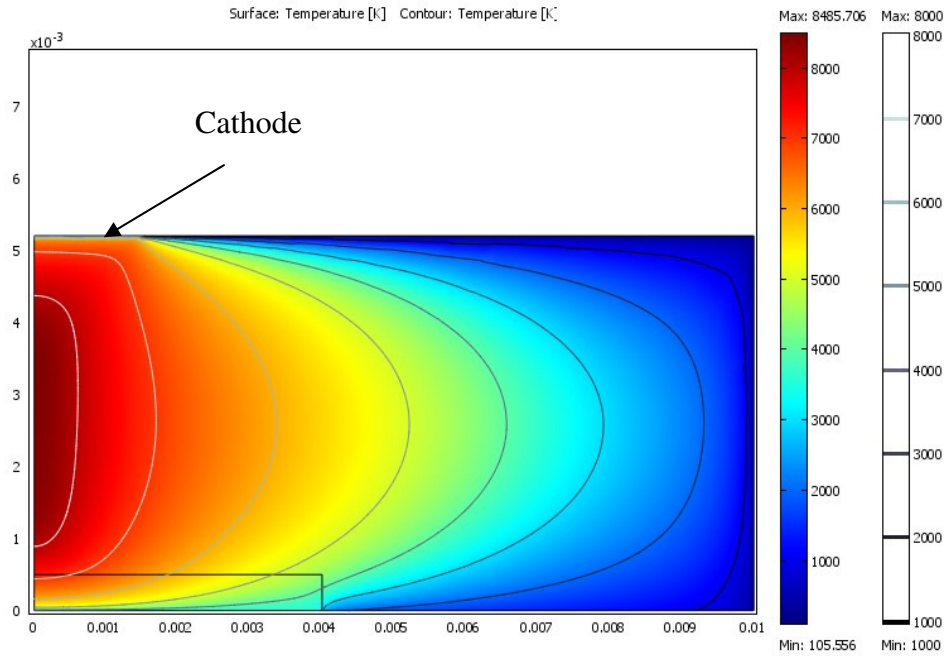

a) Case D (maximum flow)

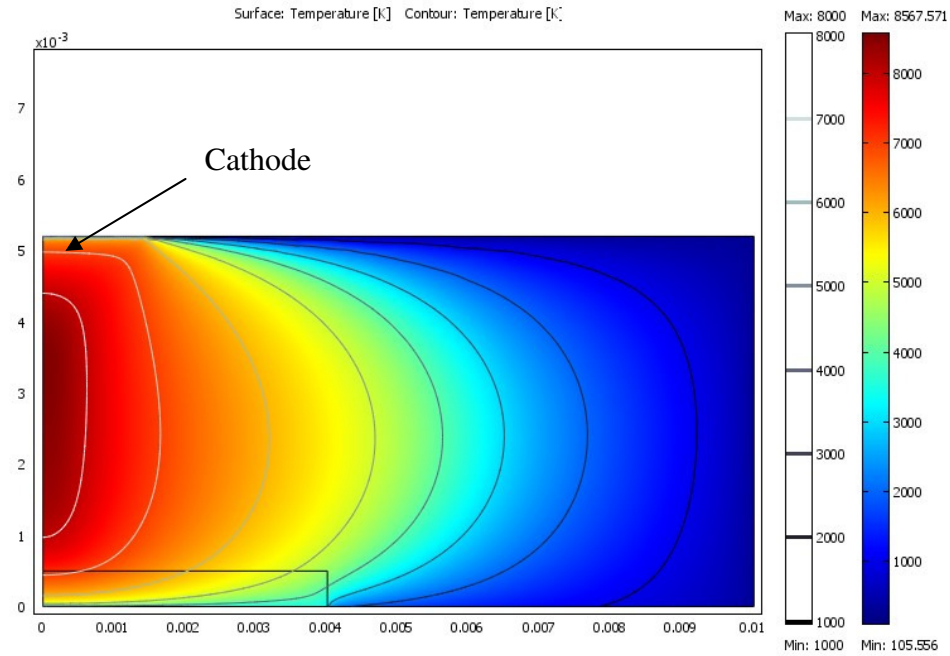

b) Case E (no flow)

Figure 5.21 Temperature isotherms of the plasma a) with maximum nitrogen velocity~2.5 m / s, b) without nitrogen flow from the anode

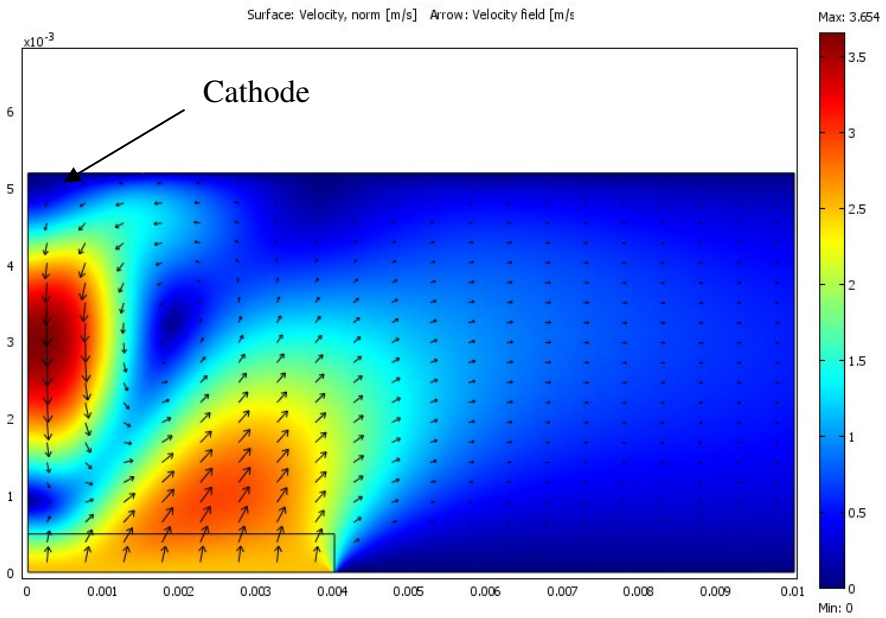

a) Case D (maximum flow)

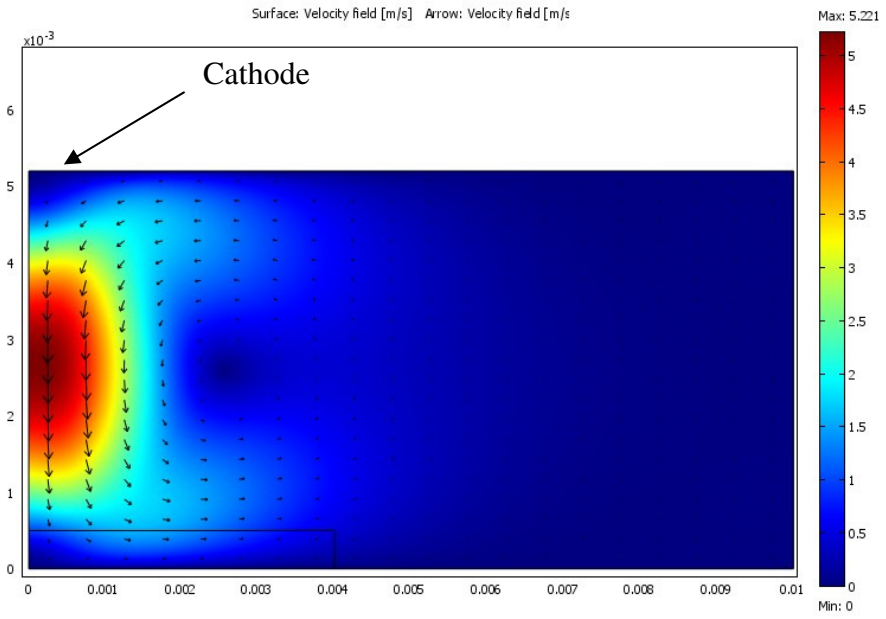

b) Case E (no flow)

Figure 5.22 Velocity field in the plasma, a) with maximum nitrogen velocity ~ 2.5 m / s, b) without nitrogen flow from the anode

5.7.6 Effect of inter-electrode gap

The effect of inter-electrode gap on the plasma temperature is studied by simulating Case F and Case G which represent the largest and the shortest gap. At the largest gap, the hottest region (T>8000 K) reaches 2 mm radius as shown in Figure 5.23, which is bigger than the hottest region at optimum inter-electrode gap, which is normally less than 1 mm radius. Another interesting result is that the 6000 K isotherm line is very much closer to the anode surface compared with that of the plasma at optimum gap. Figure 5.24 shows the effect on the temperature profile when the inter-electrode gap is reduced to 2.7 mm. In this case, the hottest region become smaller and the plasma temperature at the centre of the arc reached 9000 K (hotter than at largest gap). The 6000 K isotherm line is also closer to the anode surface.

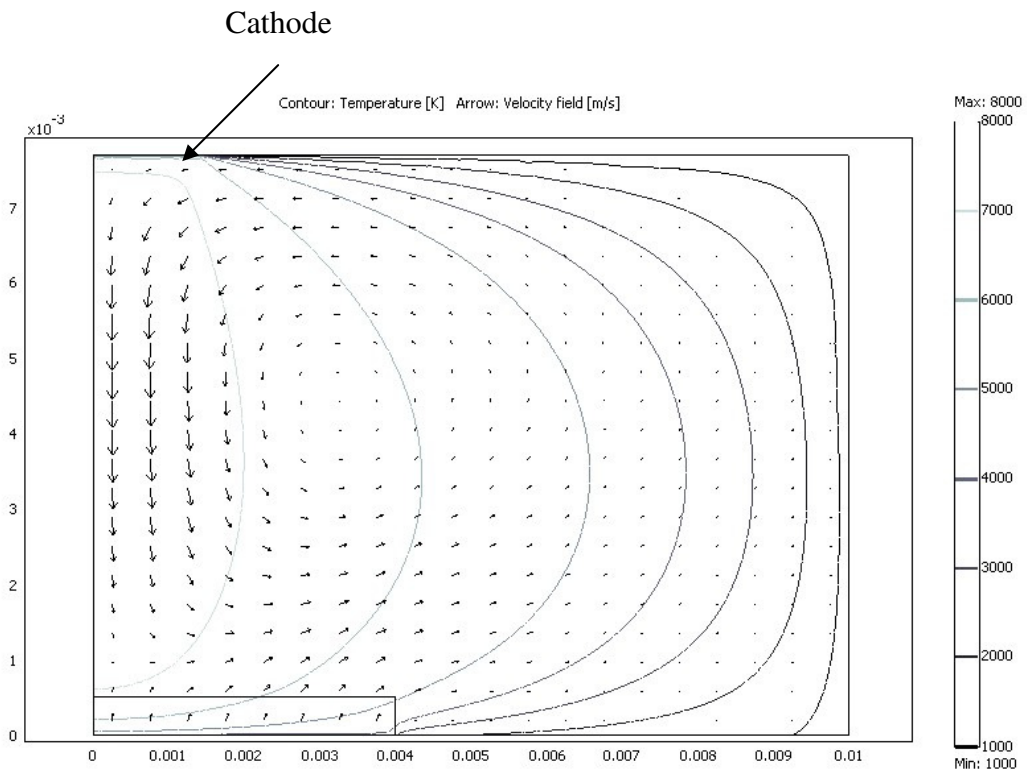

Figure 5.23 Temperature and velocity profile of arc plasma at 16 A and 7.7 mm inter-electrode gap (Case F)

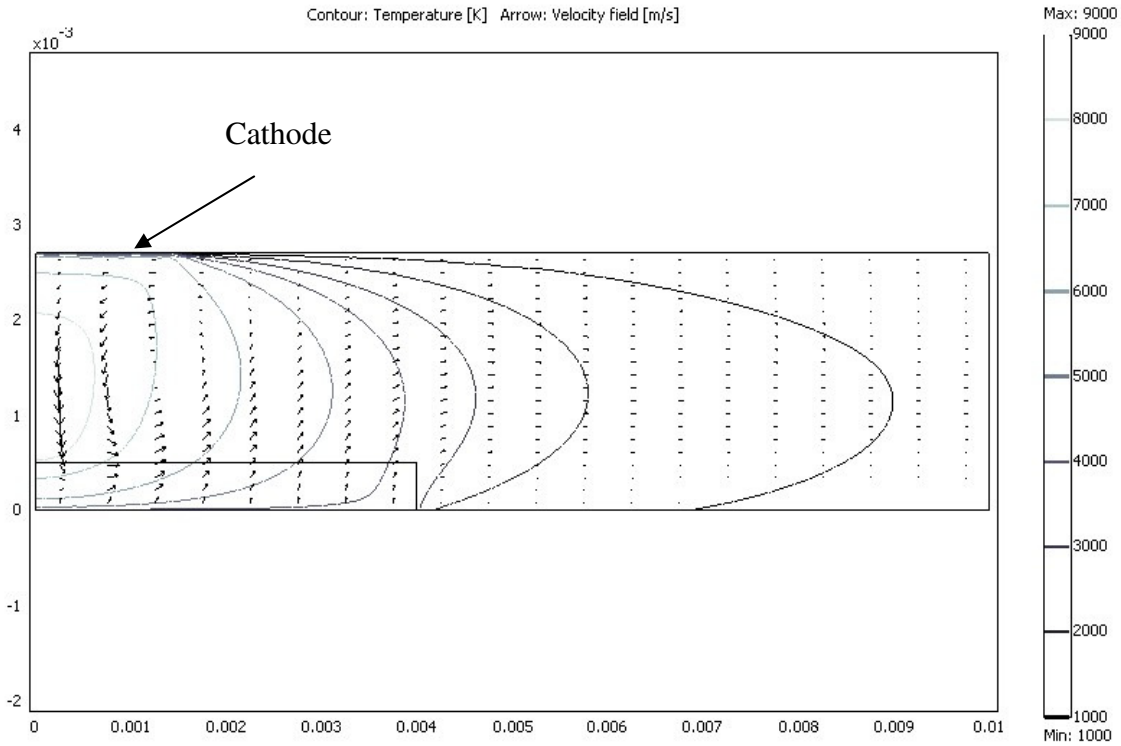

Figure 5.24 Temperature and velocity profile of arc plasma at 16 A and 2.7 mm inter-electrode gap (Case G).

5.8 Reliability of the model

This model was formulated under specific conditions as describe earlier in Section 5.5.2, in which the buoyancy effect, carbon vapour composition, graphene concentration and the existence of protruding CNTs on the anode/cathode surface were assumed negligible. In reality, the buoyancy effect is important in this model. It has been shown that the upward motion of the carbon tape will create unsymmetrical arc attachment because the adhesion and buoyancy force acting on the same direction (Querrioux 2004). Carbon composition and graphene concentration in the plasma are also important parameters when modelling the arc. Any introduction of carbon vapour will alter the fluid properties hence the temperature and velocity profiles in the plasma. The presence of CNTs on the cathode surface is another factor need to be considered when modelling this arc. These CNTs, protruding from the surface have a great impact on the generating electric field in the CNTs formation zone (Bao, Zhang et al. 2007; Shastry 2007). Unfortunately, due to time constraint and the limitation of the CFD software those parameters were not included in our model.

However, based on the results we are certain that this model is adequate enough to represent the carbon arc plasma. The model is useful as a groundwork for understanding the plasma behaviour of the arc producing carbon nanotubes. It solves for temperature and velocity profiles in a steady state 2-Dimensional profile and incorporates temperature-dependent plasma properties.

5.9 References

Abrahamson, J. (1974). "Graphite Sublimation Temperatures, Carbon Arcs and Crystallite Erosion." Carbon **12**(2): 111.

Bao, Q., H. Zhang, et al. (2007). "Simulation for growth of multi-walled carbon nanotubes in electric field." Computational Materials Science **39**(3): 616-626.

Beilis (2001). "State of the theory of vacuum arcs." IEEE Trans. Plasma Scie **29**(5): 657-670.

Beilis (2006). "Kinetics of Plasma Particles and Electron Transport in the Current-Carrying Plasma Adjacent to an Evaporating and Electron Emitting Wall." Trans. Plasma Scie **34**(3): 855-866.

Bilodeau, J. F., J. Pousse, et al. (1998). "A mathematical model of the carbon arc reactor for fullerene synthesis." Plasma Chemistry and Plasma Processing **18**(2): 285-303.

Boulos, M., I. Fauchais, et al. (1994). Thermal plasmas: Fundamentals and Applications, Plenum Publishing Corporation.

Chabrerie, J. P., J. Devautour, et al. (1992). "A Numerical Model for Thermal Process in an Electrode Submitted to an Arc in Air and its Experimental Verification." IEEE: 65-70.

Chaney, N. K., V. C. Hamister, et al. (1936). "The properties of Carbon at the Arc Temperature." Transaction of the Electrochemical Society: 107-150.

Davis, W. and H. C. Miller (1969). "Analysis of electrode products vacuum arcs " J .Appl. Phys **40**(1969): 3074.

Einbinder, H. (1957). "Generalized Equation for the Ionization of Solid Particles." The Journal of Chemical Physics **26**(4): 948-953.

Gleizes, A., J. J. Gonzalez, et al. (2005). "Thermal plasma modelling." J. Phys. D : Appl. Phys **38**: R153-R183.

Hsu, K. C., K. Etemadi, et al. (1983). "Study of the free-burning high-intensity argon arc." Journal of Appl. Phys. **54**(3): 1293-1301.

Hsu, K. C. and E. Pfender (1983). "Two-temperature modelling of the free-burning, high-intensity arc." Journal of Appl. Phys. **54**(8): 4359-4366.

Lago, F., J. J. Gonzalez, et al. (2004). "A numerical modelling in an electric arc and its interaction with the anode: Part I. The two-dimensional model." J. Phys. D : Appl. Phys **37**: 883-897.

Lowke, J. J. (1979). "Calculated properties of vertical arcs stabilized by natural convection." J .Appl. Phys **50**(1): 147-157.

Lowke, J. J. (1979). "Simple theory of free-burning arcs." J.Phys. D : Appl. Phys **12**: 1873-1886.

Michelina, S. E., H. L. Oliveiraa, et al. (2005). "Cross sections for electron–C_2 collisions." Chemical Physics **309**(2-3): 177-182.

Murooka, Y. and K. R. Hearne (1972). "Measurement of Arc Electrode Temperatures and Reignition Characteristics." Journal of Appl. Phys. **43**(6): 2656-2663.

Newby, D. (1967). "Comments on the paper 'Conductivity of dust-laden gases'." Brit. J. Appl. Phys **18**: 383-384.

Querrioux, T. (2004). Carbon Nanotube Continuos Production. Chemical and Process Engineering, University of Canterbury. **Master of Chemical and Process Engineering**.

Raizer, Y. P. (1997). Gas Discharge Physics, Springer.

Shastry, R. K. (2007). Continuous Deposition of Carbon Nanotubes in an Arc-reactor and their Application in Field Emission Devices. Chemical and Process Engineering. Christchurch, New Zealand, University of Canterbury. **Doctor of Philosopy in Chemical Engineering**.

Sodha, M. S., P. K. Kaw, et al. (1965). "Conductivity of dust-laden gases." Brit. J. Appl. Phys **16**: 721-723.

Ushio, M. (1988). "Arc discharge and electrode phenomena." Pure & Appl. Chem. **60**(5): 809-814.

Walters, D. A., L. M. Ericson, et al. (1999). "Elastic strain of freely suspended single-wall carbon nanotube ropes." Appl. Phys. Letter **74**: 3803-3805.

Wendelstorf, J. (2000). Ab initio modelling of thermal plasma gas discharges (electric ars), Universitat Carolo-Wilhelmina. **PhD**.

Zhu, S. L. and A. v. Engel (1982). "Fall region and electrode effects in atmospheric arcs of vanishing length " J Phys D: Appl. Phys. **4**: 2225-2235.

Chapter 6 : Discussion 6-1
6.1 Dusty plasma in carbon arc 6-1
6.2 Overall observation 6-2
6.2.1 Effect of inter-electrode gap 6-3
6.2.2 Effect of arc current 6-6
6.2.3 Effect of nitrogen flushing 6-7
6.2.4 Effect of substrate speed 6-9
6.2.5 Effect of background gases 6-11
6.3 Growth mechanisms of multiwalled NT by arc-evaporation 6-14
6.4 References 6-22

Chapter 6: Discussion

6.1 Dusty plasma in carbon arc

The plasma in this work was considered as dusty plasma. The presence of nanoparticles in front of the anode surface is believed to have a huge effect on the electrical conductivity of the plasma. Abrahamson(1974) in his review, recognized that the presence of small particles will cause an error in the surface temperature measurement using an optical pyrometer. These particles could emit radiation and absorb some of the radiation from the graphite surface as well. Therefore as the cloud of these particles builds up in the front of the graphite surface, less radiation or lower black body temperature would be observed (Treekrem 1968; Abrahamson 1974). He also suggests that the major fraction of the crystallites ejected from the graphite surface is less than 5 nm in size.

During the initial stage, the carbon arc model was solved without considering the presence of nanoparticles in front of the anode layer. At this stage we were experiencing some difficulties in modelling the arc close to anode using only gas conductivity. The model was not stable and a solution could not be reached. In order to reach a solution, a fixed value of electrical conductivity, 100 $A/V.m^2$ was used in the near anode region. This value is very much higher compared to the electrical conductivity in pure nitrogen plasma at the same temperature. (For example at 3800 K, the electrical conductivity of pure nitrogen plasma is 5.5961×10^{-4} A/V.m). Figure 5.17 shows the temperature profile of the arc. However, this result is not consistent with experimental data (which did not produce bell shape plasma as observed by high-speed camera). Therefore, the gas only assumption must be faulty.

As previously mentioned, the equilibrium electrical conductivity at plasma-electrode interfaces is very low *i.e.* at $T < 6000$ K. In real situations, the connection of the arc using either electrode is localised, so that the mechanism of electron generation can be more intense. Cathode surface emit electrons either thermionically or by secondary process so that the electrical conductivity at the electrode surface must be higher than the equilibrium value. Therefore, to ensure the continuity of current intensity between the two media, plasma and anode, we introduced a new approach. We assumed these nano-particles cloud act as charge carrier for the current continuity in this arc.

We then estimated the actual electrical conductivity in front of the anode surface by taking into account the presence of a cloud of nanoparticles in front of the anode as describe earlier in Chapter 5. The electrical conductivities values at different anode surface temperatures are then calculated and shown in Table 5.4. This conductivity of suspension of carbon nano-crystallites (applied in 2 mm region near the anode surface) was adequate enough to allow a stable solution for the model. The arc plasma producing CNT was then successfully simulated using Comsol Multiphysics 3.2. The results of this simulation were analysed and all data were extracted using post processing mode of Comsol Multiphysics.

6.2 Overall observation

A general overview of the continuous arc process is given in this chapter. The experimental results are summarized in Figures 6.1 -6.4 in order to understand the relationship between independent arc variables such as inter-electrode gap, substrate speed, cathode diameter, anodic flushing and background gas. The dependent arc variables such as anode surface temperature and arc stability are also incorporated in the evaluation of the effect of arc parameters on the CNTs growth in this continuous reactor.

The structures of the fine fibers produced on the surface of the carbon tape (seen in SEM images) show similar characteristics with CNTs normally produced by arc-discharge method. These structures normally are MWNTs which usually confirmed by examine them using Transmission Electron Microscope. SWNTs may present in the deposited if metal catalyst is used in the process. Throughout this study, SEM is the only method used to characterize the fine structures found on the substrate. Therefore, other evidences are needed in order to support that those fine structures are MWNTs.

The impurities in the electrodes and carbon tape may contribute to the catalytic growth in the arc-discharge and produced SWNTs. Since, the graphite electrodes used are 99.99 % pure (impurities < 6 ppm) and the carbon substrate is 99.9 % this possibility can be ruled out. In addition, the substrate used is RAYON based carbon-fibre which the major impurity is normally sulfur (Lieberman and Noles 1972). Sulfur containing compounds have been successfully used to improve SWNTs yield in the solar method. However, if the sulfur is used without mixing with metal, SWNTs will never be produced. High concentration of sulfur may poison the catalyst particle and impede the SWNTs formation (Laplaze, Alvarez et al. 2002). In addition, Kim et al (Kim, Cota-Sanchez et al.

2007) also reported that too high sulfur content is not favourable for SWNTs production. In their work, they used a RF plasma torch to produce SWNTs from carbon black.

6.2.1 Effect of inter-electrode gap

Figure 6.1 shows the arc characteristic and deposition type at two different arc conditions, i.e. ~ at 16 A arc current and 20 A arc current. It shows that an inter-electrode gap strongly influenced the arc characteristic and the anode surface temperature and hence the formation of carbon nanotubes.

It was found that the substrate surface temperature (anode surface temperature) changed as the inter-electrode gap changed as shown in Figure 4.3. The minimum temperature at around 3650 K appeared to be associated with rapid NT formation. As mentioned earlier in Section 4.3.2, when the inter-electrode gap was 5.2 $\pm$ 0.2 mm, which corresponded to the lowest surface temperature, the CNTs produced were abundant. In contrast, at a very narrow gap *i.e.* 2.7 $\pm$ 0.2 mm, the substrate surface temperature was found to be significantly higher ~ 3855.0 $\pm$ 50 K. Although few NT were obtained at this narrow gap, nanoparticles were observed, with nanorods beneath them. A short arc causes an increase in heat load on the cathode with an increase in number density and averaged size of emitted particles (Kandah and Meunier 1995).

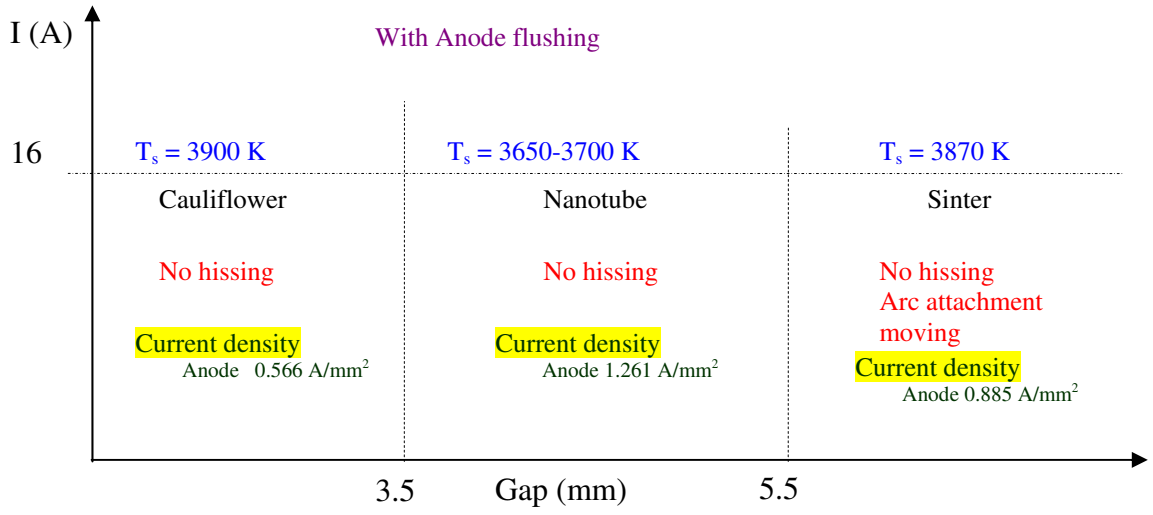

Figure 6.1 Arc characteristics and surface deposit type for 16 A arc current s using a 3 mm dia. cathode, for nitrogen. All done with anode flushing 0.6 L/min and tape speed of 3 mm / s.

It was found also that the substrate surface temperature (anode surface temperature) changed as the inter-electrode gap changed as shown in Figure 4.3. The minimum temperature at around 3650 K appeared to be associated with rapid NT formation. As mentioned earlier in Section 4.3.2, when the inter-electrode gap was 5.2 $\pm$ 0.2 mm, which corresponded to the lowest surface temperature, the CNTs produced were abundant. In contrast, at a very narrow gap *i.e.* 2.7 $\pm$ 0.2 mm, the substrate surface temperature was found to be significantly higher ~ 3855.0 $\pm$ 50 K. Although few NT were obtained at this narrow gap, nanoparticles were observed, with nanorods beneath them. A short arc causes an increase in heat load on the cathode with an increase in number density and averaged size of emitted particles (Kandah and Meunier 1995).

For a larger inter-electrode gap, i.e. 7.7 + 0.2 mm, the substrate surface temperature increased again to ~ 3800 K. From our observation, at this larger gap, the arc attachment is moving around which is likely cause by instability in the plasma. The energy transport to the anode substrate surface at larger gaps is also probably reduced due to easier convection and loss of carbon particles to the surroundings, leading to a slower growth rate and a sintered deposit. The micrographs obtained for this condition show few or no sign of nanotubes but instead depict a crumble mass of carbon forms.

Based on the above reason for lower observed temperatures in front of a hot carbon surface and the observed relationship between surface temperature and NT formation, there is strong evidence that the formation of NT in a carbon arc is associated with the presence of these graphene fragments. These graphene fragments may fold and formed nanotube "seeds" and then multiwalled nanotubes. CNT growth is then terminated when the arcing is finished or the carbon supply is exhausted (Harris, Tsang et al. 1994). For narrow or larger inter electrode gaps, the observed surface temperatures are higher which indicate less or no graphene fragment in front of the anode surface.

The arc condition at the optimum gap (5.2 $\pm$ 0.2 mm) was simulated using the commercial CFD software, Comsol Multiphysics, as described earlier in Section 5.7.2. For this case, which was labelled Case A, the anode surface temperature is taken as 3700 K and the plasma electrical conductivity of 1.567×10^6 (based on estimated value described in section 5.6.3) was used as an input. The results of the temperature and the velocity profile in the arc region are illustrated in Figure 5.18 and Figure 5.19, respectively.

The plasma spread radially near to the anode surface. Close to the anode surface, we notice flattened temperature isotherms due to the uniform value of the temperature imposed as a boundary condition at the anode surface. This temperature is controlled through the cooling of the plasma by the electrode, including the effect of the graphite sublimation and production of vapour in the plasma. The shape of the plasma from the simulation is also similar to the plasma picture observed through a neutral density as shown in Figure 5.3.

From Figure 5.19 it was shown that the maximum velocity in the plasma is 4.4 m/s in the jet coming from the cathode. From the observation, we believed that this cathode jet was deflected to the side when approaching the anode surface. This simulation is otherwise consistent with the analysis of images captured by high speed camera described in the Section 4.8. Figure 4.21 shows some of the images extracted from the high speed camera movie at 3200 fps. The size of the particle ejected from the cathode tip shown in these images was approximately 100 μm. This particle was ejected towards the outer side of the arc plasma and within 5 ms the particle had reached the anode region. From the analysis, it was found that the particle was ejected from the cathode tip at a speed of 0.7 m / s and then reached a maximum velocity of 5.0 m / s within 1 ms. The particle was dragged to the side by the plume expansion from the anode surface and lost much of its momentum. The path of the particle movement and the velocity profile is shown in Figure 4.21. Here we found that the modelling and experimental observation gave similar velocities. On the other hand, the particle ejected from the anode surface seems to be re-circulating in the anode plume –with a 1-2 mm from the surface.

The conditions at the largest gap (7.7 mm) and the narrowest gap (2.7 mm) were also simulated (termed Case F and G respectively). For both cases, a constant surface temperature of 3700 K was also used. For both cases F and G, the 6000K isotherm line is very much closer to the anode surface compared with that of the plasma at optimum inter-electrode gap (5.2 mm gap). This modelled difference must have come from the arc behaviour as a whole, rather than from the local anode behaviour, since the same assumptions were made for anode conditions. The higher modelled temperature gradient from the arc to the anode surface will lead to a higher vaporization of graphene fragments and closer to the anode. This will reduce the screening cloud of suspended carbon over the anode, and explain the higher observed temperatures. In both cases F and G, the velocity

profile shows the plasma circulating at the centre of the arc (far from the anode surface) and in the very high temperature region compared to the plasma at 5.2 mm gap.

6.2.2 Effect of arc current

The current also strongly influences the arc characteristics and hence the anode surface temperature. For a run with 3 mm diameter graphite rod and under pure nitrogen atmosphere at 20 A current, anode surface temperatures are about 200-400 K higher than at the current of 16 A for all inter-electrode gaps as shown in Figure 4.13. The nanotube formation is favourable at a lower arc current and under conditions where the arc does not hiss. At high current (with 3 mm cathode diameter), only carbon with cauliflower shapes were observed when the arc was run at the lowest gap, i.e. at 6.5 mm (the lowest gap possible for high current power supply using 3 mm cathode dia.) and no nanotubes were found at other inter-electrode gaps. The carbon cauliflowers formed have a uniform size and distribution throughout the treated area as shown in Figure 4.12.

However, when the cathode was changed to an 8 mm graphite rod, the anode surface temperature dropped significantly to a temperature range of 3600 to 3900 K. These temperatures are similar to those for runs with a 3 mm cathode at 16 A arc current. This large overall change in observed temperature is consistent with the interpretation given above for changes in temperature as the arc gap was changed; the influence from the arc as a whole and in particular the cathode, probably through the cathode jet, appears to be dominating the observed temperature. Figure 6.2 shows the arc characteristics and deposit type for the 20 A arc current with an 8 mm cathode diameter.

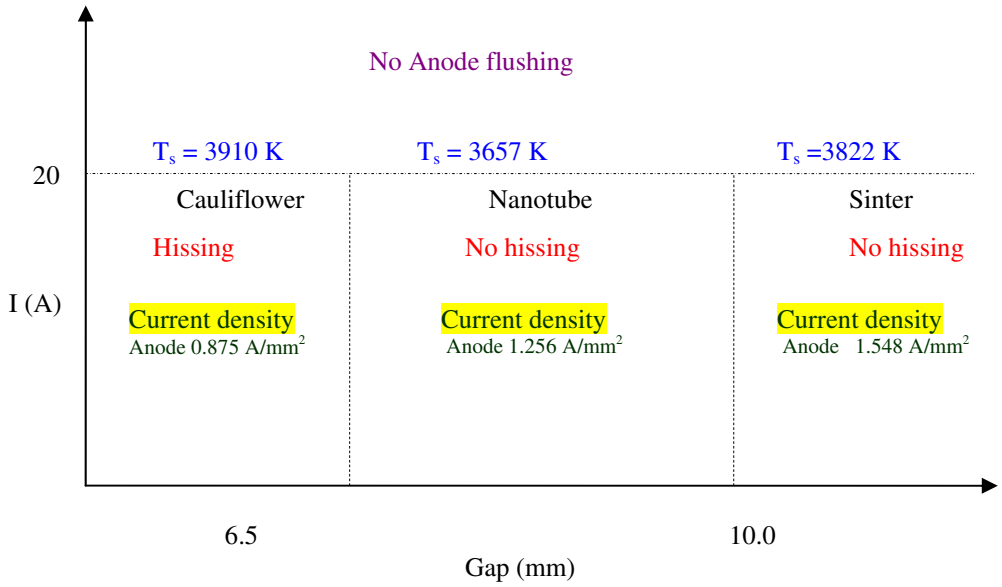

Figure 6.2 Arc characteristics and surface deposit type for a 20 A arc using a 8 mm diameter cathode. Tape speed is 4.13 mm/s.

Using the 8 mm cathode, the anode surface temperature was found to be lower by about 300-400 K. As mentioned earlier in Section 4.4, nanotubes were found using a current of 16 A when the anode surface temperature was around 3600 -3650 K. This behaviour has now been found for both 16 A and 20 A arc currents, with 3 mm and 8 mm cathode diameter, respectively. However, the nanotube formation is much favourable at a lower arc current and at a specific arc gap and under conditions where arc does not hiss.

It was found that the NT formation associated also with the current density. In both cases, (16 A and 20 A arc current), NT was formed when the anode current density is around 1.26 A/mm2, and not with lower or higher current densities.

6.2.3 Effect of nitrogen flushing

The effect of anodic flushing on the CNTs growth at a constant arc gap was also studied in this work. From these runs, it was found that varying the nitrogen flow rate in the range of 0-0.6 L/min, at 5.2 $\pm$ 0.2 mm gap, had no significant effect on the substrate surface temperature. However, it was found that CNTs produced with anodic flushing have higher purity (less attached carbon particles) compared to those produced without nitrogen flushing at the anode. The effect of nitrogen flushing is illustrated in Figure 4.9. The

analysis done by Shastry (2007) shows that the diameter of the CNTs produced also became smaller (from 50-60 nm to 30-40 nm) when the nitrogen flow into the system (through the anode) was increased. However, there was no detectable change in the number of nanotubes produced observed (Shastry, Abrahamson et al. 2006).

Our finding appears to be related to the work by Nishio et al (Nishio, Akita et al. 2004), who operated their arc for just 3-8 s, providing a similar residence time for electrode surfaces to that experienced by the moving anode in our continuous reactor. They also observed anode CNT growth, and found this was enhanced by directing a helium jet onto the arc and anode. This enhancement may have been related to the jet flow pattern which is similar to that in our arc with a small cathode, or it may have been due to cooling, or both. They did not measure anode surface temperature, but any cooling may have caused a similar effect. The cooling may have lead to a reducing rate of lateral attachment as proposed by Gamaly *et al* (Gamaly and Ebbesen 1995) leading to nanotubes with smaller diameters (Nishio, Akita et al. 2004).

If we consider a vapour condensation growth model, the temperature of the gas close to the anode surface does not change with gas flow from the anode but the carbon vapour is expected to dilute with increasing nitrogen flow. Thus, fewer nanotubes will be deposited from this diluted vapour. However, our finding shows that the amount of nanotubes produced are not reduced noticeably with increased flow.

The effect of this nitrogen flow was also simulated and was presented in Case D (maximum flow) and Case E (no flow) as described in Section 5.7.5. At the maximum anode flushing rate, the arc plasma diameter expands up to 6.5 mm in the radial direction. The plasma flows from the cathode are deflected away by the nitrogen from the anode surface. This may explain the cleaner nanotube produced with the increased of nitrogen flow from the anode as shown in Figure 4.9. The additional nitrogen gas flow pumps away carbon atoms and nanoparticles from the anode surface, so they spend less time in the vicinity and have less chance to diffuse or stick to nanotubes there.

6.2.4 Effect of substrate speed

The general observations for runs with a range of substrate speed of 0.8 to 5.6 mm/s are summarized in the Figure 6.3. This figure shows the arc characteristic when run at various carbon substrate speeds. These runs were done at 5 mm inter-electrode gap and using 3 mm graphite rod as a cathode. From these observations, the retention time of the carbon substrate in the arc zone seems to be crucial in forming the carbon nanotubes. At a lower speed, the carbon substrate stays longer in the arc. Cauliflowers and nanorods were formed on the substrate surfaces. Nanotubes were found only when the reactor was operated at optimum retention time, i.e. at optimum tape speed 3.0 mm / s. A stable arc was also observed throughout runs at this optimum speed and this was indicated by a quiet arc. The appearance of the arc attachment changed for speed above 3.0 mm/s, from being coherent and steady to an unsteady wandering attachment.

Various research groups have shown that the nanotube forms is completely in high thermal environment and within a time scale of milliseconds to seconds (Kokai, Takahashi et al. 2000; Harris 2007). Therefore, the substrate speed strongly influences the arc characteristic and its surface temperature.

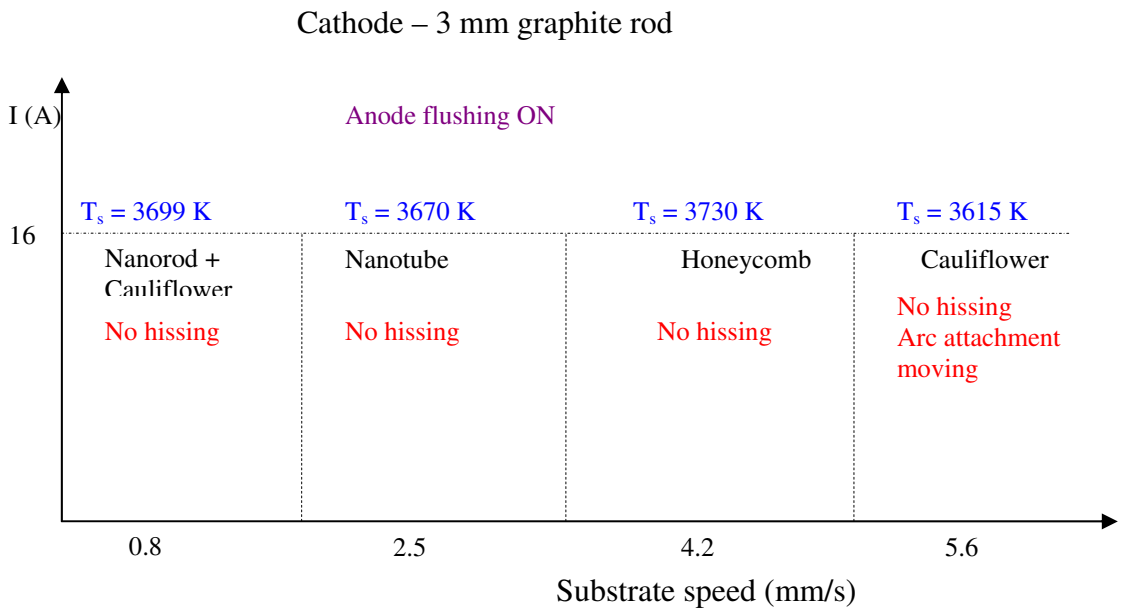

Figure 6.3 Mapping for CNT formation at various substrate speeds

The effect of substrate speed on the measured surface temperature was shown in Figure 4.10. From the figure, it was found that when the tape moved at 5mm / s or below, the anode surface temperatures seemed to be independent of the speed of the carbon substrate, fluctuating around 3700 $\pm$ 60 K. This indicates that the temperature of 3700 K is not controlled by the rate of heating, and must represent a balanced state. However, at a speed close to 6 mm / s, the surface temperature dropped to about 3600 $\pm$ 30 K. The fall-off of temperature at this highest speed may be explained by heating rate or thermal capacitance effect because at highest speed, the tape/substrate experiences a shorter time in the arc. The other possibility is a change in current density at the higher speeds.

The SEM images of the treated carbon tapes at various tape speeds are shown in Figure 4.11. In contrast to the anode surface temperature, the growth of CNTs seems to be strongly dependent on the speed of the carbon tape. At a very low speed, 0.85 mm / s, cauliflowers and nanorods were formed while at 2.56 mm / s lots of nanotubes were found on the substrate surface. Another type of nanostructure, *i.e*. a honeycomb structure, was produced when the tape speed was set at 4.2 mm / s. Finally, at a speed of 5.64 mm / s, the carbon cauliflowers structures were observed again.

At lower speed, i.e. 0.85 mm/s, the substrate stays a longer time in the plasma. This results in high carbon vapour composition with an excess energy leading to a formation of nanorods. This may be explained by the condensation of carbon vapour when the substrate moving out from the hot temperature region to the cooler region at lowers speed. Further deposition of graphene fragments onto nanotubes (which form in 3 s timeframe) may also develop nanorods and cauliflowers as suggested by Querrioux (Querrioux 2004). A tape speed of 4.2 mm/s results in a very short residence time and the arc probably start to become unstable. With a further increase of speed, the arc became unstable with the arc root keep moving around the anode surface. This happens because of not enough charge carriers being generated from the same area to support the arc so the attachment moves to other areas where fine structures exist.

6.2.5 Effect of background gases

As mentioned earlier in Section 4.7, the environment of the arc has a significant effect on the formation of CNTs. Carbon nanotubes can be found in both runs with nitrogen and argon even though the average substrate temperatures were differed as shown in Figure 4.18. Nitrogen, helium or argon atmospheres have been used for preparation of nanotubes in a conventional arc discharge (Zhang, Xue et al. 1999; Zhao, Okazaki et al. 1999; Lange and Huczko 2001). However, in their work, the arc was operated under vacuum and they found different optimal pressures for different kinds of atmosphere.

From the micrograph analyses, it was found that carbon nanotubes were also formed when our continuous arc was operated under an argon environment. However the amount of CNTs produced was far less compared to the runs with nitrogen used as a buffer gas. This is shown in Figure 4.15 (a-c). These nanotubes were formed in argon when the arc was operated with the inter-electrode gap in a range of 6.3 to 8 mm. A large amount of CNTs was produced when the reactor operated at the lowest gap *i.e*. 3.0 mm. Here, the nanotubes produced were short and had a big diameter. However, when the gap was increased to 5.0 mm, cauliflowers with a size varying from 1 to 5 micrometers covered the carbon tape surface. Ironically, at higher inter-electrode gap of 6.3 mm, the cauliflowers disappeared and a small amount of CNTs was formed. The nanotubes produced were long and very small in diameter compared to the tubes produced at the lowest gap.

Figure 6.4 shows the arc characteristic and anode surface deposition using different atmospheres for our continuous arc discharge. The anode surface temperatures under a helium atmosphere were found to be far lower than the sublimation temperature of graphite *i.e*. less than 4050 K for all inter-electrode gaps. At the lowest gap the anode surface temperature was 3672 ± 44 K. The lowest anode surface temperature was 3628 ± 17 K, at 6.3 mm inter-electrode gap. Unfortunately, from the SEM analysis, it was found that CNTs were not produced in any of these runs as shown in Figure 4.17. This is very strange as several groups have reported formation of CNTs under helium atmospheres. At the lowest inter-electrode gap, cauliflowers were formed with a few nanorods protruding from the cauliflower bunch.

It is worth noting that all runs with Argon and Helium were done using a larger power supply, which was described in Section 4.4. A DC power supply with a capacity of up to 50 A and an open-circuit voltage of 200 V was used; for experimental purposes and the current supply was set at 16 A. It was found later that the high current power supply had a higher component i.e. higher ripple compared to the low current power supply that may have caused some instability in the arc, hence affected the production of carbon nanotubes.

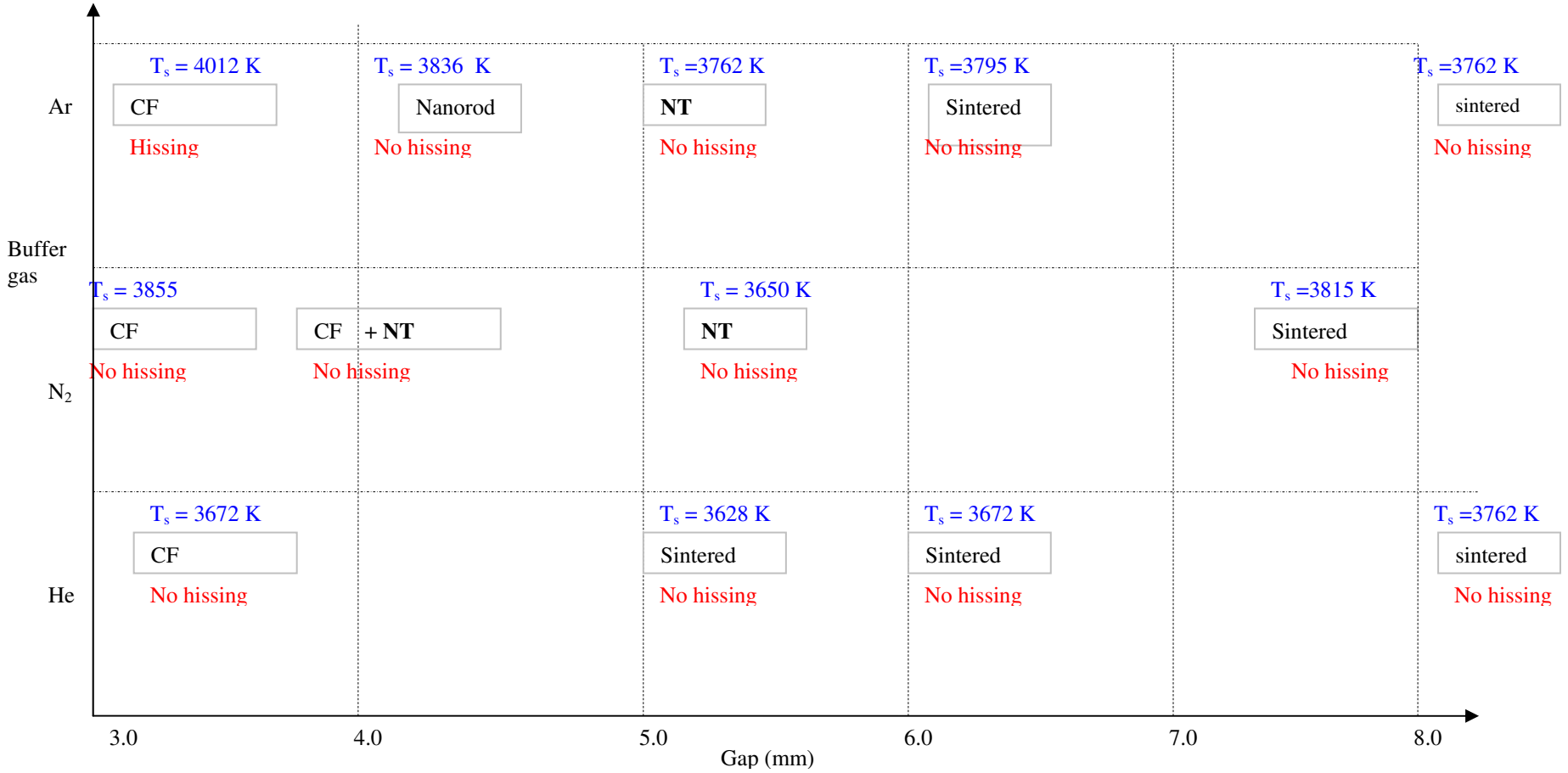

Figure 6.4 Arc characteristics and surface deposition using different atmospheres with 3 mm cathode diameter and arc current of 16 A

6.3 Growth mechanisms of multiwalled NT by arc-evaporation

As discussed before in Chapter 2, most of the growth models (Gamaly and Ebbesen (1995), Iijima (1993), Endo and Kroto (1992)) suggest that the primary source of CNT growth comes from carbon vapour. They assume that nucleation and growth occur as a result of direct condensation from the vapour phase. Another vapour phase growth model has been given by Louchev and co-workers (Louchev and Hester 2003). They suggest that the process is not the direct condensation of carbon atom onto a growing edge but adsorption of atoms onto a nanotube surface.

In Chapter 2, we argued the possibility that nanotubes or cylindrical seeds can be nucleated by spontaneous rolling of small fragments of graphite sheet or graphene due to high temperature thermal fluctuations. A molecular dynamic simulation of the free fluctuation of a small graphite nano-fragment was performed by Volpe and Cleri (Volpe and Cleri 2001) for T = 4000 K. This temperature represents the arc discharge and laser ablation environment and is near the sublimation temperature. Their simulation result showed that in the vibrational spectra of a finite size nano-fragment (*e.g.* N = 160), the density of low-frequency modes increases with temperature. This condition can tend to fold over the flat fragment into a cylindrical shape.

Louchev et al (2003) described a detailed analysis of nanotube nucleation from a graphitic nanofragment by thermal vibration. Using a molecular dynamic study, they suggest a kinetic pathway in which an initially flat graphite nanosheet formed in a vapour and collided with nanoparticles. The sheet tended to fold into a nanoring segment (Louchev and Hester 2003). They also proposed a model that suggests the cluster assembly carbon nanostructure will spontaneously disintegrate back into a smaller fragment because of its energy. The existence of cluster assembly was also observed by Kokai *et al*. (Kokai, Takahashi et al. 2000) and Puretzky *et al. (*Puretzky*, Geohegan et al. 2000)*. However their descriptions differed from that of Louchev *et al.* (2004*)*. The fragments in Louchev et al. can permanently assemble into a larger structure provided they reach a solid substrate where the condensation heat may be easily dissipated by heat conduction into the solid (Louchev, Kanda et al. 2004).

The presence of small particles ejected from the heated graphite/carbon surfaces at temperature above 3000K have been observed by many researchers (Finkelnburg 1946; Whittaker and Kintner 1969; Abrahamson 1971). A large number of small particles (d ~ 5 – 50 nm) were observed by Whittaker and Kintner(1969) while studying a heated graphite rod centrally held in a rarefied carrier gas flow (Ar or He) with an axial velocity about 5 – 10 ms^{-1}. They claimed that these particles observed on the inner surface of the gas flow tube could not be formed from carbon vapour condensation because of the estimated small number of collisions in the short time of travel between the graphite surface and the collection point (Whittaker and Kintner 1969). Most of the particles were cleavage fragments and electron diffraction studies indicated that they were crystalline.

A continuum emission spectrum was observed by Finkelnberg (1946), from an arc discharge with a graphite electrode operated in the air. He also observed a deposition of carbon on the cathode when the high current arc was operated with a small gap, less than several centimetres, and the cathode tip was placed in the luminous plume. He also found that about 40% of the carbon ejected from anode was deposited on the cathode.

In experimental work done by Abrahamson (1971) using a DC electric arc with a graphite anode, a milky haze was observed in front of the anode. The arc radiation showed a continuum spectrum which was interpreted as the radiation from many hot graphite particles similar to that observed by Finkelnberg (Abrahamson 1971).

Abrahamson (1974) in his review on carbon vaporization, recognized that the presence of these small particles will cause an error in the surface temperature measurement using an optical pyrometer. These particles will emit radiation and also absorb some of the radiation from the graphite surface. Therefore as the cloud of these particles builds up in the front of the graphite surface, less radiation or lower black body temperature would be observed (Treekrem 1968; Abrahamson 1974). Abrahamson also suggested that the major fraction of the crystallites ejected from the graphite surface is less than 5 nm in size.

In this study, it was found that there is an increased CNT growth when the anode surface temperature is lower than 3800 K as discussed in previous sections. This lower surface temperature observed through a pyrometer is likely due largely to the presence of small crystallite in front of anode surface as proposed earlier.

If one considers the vapour growth model for the arc discharge process, one can examine whether the high growth rate at the lower temperature is consistent with expected changes in the concentration of carbon vapour near to the anode surface. Near the sublimation temperature, each drop in temperature of 100 K corresponds to a 50% reduction of carbon vapour in equilibrium with a graphite surface (Meyer and Lynch 1973). The vapour within several mean free paths of the surface (for example C_3 mean free path is 0.7 μm at 4000 K) will be close to being in equilibrium with the surface. In other words, the vapour condensation rate is almost equal to the sublimation rate. Thus, a drop of temperature from round 3900 K to 3600 K is expected to markedly reduce the condensation rate, and thus also reduce the rate of CNT growth. However, this was the opposite of what was observed, causing some doubt that carbon vapour condensation is primarily involved in the growth of CNT in the electric arc.

A similar doubt about carbon vapour as an intermediate for CNT comes from the work of Lange *et al* (Lange, Bystrzejewski et al. 2006) in which they compared the yield of single-walled carbon nanotubes (SWNTs) from arcs using electrodes of different grain size. Carbon electrodes with grain sizes ranging from 1 – 26 nm and doped with Fe catalyst were tested in an Ar-He arc discharge. In their work, they found that the use of carbon materials with smaller microcrystalline structure (1-5 nm) in their electrodes radically increased the yield of SWNTs, although plasma parameters, such as temperature, C_2 molecule content and carbon vapour pressure, remained at similar levels. They also found that even at a very low current (10 A) where C_2 concentrations were much lower, the SWNTs still formed. It is difficult to imagine higher concentrations of vapour next to surfaces composed of smaller crystallites, unless the crystallites were suspended in the vapour. In this case, the graphene deposition also becomes a good possibility.

In another work, Chen *et al.* (2004) reported that NT can be formed without a vapour phase from a mechano-thermal process. In this method, the graphite powder was mechanically ground at room temperature for 150 hours and then annealed at 1400 ^{o}C for 3 hours (Chen, Conway et al. 2004). The results showed that clusters containing CNT and nanoparticles were found in the sample after the annealing process. The high resolution TEM micrograph clearly showed the presence of a MWNT structure with a hemispherical cap (Chen, Conway et al. 2004). No nanotubes were formed during the ball milling process.

The ball milling process may create precursors containing nucleation seed. Chen *et al*. suggested that large number of a meta-stable curved graphene layers might be produced during this process. These layers transform to a more stable shape and geometry, such as nanotubes on annealing (Chen, Conway et al. 2004). He also found that MWNT are normally formed in the temperature range of 1000 – 1500^{o}C. However, if the heating is increased to 1800^{o}C, thick NT bamboos (> 20nm diameter) were observed. From the study, they concluded that the source of carbon atoms for CNT formation must be disordered carbon since only a very small amount of vapour phase exists at low annealing temperature, T ~ 1400K (Chen and Yu 2005).

The growth of CNT during arc evaporation from solid phase intermediates was put forward by Harris and his colleagues (Harris, Tsang et al. 1994). In their work, fullerene soot was heated to approximately 3000 °C in a positive-heart electron gun. They found that nanotube-like structures were formed after the high temperature heat treatment. A solid state growth model was proposed in which the fullerene soot was considered as an intermediate product. The model can be described as follows. During the initial stage of arc-evaporation, carbon vapour condenses onto the cathode as fullerene soot-like material. As the arcing process continues, this condensed carbon vapour is exposed to the high temperature and forms nanotube "seeds" and then multiwalled nanotubes. CNT growth is then terminated when the arcing is finished or the carbon supply is exhausted. The model is illustrated in Figure 6.5.

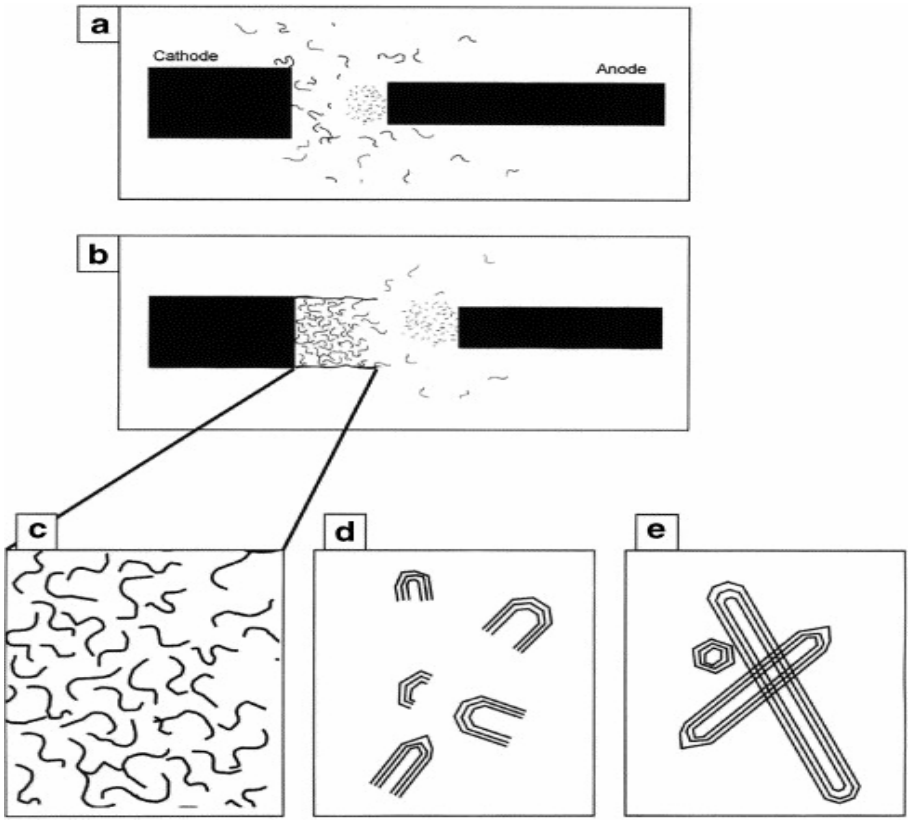

Figure 6.5 Schematic illustration of the solid phase growth model for multiwalled carbon nanotubes. (a) Electron bombardment from cathode causes heating of anode surface, and evaporation of C_2 and other species. These rapidly coalesce into fullerene soot fragments. (b) Some of the fullerene soot condenses onto the cathode, with the remainder being deposited on the walls of the vessel. (c), (d), (e) Enlarged views of interior of cathodic deposit, showing transformation of fullerene soot into firstly open-ended "seed" structures and then multiwalled nanotubes and nanoparticles. (Harris, Tsang et al. 1994)

This model suggests that rapid heating to high temperature is an important element because it was shown that slow heating of fullerene soot results in formation of nanoparticles rather than carbon nanotubes (Ugarte 1994). Chang and his colleagues (2000) showed that heating a non-graphitizing microporous carbon (doped with boron) to 2200-2400 °C produced MWNTs structures very similar to those produced by arc discharge (Setlur, Doherty et al. 2000). The group also found that a similar heat treatment of carbon black will produced MWNTs (Doherty and Chang 2002).

The main factor for a solid state growth mechanism therefore is high temperature annealing of carbon or graphene fragments. However, an important question arises: why does this annealing process form nanotubes rather than nanoparticles? As discussed earlier, MWNTs form only when the fullerene soot or carbon black are heated rapidly to high temperatures. A slow heating rate tends to produced nanoparticles rather than nanotubes (Ugarte 1994).

The author's thoughts are now summarized on what occurs during the deposition of CNT onto the substrate in the experimental study for this thesis. In this study, there is rapid heating of carbon tape (woven tape with fibre diameter of 10 μm) which breaks up the surface of the fibres to nano-fragments and vapour. It is first useful to follow what happens on striking the arc. Immediately after the arc ignition, when the anode is still cold, the arc operates as a conventional cathodic arc. At this stage, ~ 1-8 ms after arc ignition, the plasma jet produced by the cathode spot, expands into the inter-electrode gap. Part of the cathode material is then deposited on the anode surface. The anode (carbon tape) is then rapidly heated by cathode plasma jets. It reaches a temperature at which the anode starts to break into small fragments and partly eject and partly evaporate/sublime from the anode surface and forms a plasma plume. The material which is expelled from the anode then forms a highly ionized anode plasma plume due to its interaction with the cathode plasma jet (Beilis, Shashurin et al. 2005).

Vaporization of carbon from the anode was the subject of many detailed studies (Abrahamson 1974). Carbon is vaporised from the surface layer of the anode mainly in a form of graphite crystallite exceeding 3 nm in linear size. Small crystallites serve as the main positive charge carrier in the carbon plasma as their work function is lower than the ionization potential of small carbon molecules, which are the minor carbon ingredient. Approximating the crystallites to spherical particles with Φ=4.6 eV, Abrahamson (Abrahamson 1974) estimates that a crystallite of 50 nm dia could carry more than 100 electronic charges before the ionization potential rose to 11 eV, to be in competition with the most easily ionized molecules. Similarly a 10 nm crystallite could carry 20 charges and 1 nm crystallite only 3 charges.

Parts of the crystallites undergo the vaporization on the way to cathode, generating small carbon clusters (mainly C_3) and diminishing in size. It takes 1 ms for carbon species to cross a few millimetres arc gap and during this time the smaller crystallite are fully vaporised. Larger particles reach the cathode surface and thus present in the deposit.

As the tape moves, it enters a cooler region and the arc on the carbon tape surface extinguishes locally. Carbon vapour condenses and nano fragments deposit on the colder anode surface being fed into the arc region and form nanoparticles and nanotubes. These structures were protruding from the anode surface. These protrusions are expected to distort the electric field as shown in Figure 6.6. This electric field will activate the motion

of charged particles towards the anode or the cathode depending on their sign. The distorted electric field will collect charged carrier like a funnel as shown in Figure 6.7 (Shastry 2007).

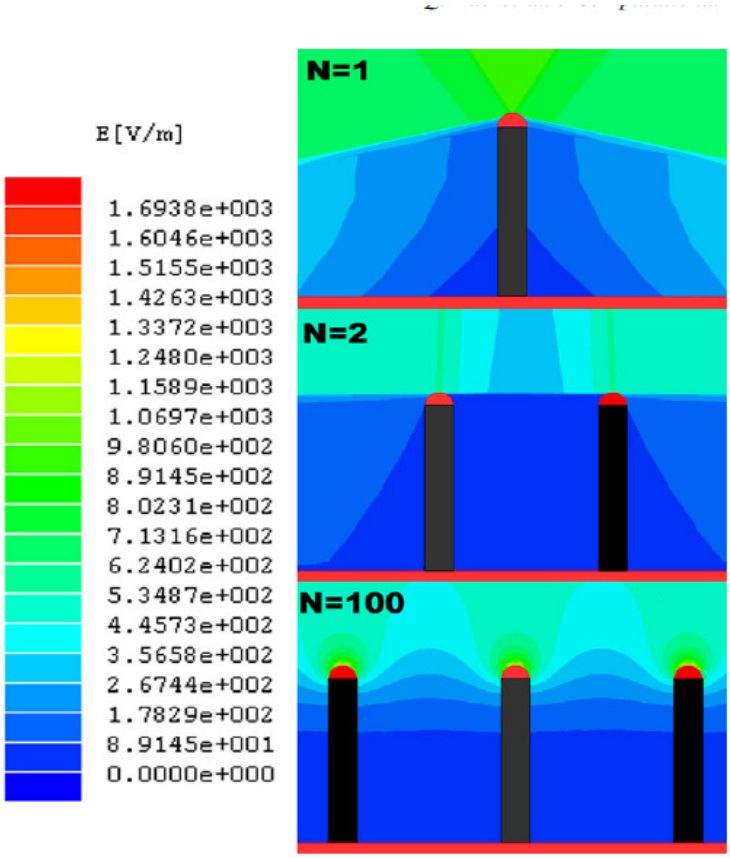

Figure 6.6 Electric field distribution around MWNTs with various amounts. (MWNT amount, N = 1, 2 and 100, length L = 100 nm, diameter D = 20 nm and inter-tube distance d = 20 nm) (Bao, Zhang et al. 2007).

These charged particles/nano-fragments then aligned and became a building block of nanotube. Along with the nanotube growth, the local electric field enhanced and charge density increased which then lead to a strong 'point effect'. The nanotube tip becomes a preferred site for further addition of carbon clusters and one-dimensional growth continues. In addition less material deposits on the tube surrounding due to repulsive force from the tube. This elongated structured is speculated to be the base of a multiwalled nanotube. The nanotube growth is terminated when the arc locally extinguished.

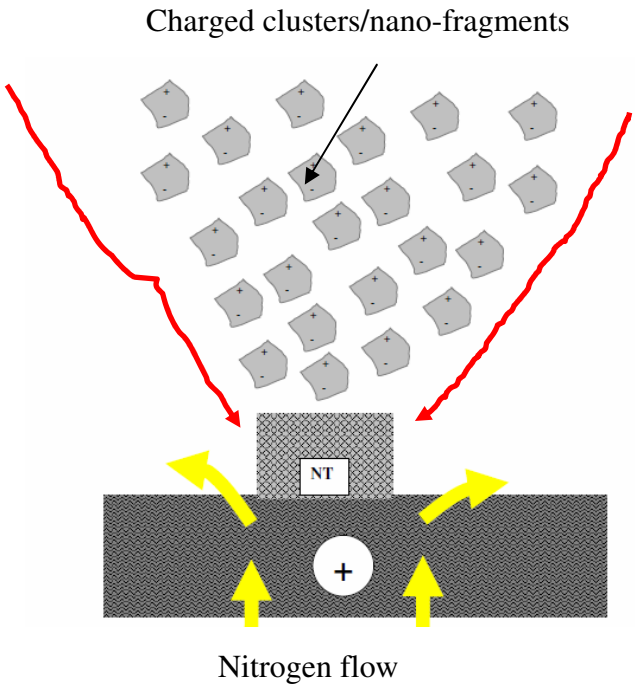

Figure 6.7 Acceleration of charged cluster due towards anode surface due to polarization, (adapted from (Shastry 2007)).

Hwang and Kim (Hwang and Kim 2004) suggested that selective deposition of charged cluster (nanoparticles) can lead to one-dimensional growth when charged particles are attracted more strongly to the tip than to the side wall of the deposits. When two charged conducting particles approach each other, the charge will be move backwards in the clusters. Their analysis on Coloumb interaction show that the interaction between the large and the small particles charged with same sign can be attractive. On the other hand, the interaction between clusters with similar size tends to be repulsive. A similar concept can be applied to the electrostatic interaction between an incoming charged particles and a charged rod (NT) in the arc plasma process.

As discussed earlier, CNTs can be grown on both electrodes surface. Jones et al (Jones, Malcolm et al. 1996) also reported NTs grew on cathode and anode while working with arc-discharge with same electrode diameter. They found that the nanomaterials formed on the anode have a very similar structure to that found in the cathode deposit. The structural resemblance suggests that they are formed by similar mechanism. This phenomenon probably can be explained by the existence of induce dipole nanoparticles in the arc discharge. On each nanoparticle, several surface charges (some positive and some negative) are deposited at different places on the particle, in general forming both net charge and an electrical dipole on each particle.

6.4 References

Abrahamson, J. (1971). The reactions of coal in a high intensity electric arc. Chemical and Process Engineering. Christchurch, University of Canterbury. **PhD thesis**.

Abrahamson, J. (1974). "Graphite Sublimation Temperatures, Carbon Arcs and Crystallite Erosion." Carbon **12**(2): 111.

Bao, Q., H. Zhang, et al. (2007). "Simulation for growth of multi-walled carbon nanotubes in electric field." Computational Materials Science **39**(3): 616-626.

Beilis, I. I., A. Shashurin, et al. (2005). "Imaging of the anode plasma plume development in a hot refractory anode vacuum arc." Plasma Science, IEEE Transactions on **33**(2): 408-409.

Chen, Y., M. J. Conway, et al. (2004). "The nucleation and growth of carbon nanotubes in a mechano-thermal process " Carbon **42**: 1543-1548.

Chen, Y. and J. Yu (2005). "Growth direction control of aligned carbon nanotubes " Carbon **43**(Letters to Editors): 3181-3194.

Doherty, S. P. and R. P. H. Chang (2002). "Synthesis of multiwalled carbon nanotubes from carbon black." Applied Physics Letters **81**(13): 2466-2468.

Endo, M. and H. W. Kroto (1992). "Formation of Carbon Nanofibers." J. Phys. Chem **96**: 6941-6944.

Finkelnburg, W. (1946). The high current carbon arc. FIAT Final Report No.1052. Washington, D.C., Department of Commerce.

Gamaly, E. G. and T. W. Ebbesen (1995). "Mechanism of carbon nanotube formation in the arc discharge." Physic review B **52**(3): 2083-2089.

Harris, P. J. F. (2007). "Solid state growth mechanisms for carbon nanotubes." Carbon **45**(2): 229-239.

Harris, P. J. F., S. C. Tsang, et al. (1994). "High resolution electron microscopy studies of a microporous carbon produced by arc-evaporation." J Chem Soc - Faraday Trans **90**(18): 2799-2802.

Hwang, N. M. and D. Y. Kim (2004). "Charged clusters in thin film growth." International Materials Review **49**(3-4): 171-190.

Iijima, S. (1993). "Growth of carbon nanotubes." Materials Science and Engineering B **19**(1-2): 172-180.

Jones, J. M., R. P. Malcolm, et al. (1996). "The anode deposit formed during the carbon-arc evaporation of graphite for the synthesis of fullerenes and carbon nanotubes." Carbon **34**(2): 231-237.

Kandah, M. and J.-L. Meunier (1995). "Study of microdroplet generation from vacuum arcs on graphite cathodes" Journal of Vacuum Science & Technology A: Vacuum, Surfaces, and Films **13**(5): 2444-2450.

Kim, K. S., G. Cota-Sanchez, et al. (2007). "Large-scale production of single-walled carbon nanotubes by induction thermal plasma." Journal of Physics D: Applied Physics **40**: 2375-2387.

Kokai, F., K. Takahashi, et al. (2000). "Laser Ablation of Graphite-Co/Ni and Growth of Single-Wall Carbon Nanotubes in Vortexes Formed in an Ar Atmosphere." J. Phys. Chem. B **104**(29): 6777-6784.

Lange, H., M. Bystrzejewski, et al. (2006). "Influence of carbon structure on carbon nanotube formation and carbon arc plasma." Diamond and Related Materials **15**(4-8): 1113-1116.

Lange, H. and A. Huczko (2001). "Influence of nitrogen on carbon arc plasma and formation of fullerenes." Chemical Physics Letters **340**(1-2): 1-6.

Laplaze, D., L. Alvarez, et al. (2002). "Carbon nanotubes: dynamics of synthesis processes." Carbon **40**(10): 1621-1634.

Lieberman, M. L. and G. T. Noles (1972). "Impurity effects in carbon fibres." Journal of Materials Science **7**(6): 654-662.

Louchev, O. A. and J. R. Hester (2003). "Kinetic pathways of carbon nanotube nucleation from graphitic nanofragments." Journal of Applied Physics **94**(3): 2002-2010.

Louchev, O. A. and J. R. Hester (2003). "Kinetic pathways of carbon nanotube nucleation from graphitic nanofragments." Journal of Applied Physics **94**(3): 2002-2010.

Louchev, O. A., H. Kanda, et al. (2004). "Thermal physics in carbon nantube growth kinetics." Journal of Chemical Physics **121**(1): 446-456.

Meyer, R. and A. Lynch (1973). High Temp Sci **5**: 192.

Nishio, M., S. Akita, et al. (2004). "Cooling effect on the growth of carbon nanotubes and optical emission spectroscopy in short-period arc-discharge." Thin Solid Films **464-465**: 304-307.

Puretzky, A. A., D. B. Geohegan, et al. (2000). "In situ imaging and spectroscopy of single-wall carbon nanotube synthesis by laser vaporization." Applied Physics Letters **76**(2): 182-184.

Querrioux, T. (2004). Carbon Nanotube Continuous Production. Chemical and Process Engineering, University of Canterbury. **Master of Chemical and Process Engineering**.

Setlur, A. A., S. P. Doherty, et al. (2000). "A promising pathway to make multiwalled carbon nanotubes." Applied Physics Letters **76**(21): 3008-3010.

Shastry, R., J. Abrahamson, et al. (2006). Parameters affecting deposition of multiwalled carbon nanotubes on a continuously fed substrate using arc discharge. ICONN 2006, Melbourne , Australia.

Shastry, R. K. (2007). Continuous Deposition of Carbon Nanotubes in an Arc-reactor and their Application in Field Emission Devices. Chemical and Process Engineering. Christchurch, New Zealand, University of Canterbury. **Doctor of Philosopy in Chemical Engineering**.

Treekrem, J. O. (1968). J. Chem. Phys. **49**: 2878.

Ugarte, D. (1994). "High-temperature behaviour of "fullerene black"." Carbon **32**(7): 1245-1248.

Volpe, M. and F. Cleri (2001). "Vibrational modes of graphitic fragments and the nucleation of carbon nanotubes." The Journal of Chemical Physics **115**(7): 3308-3314.

Whittaker, A. G. and P. Kintner (1969). " Particle emission during sublimation of graphite." Carbon **7**: 414-415

Zhang, H., X. Xue, et al. (1999). "The effect of different kinds of inert gases and their pressures on the preparation of carbon nanotubes by carbon arc method." Materials Chemistry and Physics **58**(1): 1-5.

Zhao, X., T. Okazaki, et al. (1999). "Optical Emission Spectra during Carbon Nanotube Production by Arc Discharge in H_2, CH_4 or He Gas." Jpn. J. Appl. Phys. **38**(Part 1, No. 10): 6014-6016.

Chapter 7: Conclusion and Future Directions 7-1
7.1 Conclusions 7-1
7.2 Future works 7-2
7.3 References 7-4

Chapter 7: Conclusion and Future Directions

7.1 Conclusions

During the last decade, extensive studies have been done all over the world to improve the synthesis method of producing CNTs and to explore the potential applications of it. In this Thesis we have presented a modified version of a conventional arc discharge apparatus to improve CNTs synthesis process. A continuous method of producing nanotubes on a carbon substrate is shown. The early part of this thesis consists of introduction and description of the continuous arc reactor providing most of the necessary background for understanding the experiments presented here.

The formation of CNTs in an electric arc is a very complex phenomenon and only partially understood. This is due to the extreme conditions *e.g.* high temperature and low pressure in the synthesis process which involves a kinetic controlled mechanism. These rough conditions also make it difficult to validate the theories via experimental work (Marcos, Lopez et al. 1997). The main attention is given to a new continuous method of CNTs production in arc discharge and measurements made of nanotubes deposition on a carbon substrate. From the current set-up, it was found that the system can produce good CNT products at low temperature provided optimum conditions are reached, *i.e.* T_s ~ 3650 K at 5.2 $\pm$ 0.2 mm gap.

This work has also shown that a simple technique to study the surface temperature of the anode, which is related to the CNT yield, can be developed and is viable. In order to understand the growth mechanism of CNTs in an arc discharge, it was crucial to study the anode surface temperature, where the CNT grow. This novel approach of studying the apparent surface temperature of the anode, which was the carbon substrate to be treated, was presented. We have described the detailed procedures of measuring anode surface temperature as relevant to this thesis. A frontal view of the anode was able to be viewed and studied due to a larger gap (than in most published work) between the electrodes. The gap can be adjusted in a range of 1-10 mm. The effect of arc parameters, such as the inter-electrode gap, the substrate speed and the background gas used, on the anode surface temperature, hence the CNT yield was also presented in this work. The gas flow rate was found to have no effect on the anode surface temperature and CNTs production but has effects on the purity of the products.

Our CFD modelling of the arc plasma argues strongly for the presence of crystallites in the space close to the anode surface. During the initial stage the model was solved without considering the presence of nanoparticles in front of the anode layer. However, the model was not stable and a solution could not be obtained. Experimentally a diffuse arc attachment was seen. Later, by using the calculated values for electrical conductivities with carbon nanoparticles included near the anode a stable solution for the diffuse geometry was achieved.

Finally, the results from our work supported the contention that the tiny carbon crystallites are the main intermediates for CNT growth in an electric arc. The main factor for a solid state growth mechanism therefore is high temperature annealing of carbon or graphene fragments.

7.2 Future works

Further investigations are still recommended, some related to industrial implications. Since our reactor can be operated continuously at pressure slightly higher than atmospheric pressure, it gives a good indication for a mass production of CNTs. However, the growth mechanism of CNTs must be fully understood in order to control the properties of the product.

The next step in the development of this research should entail a comprehensive analysis on the arc plasma composition of the arc, especially in the region closed to the anode surface. Given the larger range of inter-electrode gap, the spectroscopic study will be valuable. At present, to simplify our model, we use nitrogen plasma properties to solve the model. The carbon arc plasma should consist of carbon species such as C_1, C_2, and C_3 etc. Therefore, it is more useful to include these species in calculating the plasma composition for arc plasma simulation. The buoyancy effect in the plasma and the effect of protruding nanostructures on electric field must also incorporate in order to have more reliable model.

Further experimental work must be done to explore the possibilities of producing CNTs at higher volume per unit time by introducing a higher current power supply. The present high current power supply may not be suitable to meet this objective since the high current power supply had a higher AC component i.e. higher ripple which may have caused some instability in the arc, hence affecting the production of carbon nanotubes.

The characterization of the CNTs produced must be expanded. Using SEM only is not adequate and does not follow the international standard for a true evaluation of the CNT nature of the product. TEM or FESEM characterization is very beneficial on proving the growth mechanism of CNT in this reactor. It provides detailed analysis of the SWNTs or MWNTs produced, for example the tube diameter, number of walls and some defect content evaluation. Energy dispersive x-ray spectroscopy (EDS) measurement should be done to identify any impurity elements that might influence the CNTs formation process (Kim, Cota-Sanchez et al. 2007). Finally, the thermogravimetry (TGA) analysis of the tape for some unit length coupled with FESEM can also yield a mass analysis on the MWNTs structure. It is an interesting tool when discussing the continuous production and large scale production method (Harbec, Meunier et al. 2007).

7.3 References

Harbec, D., J. L. Meunier, et al. (2007). "A parametric study of carbon nanotubes production from tetrachloroethylene using a supersonic thermal plasma jet." Carbon **45**(10): 2054-2064.

Kim, K. S., G. Cota-Sanchez, et al. (2007). "Large-scale production of single-walled carbon nanotubes by induction thermal plasma." Journal of Physics D: Applied Physics **40**: 2375-2387.

Marcos, P. A., M. J. Lopez, et al. (1997). "Thermal road for fullerene annealing." Chemical Physics Letters **273**: 367-370.

List of publications

1. Hamdan M. Yusoff, Rahul Shastry, Thomas Querrioux and John Abrahamson. "Nanotube deposition in a continuous arc reactor for varying arc gap and substrate temperature"Current Applied Physics Volume 6, Issue 3, June 2006, Pages 422-426

2. Hamdan Mohamed Yusoff, Abrahamson, J.and Rahul Shastry. "Influence of anode surface temperature in a continuously-fed arc discharge depositing carbon nanotubes" Nanoscience and Nanotechnology, 2006. ICONN '06. International Conference on July 2006 Brisbane, Qld

3. Shastry, R., Abrahamson, J., Yusoff, H., Querrioux, T "Parameters affecting deposition of multiwalled carbon nanotubes on a continuously fed substrate using arc discharge": Nanoscience and Nanotechnology, 2006. ICONN '06. International Conference on July 2006 Brisbane, Qld.,

4. H. M. Yusoff , R. Shastry and J. Abrahamson "Effect of Arc parameters on CNT growth using a continuous reactor" Second International Conference on Advanced Materials and Nanotechnology (AMN-2), Queenstown, New Zealand, 6-11 Feb 2005. Oral Presentation

Appendix A

Arc cycles analysis using high speed camera

The purpose of this analysis is to investigate plume (luminous region) development in the arc. The images were photographed using a high speed B/W CMOS camera (Model # CPL MS50 K). The number of frames per second can be varied by changing the image size as shown below;

Image size	Number of frame per second
1280 x 1020	500 fps
1289 x 512	1000 fps
1280 x 256	2000 fps
1280 x 100	5000 fps
1280 x 50	10000 fps

Three videos with different image sizes were taken using the high speed camera which is 500 fps, 1080 fps and 3200 fps. The still images of the arc cycles at different frame rate are given in Figure A.1 – A.3

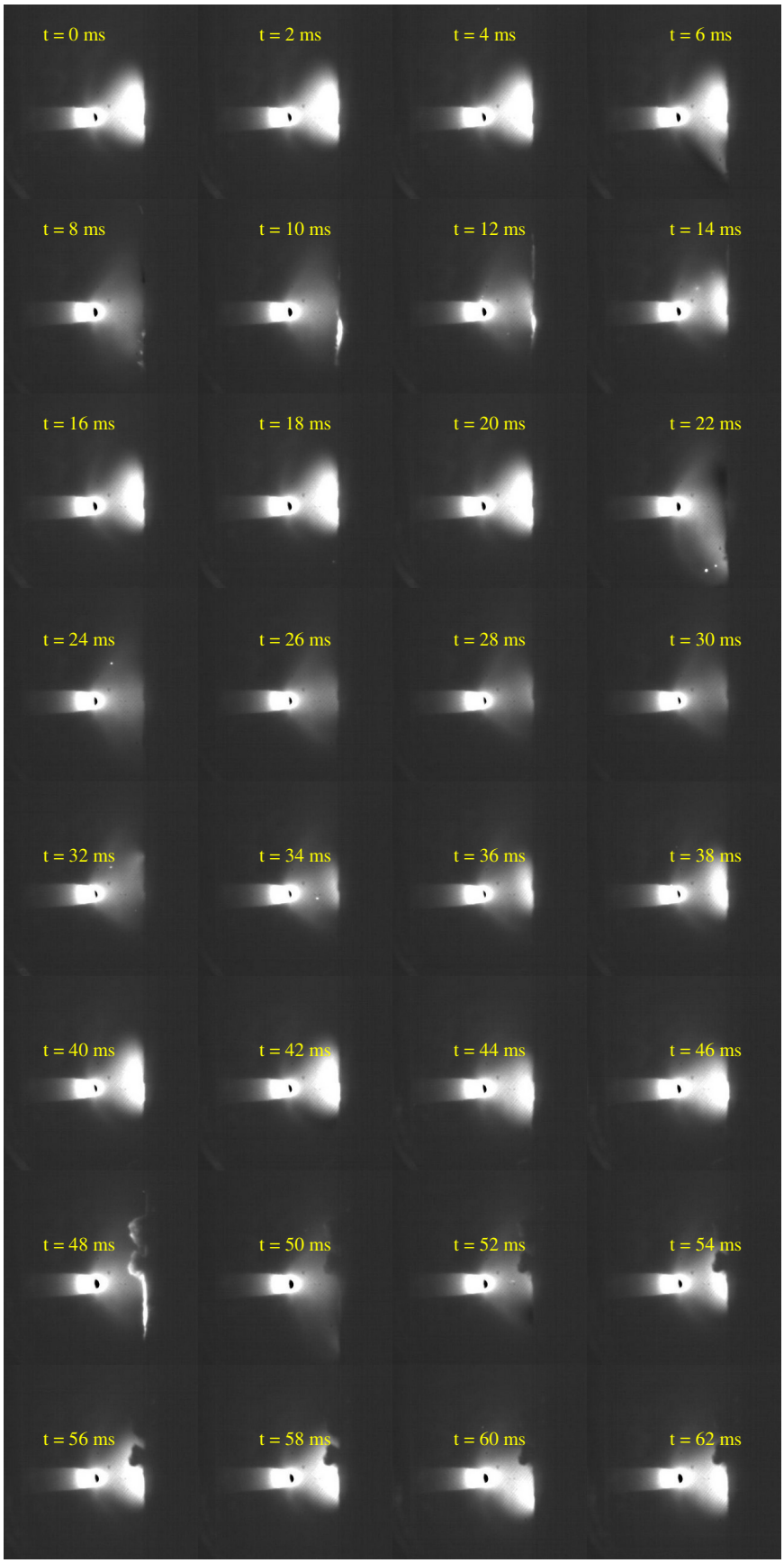
t = 0 ms
t = 2 ms
t = 4 ms
t = 6 ms
t = 8 ms
t = 10 ms
t = 12 ms
t = 14 ms
t = 16 ms
t = 18 ms
t = 20 ms
t = 22 ms
t = 24 ms
t = 26 ms
t = 28 ms
t = 30 ms
t = 32 ms
t = 34 ms
t = 36 ms
t = 38 ms
t = 40 ms
t = 42 ms
t = 44 ms
t = 46 ms
t = 48 ms
t = 50 ms
t = 52 ms
t = 54 ms
t = 56 ms
t = 58 ms
t = 60 ms
t = 62 ms

Figure A.1 Arc cycles photographed at 500 fps

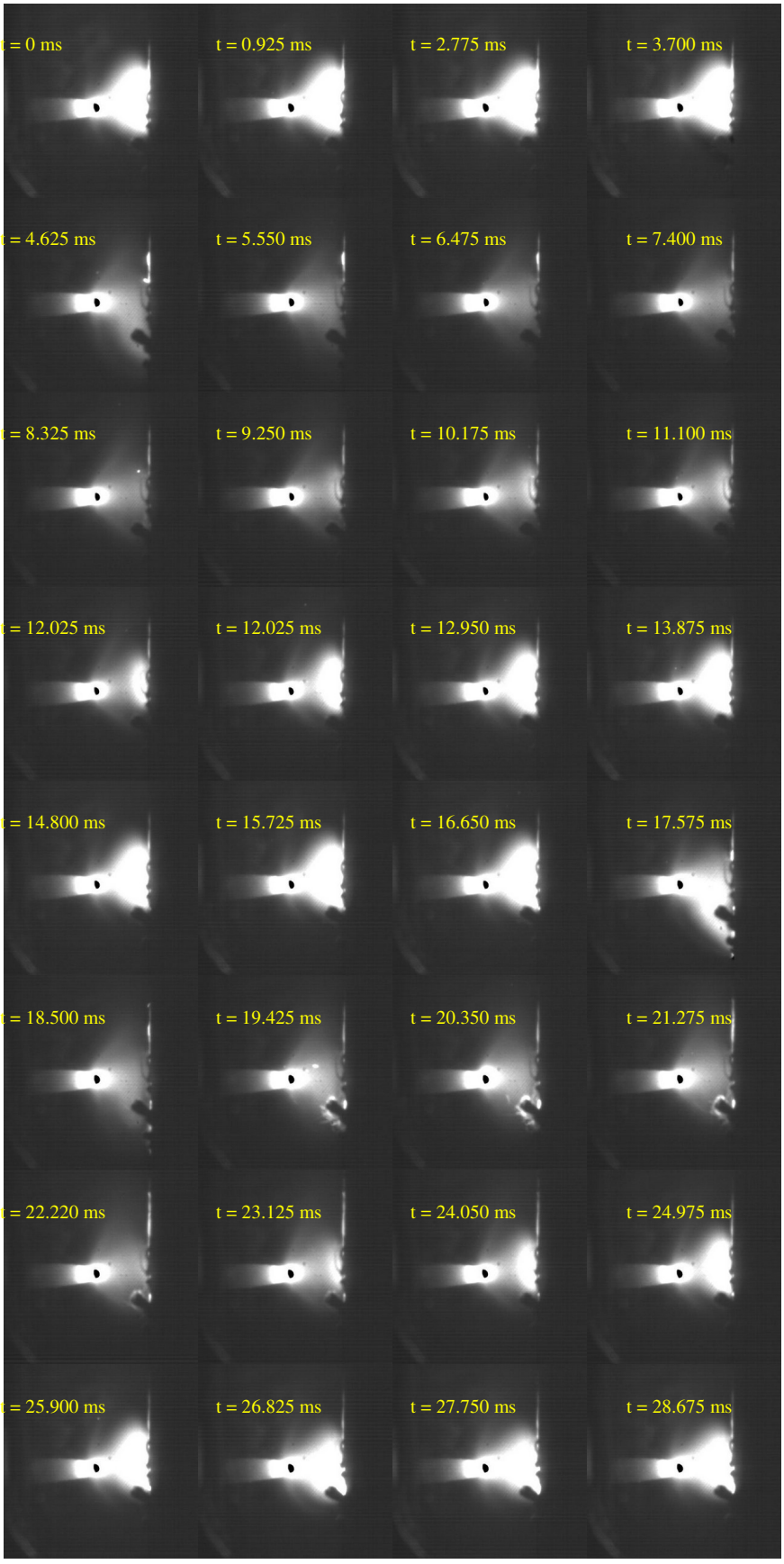

Figure A.2 Arc cycles photographed at 1080 fps

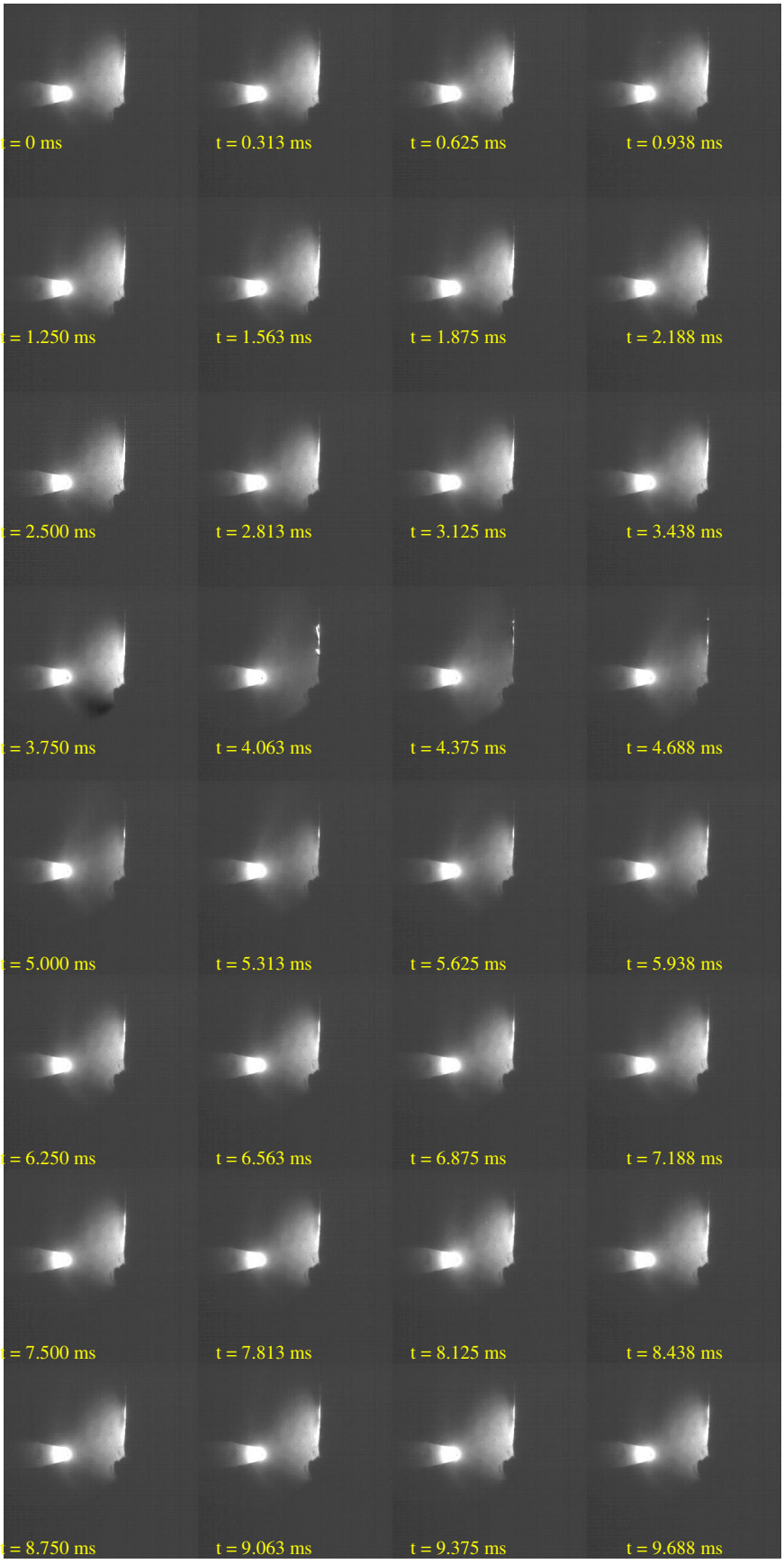

(a) 0 – 9.688 ms

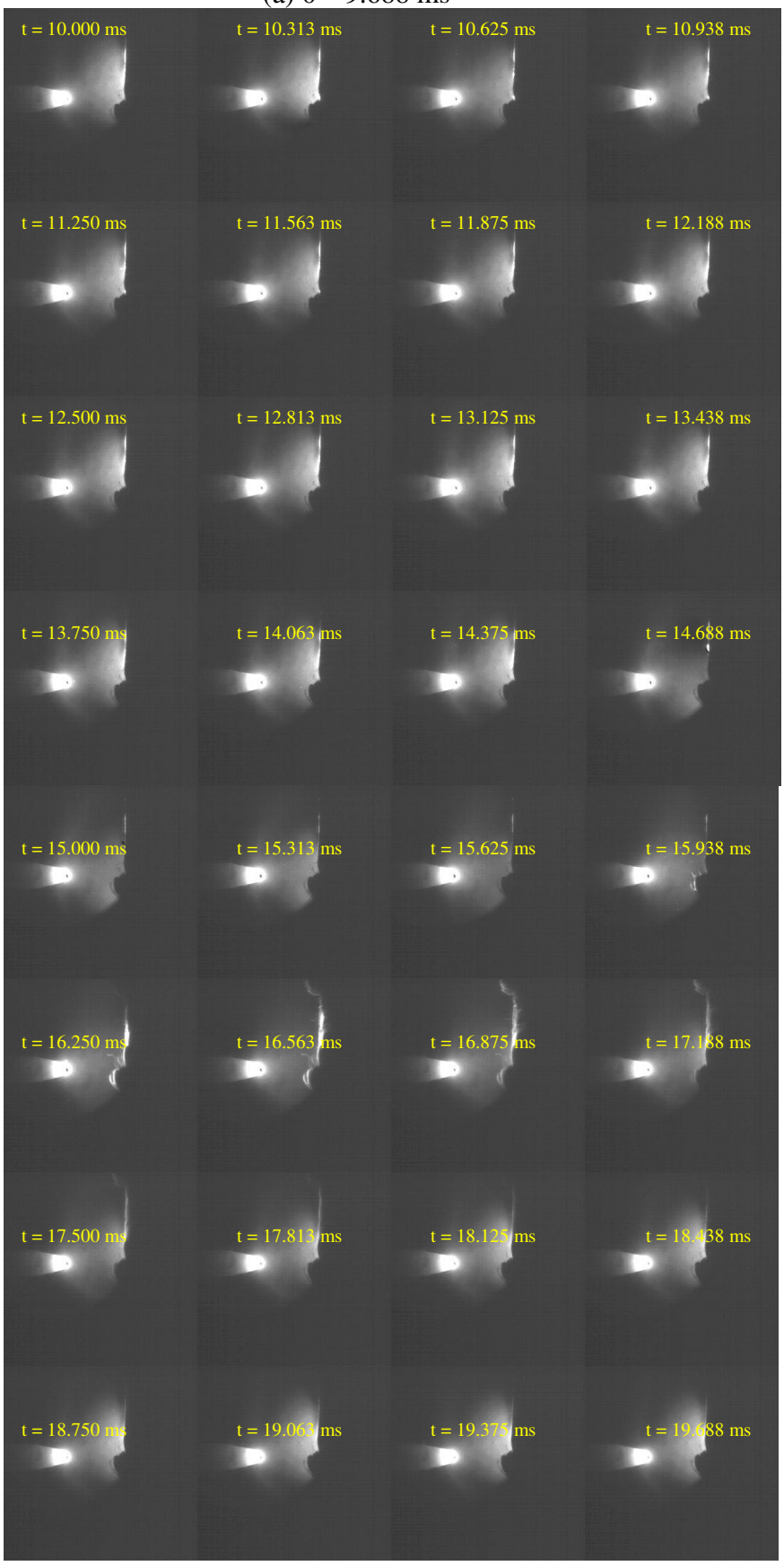

(b) 10.0 – 19.688 ms

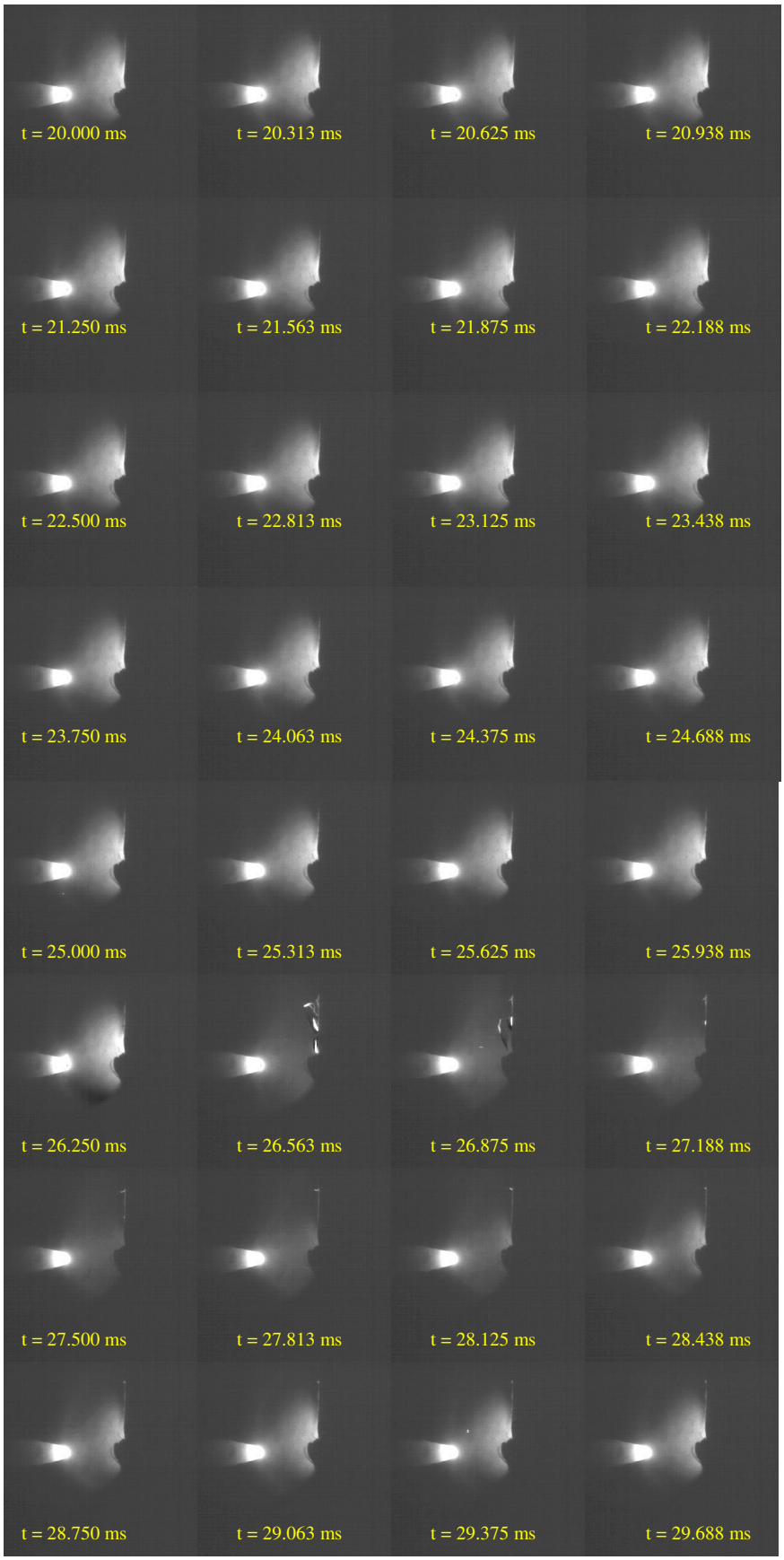

(c) 20.0 – 29.88 ms

Figure A.3 Arc cycles photographed at 3200 fps

Consecutive arc cycles numbered 1 to 22 are summarized in the table below

Table A.1 Cycles of anode plume

Photographed at 1080 fps t = 0.926 ms				
	With PLUME		*NO PLUME*	
Cycle	Consecutive no. of frames	Duration (ms)	Consecutive no. of frames	Duration (ms)
1	12	11.11	1	0.93
2	16	14.82	5	4.63
3	11	10.19	5	4.63
4	14	12.96	4	3.70
5	14	12.96	3	2.78
6	3	2.78	2	1.85
7	3	2.78	3	2.78
8	28	25.93	3	2.78
9	38	35.19	1	0.93
10	20	18.52	1	0.93
11	20	18.52	8	7.41
12	6	5.56	1	0.93
13	3	2.78	4	3.70
14	10	9.26	1	0.93
15	4	3.70	2	1.85
16	10	9.26	1	0.93
17	15	13.89	1	0.93
18	38	35.19	1	0.93
19	4	3.70	6	5.56
20	8	7.41	5	4.63
21	5	4.63	1	0.93
22	15	13.89	3	2.78

Different stages of anode plume development were observed by photographing the arc using the high speed camera (images were not shown here), which was used to determine characteristics of anode plume development. Table A.1 describes the cycles of anode plume development. Column ‘With PLUME’ shows periods over which the anode plume developed and stayed before extinguishing. On the other hand, column ‘NO PLUME’ shows periods where there is no luminous region in front of the anode.

In order to have a better picture, the duration was then plotted with arc cycle number for consecutive arc cycles. The cycles are shown in Figure A.4. It was found that the periods of highly luminous anode region (with plume) varied between 3 and 35 ms, but mostly remained about ~8-14 ms. On the other hand, the periods with no luminous region (no plume) were shorter, normally around 1 to 4 ms. It is believed that this was the time taken to heat up the anode surface by the cathode jet before the surface vaporized and formed a plume.

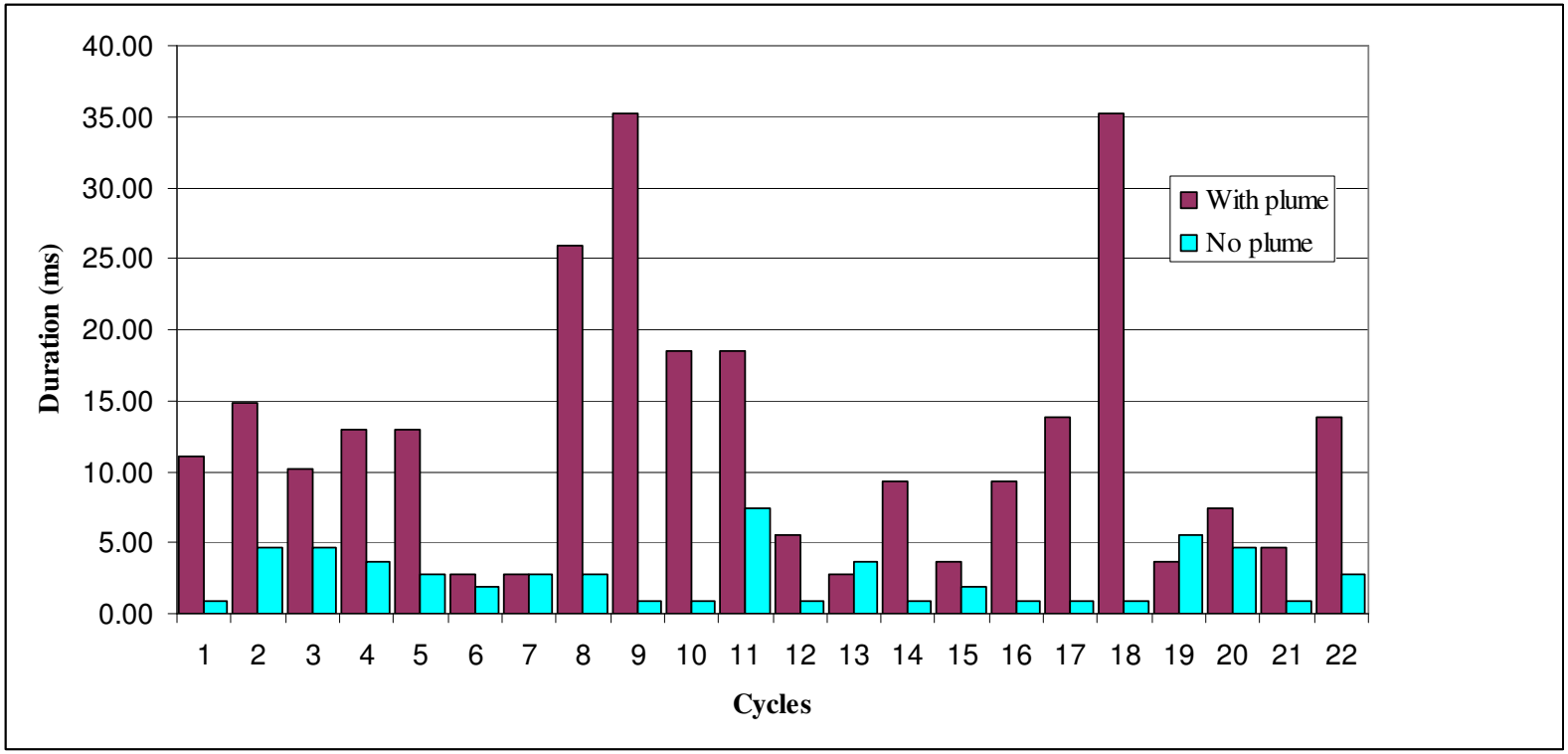

Figure A.4 Consecutive cycles of arc (duration of arc with and without plume) in the continuous arc discharge at 16 A arc current and 5.2 mm gap.

Appendix B

Estimation of electrodes erosion rates and vapours velocity

1. Cathode

For cathode, the erosion rate is taken from (Beilis1999), which shows for a 10 A carbon arc in the vacuum, the erosion rate is 4mg/C. Since the current for our reactor is 16 A, therefore the estimated erosion rate for that current is given as;

For 16 A arc current, *Mass flux* = *I* x 4 mg/C where *I* is arc current.

Therefore,

$$\textit{Mass flux} = 16 \text{ C/s} \times 4 \text{ mg/s}$$

$$= \textbf{64 mg/s} \text{ or equivalent to } 6.40\text{E-}08 \text{ kg/s}$$

The vapour velocity in front of the cathode, $\nu_{cathode}$, is then can be calculated using the following relationship.

$$\nu_{cathode} = \textit{mass flux/ plasma density}$$

For nitrogen plasma, the plasma density at 3800 K, ρ_{3800K} is 0.089803 kg/m^3 (Boulus, 1995).

$$\textit{Volumetric flowrate} = \frac{6.40 \times 10^{-8} \text{kg/s}}{0.089803 \text{ kg/m}^3}$$

$$= 7.127 \times 10^{-7} \frac{\text{m}^3}{\text{s}}$$

Assuming all the emissions are coming from the cathode face, the cathode emission area, $A_{cathode}$, is

$$A_{cathode} = \pi(1.5\times10^{-3})^2 \text{ m}^2$$

$$= 4.122 \times 10^{-6} \text{m}^2$$

Therefore,

$$\nu_{cathode} = 0.173 \text{ m/s}$$

2. Cathode erosion rate (from experimental work)

However from our experimental work, the cathode erosion rate for 16 A arc current with a substrate speed of 2.5 mm/s and inter-electrode gap of 5.2 mm, the erosion rate was found to be **0.58 mg/s**.

Therofe the velocity is

$$v_{cathode} = \frac{mass\ flux}{\rho_{3800K} \times A_{cathode}} \qquad \text{(B.1)}$$

$$= \frac{5.80 \times 10^{-7} \text{kg/s}}{(0.089803\ \text{kg/m}^3)(4.122 \times 10^{-6}\ \text{m}^2)}$$

$$= 1.57\ \text{m/s}$$

Note : The cathode erosion rate from the experimental work is much lower because the arc was operated at atmospheric pressure, whereas Beilis was working with high vacuum arc. Therefore, the value is expected ~100 times higher.

2. Anode

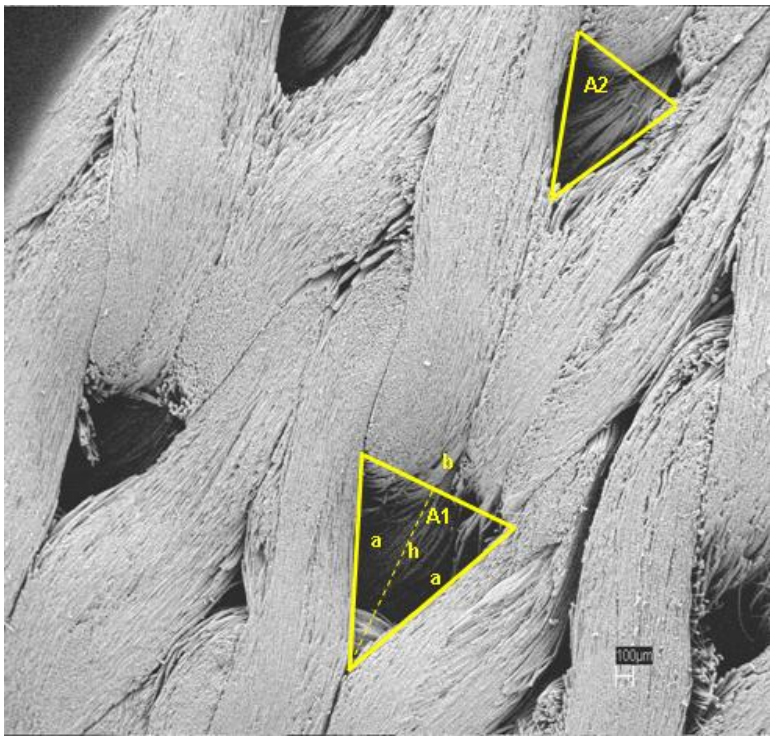

Figure B.1 Treated surface of the woven carbon fibre tape

From the experimental work, it was found that the anode attachment diameter, *d*, is 8 mm. therefore, the total area, $A_T = \frac{\pi d^2}{4}$. In order to find the effective area, A_{anode} we need to estimate the holes area on the substrate surface as shown in Figure B.1 as A1 and A2.

$$A_{anode} = A_T - \sum A1 + A2 \qquad \text{(B.3)}$$

From Figure B.1 it was found that the general formulation for calculating the area is given as below

$$A = ½(b)\,(h) \quad \text{where } h = \sqrt{a^2 + b^2}$$

For area A1,

a = 1000 μm, b = 800 μm and h = 1077.0 μm

$$A1 = \frac{1}{2}(1000)(1077)\ \mu\text{m}^2\left(\frac{1\text{mm}}{1000\ \mu\text{m}}\right)^2$$
$$= 0.4308\ \text{mm}^2$$

and for area A2,

a = 800 μm, b = 600 μm and h = 854.4 μm

$$A1 = \frac{1}{2}(600)(854.4)\ \mu\text{m}^2\left(\frac{1\text{mm}}{1000\ \mu\text{m}}\right)^2$$
$$= 0.2563\ \text{mm}^2$$

Base on the image analysis there are 6 numbers of holes A1 and 6 numbers of holes A2 within the anode attachment area. Therefore,

$$A_{anode} = A_T - 6(A1 + A2)$$
$$= \frac{\pi(8)^2}{4} - 6(0.4308+0.2563)\ \text{mm}^2$$
$$= 46.14\ \text{mm}^2$$

Since the diameter of single carbon fibre of the substrate, d_f, is 10 μm and assuming that about ten layers of the fibres have been eroded, the erosion volume can be calculated.

$$Volume = A_{anode} \times number\ of\ layer \times d_f$$
$$= 46.14(10)(0.01)\ \text{mm}^2$$
$$= 4.614\ \text{mm}^2$$

and knowing that the carbon substrate travelled at a speed($v_{substrate}$) of 2.5 mm/s, therefore, the time taken to passing through the arc is

$$t = \frac{d}{v_{substrate}}$$
$$= \frac{8\ \text{mm}}{2.5\ \text{mm/s}}$$
$$= 3.2\ \text{s}$$

The erosion rate is then can be calculated by the following equation,

$$Erosion\ rate = \frac{Volume}{t} \times \rho_f$$

where the carbon density value was taken as fibre density, ρ_f ,which is 2×10^{-3} g/mm^3

$$mass\ flux = \frac{erosion\ rate}{A_{anode}}$$

And assuming that only 20 % of the graphite vaporized, and then the vapour velocity due to carbon vaporization in front of the anode can be determined

$$v_{anode} = \frac{(0.2)(mass\ flux)}{\rho_{3800K}}$$

By substituting all the value into the above equation we found

Erosion rate = 2.88×10^{-3} g/s

Mass flux = 6.25×10^{-2} kg/m^{2}s

Another rough estimation on anode loss is by weighing the treated and untreated Carbonic tape. A square sample with same size (treated and untreated tape) was weighing. .

	Weight (mg)	Mass loss (mg)
Untreated sample	328.44	
Treated sample 1	304.98	23.46
Treated sample 2	271.27	57.17
	Average	40.315

$$\text{Erosion rate} = \frac{\text{massloss} \times \text{tape speed}}{\text{tape length}}$$

$$= \frac{40.315 mg \times 2.5 mm/s}{22 mm}$$

$$= 4.831 \text{ mg/s or } 4.831 \times 10^{-3} \text{ g/s}$$

The estimated value by weighing the sample is twice the value by image analysis. However, in image analysis only 10 layers of fibre assumed to be eroded. That probably explains the discrepancy in the anode erosion rate.

Appendix C

1. Calculation of particle number density in the plasma in front of the anode surface

According to Finkelnberg, 80 % of graphite were ejected as crystallites (Finkelnburg 1946)..

Calculation of mass concentration

The erosion rate was estimated using the image analysis software, Sigma scan Pro 5.0 as describe in Appendix B

For a 16 A arc current, using the woven carbon fibre, the erosion rate is found to be 180 μg/C. Therefore the mass flux can be calculated.

$$\text{The mass erosion rate} = I \times \text{erosion rate per unit Coulomb}$$

$$= 16\ \text{A} \times 180\ \mu\text{g/C}$$

$$= 2.88 \times 10^{-6}\ \text{kg/s}$$

However, taking a conservative figure by assuming only 80 % was ejected as particulate, the mass flux can be determined.

$$\text{Mass flux} = (0.8)\ (2.88 \times 10^{-6}\ \text{kg/s})$$
$$= 2.304 \times 10^{-6}\ \text{kg/s}$$

From Boulos (1995) the nitrogen plasma density at 3800 K is 0.089803 kg/m^3

Therefore,

$$\text{Volumetric flow rate} = \frac{\text{erosion rate}}{\rho}$$

$$= \frac{2.304\times10^{-6}\ \frac{kg}{s}}{0.089803\ \frac{kg}{m^3}}$$

$$= 2.566\times10^{-5}\ \frac{m^3}{s}$$

From the experimental image analysis, the calculated anode emission area is 4.164×10^{-5} m^2.

$$\text{Particle velocity} = \frac{\text{volumetric rate}}{\text{emission area}}$$

$$= \frac{2.566\times10^{-5}\ m^3/s}{4.164\times10^{-5}\ m^2}$$

$$= 0.616\ m/s$$

Using C_3 representing the vapour with a molecular weight of 36 g/mol the molar concentration can be calculated.

The mass flow of crystallite can be determined by knowing the erosion rate and the emission area;

$$\text{Mass flux} = \frac{\text{erosion rate}}{\text{emission area}}$$

$$= \frac{2.304\times10^{-3}\ g/s}{4.164\times10^{-5}\ m^2}$$

$$= 55.33\ g/m^2.s$$

By having the velocity and the mass flux of crystallite of 10 mm diameter of treated area, one can estimate the concentration of the crystallites close to the anode surface.

$$\text{Concentration} = \frac{\text{mass flux}}{\text{velocity}}$$

$$= \frac{55.33\ \text{g/m}^2\,\text{s}}{0.616\ \text{m/s}}$$

$$= 90.11\ \text{g/m}^3$$

For a 3 nm graphite sphere, the mass of a single particle is 6×10^{-20} g. Therefore, the number density of the particle can be estimated.

Number of density is = concentration/particle mass

$$= \frac{90.11\ \text{g/m}^3}{6\times10^{-20}\ \text{g}}$$

$$= 1.502 \times 10^{21}\ \text{m}^{-3}$$

2. Effect of surface temperature (T_s) on the number density of particle (*N*).

The number of density can be defining as follows;

where m_p is particle m $N = \frac{\lfloor \text{concentration} \rfloor}{m_p}$ kg. The relationship between vaporization rate function of surface temperature is shown Figure C.2.

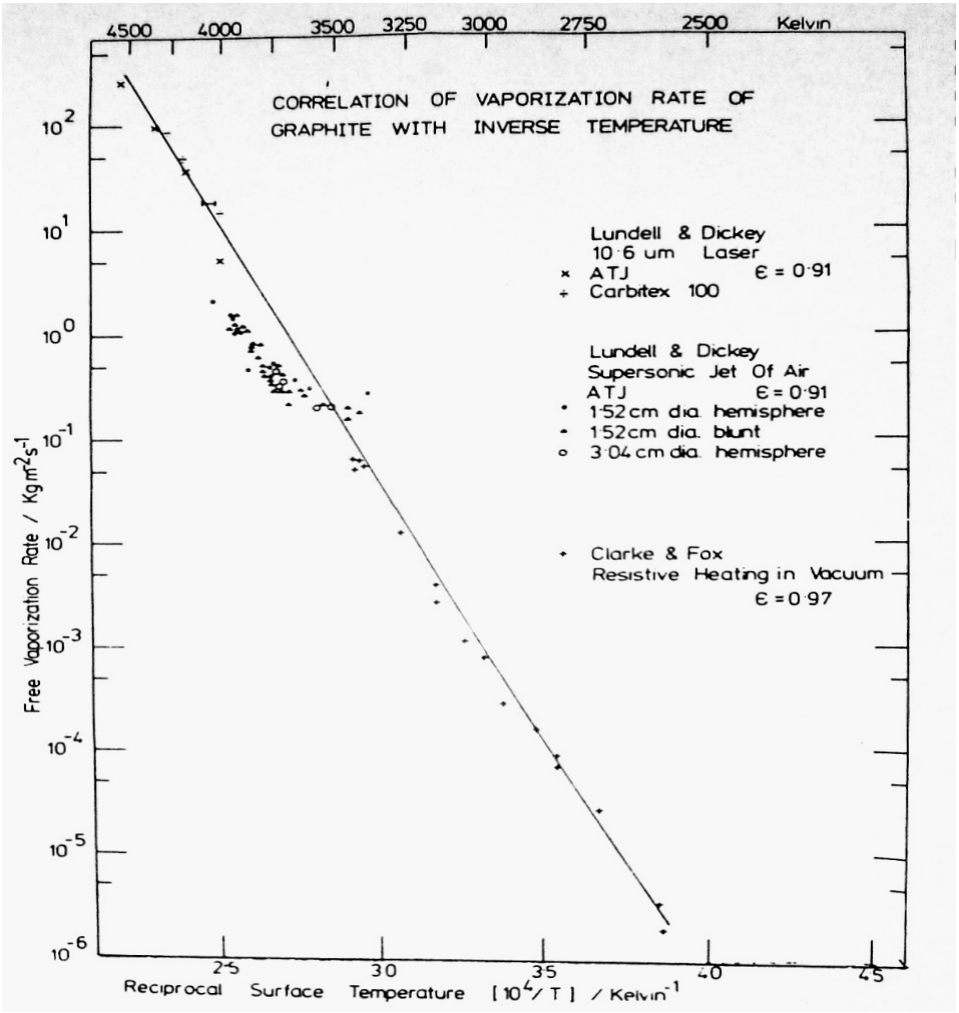

Figure C2 Correlation of vaporization rate of graphite with inverse temperature for high current arc (Abrahamson, Davies et al. 1980).

Using regression method and fitting the values from the graph, a mathematical equation can be derived to describe the free vaporization rate (mass flux) with a function of anode surface temperature. However, the correlation below was valid for a high current carbon arc.

$$massflux = 3\times10^{13e-11.352(\frac{10^4}{T_s})} \qquad \text{(C.1)}$$

Given that particle mass, m_p is 6 X10-23 kg and knowing that the particle velocity, v_p is 0.385 m/s, therefore the particle number density for various anode surface temperature can be estimated.

$$N = \frac{3\times10^{13e-11.352(\frac{10^4}{T_s})}}{2.31\times10^{-23}} \qquad \text{(C.2)}$$

Note: when comparing the erosion rate at certain surface temperature between the experimental work (image analysis in Appendix B) and the erosion rate from Figure C.2, it was found that the ratio is 0.054:1. We concluded the actual value of the erosion rate in our reactor is 5.5 % from the high current vaporization rate. This is reasonable since our continuous arc current is 10-15 times smaller than the normal high current carbon arc.

The effect of anode surface temperature is shown in the table below.

Table C1 Particle number density at various anode surface temperatures

$T_{s\,(K)}$	N
3000	1.355E+18
3200	1.442E+19
3300	4.225E+19
3400	1.162E+20
3500	3.017E+20
3600	7.428E+20
3700	1.742E+21
3800	3.905E+21
3900	8.400E+21
4000	1.739E+22
4100	3.475E+22
4200	6.718E+22

Appendix D COMSOL Model Report (Summarized)

8.1 1. Table of Contents

8.2 2. Model Properties

Property	Value
Model name	Arc plasma
Author	Hamdan Yusoff
Company	University of Canterbury
Department	Chemical and Process Eng.
Saved date	Nov 28, 2006 9:29:57 AM
Creation date	Jan 9, 2006 10:26:01 AM
COMSOL version	COMSOL 3.3.0.405

Application modes and modules used in this model:

- Geom1 (Axial symmetry (2D))
  - Incompressible Navier-Stokes
  - Meridional Electric and Induction Currents, Potentials (AC/DC Module)
  - General Heat Transfer (Heat Transfer Module)

8.3 3. Constants

Name	Expression	Value	Description
I0	16		Current (A)
diam	0.003		Cathode diameter (m)
area	pi*(diam^2)/4		Area (m2)
Js0	I0/area		Surface current density (A/m2)
T0	300		
sigma3	1e6		electrical conductivity close to anode

8.4 4. Geometry

Number of geometries: 1

8.4.6 4.1. Geom1

8.4.7 4.1.2. Boundary mode

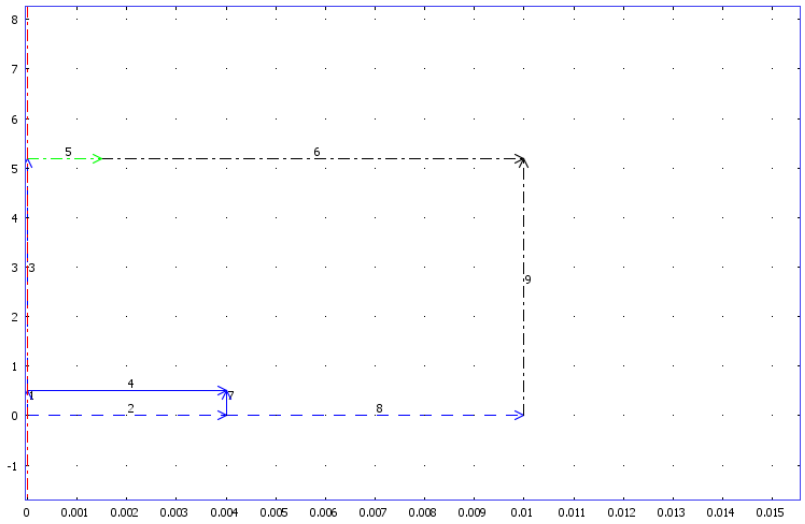

8.5 5. Geom1

Space dimensions: Axial symmetry (2D)

Independent variables: r, phi, z

8.6 5.1. Scalar Expressions

Name	Expression
p	10103
rho1	4752.8*(T^-1.3461)
k1	-1.055e-21*T^6+1.509e-17*T^-4.722e-14*T^4-1.368e-10*T^3+9.041e-7*T^2-1.293e-3*T+0.5725
cp1	-7.122e-18*T^6+1.432e-13*T^5-1.060e-9*T^4+3.703e-6*T^3-6.366e-3*T^2+5.134*T-359.8
Ts	-8.206e17*r^6+5.704e15*r^5-1.986e13*r^4+5.626e10*r^3-1.321e8*r^2+1.311e5*r+3708
Vs	-1.81e15*r^6+3.96e13*r^5-3.28e11*r^4+1.24e9*r^3-2.02e6*r^2+3.67e2*r+4

8.7 5.2. Mesh

8.7.8 5.2.1. Mesh Statistics

Number of degrees of freedom	44108
Number of mesh points	2498
Number of elements	4783

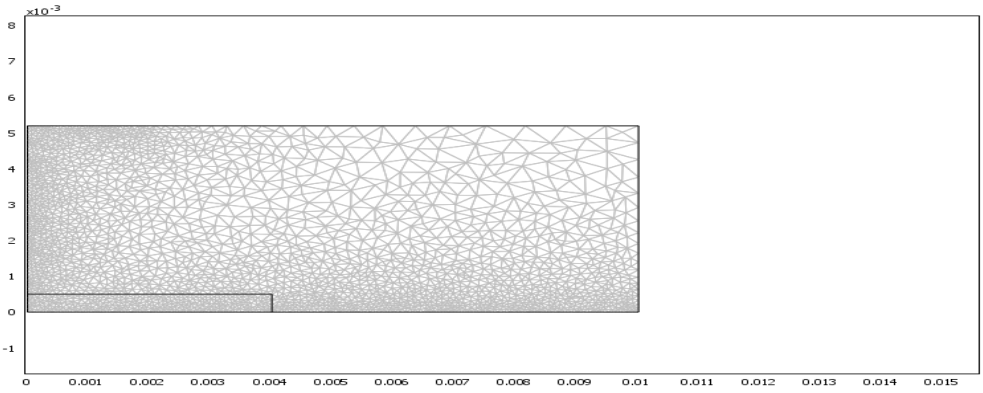

8.8 5.3. Application Mode: Incompressible Navier-Stokes (ns2)

8.8.9 5.3.1. Application Mode Properties

Property	**Value**
Default element type	Lagrange - P_2 P_1
Analysis type	Stationary
Stress tensor	Total
Corner smoothing	Off
Frame	Frame (rz)
Weak constraints	Off

8.8.10 5.3.2. Variables

Dependent variables: u3, v3, p3, nrw, nzw

8.8.11 5.3.4. Boundary Settings (e.g)

Boundary		1, 3	2
Type		Axial symmetry	Inflow/Outflow velocity
name			
r-velocity (u0)	m/s	0	0

z-velocity (v0)	m/s	0	**1**
phi-velocity (w0)	m/s	0	0
Pressure (p0)	Pa	0	0
weakconstr		1	1
Integration order (wcgporder)		{1;1}	{1;1}
Initial value (wcinit)		{0;0}	{0;0}

Boundary	4, 7	5, 8	6
Type	Neutral	Inflow/Outflow velocity	No slip
name			
r-velocity (u0)	0	0	0
z-velocity (v0)	0	0	0
phi-velocity (w0)	0	0	0
Pressure (p0)	0	0	**101300**
weakconstr	1	1	1
Integration order (wcgporder)	{1;1}	{1;1}	{1;1}
Initial value (wcinit)	{0;0}	{0;0}	{0;0}

Boundary	9
Type	Normal flow/Pressure
name	
r-velocity (u0)	0
z-velocity (v0)	0
phi-velocity (w0)	0
Pressure (p0)	**101300**
weakconstr	1
Integration order (wcgporder)	{1;1}
Initial value (wcinit)	{0;0}

8.8.12 5.3.5. Subdomain Settings

Subdomain		1	2
Shape functions (shape)		shlag(2,'u3') shlag(2,'v3') shlag(1,'p3')	shlag(2,'u3') shlag(2,'v3') shlag(1,'p3')
Integration order (gporder)		**4 4 2**	**4 4 2**
Constraint order (cporder)		**2 2 1**	**2 2 1**
name			
Density (rho)	kg/m^3	**rho(T)**	**rho(T)**

Dynamic viscosity (eta)	Pa·s	**eta(T)**	**eta(T)**
Volume force, r-dir. (F_r)	N/m^3	0	**-Jr_emqap*Bphi_emqap**
Volume force, z-dir. (F_z)	N/m^3	0	**-Jz_emqap*Bphi_emqap**
Volume force, phi-dir. (F_phi)	N/m^3	0	0
Isotropic diffusion switch (idon)		**1**	**1**
Tuning parameter (delid)		0.5	0.5
Streamline diffusion switch (sdon)		0	0
Streamline diffusion type (sdtype)		pgc	pgc
Tuning parameter (delsd)		0.25	0.25
Crosswind diffusion switch (cdon)		0	0
Crosswind diffusion type (cdtype)		sc	sc
Tuning parameter (delcd)		0.35	0.35
Pressure stabilization switch (pson)		0	0
Tuning parameter (delps)		1	1

Subdomain initial value		1	2
r-velocity (u3)	m/s	0	0
z-velocity (v3)	m/s	0	0
Pressure (p3)	Pa	0	0

8.9 5.4. Application Mode: Meridional Electric and Induction Currents, Potentials (emqap)

Application mode type: Meridional Electric and Induction Currents, Potentials (AC/DC Module)

8.10 5.5. Application Mode: General Heat Transfer (htgh)

Application mode type: General Heat Transfer (Heat Transfer Module)

Application mode name: htgh

8.10.135.5.1. Scalar Variables

Name	Variable	Value	Description
sigma	sigma_htgh	5.67e-8	Stefan-Boltzmann constant

6. Materials/Coefficients Library

9.1 6.1. Nitrogen, 1 atm

Parameter	Value
Heat capacity (C)	Cp(T)
Dynamic viscosity (eta)	eta(T)
Thermal conductivity (k)	k(T)
Kinematic viscosity (nu0)	nu0(T)
Density (rho)	rho(p,T)

7. Interpolation Functions

10.1 7.2. Interpolation Function: k

Interpolation method: Linear

x	f(x)

10.2 7.3. Interpolation Function: Cp

10.3 7.4. Interpolation Function: sigma

10.4 7.5. Interpolation Function: eta

10.5 7.6. Interpolation Function: rho

10.6 7.7. Interpolation Function: sigma2

Interpolation method: Piecewise Cubic

Data source type: Table

x	f(x)
3000	2.59e6
3400	3.80e6

3800	7.25e6
4000	1.36e7

8. Solver Settings

Solve using a script: off

Analysis type	Stationary
Auto select solver	On
Solver	Stationary
Solution form	Automatic
Symmetric	Off
Adaption	Off

11.1 8.1. Direct (UMFPACK)

Solver type: Linear system solver

11.2 8.2. Advanced

Parameter	**Value**
Constraint handling method	Lagrange multipliers
Null-space function	Automatic
Assembly block size	5000
Use Hermitian transpose of constraint matrix and in symmetry detection	Off
Use complex functions with real input	On
Stop if error due to undefined operation	On
Type of scaling	Automatic
Manual scaling	
Row equilibration	On
Manual control of reassembly	Off
Load constant	On
Constraint constant	On
Mass constant	On
Damping (mass) constant	On
Jacobian constant	On
Constraint Jacobian constant	On

9. Postprocessing

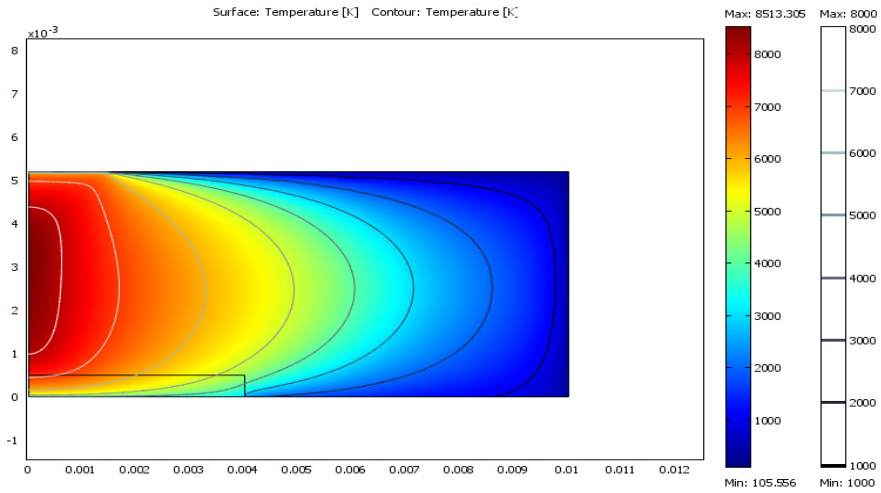

10. Variables (Example)

13.1 10.1. Boundary

13.1.1410.1.1. Boundary 1, 3, 6

Name	Description	Expression
K_r_ns2	Viscous force per area, r component	2 * nr_ns2 * eta_ns2 * u3r+nz_ns2 * eta_ns2 * (u3z+v3r)
T_r_ns2	Total force per area, r component	-nr_ns2 * p3+2 * nr_ns2 * eta_ns2 * u3r+nz_ns2 * eta_ns2 * (u3z+v3r)
K_z_ns2	Viscous force per area, z component	nr_ns2 * eta_ns2 * (v3r+u3z)+2 * nz_ns2 * eta_ns2 * v3z
T_z_ns2	Total force per area, z component	-nz_ns2 * p3+nr_ns2 * eta_ns2 * (v3r+u3z)+2 * nz_ns2 * eta_ns2 * v3z
dVolbnd_emqap	Volume integration contribution	Sr_emqap
nJ_emqap	Current density outflow	nr_emqap * Jr_emqap+nz_emqap * Jz_emqap
nJs_emqap	Source current density	unr * (Jr_emqap_down-Jr_emqap_up)+unz * (Jz_emqap_down-Jz_emqap_up)
unTMr_emqap	Magnetic Maxwell surface stress tensor, r component	-0.5 * Bphi_emqap_up * Hphi_emqap_up * dnr
dnTMr_emqap	Magnetic Maxwell surface stress tensor, r	-0.5 * Bphi_emqap_down * Hphi_emqap_down * unr

	component	
unTMz_emqap	Magnetic Maxwell surface stress tensor, z component	-0.5 * Bphi_emqap_up * Hphi_emqap_up * dnz
dnTMz_emqap	Magnetic Maxwell surface stress tensor, z component	-0.5 * Bphi_emqap_down * Hphi_emqap_down * unz
Jsr_emqap	Surface current density, r component	unz * (Hphi_emqap_down-Hphi_emqap_up)
Jsz_emqap	Surface current density, z component	-unr * (Hphi_emqap_down-Hphi_emqap_up)
normJs_emqap	Surface current density, norm	sqrt(abs(Jsr_emqap)^2+abs(Jsz_emqap)^2)
nPo_emqap	Power outflow	nr_emqap * Por_emqap+nz_emqap * Poz_emqap
Qs_emqap	Surface resistive heating	Jsr_emqap * Er_emqap+Jsz_emqap * Ez_emqap
plasma_nTMr_emqap	Exterior magnetic Maxwell stress tensor	unTMr_emqap
plasma_nTMz_emqap	Exterior magnetic Maxwell stress tensor	unTMz_emqap
plasma_nTr_emqap	Exterior Maxwell stress tensor (plasma), r component	plasma_nTMr_emqap
plasma_nTz_emqap	Exterior Maxwell stress tensor (plasma), z component	plasma_nTMz_emqap
ndflux_htgh	Normal conductive heat flux	nr_htgh * dflux_r_htgh+nz_htgh * dflux_z_htgh
ncflux_htgh	Normal convective heat flux	rho_htgh * C_htgh * T * (nr_htgh * u_htgh+nz_htgh * v_htgh)
ntflux_htgh	Normal total heat flux	ndflux_htgh+ncflux_htgh
J0_htgh	Surface radiosity expression	

rflux_htgh	Radiative flux	

13.1.1510.1.2. Boundary 2, 8

13.1.1610.1.3. Boundary 4, 7

13.2 10.1.4. Boundary 5

13.3 10.2. Subdomain

Name	Description	Expression
U_ns2	Velocity field	sqrt(u3^2+v3^2)
V_ns2	Vorticity	u3z-v3r
divU_ns2	Divergence of velocity field	u3r+v3z+u3/r
cellRe_ns2	Cell Reynolds number	rho_ns2 * U_ns2 * h/eta_ns2
res_u3_ns2	Equation residual for u3	r * (rho_ns2 * (u3 * u3r+v3 * u3z)+p3r-F_r_ns2)+2 * eta_ns2 * (u3/r-u3r)-eta_ns2 * (2 * r * u3rr+r * (u3zz+v3rz))
res_tst_u3_ns2	Variational equation residual for u3	r * (nojac(rho_ns2) * (nojac(u3) * u3r+nojac(v3) * u3z)+p3r)+2 * nojac(eta_ns2) * (u3/r-u3r)-nojac(eta_ns2) * (2 * r * u3rr+r * (u3zz+v3rz))
res_sc_u3_ns2	Shock capturing residual for u3	r * (rho_ns2 * (u3 * u3r+v3 * u3z)+p3r-F_r_ns2)+2 * eta_ns2 * (u3/r-u3r)
res_v3_ns2	Equation residual for v3	r * (rho_ns2 * (u3 * v3r+v3 * v3z)+p3z-F_z_ns2)-eta_ns2 * (r * (v3rr+u3zr)+2 * r * v3zz+u3z+v3r)
res_tst_v3_ns2	Variational equation residual for v3	r * (nojac(rho_ns2) * (nojac(u3) * v3r+nojac(v3) * v3z)+p3z)-nojac(eta_ns2) * (r * (v3rr+u3zr)+2 * r * v3zz+u3z+v3r)
res_sc_v3_ns2	Shock capturing residual for v3	r * (rho_ns2 * (u3 * v3r+v3 * v3z)+p3z-F_z_ns2)
beta_r_ns2	Convective field, r component	r * rho_ns2 * u3
beta_z_ns2	Convective field, z component	r * rho_ns2 * v3
Dm_ns2	Mean diffusion coefficient	r * eta_ns2
da_ns2	Total time scale factor	r * rho_ns2

SR_emqap	Infinite element radial coordinate	
Sr_emqap	Infinite element r coordinate	r
S0r_guess_emqap	Inner r coordinate default guess	0
Sdr_guess_emqap	Width in r direction default guess	0
rCylr_emqap	Infinite element r cylindrical vector, r component	
Sz_emqap	Infinite element z coordinate	z
S0z_guess_emqap	Inner z coordinate default guess	0
Sdz_guess_emqap	Width in z direction default guess	0
rCylz_emqap	Infinite element r cylindrical vector, z component	
detJ_emqap	Infinite element transformation matrix determinant	1
Jrr_emqap	Infinite element transformation matrix determinant, element rr	1
invJrr_emqap	Infinite element inverse transformation matrix, element	1

	rr	
Jrz_emqap	Infinite element transformation matrix determinant, element rz	0
invJrz_emqap	Infinite element inverse transformation matrix, element rz	0
Jzr_emqap	Infinite element transformation matrix determinant, element zr	0
invJzr_emqap	Infinite element inverse transformation matrix, element zr	0
Jzz_emqap	Infinite element transformation matrix determinant, element zz	1
invJzz_emqap	Infinite element inverse transformation matrix, element zz	1
dVol_emqap	Volume integration contribution	Sr_emqap * detJ_emqap
curlAphi_emqap	Curl of magnetic potential, phi component	Ar2zAz2r
depAr_emqap	Magnetic potential test variable, r component	Ar2
depAz_emqap	Magnetic potential test	Az2

	variable, z component	
Bphi_emqap	Magnetic flux density, phi component	curlAphi_emqap
Hphi_emqap	Magnetic field, phi component	(Bphi_emqap-Brphi_emqap)/(mur_emqap * mu0_emqap)
mu_emqap	Permeability	mu0_emqap * mur_emqap
Er_emqap	Electric field, r component	-V2r
Jpr_emqap	Potential current density, r component	-sigmarr_emqap * V2r
Jvr_emqap	Velocity current density, r component	-sigmarr_emqap * vz_emqap * Bphi_emqap
Jr_emqap	Total current density, r component	Jer_emqap+Jpr_emqap+Jvr_emqap
Ez_emqap	Electric field, z component	-V2z
Jpz_emqap	Potential current density, z component	-sigmazz_emqap * V2z
Jvz_emqap	Velocity current density, z component	sigmazz_emqap * vr_emqap * Bphi_emqap
Jz_emqap	Total current density, z component	Jez_emqap+Jpz_emqap+Jvz_emqap
normE_emqap	Electric field, norm	sqrt(abs(Er_emqap)^2+abs(Ez_emqap)^2)
normM_emqap	Magnetization, norm	abs(Mphi_emqap)
normBr_emqap	Remanent flux density, norm	abs(Brphi_emqap)
normB_emqap	Magnetic flux density, norm	abs(Bphi_emqap)
normH_emqap	Magnetic field, norm	abs(Hphi_emqap)
normJv_emqap	Velocity current density, norm	sqrt(abs(Jvr_emqap)^2+abs(Jvz_emqap)^2)
normv_emqap	Velocity, norm	sqrt(abs(vr_emqap)^2+abs(vz_emqap)^2)

normJp_emqap	Potential current density, norm	sqrt(abs(Jpr_emqap)^2+abs(Jpz_emqap)^2)
normPo_emqap	Power flow, norm	sqrt(abs(Por_emqap)^2+abs(Poz_emqap)^2)
normJe_emqap	External current density, norm	sqrt(abs(Jer_emqap)^2+abs(Jez_emqap)^2)
normJ_emqap	Total current density, norm	sqrt(abs(Jr_emqap)^2+abs(Jz_emqap)^2)
Wm_emqap	Magnetic energy density	0.5 * Bphi_emqap * Hphi_emqap
W_emqap	Total energy density	Wm_emqap
Q_emqap	Resistive heating	Jr_emqap * Er_emqap-Jr_emqap * vz_emqap * Bphi_emqap+Jr_emqap * Jer_emqap/sigma_emqap+Jz_emqap * Ez_emqap+Jz_emqap * vr_emqap * Bphi_emqap+Jz_emqap * Jez_emqap/sigma_emqap
Por_emqap	Power flow, r component	-Ez_emqap * Hphi_emqap
Poz_emqap	Power flow, z component	Er_emqap * Hphi_emqap
gradT_htgh	Temperature gradient	sqrt(Tr^2+Tz^2)
da_htgh	Total time scale factor	r * Dts_htgh * rho_htgh * C_htgh
dflux_r_htgh	Conductive heat flux, r component	-krr_htgh * Tr-krz_htgh * Tz
cflux_r_htgh	Convective heat flux, r component	rho_htgh * C_htgh * T * u_htgh
tflux_r_htgh	Total heat flux, r component	dflux_r_htgh+cflux_r_htgh
beta_r_htgh	Convective field, r component	r * rho_htgh * C_htgh * u_htgh
dflux_z_htgh	Conductive heat flux, z component	-kzr_htgh * Tr-kzz_htgh * Tz
cflux_z_htgh	Convective heat flux, z component	rho_htgh * C_htgh * T * v_htgh

tflux_z_htgh	Total heat flux, z component	dflux_z_htgh+cflux_z_htgh
beta_z_htgh	Convective field, z component	r * rho_htgh * C_htgh * v_htgh
dflux_htgh	Conductive heat flux	sqrt(dflux_r_htgh^2+dflux_z_htgh^2)
cflux_htgh	Convective heat flux	sqrt(cflux_r_htgh^2+cflux_z_htgh^2)
tflux_htgh	Total heat flux	sqrt(tflux_r_htgh^2+tflux_z_htgh^2)
Dm_htgh	Mean diffusion coefficient	r * (krr_htgh * beta_r_htgh^2+krz_htgh * beta_r_htgh * beta_z_htgh+kzr_htgh * beta_z_htgh * beta_r_htgh+kzz_htgh * beta_z_htgh^2)/(beta_r_htgh^2+beta_z_htgh^2+eps)
cellPe_htgh	Cell Peclet number	h * sqrt(beta_r_htgh^2+beta_z_htgh^2)/(Dm_htgh+eps)
res_htgh	Equation residual	r * (-krr_htgh * Trr-krz_htgh * Trz+rho_htgh * C_htgh * u_htgh * Tr-kzr_htgh * Tzr-kzz_htgh * Tzz+rho_htgh * C_htgh * v_htgh * Tz-Q_htgh)
res_sc_htgh	Shock capturing residual	r * (rho_htgh * C_htgh * u_htgh * Tr+rho_htgh * C_htgh * v_htgh * Tz-Q_htgh)